Study of Laboratory and Field Techniques to Measure Shear Wave Parameters - Frequency Effects

by

Hassan Ali

A thesis
presented to the University of Waterloo
in fulfillment of the
thesis requirement for the degree of
Doctor of Philosophy
in
Civil Engineering

Waterloo, Ontario, Canada, 2015

Author's Declaration

I hereby declare that I am the sole author of this thesis. This is a true copy of the thesis, including any required final revisions, as accepted by my examiners.

I understand that my thesis may be made electronically available to the public.

Abstract

Over the last decade, significance of correctly evaluating the dynamic properties of soil has been widely recognized by the research community. Among various parameters, shear wave velocity and damping ratio has been recognized as the key parameter for the soils subjected to dynamic loading. The shear wave velocity is used in the geotechnical assessments for site characterization, ground response analysis, and liquefaction potential. The dynamic properties of the soils can be attained in the lab or in-situ.

The dynamic soil properties are dependent on different state parameters, such as, void ratio, confining stress, water content, strain levels, and drainage conditions. Apart from the influence of the above parameters, the dynamic soil parameters are also affected by the frequency and the amplitude of the dynamic load applied to the soil. The in-situ tests compliments the laboratory testing in the evaluation of the dynamic soil parameters. Although, correlations can be used to estimate the in-situ parameters but a direct measurement is necessary. To develop a greater confidence of the results of the in-situ tests, it is helpful to compare the field results to conventional laboratory tests.

In the RC testing, the effect of base stiffness has a significant effect on shear modulus and damping values. In literature, only two studies have shown the effect of base fixidity. In this thesis, the issue is addressed by testing sand and clay sample on traditional bench and isolation table. In addition to base fixidity, coupling between the specimen and base platen is also very critical. Radial blades in top and bottom platen are introduced along with porous stone fixed underneath the blades.

Aluminum probes are recommended for the calibration of the RC device, however, the effect on shear modulus and damping as function of shear strain is not well studied. Therefore, the stiff probe is tested from low to large strains and effect on damping ratio is studied. Finally, a new BE method is proposed to understand the estimation of shear wave velocity at higher frequencies.

Due to the large variation in the interpretation of the BE tests results, there is no standard method for the estimation of the shear wave velocity. In this thesis, a new calibration procedure using state of the art laser vibrometer is used to understand the bending behavior of benders in air and in tip to tip configuration. Shear wave velocity comparison between RC and BE tests is done in usual practice, however, the frequency effects from these two tests are not well stated. In this study, the frequency effects are studied and a new methodology, modified frequency domain method, is introduced and tested on dry specimen. The results of the BE tests match well with the RC test

values.

MASW is a practiced field test to evaluate the shear wave velocity profile for geomaterials, however, the effect of frequency in the case of an anomaly has not been well understood. Therefore, this study uses numerical simulations and a lab scale model to study these effects. In addition, the effect of actual accelerometers on the measurements is studied for the first time using a high frequency laser vibrometer.

The frequency effects in field theory of the MASW and SCPT is also studied to address the actual limitations in the analysis of SCPT data without the consideration of frequency effects.

Based on the objective, this research focuses on: (1) the study of the laboratory resonant column and bender element tests, (2) numerical simulations and laboratory surface waves testing, and (3) field testing using surface waves and seismic cone penetration method for the estimation of shear wave parameters with emphasis on the frequency effects.

An important aspect of the laboratory testing is the calibration of the equipment. Standard procedures are available for the calibration of the resonant column (RC) device, however, the same is not true for the bender element (BE). In this study, the bender elements are calibrated using three different configurations, tip-to-tip, aluminum rods, and using state-of-art laser vibrometer. The State of art laser vibrometer is used to characterize the bending behavior of the bender elements showing the resonance frequency of 12 kHz and damping of 2 % when vibrating in air. The top and bottom platen of RC device were modified to allow better coupling between the specimen and benders. Radial blades were introduced to account for coupling of stiff clay specimens.

Four different soils (sand, stiff clay, mine paste, and leda clay) were tested in this study. The results of the tests, from the RC and the BE tests, were analyzed in the time and the frequency domains. Comparison of the results show, a maximum of 45 % difference in the velocity obtained from the RC and BE tests. Leda clay tests were done on the modified base platens and the difference in the V_s between the RC and BE is 6% compared to the stiff clay specimen where the difference is 28%.

To study the difference in the V_s values between the RC and BE, a new modified frequency domain method for BE testing is presented. The method was applied to the sand specimen. The sample is excited with a frequency sweep ranging from 0 to 52 kHz and change in unwrapped phase, between the input excitation and output response, is evaluated outside the range of resonant peaks of

the specimen. The V_s values from the two tests match well for the frequency range between 29 and 23 kHz, with overall less than 10 % error for the range of confinement range studied in this thesis.

Numerical simulations on homogeneous and non-homogeneous medium showed the change in the phase velocity of the Rayleigh waves (R-waves) due to the presence of a void. To introduce non-homogeneity, voids of various size and depth were used. Nine numerical models were analyzed, change in the phase velocity as a function of frequency was observed. A new methodology was introduced in which the receivers were divided into three sections, before, on-top, and after the void. Results from the dispersion curves show that the change in the phase velocity (function of frequency) is between 3% to 50% for different void width and depth.

Multichannel analysis of surface waves (MASW) test method was used as the geophysical testing method. The laboratory tests were conducted using three different configurations on sandbox. Two tests involved use of accelerometers as receivers, however, the input source was different. While the third test consisted of using state of art laser vibrometer as receiver. Using the laser vibrometer, 96 surface responses were recorded compared to 12 using accelerometers. The results from the laboratory MASW test showed the frequency effect on the measurements due to the source used in this method. Coupling of the geophone/transducer in surface wave testing is an important issue. Results from the lab test using laser vibrometer showed that the mass loading effect of accelerometer affects the frequency content of the signal.

The field MASW and the SCPT tests were done at the University of Waterloo Columbia Lake Test Site (UW-CLTS). The comparison of shear wave velocity from the field MASW and the SCPT shows the average shear wave velocity profile from the two tests, however, importance in not paid to the frequency of the input signal and main frequency difference between the MASW and SCPT tests. In this study, the frequency spectrum from the MASW and the SCPT tests data were analyzed to understand the change in the shear wave velocity at different depths. From the analysis, the percentage change in shear wave velocity between MASW line 1 and SCPT 1 and 2 is more than 90 % for depths between 0 and 2 m, while it reduces to 10 % for depths between 7 and 13 m.

Acknowledgements

First and foremost, thank to Almighty Allah for granting me strength, wisdom, confidence, and perseverance in completing this thesis. Without His grace and mercy, I would not have been able to accomplish this task.

My sincere gratitude to my supervisor Professor Giovanni Cascante, for his continuous support and guidance in the last five years. I hope that I could be as lively, enthusiastic, and energetic as him. He has a strong influence on my way of thinking about academics and life, which is definitely going to stay with me for years to come. Thank you for providing insightful discussions about the research and always being there for help.

I would like to thank my thesis committee: Professor J.D. Frost, Professor M. Pandey, Professor W. Xie, and Professor. Ponnu for their valuable feedback and suggestions.

A special thank you to all the members of the NDT and geotechnical engineering group: Dr. Kirlangic, S. Moayerian, Y. Wu, Dr. Atefi, S.B. Mahbaz, M.J. Rodriguez, M. Irfan, F. Alonso Diaz, Sabah Hassan, and W. Zhang. The time that I spent, with friends like you, at the school were one of the best days of my life and I will cherish them for my entire life. You all have been very kind to me and my family during this time, thank you! I would like to thank Dr. D. Basu for his suggestions during preparation and delivering of tutorials. Extended gratitude to Dr. Tallavo for his help and guidance and always taking out time to answer my questions.

No research is possible without the help of the non-teaching staffs. Special thanks to A. Allen, and T. Ridgway in the geotechnical lab; J. Bolt, Rick, C. Boyle, and Mark in the machine shop for providing assistance with the testing and development of new platens for RC tests. Thanks to all staff members of the Civil and Environmental Engineering department for providing continuous support during these years.

I also want to thank C. Philipps in Golder Associates for helping with MASW test; especially since the test is done in two inches of snow and $-30'C$ temperature! I am grateful to A. Nasseri-Moghaddam in Inspec Sol. for letting us borrow Geode for MASW testing and providing useful discussions for our conference paper.

Next, my sincere thanks to S. Bouchard, M. Finas, Professor P. Vanheeghe, Dr. J. Camacho-Tauta, and Professor A. Viana da Fonesca for their research collaboration and believing in me and my work.

No acknowledgments would be complete without extending thank you to my parents and family. My parents have been a constant source of love and inspiration for me during all these years. My sisters and brother appreciated by hardwork and gave me moral support for which I will always be thankful to them. Special thanks to my wife's parents and family as well for their understanding and encouragement.

Last,but not the least, I thank my wife Tasneem, for her unconditional love and support. It has been due to her patience, support, and unwavering belief in me that I have been able to complete this dissertation. These past five years have been very tough both financially and academically, but she stood beside me without complaint, just so that I could focus on my research and thesis. Two most valuable gifts that she has given me are Burhanuddin and Ruqaiya. They mean a world to me and I thank them for bringing joy in my life and smile on my face when the days got tense.

Finally, I would like to recognize the financial support provided by Natural Science and Engineering Research Council of Canada (NSERC); the University of Waterloo GRS program; GEOIDE; and OSAP. I also want to acknowledge the initial support from University of Engineering and Technology, Peshawar, Pakistan by providing funds in my first year of PhD studies.

Dedication

To my parents, loving wife Tasneem
and my two angels Burhanuddin and Ruqaiya.

Table of Contents

List of Tables

List of Figures

Glossary of Terms

Abbreviations and Notations

BE Bender Elements

SASW Spectral analysis of surface waves

CPT Cone Penetration Test

DC Dispersion Curve

FFT Fast Fourier Transform

MASW Multichannel analysis of surface waves

RC Resonant Column

SCPT Seismic Cone Penetration Test

2D FFT Two-dimensional Fast Fourier Transform

v Propagation velocity

∇^2 Laplacian operator

β Beta parameter for shear wave velocity coefficient

G shear modulus of soil

N total number of records in time

$S(f,k)$ set of data in frequency-wave number domain

T Length of record in time

V_P P-wave velocity

V_S Shear wave velocity

V_R Rayleigh-wave velocity, Phase velocity

F_b Lamb source constant parameter

σ_{ij} stress component, where i is the direction of the axis perpendicular to the plain of the stress, and j is the direction of the stress

ε_{ij} strain component, where i is the direction of the axis perpendicular to the plain of the strain, and j is the direction of the strain

$\overline{\varepsilon}$ cubical dilation or volumetric strain

$\overline{\omega}$ rotation about an axis

Δt sampling time

ρ mass density

λ wavelength

λ Lam constant

$\phi(f)$ phase difference for frequency

k wave number

K ratio of the surface wave velocity and shear velocity

u displacement

t time

$\overline{\omega}$ rotation about each axis

γ shear strain

M constraint modulus

Φ potential funtion associated with dilation for Rayleigh waves solution

Ψ potential function associated with rotation for Rayleigh waves solution

A_r amplitude of the reflected wave

A_t amplitude of the transmitted wave

R reflection coefficient

T transmission coefficient

z mechanical impedance

r distance to the source

ζ the coefficient that depends on the shape of the wave front for geometric attenuation

D damping ratio for intrinsic attenuation

Δ logarithmic decrement for intrinsic attenuation

Q quality factor for intrinsic attenuation

α attenuation coefficient for intrinsic attenuation

f_{nyq} Nyquist frequency

f_s sampling frequency

a_0 coefficient of the Fourier series that represents the average or mean value of the periodic signal

a_n coefficient of the Fourier series that represents the projection of the periodic signal on sine fuctions

b_n coefficient of the Fourier series that represents the projection of the periodic signal on cosine fuctions

ω angular frequency

i imaginary component of complex numbers

ω_N Nyquist angular frequency

DFT Discrete Fourier Transform

$IDFT$ Inverse Discrete Fourier Transform

$STFT$ Short Time Fourier Transform

$w(t)$ window function in the Short Time Fourier Transform

b time-shift parameter in the Short Time Fourier Transform

WT Wavelet Transform

$\Psi(t)$ Wavelet function in Wavelet Transform

a frequency scale parameter in Wavelet Transform

b time shift parameter in Wavelet Transform

CHAPTER 1

Introduction

Structural damage produced by earthquakes is strongly influenced by the response of soils to cyclic loading. Because the local site response is largely controlled by the dynamic properties of the soils. Recent earthquakes (e.g. Mexico City 1985, Northridge, 1994, and Hyogo-Ken Nanbu, 1995) have emphasized the importance of the local site response analysis and the soil amplification. Crow et al. (2011) showed the effect of high soil amplification in a soft soil even for low magnitude earthquakes ($M > 3.0$). Therefore, accurate determination of the dynamic soil parameters, shear modulus and damping ratio is critical for the geotechnical earthquake engineering problems.

According to 2010 National Building Code of Canada (NBCC) (NRC, 2010), measurement of the average shear wave velocity to a depth of 30 meters (V_{S30})is used to define the seismic site category for the design of civil infrastructures. Figure 1.1 presents the seismic hazard zones in Canada (Adams and Atkinson, 2003). Based on the geological history of these zones, there is a large variation in the stiffness and impedance of the subsurface and poses a challenge for the geotechnical engineers to use the design parameters for a similar site analysis. Hence, it is important to address these variations by evaluating the site specific dynamic soil parameters, namely shear wave velocity and damping ratio (Hunter and Atukorala, 2012).

The dynamic soil properties are dependent on different state parameters such as, void ratio,

confining stress, water content, strain levels, and drainage conditions. Apart from the influence of the above parameters, the dynamic soil parameters are affected by the frequency and amplitude of the dynamic load applied to the soil. In-situ tests compliments the laboratory testing in evaluation of the shear wave velocity and damping ratio. Although, correlations can be used to estimate the in-situ parameters, a direct measurement is required. A representation of the in-situ and laboratory test procedures is shown in Figure 1.2. Laboratory measurements have long been the reference standard for determining the properties of the geomaterials. To develop a greater confidence in the results of the in-situ tests, it is helpful to compare the field results to conventional laboratory testing (Schneider et al., 1999).

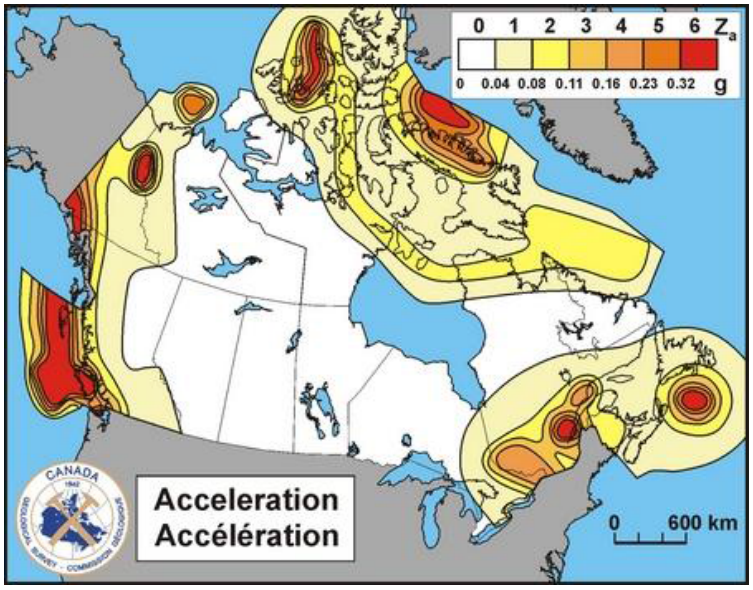

Figure 1.1: Ground motion acceleration hazard map for Canada according to NERHP zone classification (Adams and Atkinson, 2003), reported by (Hunter and Atukorala, 2012).

1.1 Research objective

There is a fundamental relationship between wave velocity , frequency, and wave-number $(V = f\lambda)$. However, the importance of the ratio between the specimen size and the wavelength has not been properly studied in the literature. Thus, this work presents a new comprehensive study of the effects

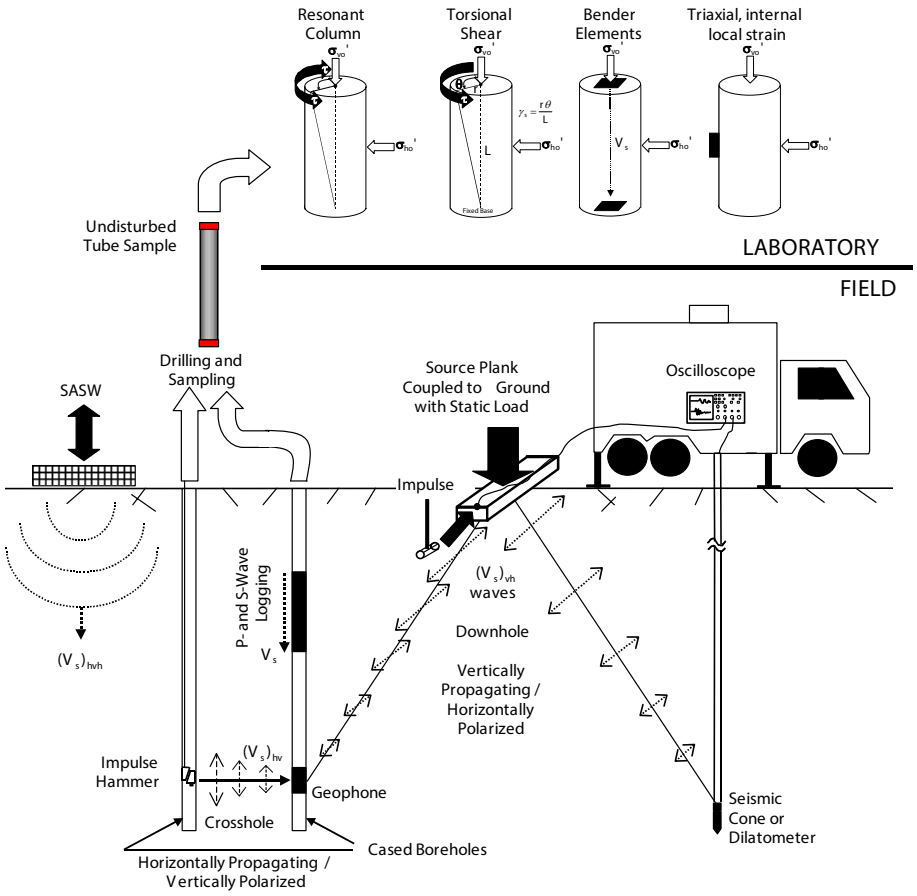

Figure 1.2: Schematic of laboratory and field methods for determination of shear modulus (Schneider et al., 1999).

of specimen size and wavelength using resonant column (RC), bender element (BE), multichannel analysis of surface waves (MASW), seismic cone penetration test, and numerical simulations.

The RC and BE tests are standard procedures in determining dynamic properties of soils at low strains; however, the effects of the different frequency ranges used in these tests has not been well understood.

In the RC tests, the effect of base fixidity has a significant effect on shear modulus and damping values. In literature, only two studies have shown the effect of base fixidity. In this thesis, the issue is addressed by testing sand and clay sample on traditional bench and isolation table. In addition to base fixidity, coupling between the specimen and base platen is very critical. A new coupling for top and bottom platen is designed which uses radial blades and degradation curves are studied for clay specimens to understand the effect at various strain levels. Aluminum probes are recommended for

the calibration of the RC device, however, the effect on shear modulus and damping as function of shear strain is not well studied. Therefore, the stiff probe specimen is tested from low strain to large strain and effect on damping ratio is studied. Finally, a new BE method is proposed to understand the estimation of shear wave velocity at higher frequencies.

Due to the large variation in the interpretation of the BE tests results, there is no standard method for the estimation of the shear wave velocity. In this thesis, a new calibration procedure using state of the art laser vibrometer is used to understand the bending behavior of benders in air and in tip to tip configuration. Shear wave velocity comparison between RC and BE tests is done in usual practice, however, the frequency effects from these two tests are not well stated. In this study, the frequency effects are studied and a new methodology, modified frequency domain method, is introduced and tested on dry specimen. The results of the BE tests match well with the RC test values.

MASW is a practiced field test to evaluate the shear wave velocity profile for geomaterials, however, the effect of frequency in the case of an anomaly has not been well understood. Therefore, this study uses numerical simulations and a lab scale model to study these effects. In addition, the effect of actual accelerometers on the measurements is studied for the first time using a high frequency laser vibrometer. No previous study using laser vibrometer as receivers is done for geomaterials for an MASW testing configuration.

The frequency effects in field theory of the MASW and SCPT is also studied to address the actual limitations in the analysis of SCPT data without the consideration of frequency effects.

The objectives are achieved using the following methodology:

- Resonant column and bender element test on four different four soils consisting of over consolidated stiff clay, mine paste, leda clay, and dry sand. Ten samples were tested (4 - stiff clay, 3 - leday clay, 2 - sand, and 1 - mine paste). The shear wave velocity obtained from RC and BE are compared as a function of confinement and strain.

- Development of a modified frequency domain methodology in bender element testing to compute shear wave velocity in soils. One sand sample is tested at effective confinement of 50, 100, 200, and 400 kPa. At each confinement RC and BE tests are done. In the modified frequency domain BE method, a frequency sweep (0 - 52 kHz) is applied to the transmitter

bender and transfer function between the output and input signal is obtained. Using the slope of the unwrapped phase, shear wave velocity is obtained. The results are compared with RC test.

- RC and BE measurements on isolation table to minimize the noise and geometric damping for sand and sensitive clay sample.

- Calibration of bender elements (transmitter and receiver) using three different test setup. Benders in air, tip to tip, and using aluminum rod. State-of-art laser vibrometer is used to evaluate the resonant frequency and damping of benders vibrations in air.

- Use of multichannel analysis of surface wave (MASW) method as a seismic survey method. The main advantage of MASW method is its ability to separate higher modes from the fundamental mode.

- Effect of coupling in laboratory surface wave testing by using three test setups: epoxy glue and stud, magnet, and laser (no contact). For each test setup, two lines of MASW tests are done. Accelerometers are used for stud and magnet configuration while laser is used for non-contact surface measurements. For each line of the MASW test, 12 accelerometers are used as recording measurements while for the laser 96 measurements are done. Effect of source and frequency content of the input source is studied.

- Numerical simulations (2D) used to understand the effect of lateral inhomogeneity on stiffness measurements. Nine models having voids (cavities) of variable width and depth are studied. A new methodology is developed in which the array of receivers is divided into three sections to understand the propagation of waves in presence of lateral inhomogeneity and effect on dispersion curves measurements as a function of frequency.

- Field test conducted at University of Waterloo geophysical test site are done using the MASW and the SCPT tests. Four lines of MASW and three SCPT tests were done. Source shots for MASW were done from sides of receivers array. Shear wave velocity profiles from the two tests are evaluated and differences in the shear wave velocity profile is studied using the frequency spectra obtained from time signals.

1.2 Thesis Organization

The thesis is organized in seven chapters. In the first chapter, motivation, objectives, and the organization of the thesis is presented.

Chapter 2 covers the review of laboratory and field methods for estimation of shear wave velocity. The chapter begins with a brief description of the available methods while detail description of bender element, resonant column, multichannel analysis of surface waves, and seismic cone penetration test is presented. Advantages and disadvantages of each methods are discussed.

Chapter 3 begins with the theory of wave propagation and presents a brief review of the seismic waves and attenuation of seismic waves. It discusses the signal processing techniques used in this research with emphasis on frequency domain analysis. A detailed review of the Fourier transform is provided which is used throughout this thesis for analysis of time signals.

Chapter 4 presents the results from the laboratory testing using BE and RC methods. The chapter begins with the calibration of the RC and the BE device. Standard calibration procedures were adopted for both tests. For the RC device, a large strain test was done to calibrate the stiff aluminum probe. For the BEs, two calibrations were performed in tip-to-tip configuration using the typical procedure and the state-of-art laser vibrometer. To understand the behavior of the BE bending, the BEs displacement to electric input signal in air was measured using laser. The results of the calibration were analyzed in time and frequency domains.

Next, the methodology, analysis, and results are presented for three different clay specimens (stiff soil, mine paste, and leda clay) and sand specimens. The test on sand and clay specimens are done using RC and BE tests. To account for the stiffness of clay specimens, the top and bottom platen of University of Waterloo resonant column (UW-RC) device is modified. Radial blades are introduced to account for coupling between the specimen and benders. RC and BE tests for leda clay and Barco sand were also performed on isolation table. In each test, shear modulus and damping ratio curves are obtained for small to large strains. Comparison between RC and BE are done to show the frequency effects in the two tests. A modified frequency domain method is presented and results of Barco sand were analyzed. The results of the modified frequency method show good agreement between the RC and BE shear wave velocities.

Chapter 5 deals with the laboratory tests using the MASW method. The motivation for this

chapter was to understand the propagation of surface waves in homogeneous medium and in the presence of lateral inhomogeneities, such as voids. This will help in understanding the field MASW test results presented in Chapter 6. The chapter begins with the analysis of results from numerical simulations. The results from the numerical model (2D) for the homogenous case (no-void) and in the presence of void are analyzed in the time and the frequency domains which includes, development of 2D Fourier transform plots and dispersion curves. Changes in the dispersion curve, due to the presence of void are tabulated and interpretation of results based on the normalized wavelengths are presented. The experimental tests were performed on a sandbox. Test was done with three different sources while the measurements are recorded using accelerometer and laser vibrometer. The MASW test method with laser vibrometer on geo-materials has not been reported previously in literature. The results are presented to show the effect of source and coupling and its effect on wave velocities and attenuation.

Chapter 6 presents the field results obtained from MASW and SCPT tests. The test was done at the geophysical test site at University of Waterloo near Columbia lake (UW-CLTS). Since Laurier creek is close to the site, the water table is at a shallow depth from the surface. The purpose of the field test is to understand the differences in the shear wave velocity profiles from MASW and SCPT tests. The difference is explained using the frequency analysis of the time domain data obtained from the two tests. The chapter begins with the experimental methodology for the test, followed by the explanation of the results of the two tests in time and frequency domains. Finally, the average shear wave velocity profile from the two tests are compared. The results are also compared with the cone penetration measurements.

Chapter 7 summarizes the key findings from this study and also provides the recommendations for the continuation of future studies.

CHAPTER 2

Brief review of laboratory and field shear wave velocity methods

2.1 Introduction

Dynamic soil properties (shear modulus and damping ratio) as a function of shear strain level and excitation frequency are critical for solving geotechnical problems involving dynamic loadings (e.g. earthquake, wind, and machine vibrations). Several methods are used to measure these dynamic properties using different devices. Each device has limitations in its attainable shear strain level and excitation frequency bandwidth. Moreover, boundary conditions, mode of excitation, and assumptions in the analysis affect the results. Therefore, test results from different devices are not always in agreement. Geomaterials store and dissipate energy; at low shear strain levels, the theory of viscoelasticity describes the phenomenon of wave energy dissipation in soils (Khan et al., 2008, Lai et al., 2001). One important property of a linear viscoelastic medium is that energy dissipation and shear modulus are not independent but related by the Kramers-Kronig equations (Booij and Thoone, 1982). Thus, the comparison of the results from different tests should be done considering differences in excitation frequencies.

Based on the typical variation of shear moduli with shear strain levels, three strain ranges are defined: (1) very small strain, (2) small strain, and (3) large strain (Sawangsuriya et al., 2005).The very small strain corresponds to the elastic threshold strain. Within this range, the material exhibits linear-elastic behavior and the shear modulus is independent of strain amplitude giving a maximum shear modulus (G_{max}). Figure 2.1 shows the variation of shear moduli with respect to shear strain levels for various geotechnical applications as measured by in-situ and laboratory tests. The evaluation of soil properties by sampling methods is a powerful tool; however, field test are

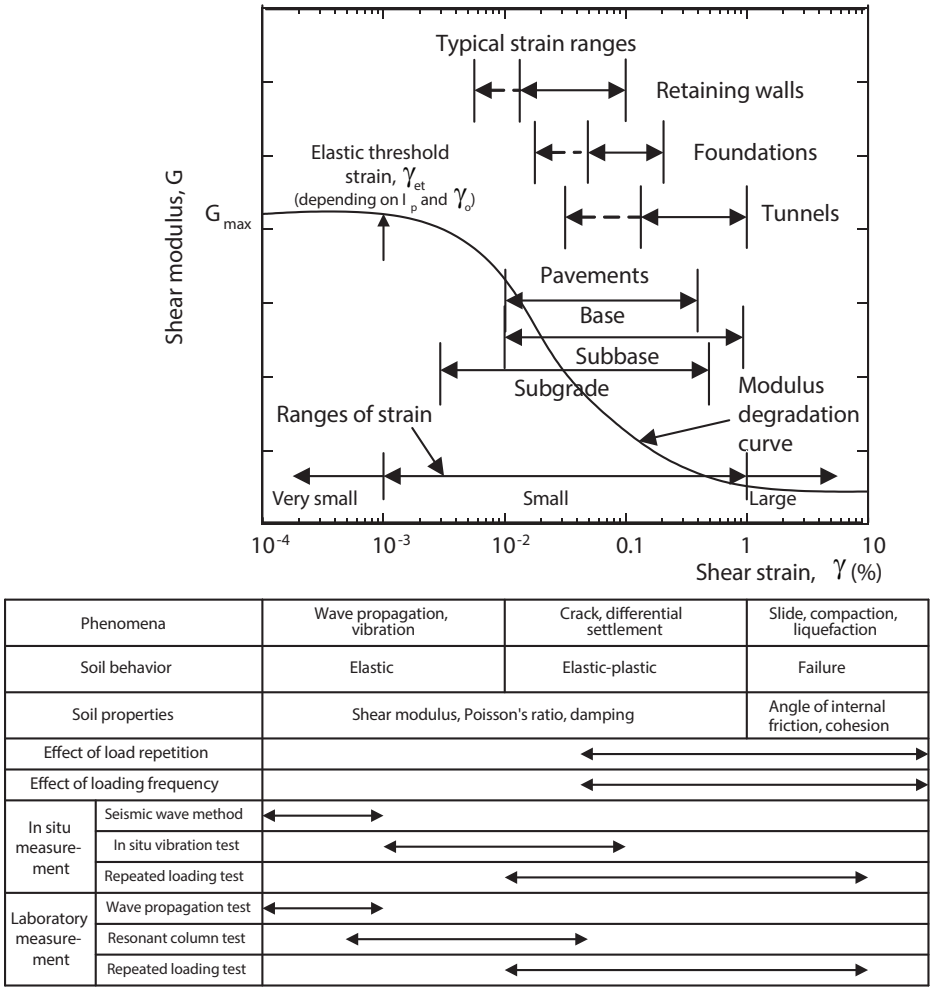

Figure 2.1: Variation of shear modulus with different strain levels (modified by (Sawangsuriya et al., 2005)

inefficient as depth increases and disturb in-situ conditions. Conversely, geophysics methods are not intrusive and can be used for to measure elastic soil properties in shallow depths. They induced small

enough strains to assume an elastic response of the medium. When a detailed space distribution of soil properties is needed, seismic methods provide unique information to complement and extrapolate data from boreholes. This chapter presents a summary of the main methods used in the laboratory and the field to evaluate the dynamic properties of soils at low strain levels. Specifically, the resonant column (RC) and bender element (BE) tests are reviewed for laboratory measurements. Whereas the multichannel analysis of surface waves (MASW) and seismic cone penetration tests (SCPT) for field measurements.

2.2 Laboratory methods

2.2.1 Bender element

In the last two decades, BE have been widely used to measure shear wave velocities at low shear strain level ($\gamma < 10^{-6}$). Shirley (1978) and Shirley and Hampton (1978) first introduced the use of piezocremaic bender elements in geotechnical equipment. Since then, BE have been used in a variety of equipment such RC, triaxial cell, oedometer, direct shear apparatus, and the centrifuge. The technique involves the use of piezocremaic bender elements at each end of a soil specimen. The BE at one end of the specimen (transmitter) is excited with a voltage signal. The signal generates a shear wave pulse which propagates along the length of the specimen and is received by the BE at the other end of the specimen (receiver). Shear wave velocity of the material is computed by evaluating the travel time between the transmitted and received signal and distance between the BEs. A typical BE signal is shown in Figure 2.2.

$$V_S = \frac{L}{\Delta t} \tag{2.1}$$

where L is the distance between the benders tip and Δt is the time for the wave to travel from transmitter to receiver bender. Measurement of distance is easy to compute and involves the distance between the transmitter and receiver tips; however, no reliable method is available for determination of first arrival and interpretive procedures vary from one user to next. The following paragraphs outline methods available in the literature.

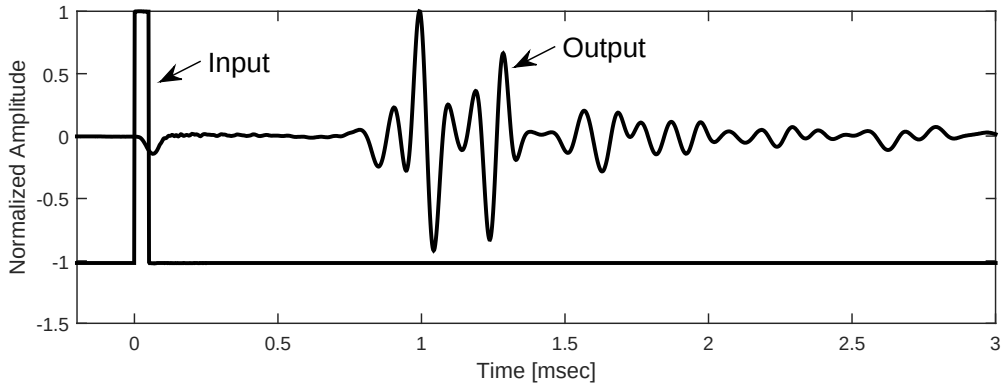

Figure 2.2: Typical BE signal showing the input and output signals.

The most common approach is by visual inspection of the received signal. The first major deflection of the signal (Figure 1) is taken as the shear wave arrival time (Viggiani and Atkinson, 1995, Jovičić et al., 1996) . However, factors such as near field effects, wave reflections, sample size and geometry, boundary effects, directivity, and cross talk results in error in the travel time approach (Sánchez-Salinero et al., 1986, Brignoli et al., 1996, Arulnathan et al., 1998, Arroyo et al., 2003, 2006, Lee and Santamarina, 2005).

Another approach that is based on both time and frequency domain was suggested by Viggiani and Atkinson (1995), Brocanelli and Rinaldi (1998),Blewett et al. (1999),and others by using multiple reflections. The method was used to limit the uncertainties in the travel time and distance between BEs; however, multiple reflections are not always obvious and are dependent on the amount of attenuation of the signal (Bonal et al., 2012). Cross-correlation was first suggested by Viggiani and Atkinson (1995) to test soil specimen at small strain using BEs. Lee and Santamarina (2005) recommended cross-correlation of first and second arrival events to provide accurate travel times. An automated system for measuring travel time based on cross-correlation was developed by Mohsin et al. (2004). Similarly, Wang et al. (2007) recommended a cross-correlation method only if the near field effect is not pronounced.

To overcome the limitations of time domain methods discussed in previous paragraphs, frequency domain approach have gained much attention. Phase-delay method, first introduced by Viggiani and Atkinson (1995) and later by Arroyo et al. (2003) and Greening and Nash (2004) developed a method in which travel time is evaluated in frequency domain. The travel time is computed from the slope of unwrapped phase angle of the cross-power spectrum. To take into account effects of

near field on received signal, Arroyo et al. (2003) developed a criterion which ensures that the shear wave velocity are computed outside the influence of near field effect.

In the last few years, wavelet analysis is used to measure shear wave arrival times (Brandenberg et al., 2008, Bonal et al., 2012). Brandenberg et al. (2008), based on wavelet analysis observed that travel times measures by wavelet correlation are less sensitive to noise and near-field effects as compared to visual picking. Bonal et al. (2012) used singularity in the signal to allow detection of first arrival of the shear wave; where it was supposed to be disguised by the presence of near-field effect due to compressive wave and noise. The approach however, requires a good quality input signal and a high sampling frequency is necessary to obtain reliable results.

The main drawback of the BE method is the difficulty in the interpretation of the results due to some degree of uncertainty. A clear identification of the arrival time is not always possible. Especially, spatial and boundary conditions (among others: wave reflections, coupling or near field effects, likewise overshooting at high frequencies) should be mentioned here as limitations of this technique. Additionally, the lack of knowledge of the actual behaviour of the peizoceramic elements inside the soil sample is one of the most important issue in BE testing. While free conditions, the main impact on the response of the transmitter has its own resonant frequency and not the excitation frequency as suspected. Under embedded conditions, the stiffening of the medium causes the increase in the natural frequency as well as in the damping ratio and the decrease in the magnitude of the oscillation (Camacho-Tauta et al., 2015). Furthermore, the applicability of BE method is restrained for stiff geomaterials such as compacted soils, cemented soils (naturally or artificially) or weak rocks, because of the greater stiffness resistance between the tested materials and the transducers (Ferreira et al., 2014).

2.2.2 Resonant column

This device permits testing a specimen under axi-symmetric loading, in steady state vibration, and in free vibration. There are different types of resonant columns, depending on the boundary conditions and mode of vibration. Wilson and Dietrich (1960) developed a fixed-free resonant column to measure both longitudinal and torsional vibrations. Hardin and Richart (1963) described two devices with free-free end conditions to measure torsional and longitudinal vibrations. Hardin

and Music (1965) developed a resonant column device which allowed the application of deviatoric axial loads. All these devices were designed to operate at small strains (in the range of 10^{-5}). In 1967, Drnevich (Drnevich, 1967) developed a free-fixed resonant column which allowed for strains greater than 10^{-4}. Later, devices that combine resonant column and torsional shear were designed to measure dynamic properties of soils for shear strains between 10^{-6} and 10^{-1} (Drnevich, 1985).

Two parameters are obtained from resonant column measurements: resonant frequency and damping coefficient. Wave velocity and attenuation are computed from these measurements. The computation of the damping coefficient assumes an equivalent, uniform, linear viscoelastic specimen, i.e. Kelvin-Voigt model (Drnevich, 1978, Hardin and Scott, 1966). This model predicts a response similar to the response observed in sand specimens, even though damping in sands is not necessarily of viscous nature. The frequency dependency of wave velocity and attenuation is difficult to obtain with this device because of problems involved in measuring high resonant modes (see (Stoll, 1979) for alternative approaches).

Several testing effects on resonant column results have been studied including: aging due to number of cycles (Drenevich and Richart, 1970), coupling between the specimen and end platens (Drnevich, 1978) , restraint of the sample due to end platens and membrane penetration Frost (1989) suggested that the latex membrane should have thickness less than 1% of the specimen diameter. In general, these effects are negligible when the shear strain amplitude is small ($\gamma < 10^{-4}$). Furthermore, small deformations permit assuming in-plane strain conditions in data interpretation. The shear strain varies radially throughout the specimen; the representative value most often selected is the shear strain at r=0.707*R, where R is the radius of the sample. This strain is an average strain for the volume of the sample.

Dynamic soil properties in RC tests are evaluated at the resonant frequency of the specimen (ASTM D 4105-92). The conventional analysis of RC tests assumes an elastic system with zero damping for the evaluation of shear modulus. The damping ratio is computed independently from the shear modulus using the free vibration, half-power bandwidth method, or transfer function method. Frequency dependent soil properties are difficult to evaluate using resonance methods, as they require significant changes in the geometry of the specimen.

The resonant column-torsional shear device is a laboratory apparatus specifically designed to measure dynamic properties of soils for shear strains between 10^{-6} and 10^{-1}. The resonant test is

essentially non-destructive; therefore, the dynamic properties can be evaluated at different confining pressures for each soil specimen. The small shear strain produced with the resonant column apparatus is in the same order of magnitude as geophysical in-situ tests. Elastic wave velocity and attenuation are sensitive to changes in soil fabric, since they are affected by the grain contact distribution and force contact distribution. Thus, resonant column testing has been suggested to evaluate low-strain soil behavior under anisotropic states of stress and varied stress-strain histories.

The impedance mismatch between the sample and the resonant column pedestal can play an important role in the energy dissipation mechanism. If boundary conditions are ignored, the damping calculated could include both specimen and apparatus damping. On the other hand, if the relative stiffness of the apparatus with respect to the specimen is not enough to ensure the fixed condition, the shear modulus will be underestimated. Drnevich (1978) recommended that the stiffness of the fixed end of the resonant column should be at least ten times the stiffness of the specimen. Avramidis and Saxena (1990) stiffened a Drnevich-type resonant column in order to test specimens with resonance frequencies grater than 300 Hz, which was the upper bound of the original apparatus. They found important differences between the results of the original apparatus and the modified one, for a Monterey sand No.O subjected to 588 kPa of confinement. The effect was more pronounced on the measured damping coefficient.

The principle advantage of the resonant column test is its flexibility. The testing environment may be changed to evaluate the effects changes in confining pressures, large shear strain amplitudes, stress-histories, and duration of loading.

Disadvantages of the method include unavoidable disturbances of the soil sample caused by unloading and reloading, possible disturbances caused by handling, and the problem of reproducing the in-situ confining pressures. Correction of damping for problems with equipment compliance. This compliance can mange the overestimation of damping, which mainly occurs at small strains.

2.3 S-wave velocity in particulate geomaterials

The S-wave velocity in particulate geomaterials depends on the state of the stress history, void ratio, degree of saturation, and type of particles. The velocity-effective stress relationship for granular materials is expressed as a power function with parameters α and β. The parameters represents the

s-wave velocity at a given state of stress and its variation with stress changes. The velocity-stress power relationship for granular media under isotropic loading is expressed as (Roosler, 1979)

$$V_S = \alpha(\sigma)^{\beta} \tag{2.2}$$

here Vs is the shear wave velocity profile, σ_o is the isotropic effective stress. Santamarina et al. (2001) described the physical meaning of the parameters α and β: the coefficient α relates to the type of packing, while the exponent β relates to the effect of contact behavior. Both parameters indicate the effects of stress history, cementation and rock weathering in the formation. For example, dense sands, overconsolidated clays, and soft rocks have higher coefficient α and lower exponent β. In the case of loose sands, normally consolidated clays, and clays with high plasticity, the coefficient α becomes lower while the exponent becomes higher. Santamarina et al. (2001) suggested an inverse relationship between α and β values for various granular media, ranging from sands and clays to lead shot and steel pheres:

$$\beta = 0.36 - \frac{\alpha}{700 m/sec} \tag{2.3}$$

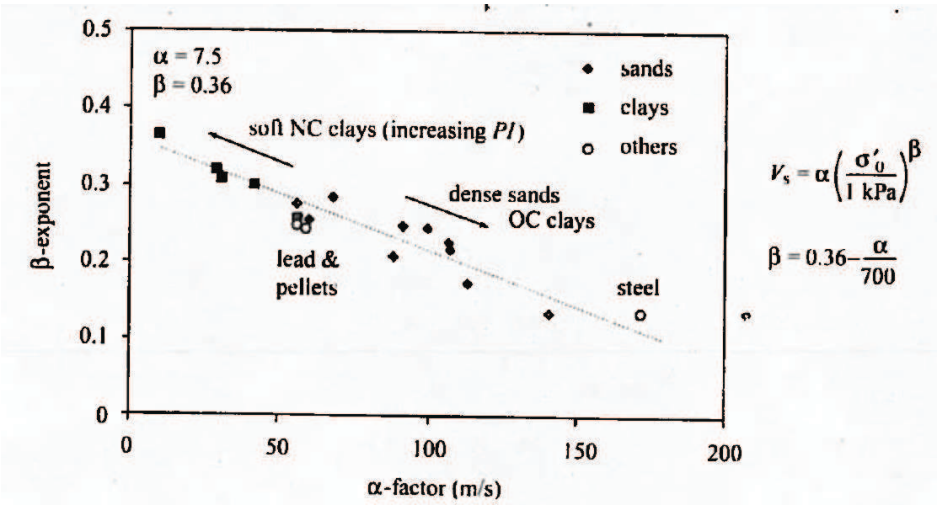

Figure 2.3: Typical values of α and β for RC test.

2.4 In-situ (field) methods

2.4.1 Multichannel analysis of surface waves (MASW)

As indicated before - about two-thirds of a seismic energy produced by seismic source propagates as Rayleigh waves (R-waves). Therefore, the propagation of R-waves is used in geotechnical site characterization. R-waves are dispersive in layered medium, i.e., the phase velocity is a function of frequency; which results in different wavelengths (λ) for each frequency component. Using the dispersive property of R-waves elastic properties of near-surface profile can be obtained. The spectral analysis of surface waves (SASW) method (Heisey et al., 1982) is widely used in estimation of near surface shear wave velocity (V_s) profile. A typical configuration of SASW method consists of an impulsive source and a pair of receivers. The main disadvantages of SASW method are low signal-to-noise ratios and the re-configuration of the receivers cover the required length of site investigation. These limitations are overcome by using the MASW method which utilizes several receivers in a single test.

A typical configuration of MASW test is shown in Figure 2.4. The MASW test is conducted in three steps:

- obtain multichannel field records (surface responses) generated by seismic sources
- determine the theoretical dispersion curve by computing the phase velocities of the surface waves
- and finally, extract the variation of the shear wave velocity with depth (1 D or 2 D V_s profile).

The source used to generate R-waves or surface waves in the MASW test can be transient load, random noise (active), ambient noise (passive), or steady state excitation. The source should generate a broad frequency range so that energy from the source is detected by the farthest receiver. The maximum investigation depth is determined by the longest wavelength generated. A longer wavelength (deeper penetration) is achieved with a greater impact power. One commonly accepted criteria for the penetration depth (z) is:

$$\frac{\lambda_R}{3} < z < 2\lambda_R \tag{2.4}$$

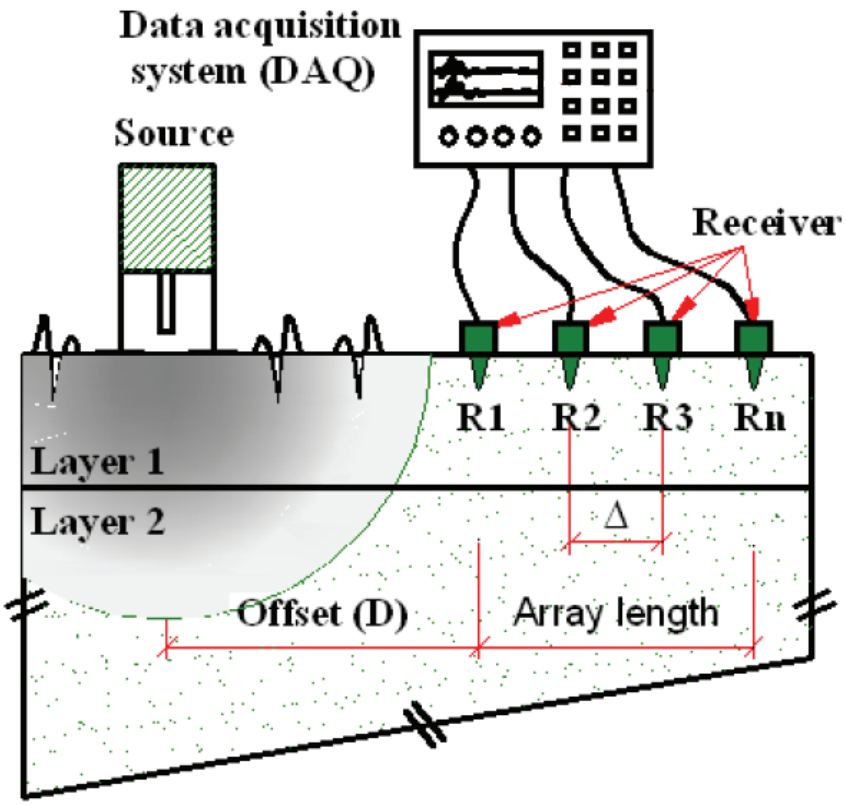

Figure 2.4: Layout of MASW field test (Nasseri-Moghaddam, 2006)

The surface responses are usually recorded on vertical geophones having a resonant frequency of 4.5 Hz. The receivers are placed in line with the seismic source at an equal spacing. The spacing of the receivers determine the minimum reliable wavelength (λ_{min}) that can be extracted from a MASW test. To avoid spatial aliasing, Park et al. (1999) suggested $\lambda_{min} = 2\Delta$. The array geometry commonly used for the MASW test is the common receiver midpoint geometry (CRMP) or common source geometry (CS) as shown in Figure 2.5. In the CRMP geometry, an imaginary midpoint is considered for the receiver array, and the array is scaled up around the center line. In the CS geometry, the source location is kept constant and the array receivers are scaled to cover large areas. In general, the choice of array length, offset value (D), and receiver spacings (Δ) have significant effect on the test results. The experimental dispersion curve is obtained by calculating the frequency content of each time signal. The time delay for each frequency component is computed from the

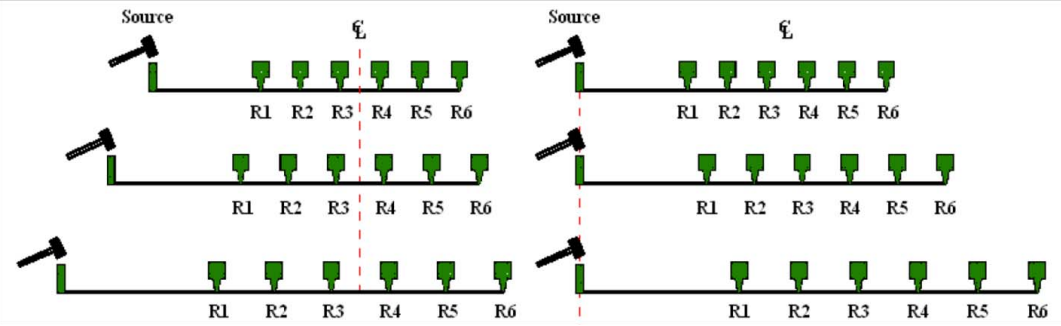

Figure 2.5: Geometry for MASW test (a) CRMP geometry and (b) CS geometry (Nasseri-Moghaddam, 2006)

phase difference between each receivers by:

$$t(f) = \frac{\phi(f)}{2\pi f} \tag{2.5}$$

where $\phi(f)$ is the phase difference in radian and f is frequency in Hz. The phase velocities are then calculated as distance over time as:

$$V_R = \frac{\Delta x}{t(f)} \tag{2.6}$$

where Δx is the receiver spacing. The wavelength is finally calculated as:

$$\lambda_R = \frac{V_R}{f} \tag{2.7}$$

The plot of values for V_R versus frequency or λ_R is called experimental dispersion curve. The theoretical dispersion is obtained by assuming the propagation of a plane wave front in a horizontally layered medium (Park et al., 1999). Poisson ratio ν , shear wave velocity V_s, density ρ, depth of layer h, and number of layers are important parameters required for the calculation of the dispersion curve. Finally, the theoretical and experimental dispersion curves are compared until a good match among the two curves are obtained. This iterative technique is called inversion.

The shear modulus profile is obtained from the final dispersion curve. Two inversions algorithms are available, the velocity-inversion approach and the complete-inversion approach. In the velocity-inversion approach, the thickness and number of layers are assumed and the shear wave velocity is

inverted; while, in the complete-inversion approach the velocity and thickness and number of layers are are unknowns and are changed during iteration.

2.4.2 Seismic cone penetration test (SCPT)

Of particular value in routine site exploration is the seismic piezocone test SCPT as it is a hybrid procedure that combines cone penetration readings (ASTM D5778) with geophysical downhole shear wave velocity measurements (ASTM D7400) into one sounding. During the penetration part of the SCPT, continuous records of q_t, f_s, and u_2 are collected over a 1-m interval, whereby during the temporary halt for the next rod addition, a downhole test is performed. This involves an impulse-type surface source generator to create a shear wave that is monitored by a velocity transducer (geophone) located within the penetrometer.

While the original setup simply employed a sledgehammer and crossbeam for the source Campanella et al. (1986), improvements in the recorded signals, reliability, and quality of the derived shear wave profiles are attained by use of an autoseis unit because of its repeatability and consistency (Mayne and McGillivray, 2008).

Advantages:

- Continuous profiling of soil layers with multiple readings with depth: q_t, f_s, u_2, and V_s
- Determination of G_{max} for all stress-strain curves, shallow and deep foundations, seismic site amplification analysis
- Economical compared with other V_s methods

	In-situ (MASW and SCPT)	Laboratory (BE and RC)
Pros	Provide precise boundary elevations often missed by drilling techniques	Enable the effects of increasing strain levels to be assessed on soil behavior particularly changes in effective stress, strength and stiffness
	Provide accurate profiling information, including the proportion of soil inclusions and the proportion of intermittent layers of higher permeability	Soil samples can be reconsolidated to take account of the increases in effective stresses caused by the foundation loading
	Provide information on natural soil variability within geological units	Tests are performed in a controlled environment of strain-rate, drainage and temperature
	Provide information on the characteristics of the soil matrix	Soil behavior under cyclic loading conditions can be assessed
Cons	Do not provide information on the effect of the foundation on soil behavior	A much smaller amount of soil is being tested so macro effects may not be representative of macrobehaviour
	Do not provide information on the effect of different rates of loading on soil behavior	Sensitive to the quality of the test specimen and the method of specimen preparation (particularly sand soils)
	Do not provide information on soil behavior under cyclic loading conditions	

CHAPTER 3

Theoretical Background

3.1 Waves Propagation

3.1.1 Waves in an infinite, homogenous, isotropic, elastic medium

The one - dimensional wave equation is expressed by (Richart et al., 1970):

$$\frac{\partial^2 u}{\partial t^2} = V^2 \frac{\partial^2 u}{\partial x^2} \tag{3.1}$$

where V is the propagation velocity. Systems that could be described by the wave equation are the longitudinal and torsional vibration in rods, pressure waves in an ideal fluid along the axis of the container, and the transverse vibrations of a string (Richart et al., 1970). The equilibrium of a small element in an elastic medium is shown in Figure 3.1. On each face of the element stresses are represented by orthogonal vectors, with solid vectors shown on the visible faces while dotted vectors shown on the hidden faces. Translational equilibrium of this element can be expressed by

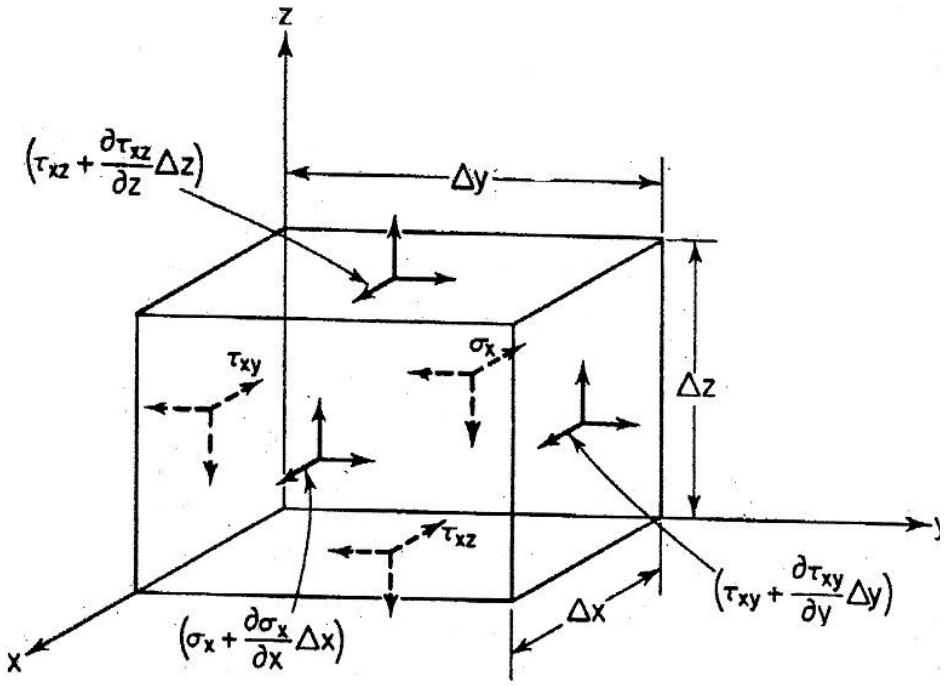

Figure 3.1: Infinitesimal cube showing stresses in x-direction on an elastic medium (Richart et al., 1970)

writing the sum of forces acting parallel to each axis. In the x-direction the equilibrium equation is

$$\left(\sigma_x+\frac{\partial\sigma_x}{\partial x}\Delta x\right)\Delta y\Delta z-\sigma_x\Delta y\Delta z+\left(\tau_{xy}+\frac{\partial\tau_{xy}}{\partial y}\Delta y\right)\Delta x\Delta z-\tau_{xy}\Delta x\Delta z+\left(\tau_{xz}+\frac{\partial\tau_{xz}}{\partial z}\Delta z\right)\Delta x\Delta y-\tau_{xz}\Delta x\Delta y \tag{3.2}$$

Similar equations can be written for the summation of forces in the y- and z-directions. Applying Newton's second law in the x-direction and ignoring body forces the equation of motion is given as

$$\left(\frac{\partial\sigma_x}{\partial x}+\frac{\partial\tau_{xy}}{\partial y}+\frac{\partial\tau_{xz}}{\partial z}\right)\Delta x\Delta y\Delta z=\rho\left(\Delta x\Delta y\Delta z\right)\frac{\partial^2 u}{\partial t^2} \tag{3.3}$$

Similar equations to Equation 3.3 can be written for y- and z- directions. Therefore, the equation of motion for x-direction in terms of stresses can be written as

$$\rho\frac{\partial^2 u}{\partial t^2}=\frac{\partial\sigma_x}{\partial x}+\frac{\partial\tau_{xy}}{\partial y}+\frac{\partial\tau_{xz}}{\partial z} \tag{3.4}$$

where u is the displacement in the x-direction. Similar equations can be obtained for y- and z-directions. To represent the right-hand side of Equation 3.4 in terms of displacement, the following relationships for an elastic medium will be used:

$$\begin{aligned} \sigma_x &= \lambda\,\overline{\varepsilon} + 2G\varepsilon_x \qquad \tau_{xy} = \tau_{yx} = G\gamma_{xy} \\ G &= \frac{E}{2(1+\nu)} \qquad \lambda = \frac{\nu E}{(1+\nu)(1-2\nu)} \end{aligned} \tag{3.5}$$

where ν is the Poisson's ratio, λ and G are Lam*é* constants. $\overline{\varepsilon}$ is the cubical dilatation or volumetric strain and is defined by $\overline{\varepsilon} = \varepsilon_x + \varepsilon_y + \varepsilon_z$. Relationships for strain and rotation in terms of displacement are given by

$$\varepsilon_x = \frac{\partial u}{\partial x} \quad \gamma_{xy} = \frac{\partial v}{\partial x} + \frac{\partial u}{\partial y} \quad 2\,\overline{\omega}_x = \frac{\partial w}{\partial y} - \frac{\partial v}{\partial z} \tag{3.6}$$

where $\overline{\omega}$ is the rotation about each axis. Substituting Equation 3.5 and Equation 3.6 into Equation 3.4 and simplifying yields the equation of motion for elastic medium in terms of stress and strain.

$$\rho\frac{\partial^2 u}{\partial t^2} = (\lambda + G)\frac{\partial \overline{\varepsilon}}{\partial x} + G\nabla^2 u \tag{3.7}$$

Similar equations can be written for displacements in y- and z-directions.

$$\rho\frac{\partial^2 v}{\partial t^2} = (\lambda + G)\frac{\partial \overline{\varepsilon}}{\partial y} + G\nabla^2 v \tag{3.8}$$

$$\rho\frac{\partial^2 w}{\partial t^2} = (\lambda + G)\frac{\partial \overline{\varepsilon}}{\partial z} + G\nabla^2 w \tag{3.9}$$

where *Laplacian* operator ∇^2 represents

$$\nabla^2 = \frac{\partial^2}{\partial x^2} + \frac{\partial^2}{\partial y^2} + \frac{\partial^2}{\partial z^2} \tag{3.10}$$

Two possible solutions to wave equation can be found by differentiating Equation 3.7. The first solution describes the propagation of wave due to volume change(irrotational wave), while the

second solution describes the wave propagation due to rotation (equivoluminal wave). The wave velocities are given by

$$V_P = \sqrt{\frac{\lambda + 2G}{\rho}} = \sqrt{\frac{M}{\rho}} \tag{3.11}$$

$$V_S = \sqrt{\frac{G}{\rho}} \tag{3.12}$$

where M is the constraint modulus and G is the shear modulus.

3.1.2 Waves in Elastic Half-Space

The two types of solution discussed in the previous section are possible only for an infinite elastic medium. In an infinite half-space, a third solution of equation of motion is obtained; which corresponds to a wave confined to the near free surface. This type of wave was first studied by Lord Rayleigh in 1885 and is known as *Rayleigh Wave* or surface wave. To define the displacements in x- and z- directions (u and w respectively), two potential functions Φ and Ψ are introduced. The potential functions in terms of displacements are represented as

$$u = \frac{\partial \Phi}{\partial x} + \frac{\partial \Psi}{\partial z} \quad and \quad w = \frac{\partial \Phi}{\partial z} - \frac{\partial \Psi}{\partial x} \tag{3.13}$$

The dilation $\overline{\varepsilon}$ and the rotation $2\ \overline{\omega}_y$ in the x-z plane is

$$\begin{aligned} \overline{\varepsilon}_x &= \frac{\partial u}{\partial x} + \frac{\partial w}{\partial z} = \frac{\partial}{\partial x}\left(\frac{\partial \Phi}{\partial x} + \frac{\partial \Psi}{\partial z}\right) + \frac{\partial}{\partial z}\left(\frac{\partial \Phi}{\partial z} - \frac{\partial \Psi}{\partial x}\right) = \nabla^2 \Phi \\ 2\,\overline{\omega}_y &= \frac{\partial u}{\partial z} - \frac{\partial w}{\partial z} = \frac{\partial}{\partial z}\left(\frac{\partial \Phi}{\partial x} + \frac{\partial \Psi}{\partial z}\right) - \frac{\partial}{\partial x}\left(\frac{\partial \Phi}{\partial z} - \frac{\partial \Psi}{\partial x}\right) = \nabla^2 \Psi \end{aligned} \tag{3.14}$$

Potential functions Φ and Ψ are associated with the dilatation and rotation and therefore Rayleigh waves can be considered as a combination of p- and s- waves that satisfy certain boundary conditions. Substitution of the expressions for u and w into equation of motion (Equation 3.7 and 3.9)gives

(Richart et al., 1970)

$$\rho \frac{\partial}{\partial x}\left(\frac{\partial^2 \Phi}{\partial t^2}\right)+\rho \frac{\partial}{\partial z}\left(\frac{\partial^2 \Psi}{\partial t^2}\right)=(\lambda+2G)\frac{\partial}{\partial x}\left(\nabla^2 \Phi\right)+G\frac{\partial}{\partial z}\left(\nabla^2 \Psi\right)$$
$$\rho \frac{\partial}{\partial z}\left(\frac{\partial^2 \Phi}{\partial t^2}\right)-\rho \frac{\partial}{\partial z}\left(\frac{\partial^2 \Psi}{\partial t^2}\right)=(\lambda+2G)\frac{\partial}{\partial z}\left(\nabla^2 \Phi\right)-G\frac{\partial}{\partial x}\left(\nabla^2 \Psi\right) \tag{3.15}$$

The above equations are satisfied if

$$\frac{\partial^2 \Phi}{\partial t^2}=\frac{\lambda+2G}{\rho}\nabla^2 \Phi=v_P^2 \nabla^2 \Phi$$
$$\frac{\partial^2 \Psi}{\partial t^2}=\left(\frac{G}{\rho}\right)\nabla^2 \Psi=v_S^2 \nabla^2 \Psi \tag{3.16}$$

In order to find the solution of above Equations, a sinusoidal wave traveling in the positive x direction is assumed, the expressions for Φ and Ψ can be written as

$$\Phi=\mathbf{F}(z)\,e^{i(\omega t-kx)} \tag{3.17}$$

and

$$\Psi=\mathbf{G}(z)\,e^{i(\omega t-kx)} \tag{3.18}$$

where the functions F and G describe the amplitude variation of the R-wave with depth and k is the wave number defined by, k = $\frac{2\pi}{L}$ where L is the wavelength. Substitution the expressions for Φ and Ψ from Equation 3.17 and 3.18 into Equation 3.16 yields

$$-\frac{\omega^2}{v_P^2}F(z)=-k^2 F(z)+\frac{d^2F(z)}{dz^2}$$
$$\textit{and} \tag{3.19}$$
$$-\frac{\omega^2}{v_S^2}G(z)=-k^2 G(z)+\frac{d^2G(z)}{dz^2}$$

Solution to these equations can be written as

$$F(z) = A_1 e^{-qz} + B_1 e^{qz}$$
$$G(z) = A_2 e^{-sz} + B_2 e^{sz} \tag{3.20}$$

where

$$q^2 = k^2 - \frac{\omega^2}{v_P^2}$$
$$s^2 = k^2 - \frac{\omega^2}{v_S^2} \tag{3.21}$$

In Equation 3.20 the component B_1 and B_2 are zero as the displacement amplitude approaches infinity with increasing depth. Finally, the potential functions can be written as (Richart et al., 1970)

$$\Phi = A_1 e^{-qz+i(\omega t - kx)} \tag{3.22}$$

and

$$\Psi = A_2 e^{-sz+i(\omega t - kx)} \tag{3.23}$$

Boundary conditions at the surface (z = 0) of half-space imply zero stresses ($\sigma_z = 0$ and $\tau_{zx} = 0$). From the solutions of Φ and Ψ and definitions of u and w, the free surface boundary condition is given as

$$\frac{A_1}{A_2} \frac{(\lambda + 2G) q^2 - \lambda k^2}{2iGks} - 1 = 0 \tag{3.24}$$

$$\frac{A_1}{A_2} \frac{2iqk}{s^2 + k^2} + 1 = 0 \tag{3.25}$$

Rayleigh wave velocity and displacements

Using Equation 3.24 and 3.25, the Rayleigh wave velocities and displacements can be determined. Adding and cross multiplying Equation 3.24 and 3.25 we get

$$4\,q\,G\,s\,k^2 = (s^2+k^2)\,[(\lambda+2G)\,q^2-\lambda\,k^2] \tag{3.26}$$

From the definition of q and s and dividing by $G^2\,k^8$, we get

$$16\,(1-\frac{\omega^2}{v_P^2\,k^2})\,(1-\ frac\omega^2 v_S^2 k^2) = (2-\frac{\lambda+2G}{G}\,\frac{\omega^2}{v_P^2\,k^2})^2\,(2-\frac{\omega^2}{v_S^2\,k^2})^2 \tag{3.27}$$

The following definitions are used to simplify above equation:

$$K = \frac{\omega^2}{v_S^2\,k^2} = \frac{v_R}{v_S} \tag{3.28}$$

$$\alpha\,K = \frac{\omega^2}{v_P^2\,k^2} = \frac{v_R}{v_P} \tag{3.29}$$

$$\frac{\lambda+2G}{G} = \frac{1}{\alpha^2} = \frac{2-2\,\nu}{1-2\,\nu} \tag{3.30}$$

Equation 3.27 can be re-written as

$$16\,(1-\alpha^2\,K^2)\,(1-K^2) = (2-\frac{1}{\alpha^2}\,\alpha^2\,K^2)^2\,(2-K^2)^2 \tag{3.31}$$

Rearranging to obtain

$$K^6-8K^4+(24-16\alpha^2)\,K^2+16(\alpha^2-1) = 0 \tag{3.32}$$

Equation 3.32 is referred to as Rayleigh Equation. It is a cubic equation in K^2, the roots of which depends on the Poisson ratio (ν) of the elastic medium. K is the ratio of the surface wave velocity

and shear wave velocity. The solution of Rayleigh equation shows that K^2 is independent of the frequency. The ratios of v_R/v_S and v_P/v_S are obtained from Equation 3.32 and are shown in Figure 3.2 for values of Poisson's ratio ν from 0 to 0.5. The Rayleigh wave displacements are obtained by

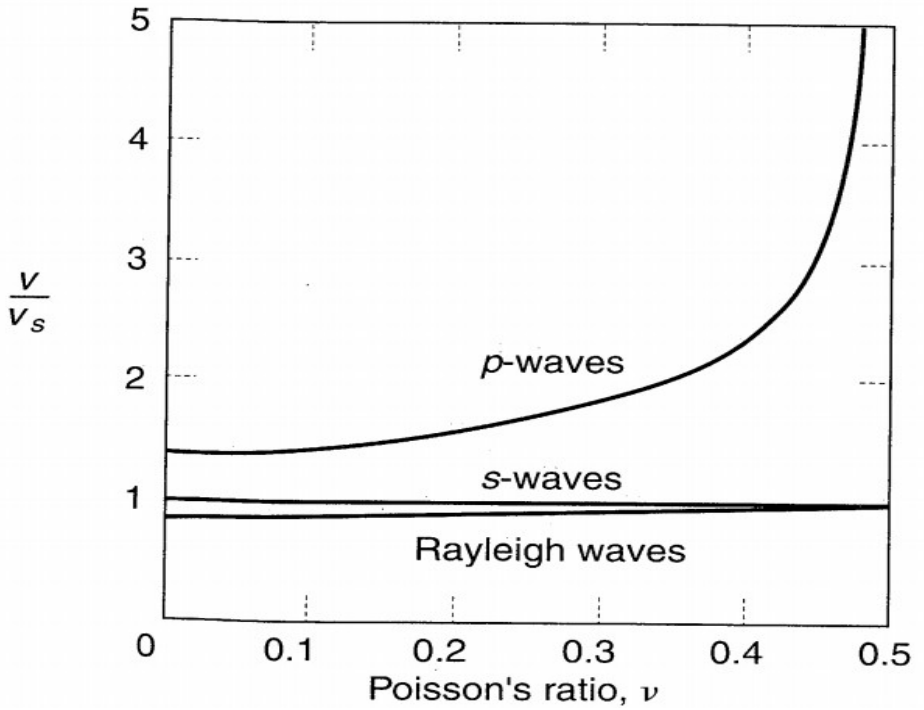

Figure 3.2: Variation of body waves and Rayleigh wave velocities as a function of *Poisson's* ratio (Kramer, 1996)

substituting the solutions for potential functions Φ and Ψ into Equation 3.13 and carrying out the necessary partial differentiations gives (Kramer, 1996):

$$u = A_1 ike^{-qz+i(\omega t-kx)} - A_2 se^{-sz+i(\omega t-kx)} \tag{3.33}$$

$$w = (-A_1 ike^{-qz+i(\omega t-kx)}) + A_2 ike^{-sz+i(\omega t-kx)} \tag{3.34}$$

Using Equation 3.25, the variation of u and w with depth is given as

$$u = A_1 (-ike^{-qz} + \frac{2q, isk}{s^2+k^2} e^{-sz}) e^{i(\omega t-kx)} \tag{3.35}$$

$$w = A_1 \left(\frac{2qk^2}{s^2+k^2} e^{-sz} - q e^{-qz} e^{i(\omega t - kx)}\right) \tag{3.36}$$

Figure 3.3 shows the variation of u and w with depth for Poisson's ratio ν = 0.25 and 0.50.

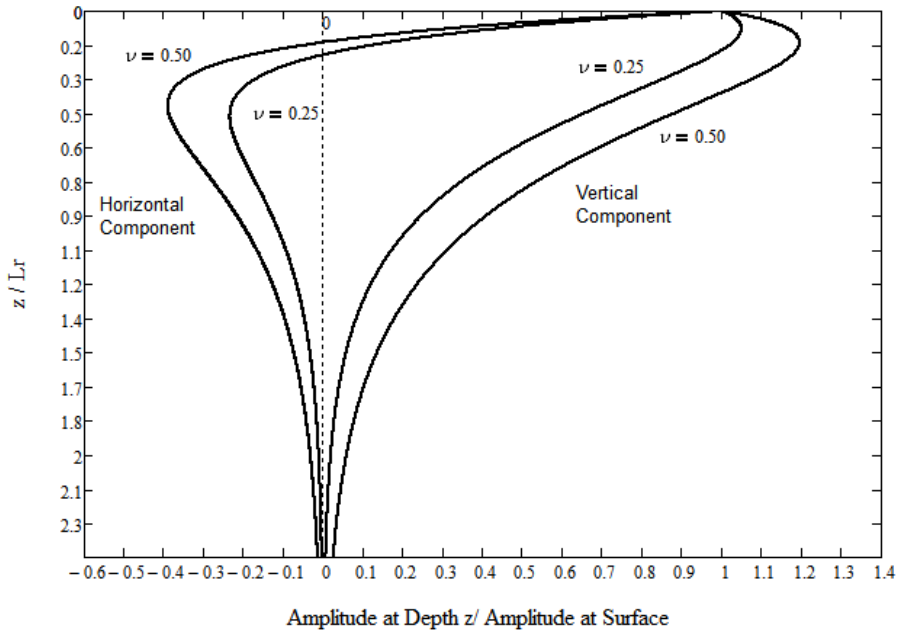

Figure 3.3: Horizontal and vertical motion of Rayleigh waves for Poisson's ratio ν = 0.25 and 0.50.

3.2 Seismic Waves

The propagation of seismic waves requires the internal deformation of the material. The arrival time of these waves on seismogram stations give information about both the type seismic source and the average wave velocity of the material through which they pass. Seismic waves can be broadly categorized into body waves and surface waves; which are described in the following sections.

Body Waves: Waves that propagate within an elastic medium are called body waves. The two types of body waves are (p-waves and s-waves) as shown in Figure 3.4. P-waves are fastest to travel within a medium. P-waves are also known as primary wave, compressional or longitudinal wave because the particle motion takes place in the direction of wave propagation. Similar to sound waves, P-waves can travel through solids and fluids.

The second type of body waves (S-waves) are known as secondary waves, shear waves, or transverse waves; they cause shear deformations as the wave propagate through the medium. The particle motion is perpendicular to the direction of wave propagation. S-waves can only travel through solids because fluids can not sustain shear deformations. The direction of particle motion in S-waves can be in the horizontal plane (SH) or in the vertical plane (SV). Body wave velocity generally increases with depth; because, the stiffness of the geologic materials increases with depth.

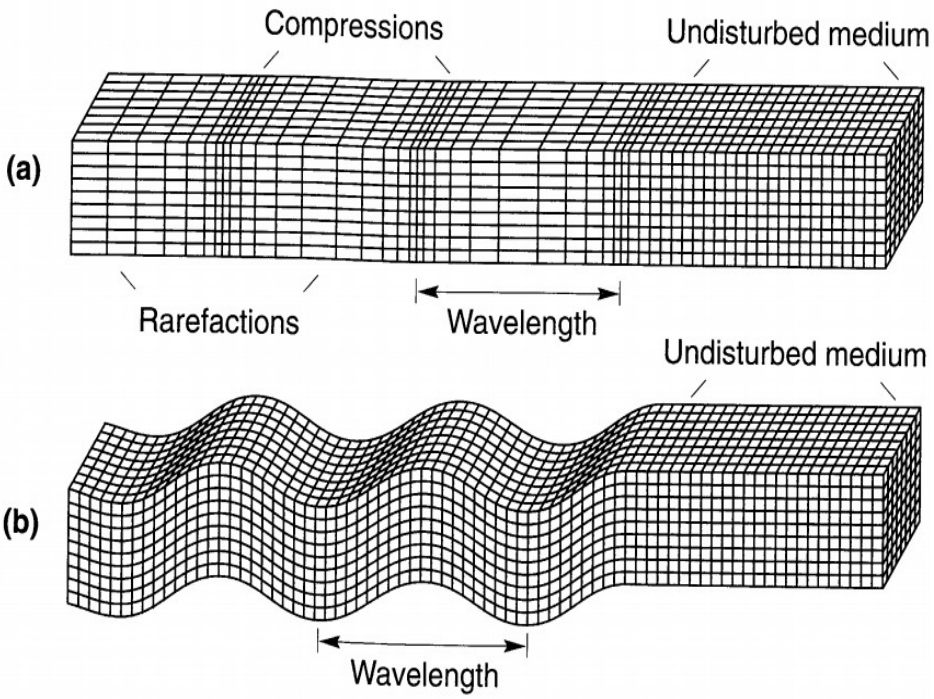

Figure 3.4: Propagation mechanism for body waves (a) p-waves and (b) s-waves (Kramer, 1996)

Surface Waves: Surface waves are produced due to the interaction of body waves and surface of the earth. Their maximum amplitude is at the surface; which decreases exponentially with depth. There are two types of surface waves; Rayleigh and Love waves (Lord Rayleigh,1885, and Love, 1911). An important property of surface waves is dispersion, i.e., different frequencies travel with different velocities. Figure 3.5 shows the propagation of Rayleigh and Love wave in an elastic medium. The Love wave results from the interaction of SH-waves with a soft superficial layer. These waves have no particle motion in vertical direction. The particle motion is parallel to the surface and decrease exponentially with depth. The Rayleigh waves are produced from the interaction of P and SV waves. The particle motion is counter clockwise (retrograde) at the surface; which changes

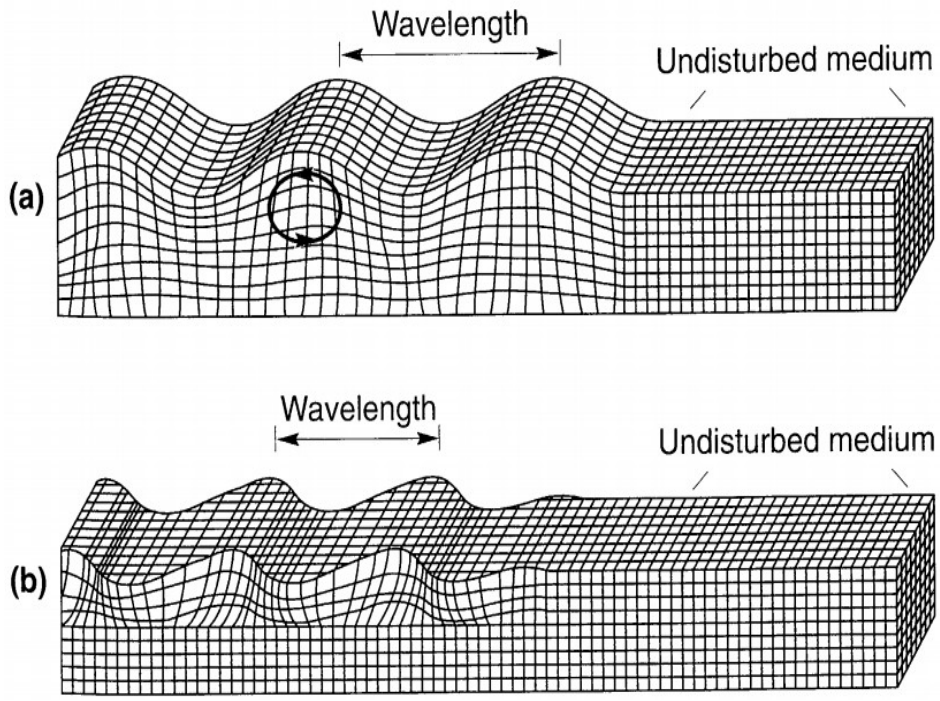

Figure 3.5: Propagation mechanism for surface waves (a) Love-waves and (b) Rayleigh-waves (Kramer, 1996)

to clockwise (prograde) at greater depth. Rayleigh waves propagating in a homogeneous medium are not dispersive. However, soils are not homogeneous and Rayleigh waves become dispersive. Long period (lower frequency) waves travel faster and reach to greater depths than short period (higher frequency) waves; which travel slow and penetrate to shallower depths. The dispersion of Rayleigh wave is an useful property in site characterization for geotechnical engineering problems. In a homogenous media the following equation gives good estimates of Rayleigh wave velocity as a function of shear wave velocity (Viktorov, 1967).

$$V_R = \frac{0.87 + 1.12\nu}{1 + \nu} \tag{3.37}$$

The assumption of an homogeneous elastic medium is useful for explaining the wave propagation of body waves and surface waves. However, in real situations the problem is much more complicated with soil layers of variable thickness and variable elastic properties. In a layered medium the incident wave front is reflected, transmitted, or refracted depending on the characteristics of the medium. In the following section, reflection, transmission, and mode conversion are discussed.

Reflection and Transmission: When a wave propagating from medium 1 (density ρ_1 and velocity v_1) to a medium 2 (ρ_2 and velocity v_2); reaches the interface with an amplitude A_i part of its energy is reflected and part of its energy is transmitted to medium 2. The amplitude of reflected and transmitted waves are given as A_r and A_t, respectively. Compatibility conditions require that the sum of incident and reflected wave must be equal to transmitted wave,($A_i + A_r = A_t$). While, equilibrium conditions are satisfied if the summation of forces at the interface are equal, i.e., $\sum F_1 = \sum F_2$. Solving the equilibrium and compatibility condition simultaneously, the following expressions for reflection (R) and transmission (T) coefficient are obtained in terms of the mechanical impedance (z).

$$R = \frac{A_r}{A_i} = \frac{1 - \frac{z_1}{z_2}}{1 + \frac{z_1}{z_2}} \tag{3.38}$$

$$T = \frac{A_t}{A_i} = \frac{2}{1 + \frac{z_1}{z_2}} \tag{3.39}$$

where $z_1 = \rho_1 v_1$, and $z_2 = \rho_2 v_2$. For an impedance ratio (z_1/z_2) greater than 1, the incident wave is approaching a stiffer material, while, for ratio less than 1, the incident is approaching a softer material.

Mode conversion: If an incident wave front approaches an interface at an angle; three waves (P, SH, and SV) impinge the interface as shown in Figure 3.6. When a P-wave hits an interface, P and S waves are reflected and transmitted. Similarly, when SV-wave strike an interface, both transmitted and reflected P and SV-waves are generated. Whereas, in the case of SH-wave there is no motion perpendicular to the interface and only reflected and transmitted SH-waves are generated (Kramer, 1996).

3.3 Seismic Wave Attenuation

Attenuation is defined as the decrease in the wave amplitude with distance. The three most important factors in decay of wave amplitude are:

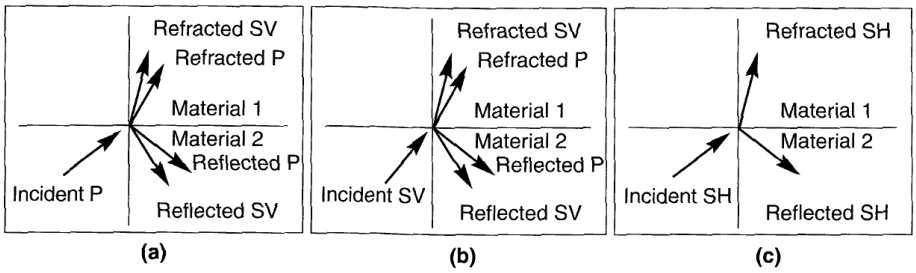

Figure 3.6: Reflected and refracted rays resulting from incident (a), P-wave, (b) SV - wave, and (c) SH - wave (Kramer, 1996)

- Geometric attenuation
- Material losses or intrinsic attenuation, and
- Apparent attenuation

Geometric Attenuation: Geometric attenuation is caused by the increase in the size of wave front as the wave propagates away from the source. The wave amplitude is proportional to the square root of the energy per unit area (e.g. for a spring $E = 1/2kx^2$). As body waves (P- and S-waves) have spherical wave front the wave amplitude decreases as $1/\sqrt{r}$ while surface wave (Rayleigh and Love waves)the amplitude decreases as $1/r$, where r is the distance from the source. The wave amplitude between two points (r_1 and r_2) decay as:

$$\frac{A_2}{A_1} = \left(\frac{r_1}{r_2}\right)^{\varsigma} \tag{3.40}$$

where A_1 and A_2 are the amplitudes of the wave front at distances r_1 and r_2 from the source. The coefficient ς depends on the shape of wave front. For surface waves $\varsigma = 0.5$ whereas for body waves $\varsigma = 1.0$. Thus, surface waves decay more slowly than body waves.

Intrinsic Attenuation: When a wave front propagates, part of the elastic energy is always converted to heat. This conversion of mechanical energy to heat is called material damping or intrinsic attenuation. Intrinsic attenuation can be quantified by following coefficients:

- Damping Ratio (D)
- Logarithmic decrement (Δ)
- Quality factor (Q)

- Attenuation coefficient (α)

The Intrinsic attenuation can be represented as exponential decay as:

$$A_2 = A_1 e^{-\alpha(r_2 - r_1)} \tag{3.41}$$

where r_1 and r_2 represent the distance from the source as shown in Equation 3.40.

Apparent Attenuation: Apparent attenuation is caused by the reflection, transmission and refraction of a wave front as it strikes an interface between two different materials. This phenomenon is termed wave scattering.

Total Attenuation: The combine effect of geometric, intrinsic, and apparent attenuation can be expressed as (Santamarina et al., 2001):

$$\frac{A_1}{A_2} = \left(\frac{r_2}{r_1}\right)^{\varsigma} e^{-\alpha(r_2 - r_1)} T^{-1} \tag{3.42}$$

3.4 Signal Processing Techniques

A time signal is considered as a variation of a dependent variable with respect to time and space. This chapter presents a summary of important techniques used to extract information from the time signals such as the Fourier transform (Discrete and Continuous) and wavelet transform.

3.4.1 Time Domain Analysis

A typical time signal is presented in Figure 3.7. The output signal shows the time of first arrival, reflections from boundaries, underneath layers and void (if present). Analog signals are mostly recorded using a digital acquisition system. The acquisition system stores signals as a sequence of equally spaced samples at constant sampling interval Δt. Figure 3.8 shows the effect of aliasing which is generated by low sampling rates. To capture all the characteristics of the actual signal, the sampling rate should be sufficiently small, this criterion is given by Nyquist sampling theorem which states the that in order to re-generate a continuous signal from discrete points the function should be sampled twice per period. Therefore, to avoid aliasing in the recorded signal, the sampling

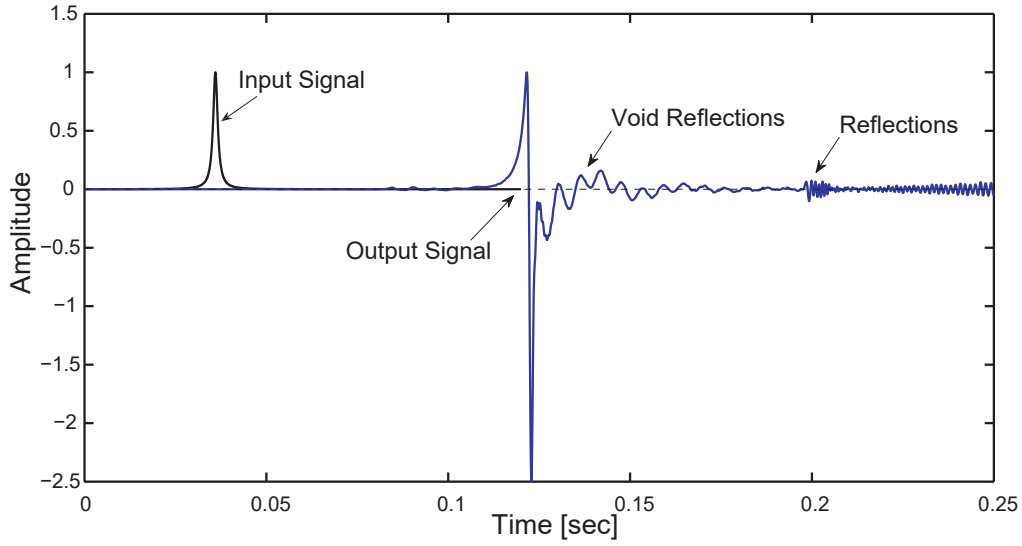

Figure 3.7: Time signal showing input and output signal

rate Δt or sampling frequency f_s should satisfy the following criterion:

$$f_s = \frac{1}{2\Delta t} \geq f_{nyq} = \frac{2}{T} \tag{3.43}$$

where, T is the largest period in the signal. A minimum of 8 to 10 points per cycle are recommended to correctly represent signals in the time domain.

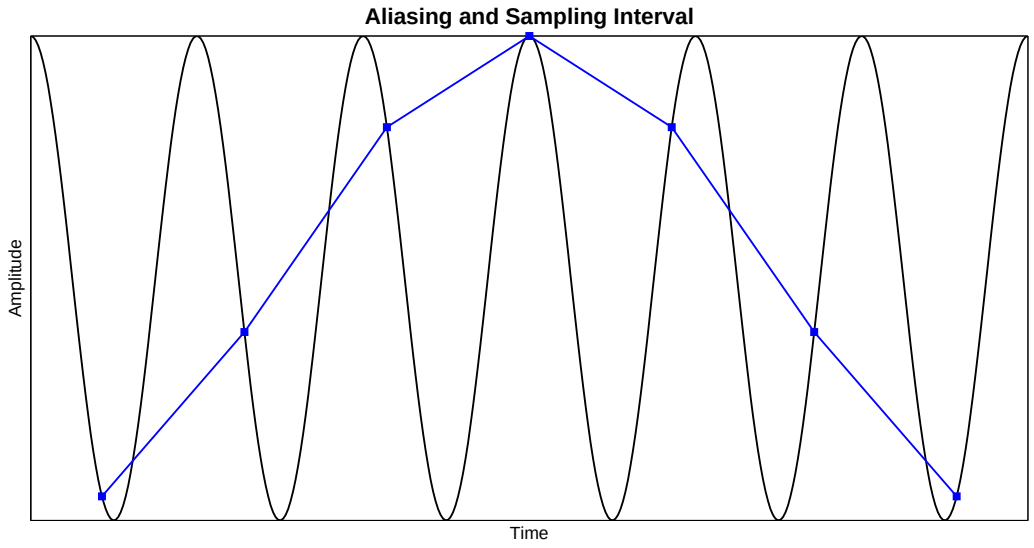

Figure 3.8: Aliasing and sampling rate effect

3.4.2 Frequency Domain Analysis

Frequency domain methods are spectral analysis methods which are based on Fourier analysis. The main principle of the Fourier method is that over a finite interval any analytic function can be approximated by taking a weighted sum of sine and cosine functions of increasing frequencies. In literature, there are a number of mathematical transforms available. The following sections present the Fourier transform and its extensions.

Fourier Analysis

Any periodic signal f(t) with period T can be expressed by the Fourier series as a superposition of sine and cosine functions by

$$f(t) = a_0 + \sum_{n=1}^{\infty} a_n cos(\omega_n t) + b_n sin(\omega_n t) \tag{3.44}$$

The coefficients a_0, a_n, and b_n are calculated by

$$\begin{aligned} a_0 &= \frac{1}{T}\int_0^T x(t)\,dt \\ a_n &= \frac{2}{T}\int_0^T f(t)\,cos(\omega_n t)\,dt \\ b_n &= \frac{2}{T}\int_0^T f(t)\,sin(\omega_n t),dt \end{aligned} \tag{3.45}$$

The coefficient a_0 represents the average or mean value of f(t), whereas the coefficients a_n and b_n represent the projection of f(t) on sine and cosine functions, respectively. When the period T tends to infinity, ω_n becomes a continuous variable and the summation is replaced by an integration; thus 3.44 and 3.45 are replaced by

$$f(t) = \frac{1}{2\pi}\int_{-\infty}^{+\infty} F(\omega)e^{i\omega t}d\omega \tag{3.46}$$

$$F(\omega) = \int_{-\infty}^{+\infty} f(t)\,e^{-i\omega t}dt \tag{3.47}$$

Equation 3.47 represents the Fourier transform while Equation 3.46 represents the Inverse Fourier transform of a signal f(t). In these equations, ω is the angular frequency, t is the time, and i represents the imaginary component of complex numbers. The Fourier transform, a complex-valued function can be written in terms of the magnitude $|F(\omega)|$ and phase $\phi(\omega)$ as (Stein and Wysession, 2003)

$$F(\omega) = |F(\omega)|\, e^{i\phi(\omega)} \tag{3.48}$$

where

$$|F(\omega)| = [F(\omega)F^*(\omega)]^{1/2} = [Re^2(F(\omega)) + Im^2(F(\omega))]^{1/2} \tag{3.49}$$

$$\phi(\omega) = tan^{-1}\left[\frac{Im(F(\omega))}{Re(F(\omega))}\right] \tag{3.50}$$

Analysis of seismic data using Fourier transforms requires computers and therefore a continuous time is measured or sampled at discrete points in time. If the function f(t) is sampled at N time points that are Δt apart the Fourier transform is written as

$$F(\omega) = \Delta t \sum_{n=0}^{N-1} f(n\Delta t)\, e^{-i\omega n\Delta t} \tag{3.51}$$

This transform is a continuous function of ω that we approximate using its values at discrete frequency points. However, sampling produces a spectrum that is periodic in angular frequency with period $2\pi/\Delta t$, or twice the Nyquist angular frequency ω_N, therefore

$$F(\omega) = F(k\Delta\omega) \quad for\, k = 0, 1, ..., N-1 \tag{3.52}$$

with

$$\Delta\omega = 2\,\omega_N/N \quad = 2\,\pi/(N\Delta t) \quad = 2\,\pi/T \tag{3.53}$$

where T = N Δ t, T is the length of the data in time.

The discrete Fourier transform (DFT)of a sampled time series is given as

$$F(k\Delta\omega) = \Delta t \sum_{n=0}^{N-1} f(n\Delta t)\, e^{-ik\Delta\omega n\Delta t} \tag{3.54}$$

The DFT gives values at angular frequencies

$$0, \Delta\omega, 2\Delta\omega, \ldots (N/2)\Delta\omega, \ldots (N-1)\Delta\omega \tag{3.55}$$

The inverse DFT (IDFT) can be given by approximating the inverse Fourier transforms integral (Equation 3.46) as

$$f(n\Delta t) = \frac{1}{2\pi} \sum_{k=0}^{N-1} F(k\Delta\omega)\, e^{i(k\Delta\omega)(n\Delta t)}\, \Delta\omega \tag{3.56}$$

Frequency spectra of the output time signal presented in Figure 3.7 is shown in Figure 3.9. The main frequency component present in the time signal are shown along with the frequency values.

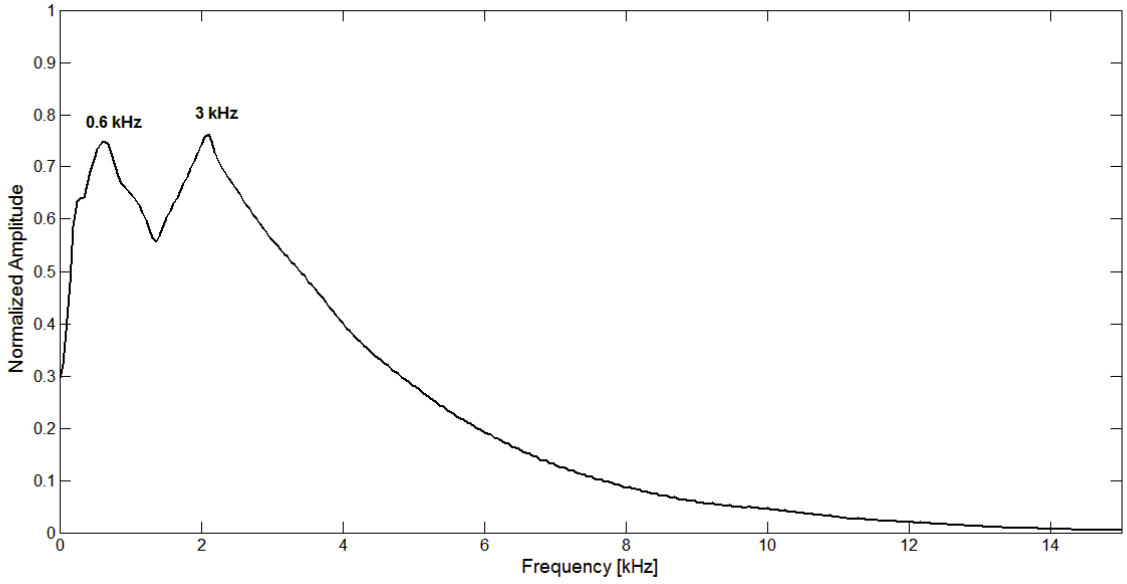

Figure 3.9: Frequency spectrum of output time signal shown in Figure 3.7. Main frequency component are shown along with frequency values

Short Time Fourier Transform (STFT)

One of the drawbacks of the Fourier transform is that it fails to define the time location of each frequency component. This drawback can be reduced by extracting time windows of the original non-stationary signal. This process is repeated for different positions of the time window and forms the basis for STFT.

$$STFT(b,\omega) = \int_{-\infty}^{+\infty} f(t)w(t-b)e^{-i\omega(t-b)}dt \tag{3.57}$$

where ω is the frequency, f(t) is the time signal, w(t) is the window function, and b is the time-shift parameter.

Wavelet Transform (WT)

Wavelets are mathematical functions that decompose non-stationary signals into different frequency components and then study each component as a function of time. Wavelet analysis developed in the 1980's by Goupilland and colleagues has been used to analyze seismic signals (Goupillaud et al., 1984) and in many other fields of engineering. The advantage of using wavelet transforms over Fourier transforms is its ability to study and process signal in time and frequency domains. Mathematically, wavelet transform of a function $f(t)$ is defined as the integral transform (Kumar and Foufoula-Georgiou, 1997)

$$WT(a,b) = \int_{-\infty}^{+\infty} f(t)\Psi^*_{a,b}(t)dt \qquad\qquad a > 0 \tag{3.58}$$

where

$$\psi_{a,b}(t) = \frac{1}{\sqrt{a}}\Psi^*_{a,b}(\frac{t-b}{a}) \tag{3.59}$$

a is the frequency scale parameter and b is the time-shift parameter. $\psi^*_{a,b}(t)$ is complex conjugate of $\Psi_{a,b}(t)$. The parameter a dilates $(a > 1)$ and contracts $(a < 1)$ the function $\Psi^*_{a,b}(t)$. Wavelet transform is analogous to a zoom lens which permits the time-scale window to narrow and focus on small scale features and widens on large-scale features (Kumar and Foufoula-Georgiou, 1997).

Equation 3.58 defines continuous wavelet transform (CWT). To obtain the original signal, the inverse wavelet transform is given as:

$$x(t) = \frac{1}{C_\psi} \int_{-\infty}^{+\infty} \int_{-\infty}^{+\infty} \frac{1}{a^2} WT(a,t)\, \Psi_{a,t}(t)\, da\, dt \tag{3.60}$$

where C_Ψ is constant, depending on the choice of the wavelet. The choice of wavelet $\Psi(t)$ is neither unique nor arbitrary. The function $\Psi(t)$ is a function with unit energy $(\int |\Psi(t)|^2 dt)$ chosen so that it has

1. compact support, or sufficiently fast decay to obtain localization in space
2. zero mean $(\int_{-\infty}^{+\infty} \Psi(t)\, dt = 0)$

The requirement of zero mean is called the admissibility condition of the wavelet. The normalizing constant $1/\sqrt{a}$ is chosen so that $\Psi_{a,b}(t)$ has the same energy for all scales a. From the two conditions several functions can be used as wavelets. Two popular wavelets for the CWT are the Mexican hat and Morlet wavelet. The Mexican hat wavelet is the second derivative of the Gaussian function, given as

$$\Psi(t) = \frac{2}{\sqrt{3}} \pi^{-1/4} (1 - t^2)\, e^{-t^2/2} \tag{3.61}$$

However, a common choice for seismic wave analysis is Morlet wavelet. The function provide good resolution in both time and frequency. The Morlet function is a complex valued function and is expressed as

$$\Psi(t) = \pi^{-1/4} e^{-i\omega_0 t}\, e^{-t^2/2} \quad \omega_0 \geq 5 \tag{3.62}$$

The Fourier transform of Morlet wavelet is given by

$$\hat{\Psi}(\omega) = \pi^{-1/4}\, e^{-(\omega-\omega_0)^2/2} \quad \omega_0 \geq 5 \tag{3.63}$$

The Fourier transform is approximately zero for $\omega < 0$. An example of Morlet wavelet is shown in Figure 3.10. Figure shows the results of wavelet real and imaginary signals and its wavelet

transform for three different values of a, i.e. $a = 1$, $a < 1$, and $a > 1$. From the Figure we can clearly see the effect of dilation on the wavelet and its Fourier spectrum. When the wave dilates, its Fourier transform contracts, and vice versa.

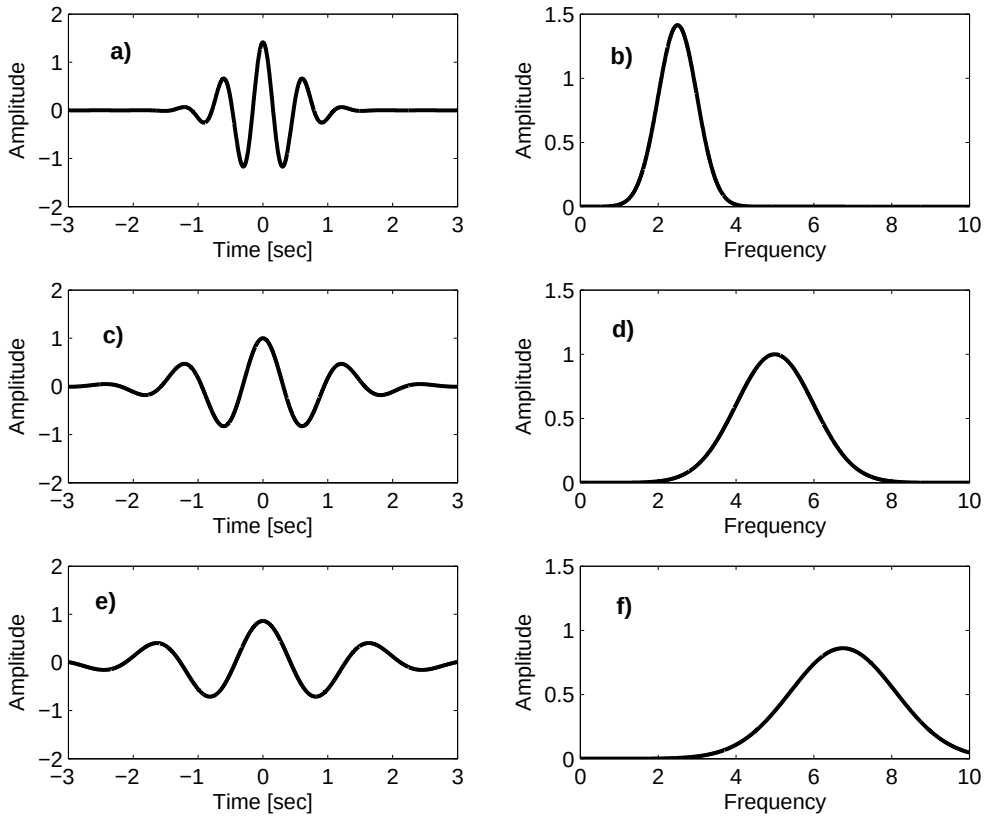

Figure 3.10: Morlet wavelet $\omega_0 = 5$ and its Fourier spectrum for different scales. Figure a) and b) $a > 1$. Figure c) and d) a = 1, and Figure e) and f) $a < 1$. The fourier transform contracts when the wavelet dilates, and vice versa

Discrete wavelet transforms

The discrete wavelet transforms are implemented on discrete values of scale and location. Similar to the continuous wavelet transform (CWT), the discrete wavelet transform (DWT) is defined as:

$$WT(a,b) = \frac{1}{\sqrt{a}} \sum_{n=0}^{N-1} [x_n \cdot \psi^*(\frac{n\Delta t - b}{a})\Delta t] \tag{3.64}$$

where N is the total number of sample points, x_n represents the discrete time signal over a time period given by $N \cdot \Delta t$.

3.5 Chapter Summary

Systems described by the one-dimensional wave equation are the longitudinal and torsional vibration in rods, pressure waves in fluid, and the transverse vibrations of the string. Two possible solutions to wave equation can be found by differentiating the Laplace equation, the first solution describes the propagation of wave due to volume change(irrotational wave), while the second solution describes the wave propagation due to rotation (equivoluminal wave). In an infinite half-space, a third solution of equation of motion is obtained; which corresponds to a wave confined to the near surface. The solution of equation of motion describes the three types of seismic waves; primary, shear, and surface waves. Primary and shear waves are called body waves while surface waves are categorized into Rayleigh and Love waves based on the propagation direction. Body waves are non-dispersive and their velocities depend only on elastic constants of the medium. Rayleigh waves which exists in a half space are non-dispersive in homogenous medium, however, soils are not homogenous and Rayleigh waves become dispersive. Waves attenuate as they travel away from the source and their amplitude decreases due to geometric attenuation, material attenuation (damping ratio), and intrinsic attenuation. Frequency spectrum of time signal is important to understand the main characteristics of the signal such the energy of the signal and phase of the wave. Fourier transform is commonly used for signal processing, which transform a time domain signal into frequency domain. One limitation of Fourier transform is that time information is not kept once the signal is transformed into frequency domain. Therefore, wavelet transform is used. Wavelet transform keeps both the information using the time shift and frequency scale property of the wavelet.

CHAPTER 4

Laboratory Bender Element and Resonant Column Tests

4.1 Introduction

RC and BE testing are standard procedures; however, the effects of the different frequency ranges used in these tests has not been well understood. Coupling between the specimen and base platen is very critical. In addition to the frequency effects, the coupling effects between the specimen and end platen are studied in this chapter. Also, the new effect of base fixation for RC testing is shown.Finally, a new BE method is proposed to understand the estimation of shear wave velocity at higher frequencies. This chapter presents the new study on the effects of different frequency ranges on BE and RC tests. A new calibration procedure is done showing the effects on the damping ratio at large strains. The coupling effects between the specimen and end platen is also studied in this chapter. A new BE method is proposed for the estimation of shear wave velocity considering excitation at large strains.

The chapter begins with the new calibration procedure of the RC and BE equipment. Next, the global methodology for the laboratory test is presented with details of individual test setup. Finally, results of the test are presented in the time and frequency domains and a comparison is made between V_S from the RC and BE tests.

4.2 Resonant Column and Bender Element Test Setup and Calibration

The resonant column device in this study is used to measure the low and mid strain shear modulus and damping ratio of soils. In order to determine the resonant frequency and material damping ratio of the soil specimen, the sample is excited harmonically for a range of different frequencies (frequency sweep). The University of Waterloo resonant column (UW-RC) device is a modified Stokoe-type RC device. The device is equipped with two sets of BE used for sending and receiving signal. The advantage of this configuration is to perform RC and BE tests simultaneously. A schematic of the test setup is shown in Figure 4.1. The BE are mounted on the bottom and top plate of the RC device as shown in Figure 4.2. The cell pressure is controlled by a pneumatic system (Brainard and Kilman) with a maximum confinement of σ_o = 700 kPa. An LVDT (Trans-Tek, 0242-0000 D-6) is mounted inside the confining chamber to measure the axial deformation of the specimen. A dynamic signal analyzer (HP 35670A) is used to provide input signal to the driving coils. The signal is then amplified through a power amplifier (Bogen, GS-250).

The amplified signal drives the four pairs of coils which induce a magnetic field onto the set of magnets that produces a torsional excitation to the specimen. Two accelerometers (PCB 353A78 and PCB 353B65) fixed to the driving plate are used to monitor the sample response during testing. The accelerometers are fed by a power source unit (Dytran 4121). The input and output signals from the coils and accelerometer are filtered and amplified by a filter unit (Krohn-Hite 3384), and are monitored by a digital oscilloscope (HP-54645A). Frequency spectra are computed in real time by a dynamic analyzer to evaluate resonant frequency (f_o) and damping ratio (ξ) of the specimen. For the computation of shear wave velocity, the mass polar moment of inertia (I_o) of the driving plate is calculated. The calibration of RC and BE devices is presented next.

4.2.1 RC Calibration

In the resonant column (RC) test method the computation of shear wave velocity requires the determination of the mass polar moment of inertia of the driving system, I_o. Due to the complex geometry of the driving plate, I_o is determined experimentally. Calibrated aluminum probes and

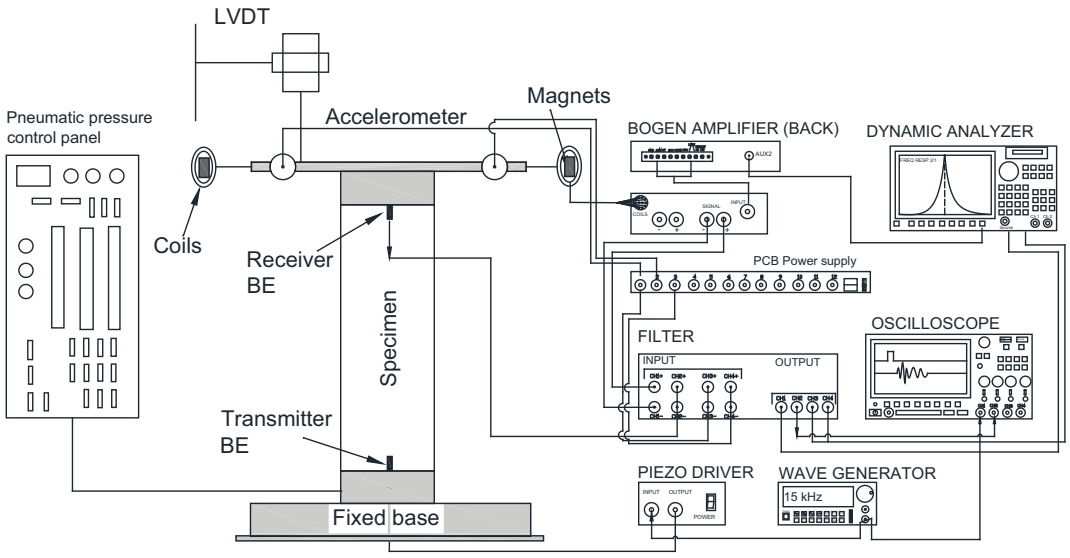

Figure 4.1: Schematic of RC and BE test setup

.

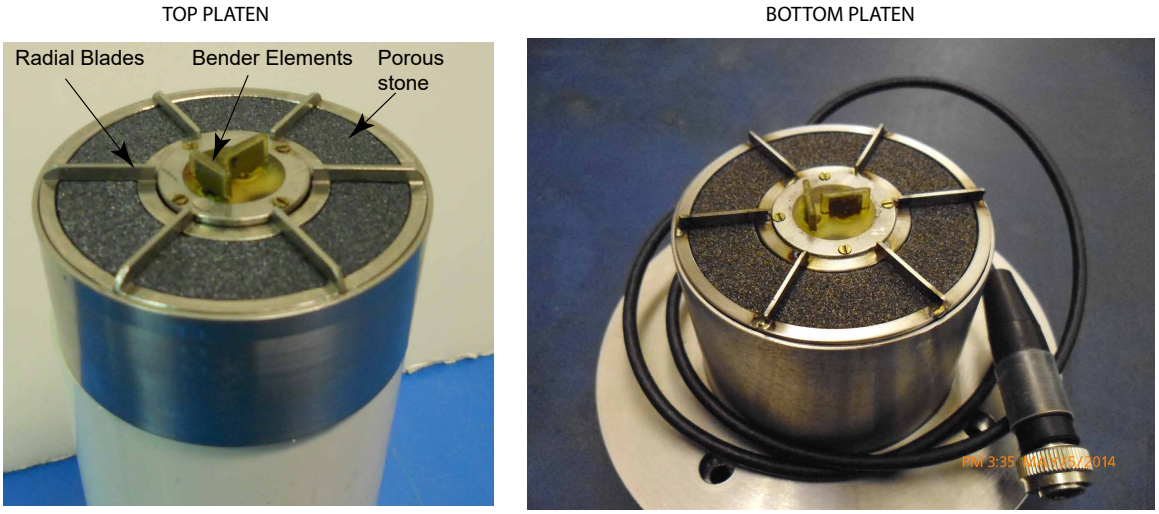

Figure 4.2: Modified RC top and bottom platens showing the blades, porous stone, and location of two BEs.

calibrated additional mass are used as shown in Figure 4.3. The aluminum probes have fixed top and bottom clamps. The bars were rigidly connected to the base pedestal of the RC device by tightening the screws. One calibrated additional mass, rectangular in shape, was attached to the top of the specimen bar. Finally, the driving plate and additional mass were tightly attached to the top of the calibration bars using bolts and nuts. The calibration tests were carried out with and without the additional mass. The calibration was done using a broad frequency range to simulate the specimen

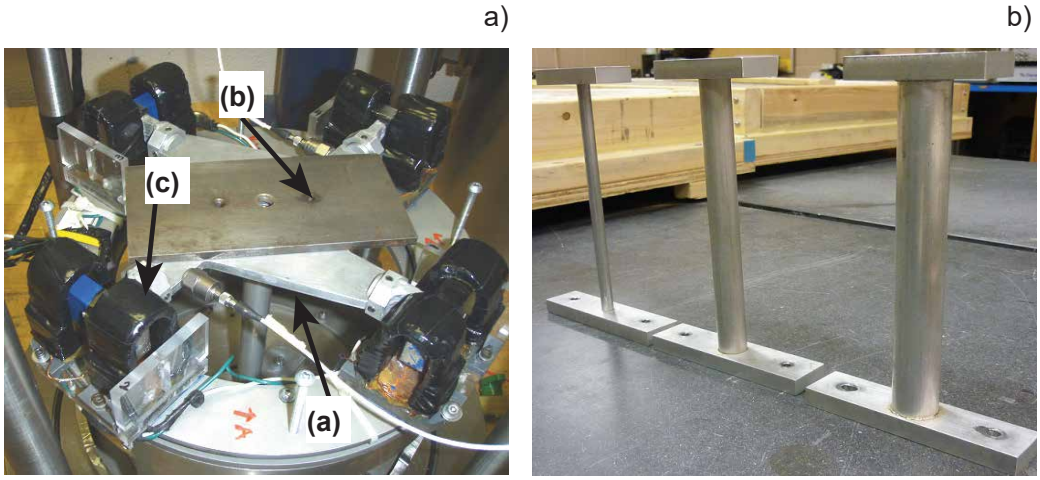

Figure 4.3: RC device showing the a) driving plate and b) calibration bars, modified after (Moayerian, 2012). In the figure (a) is the driving plate, (b) is the additional mass, and (c) are the magnets and coils

.

of various stiffness properties. Table 4.1 shows the shear strain and the moment of inertia values for the three probes used in this study. Since, most of the samples in this study were stiff specimens, the stiff probe was tested for large strain as shown in Figure 4.4 and 4.5. To check for equipment generated damping, the mounting screws for the driving plate were loosened and the large strain test was repeated (Figure 4.5). The results show no spurious modes in the shear strain range for this study. The shear wave velocity and the damping values for the tight screw setup are 0.5 % larger than the loose screw setup. The shear strain results for the stiff probe matches with the shear strain values reported by Khan (2007).

4.2.2 BE Calibration

Theoretical and experimental studies by researchers show that the propagation of waves in BE setup is complex and affected by several factors, explained in the literature review section. These factors include near-field effects, polarity, delay time, coupling to name a few. Therefore, calibration of the BE system along with its assembly is important before any test. The bender elements are located in the top and bottom platens of the UW-RC device (Figure 4.2). In each platen, two sets of benders are installed. The dimensions of the BE are 10 mm in width and 5 mm in height.

The verification of polarity was done using a single sine pulse and BE located in direct tip-to-tip

Table 4.1: Dimensions and calibration results of three aluminum probes.

Probe dia		Resonant Frequency		Damping		I_{b*}	I_{dp**}	Shear Wave Velocity	Shear Strain
Inner [mm]	Outer [mm]	w/o mass [Hz]	mass [Hz]	w/o mass	mass	(kg-m^2)	(kg-m^2)	[m/s]	%
5.91	9.47	12.63	11.69	7.31E-04	2.14E-03	3.57E-05	8.53E-03	2.43E+03	9.35E-04
15.18	19.12	50.6875	47	2.45E-03	5.92E-03	4.71E-05	8.74E-03	2.89E+03	4.20E-04
19.23	25.23	97.38	90.5	2.60E-04	1.62E-03	4.68E-05	9.08E-03	3.07E+03	2.50E-04

* top bar
** driving plate

contact. Once the polarity was determined, the arrival time was measured between the transmitter and the receiver BE. To ensure, no delay time in the measurement due to the electronics, ceramics, and coating material the calibration of BE is done in time and frequency domains.

Tip to Tip Calibration- Time and Frequency Domain

In this method, the pair of BEs are placed in direct contact and a sinusoidal signal is used to excite the transmitter bender (located in the base platen) as shown in Figure 4.7a. A sinusoidal pulse of 4 volts peak-to-peak is excited through transmitter BE. The results of the test are shown as normalized to identify the correct delay time. The receiver output signal, dotted line, shows the polarity and delay of the signal compared to the input signal (Figure 4.6). The time delay of 4.6 μs is obtained for the benders in direct contact. The frequency and damping ratio are 11.4 kHz and 2.2 %, respectively. The results from the frequency domain test are compared next.

In the frequency domain test (Figure 4.7), two tests were done. One test was done with the tip-to-tip configuration and the other test was conducted with the short sand specimen. The short sand specimen was prepared using the dry compaction method. The height of the sand sample is 6.5 cm while the diameter is 7 cm. The transmitter BE is excited for various windows, from very wide frequency range 50 kHz to window of spanning 3.2 kHz. The first test is conducted for 51 kHz window, then 25.6 kHz window (25 - 50 kHz) and so on. Figure 4.8 shows the results of transfer function and coherence for the tests performed in direct contact and in sand specimen. The main

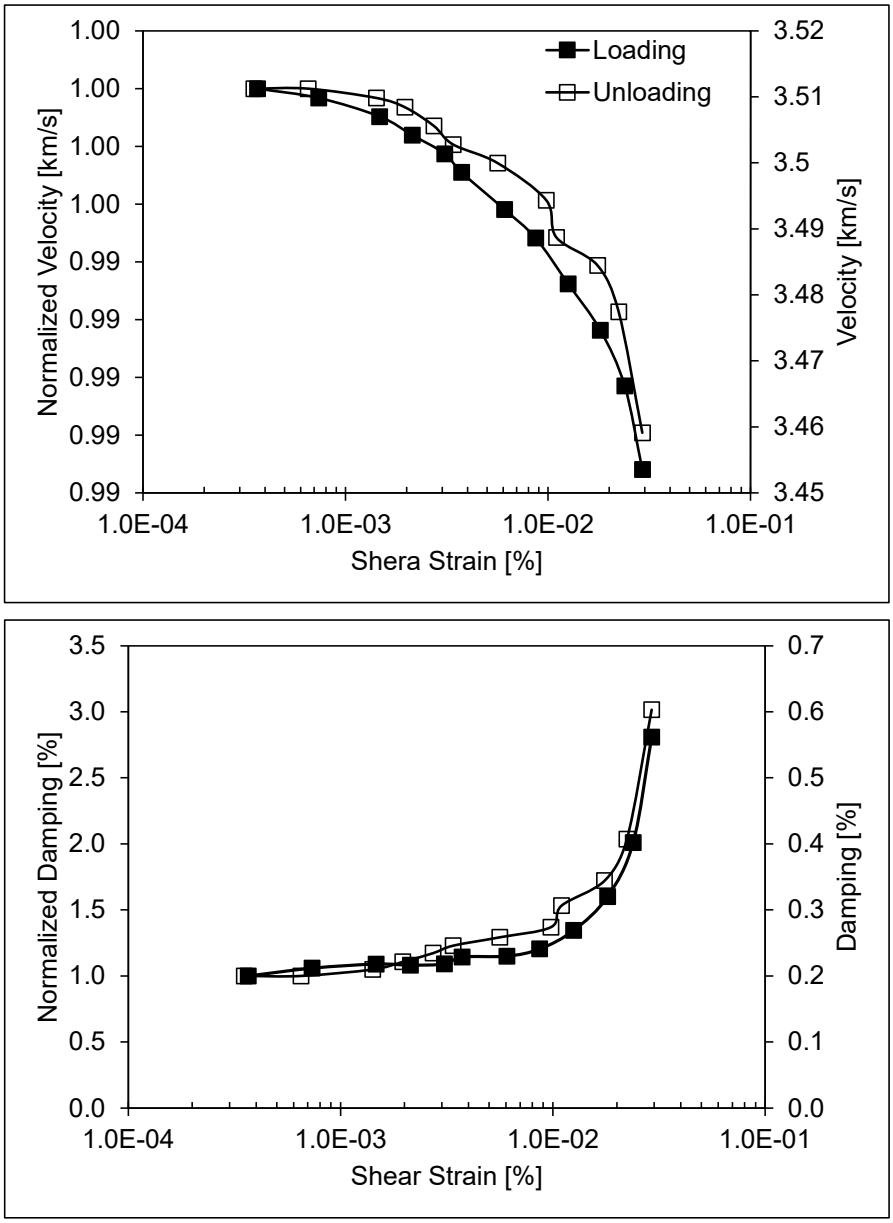

Figure 4.4: Variation of shear wave velocity and damping for Aluminum probe 3 (dia 2.54 cm). The screws for driving plate were secured tightly to the ring.

frequency and damping ratio are 11.2 kHz and 5.8 % for BE tip-to-tip.

Using the calibration procedure described in Camacho-Tauta et al. (2015), Equation 4.1 is used to calculate the resonance frequency. In Equation 4.1, L_b = 10 mm and k_L = 4.73 for double embedded condition (Doyle, 1991), the theoretical first mode resonance frequency is 17.3 kHz. The value is 30 % larger than the resonant frequency from the time domain test. The higher value in the

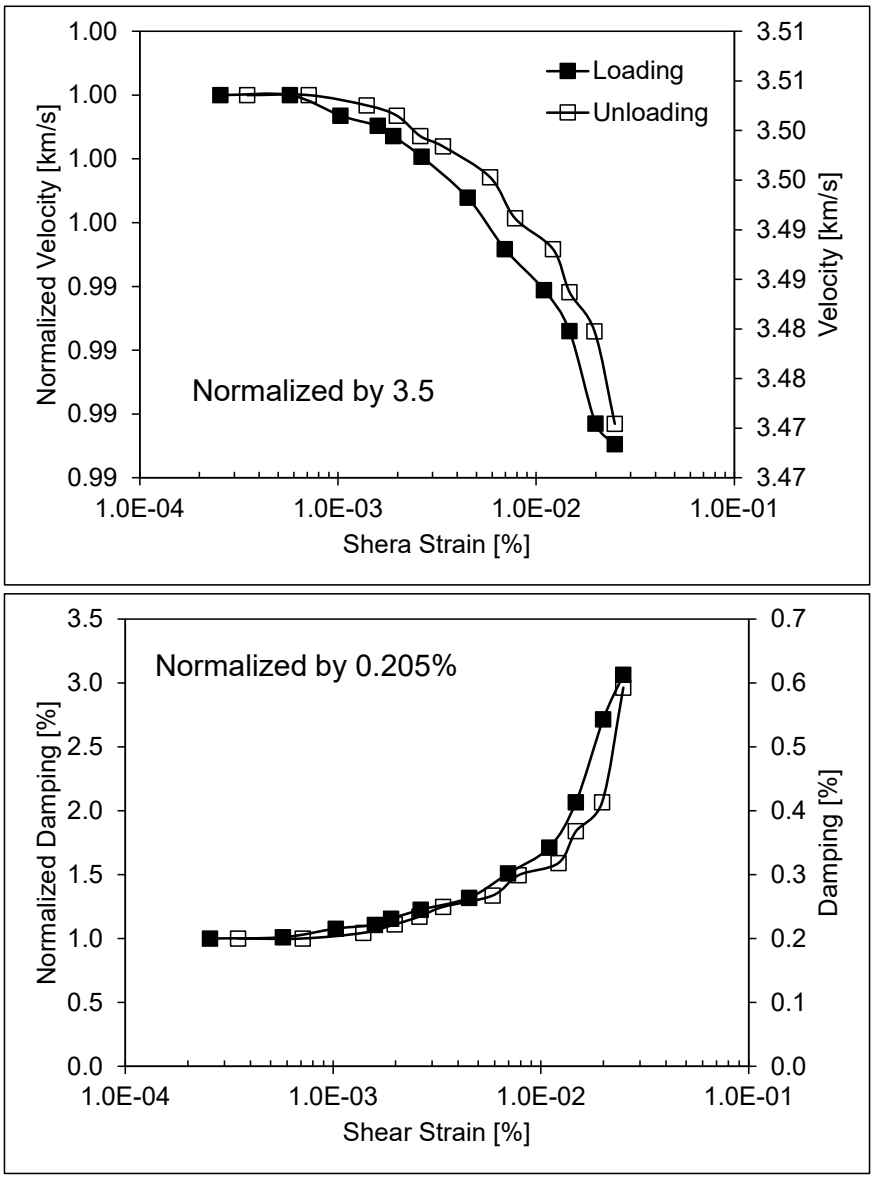

Figure 4.5: Variation of shear wave velocity and damping for Aluminum probe 3 (dia 2.54 cm). The screws for driving plate were loose to the ring.

later case could be attributed to the discontinuity between the top and bottom bender as the equation is for continuous beam. Also, the value of α - the effective length factor, is taken as 1.01 assuming perfect fixed conditions. For example, if the value of α is taken as 1.1, the resonant frequency changes to 14.58 kHz. The values for parameters used in the equation 4.1 are: $E_b = 6.3 \times 10^{10}$ N/m^2 and $\rho_b = 7700\ kg/m^3$.

The resonant frequency of the BE embedded in the soil specimen is obtained using the equation

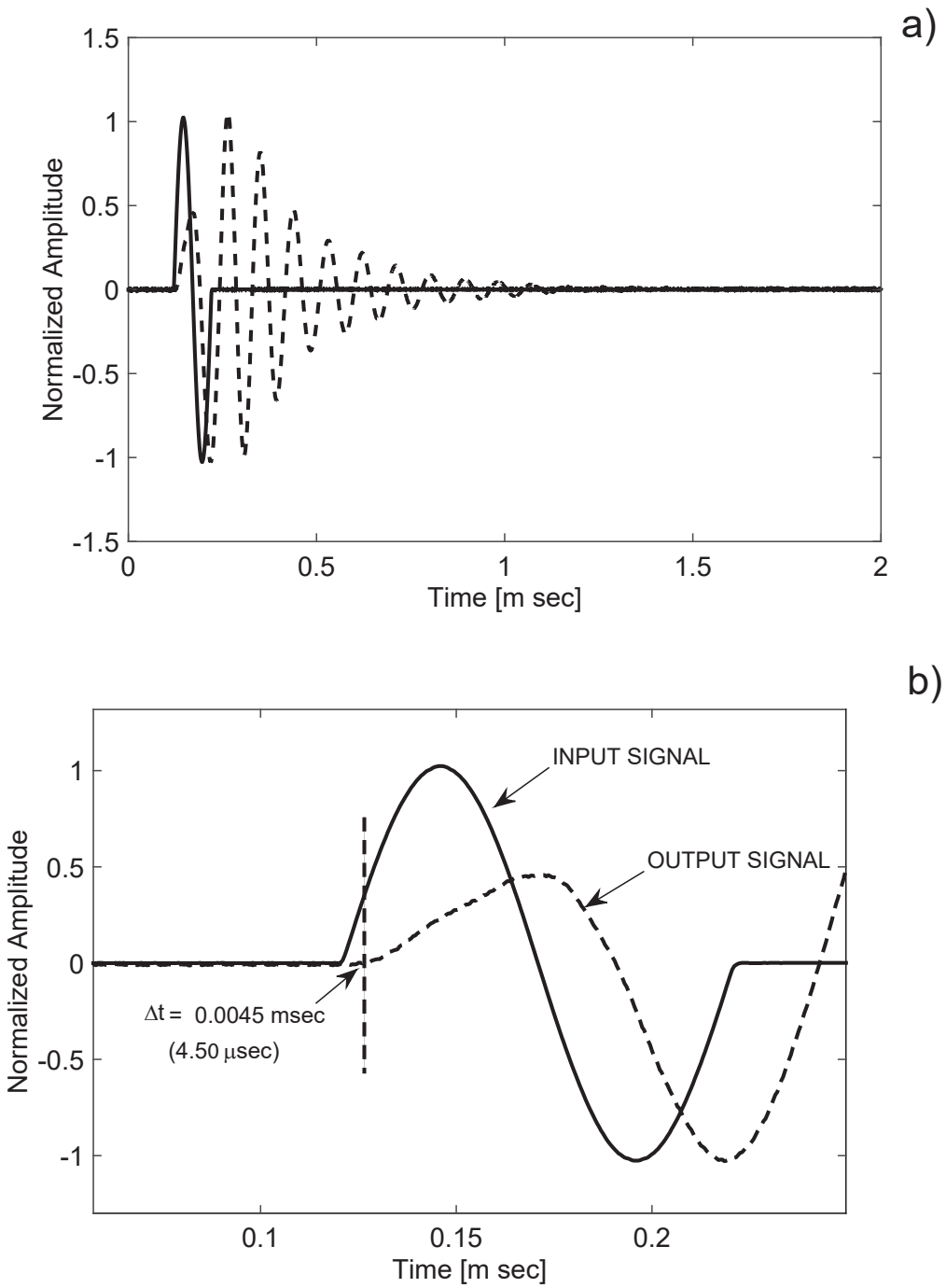

Figure 4.6: Tip to tip calibration.

4.2 derived by Lee and Santamarina (2005) for an equivalent bender element-soil system. In this equation, V_S is the shear wave velocity of the specimen, ρ_s is the soil mass density, ν is the Poisson ratio of the soil, β is an experimental factor related to the volume of soil mass affecting the vibration

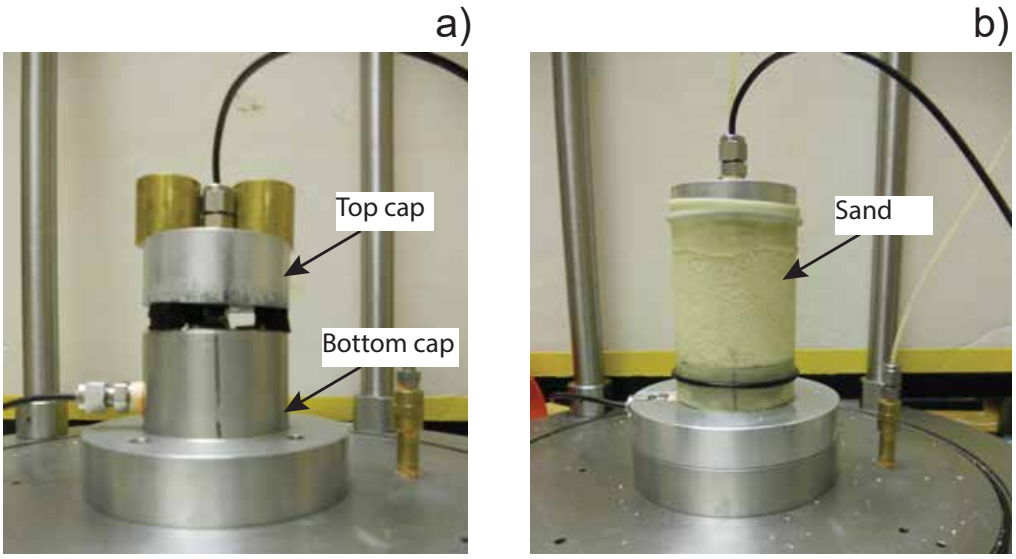

Figure 4.7: Tip to tip and short sand specimen used for calibration of benders.

of the bender element, and $\eta = 2$ is the mean displacement influence factor at the soil-element interface. The resonant frequency for BE embedded in soil specimen is 7.2 kHz. There was no confinement applied in this case and from the results of the frequency spectrum of the single sine pulse of 12 kHz, the frequency spectrum showed a peak at 7 kHz. The peak could be attributed to the resonant peak for the BE-soil equivalent system; however, further testing is required at different confinements to confirm the results. The frequency domain results show that the bender elements motion is restricted in the presence of soil and actual displacement of bender in air and soil is required to observe this change. To understand the vibration of bender in air, a state-of-art laser vibrometer is used in this study to calibrate the BE system, as presented in section 4.2.3.

$$f_n = \frac{\left(k_L^2\right)_n}{2\pi\left(\alpha\, L_b\right)^2}\sqrt{\frac{E_b\, I_b}{\rho_b\, A_b}} \tag{4.1}$$

$$f_1 = \frac{1}{2\pi}\sqrt{\frac{1.875^4\,\left(E_b\, I_b\,/\,(\alpha\, L_b)^3\right) + 2\eta\, V_S^2\, \rho_S\,(1+\nu)\, L_b}{\rho_b\, A_b\,(\alpha\, L_b) + (\rho_s\, b^2\, L_b)\, \beta}} \tag{4.2}$$

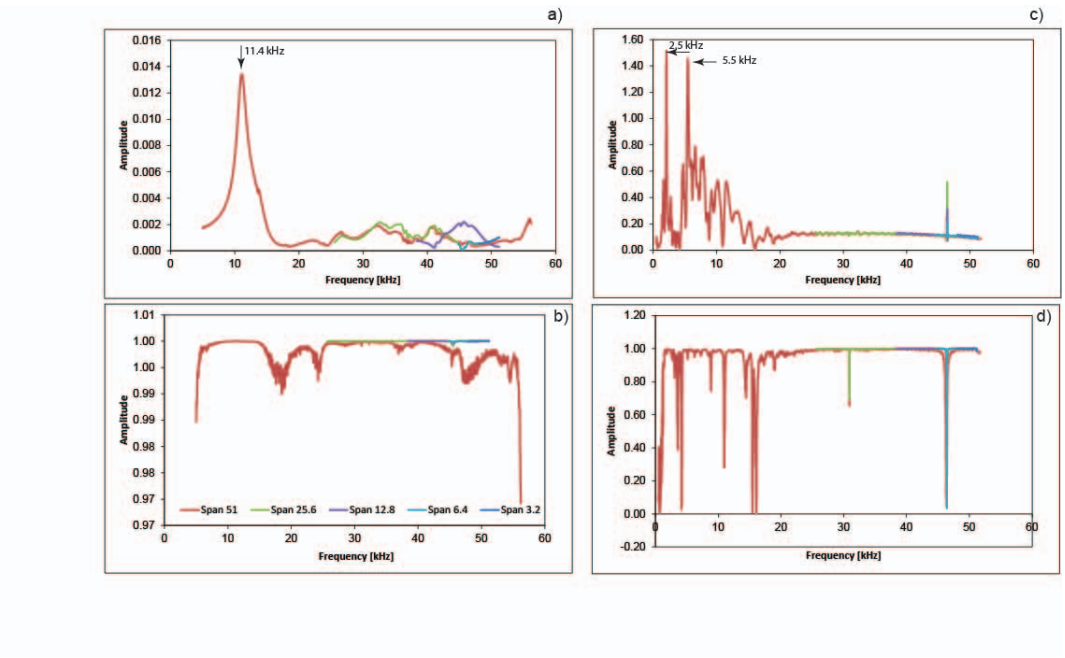

Figure 4.8: Results of BE using frequency sweep. Results on the left are for benders in the air while results on right are for benders in the sand.

Calibration of BE with Aluminium Rod

One of the procedures to measure the equipment delay involves using aluminium rod between two benders tips (Figure 4.9). The test was done on an isolation table to remove any noise from floor or surroundings. The top cap was placed above the rod without any clamps to hold it. Although, the coupling was weak the transmitter was able to produce perturbations in the rod which were detected by receiver BE. Aluminum rods of various lengths were used in the calibration. From Figure 4.9, the intersection of the curve fit line with the time axis, shows the time delay while the slope give the velocity. The time delay is 4.5 μs, while the shear wave velocity is 4247 m/sec. The shear wave velocity for aluminum is a known value (3150 m/sec), therefore, the difference between the two values is 26 %. The results are compared with the calibration of the BE using an aluminum rod done by Camacho-Tauta et al. (2012). Their test setup showed a delay time of 15 μs. However, the shear wave velocity obtained from their test is 2900 m/s compared to our test. The difference in the velocity value from our test to the standard value could be due to the anisotropy in aluminum rod because of manufacturing (rolling, extrusion, etc.).

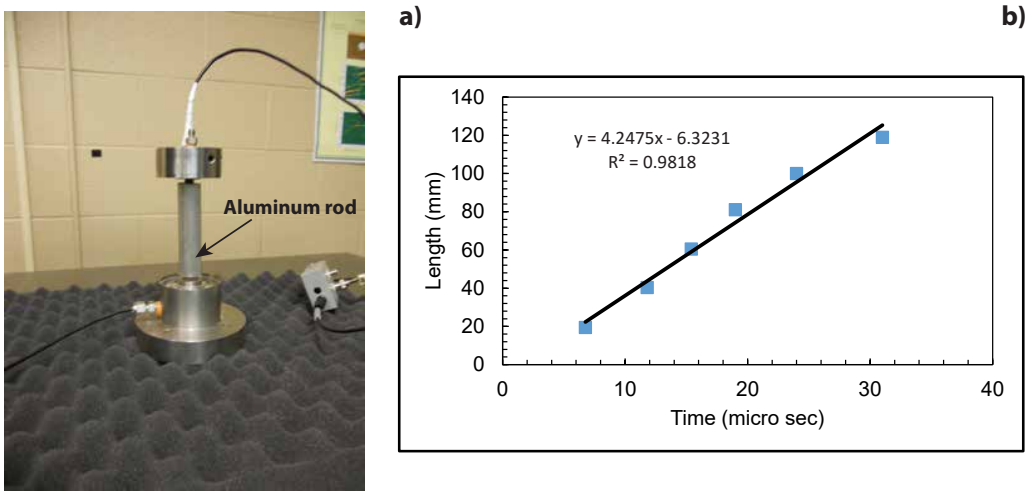

Figure 4.9: BE calibration using various aluminum rods.

4.2.3 Laser Vibrometer Testing

This section presents a new experimental testing to calibrate BEs using laser vibrometers. The main advantage of this kind of testing is its non-contact nature. Results from previous studies used accelerometers to configure the bending behaviour of BEs (Camacho-Tauta et al., 2015, Lee and Santamarina, 2005, Brocanelli and Rinaldi, 1998), tip to tip contact **?**. However, in all the testing configurations, the boundary conditions are altered and not the same as in a normal test setup. Rio (2006) used the laser vibrometer to measure the propagation of waves in bender. However, in the test, measurement was only conducted at one point. In our study, the measurements are done along a grid (5×3) for a total of 15 measurements. Also, displacements are measured directly from the laser as compared to velocity measurements by Rio (2006).

Test Setup and Configuration

The laser vibrometer testing is done in two configurations. In one case, the tip is left free to vibrate in the air and in second case tip-to-tip. Figure 4.10 shows the grid layout for the testing of transmitter and receiver BE. The basic experiment setup consists of the BE, a function generator, piezo driver, an oscilloscope, a personal computer for data acquisition, and a laser vibrometer. The University of Waterloo laser vibrometer (UW-LV) consists of a compact sensor head, a high-frequency vibrometer controller, and a tripod to mount the sensor head. The vibrometer controller incorporates a dual-range decoder with up to 10 MHz bandwidth and a single-range displacement decoder with up to

24 MHz bandwidth.

The laser vibrometer must be leveled with great care, so that the incident beam from the laser is horizontal and perpendicular to the target surface. This maximizes the light reflected back to the laser. A reflection paint or tape should be used on the target surface for maximum reflection and higher signal-to-noise ratio. To reduce scattering from the reflected light, the focus of the laser beam should be small enough to target a small area and increase the strength of signal on the vibration-controller.

Results and Discussion

The results of the BE testing using a laser vibrometer are discussed here. Figure 4.11 shows the frequency spectrum for the top line (grid # 1 - 5) obtained from the single pulse test in the tip to tip configuration. The different modes of vibration of the plate can be observed. The maximum peak for the top and bottom transmitters are at 12.52 kHz which is similar to the frequency obtained from the time and frequency domain test in previous setups. There are other peaks in the transmitter and receiver responses which correspond to 20 kHz and 16 kHz, respectively. The other modes show that the benders do not vibrate in a simple mode but in a more complex mode.

Damping values for the transmitter are obtained from three different test configurations using a laser vibrometer, i.e. tip-to-tip, transmitter in air, and transmitter in vertical position. The damping values are obtained from the free vibration decay of the signal. The values are:

ξ_1 = 2.02 % - tip to tip configuration
ξ_2 = 1.62 % - RC-BE platen in standard vertical position
ξ_3 = 1.91 % - tip to air

The average value of damping from the three tests is 1.85 % which is close to the value obtained from the frequency domain test setup discussed above. Figure 4.12 shows the surface plot obtained from the measurement of BE (transmitter and receiver) using a laser for 15 points shown on the grid. The Figure is obtained from the maximum displacement at each grid point and then interpolated between the distance to show the displacement of bender in air. The maximum displacement for the receiver is 3 nano meter while for transmitter is 15 nano meters. A sharp peak in the

maximum displacement for the transmitter at one edge can be noticed which could be due to the laser measurement on the very corner of the BE, since the grid measurements are automated and programmed in the laser controller.

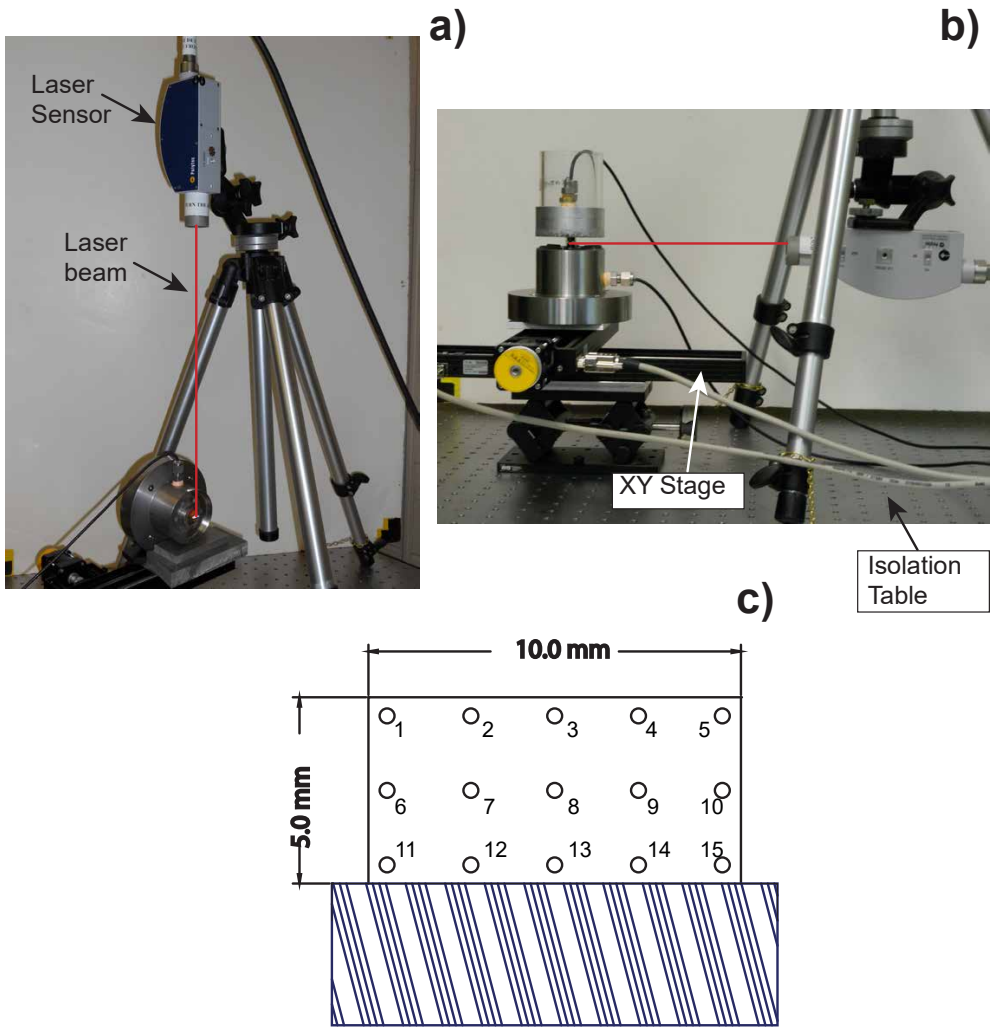

Figure 4.10: BE calibration using state of the art laser vibrometer.

4.3 Experimental Methodology for RC and BE Tests

This section presents the methodology and results of RC and BE testing on soil specimens. Four different kinds of soil specimens are studied in this thesis, i.e. stiff clay, mine paste, leda clay (or sensitive clay), and Barco sand (dry). The objective in each test is to compare the results (shear

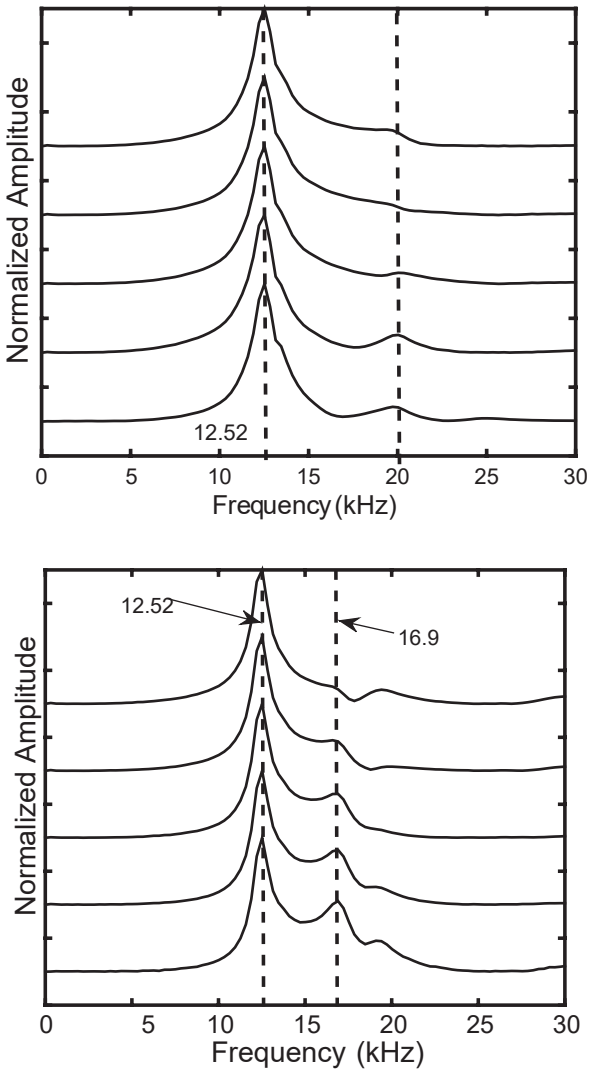

Figure 4.11: Typical frequency spectrum for a) transmitter and b) receiver bender element.

wave velocity) of RC and BE tests and understand the differences in shear wave velocity between the two tests. In particular, the behavior of bender elements and how they transmit signals through stiff soils will be addressed.

The section begins with the description of sample preparation for the four soil types. Then the RC and BE testing methodology is discussed. Finally, the results in time and frequency domain are presented.

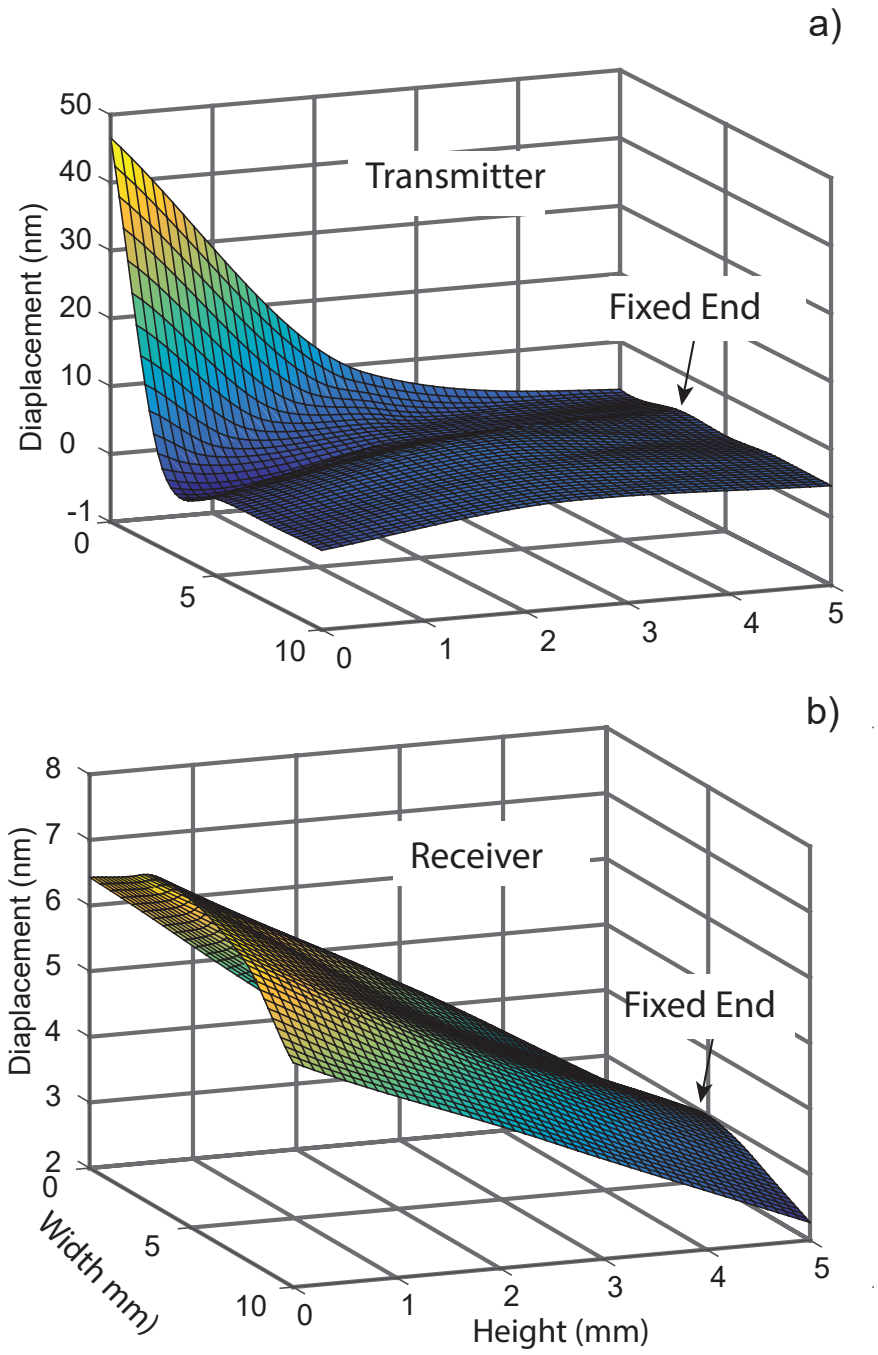

Figure 4.12: Displacements of transmitter and receiver BEs from laser vibrometer measurements, where a) is the displacement plot for transmitter while b) is the displacement for receiver bedner.

4.3.1 Preparation of Specimens

Barco Sand

Specimens of Barco (no. 71) sand were prepared by the dry compaction method. The properties for the Barco 71 sand are: Gs = 2.65, Cu = 1.78, Cz = 1.20, emin = 0.53, and emax = 0.75, e = 0.53. Based on the specimen dimensions and the required void ratio, the soil mass is taken and divided into equal portions. The sample is prepared on the RC test setup. First the base platen is fixed to the bottom plate of the RC device. The membrane and two o-rings are attached to the bottom platen and split is attached. Using the vacuum pump, the membrane is held to the walls of the split mold to prepare a circular specimen and no air is entrapped during preparation.

The sand is carefully poured into the split mold using a funnel. The funnel is kept constant at the desired height to follow the dry raining preparation method. After each layer, the sand is lightly compacted with the tamper rod. At the end of each compaction the height is checked to ensure correct density. Once the sample is prepared, the top cap is placed and membrane is stretched on the top cap. Vacuum is applied through the top cap to hold the sample intact. Two o-rings are placed on the membrane that is rolled on the top cap. The mold is removed and the final height of the sample is recorded.

Next, the driving plate system is attached to the base plate and the plate is aligned such that the magnets are in the centre of the coil. The chamber is then placed, making sure that no cables are touching the driving plate. Otherwise, the damping results could be affected. Once the setup is ready, the vacuum is gradually reduced and confinement is applied to the specimen. Two sand specimens are prepared in this thesis, and they will be referred as S1 and S2.

Mine Paste

Mine tailings are residual materials obtained as a by-product of mineral processing. Mine tailings are typically used to make cement paste backfills in hard rock mining and they may be characterized as fine-grained soil with zero to low plasticity index (Saebimoghaddam, 2010). To prepare the mine paste, the mine tailings are mixed with process water using a paint mixer. Initial water content of the mine tailings is measured in advance. The tailing is then mixed with a hand mixer to prepare a workable paste. Similar to sand specimen preparation, split mole is used to prepare the sample.

Filter paper strips are used to speed the consolidation process. After the paste is completely poured, the paste is left for dead weight consolidation (2.5 kg or 12.5 kpa) for one hour followed by back saturating the specimen. Once the setup is done, back pressure of more than 300 kPa is required to obtain the specimen with a B value of more than 0.95. At the end of saturation, the sample is consolidated until primary consolidation is done. Then, a large strain test is performed. The sample is labelled as MP1 in this thesis.

Stiff clay and Leda clay

In the case of stiff clay specimens, the specimens were received wrapped in clear plastic sheets, aluminum foil, and wax. After removing the wrappings carefully to avoid disturbance of the specimen, the specimen was cut to the required height, and the weight and dimension of the specimen were recorded. Then, the specimen was placed in a resonant column apparatus following the standard sample preparation procedures for triaxial testing. The sample was cut using an electrical masonry saw with diamond-covered cutters to guarantee parallel and horizontal cuts. Small indentations were made on the top and bottom of the specimen to facilitate the penetration of the top and bottom bender elements (depth of penetration of BEs = 5 mm). A summary of specimen properties is presented in Table 1. Two rubber membranes and two sets of O-rings were used to avoid air leakage during consolidation.

At the specified effective confinement, each specimen was allowed to consolidate until the end of primary consolidation; then, RC and BE test were performed. At the end of testing the weight and dimensions of the specimens were recorded again. To avoid a long period of consolidation, additional filter paper and vertical strips were used for the specimens. Dynamic properties were evaluated using drained conditions. RC tests were performed at low shear strain levels for first stage confinement and then the dynamic properties were evaluated at larger shear strain levels. After reaching the maximum capacity of the RC device, the dynamic properties were also evaluated during the unloading stage. At the end of each confining stage, bender element (BE) tests were performed. The samples will be known as C1, C2, C3, and C4 in this thesis

For the leda clay, a procedure similar to the stiff clay procedure was adopted. The clay was wrapped in wax in cake form. Two or three samples could be extracted from the cake. Since, leda clay is soft special care was taken during the cutting of the specimen. The sample was consolidated

Table 4.2: Soil properties for leda, mine paste, sand, and clay specimens.

Sample	σ [kPa]	γ [kN/m^3]	e	w (%)	H (cm)
Leda clay	20 – 160	16.71	1.47	54	12.94
Mine paste	50 – 200	18.16	0.87	21	13.60
Stiff clay	200 - 600	19.50	0.76	24	14.42
Sand	25 – 600	19.03	0.53	-	15.1

at the specified confinement and dynamic measurements were taken using RC and BE tests.

The grain size distribution of the sand, mine paste, and stiff clay specimen is given in Figure 4.13. The average values of height, void ratio, and density are presented in Table 4.2.

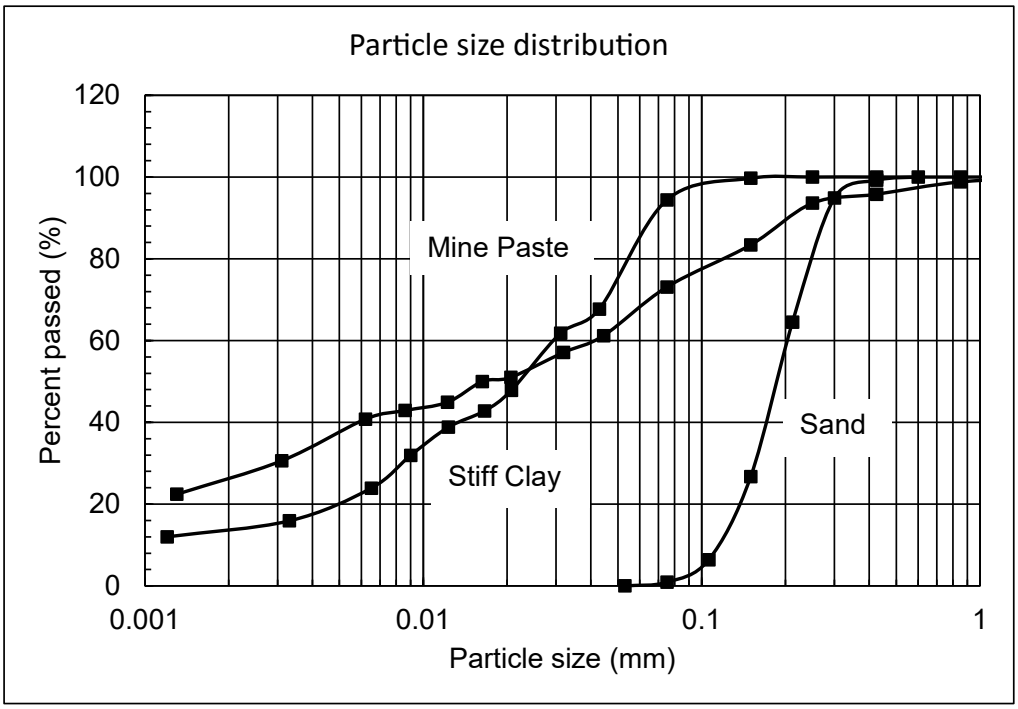

Figure 4.13: Grain size distribution of sand, mine paste, and stiff clay specimens.

4.4 Results and Discussion

The results and analysis for the soil specimens are presented in this section. First, the results from the clay specimen are presented and then the results from mine paste, stiff clay specimens, and finally from sand are presented.

Figure 4.14 shows the typical time signal from a BE test. Windowing (Tuckey window) is used for the selection of the main frequency content of the BE signal. This is done to select the main frequency of the s-wave and not the participation of P-waves and reflections. Figure 4.15 shows the typical time signal, identifying the points selected for the arrival of shear wave velocities. For the clay, mine paste, and leda clay specimens, three values are used to compare the results with RC measurements.

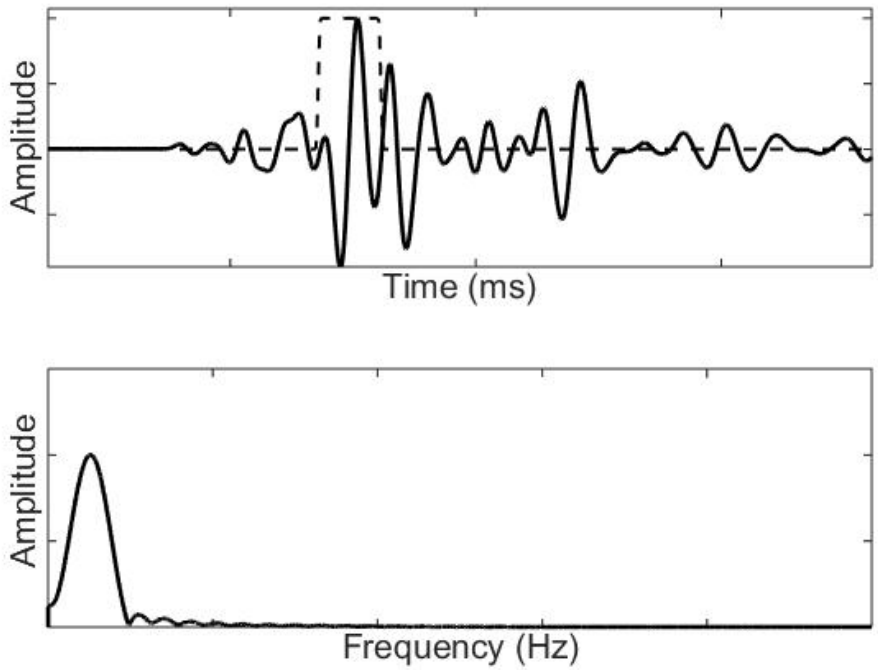

Figure 4.14: Typical time signal and frequency spectra showing the window used for selection of the main frequency content of the BE signal. The windowed signal frequency spectrum value is used to see the variation of frequency with confinement.

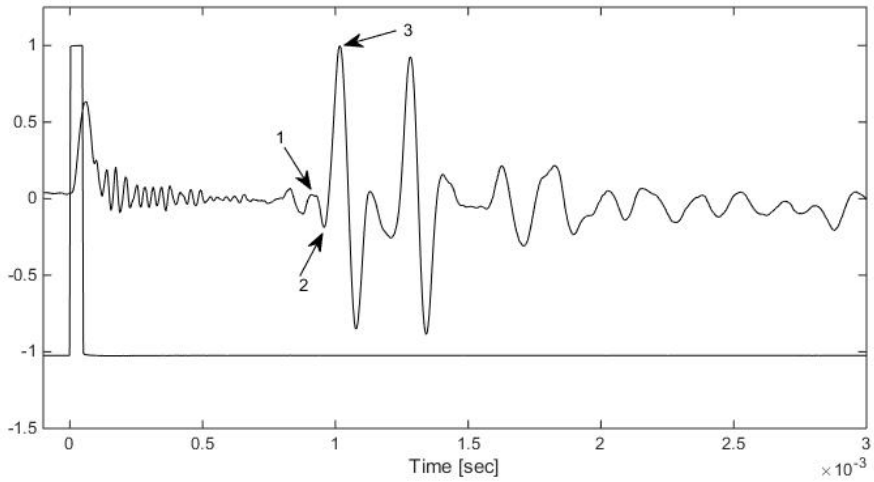

Figure 4.15: Typical time signal showing the three points for identification of travel time in BE tests. The signal is for 80 kPa confinement.

Stiff Clay

Figure 4.16 show the modulus and degradation curves for the samples tested. The large strain test is done for confinement of 200 (S1), 350 (S2), and 650 (S3 and S4) kPa. Two samples was done at 650 kPa. The samples S1 and S2 were consolidated at 600 and 550 confinement and then tested for large strain at lower confinement. Since the samples are till specimens from northern Ontario, the maximum pressure from our RC-test setup is lower than the pre-consolidation pressure of the specimens. The samples S1, S2 and S4 have similar degradation curves except for S3. Tehre are two possible explanations. Firstly, the sample was from a lower depth compared to the other till specimens. Secondly, the void ratio of the specimen is 0.50 compared to 0.74 for all the other specimens. The damping ratio curves show the general trend of increasing with the strain level. Figure 4.17 shows the comparison of the RC and BE test for the stiff clay. At the end of consolidation, the results of the RC and BE are compared. Since there is no standard interpretation method for the selection of arrival time, shear wave velocities from three different arrival times are given in Figure 4.15. The trend shows the increase in the stiffness as the confinement is increased. For effective stress between 350 and 550, the shear wave velocity is decreasing. These two confinements correspond to sample S2.

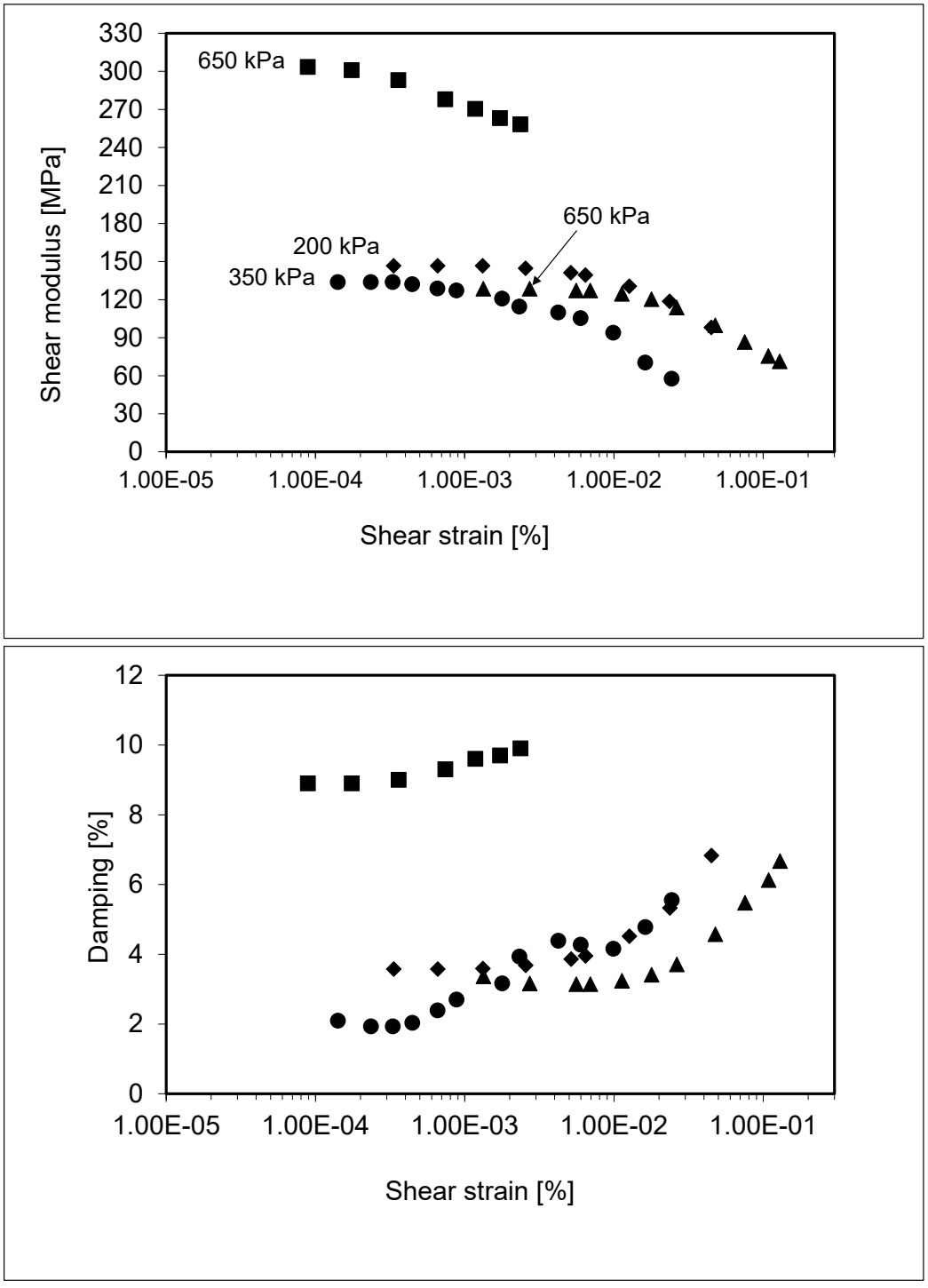

Figure 4.16: Variation of shear modulus and damping for the stiff clay specimen.

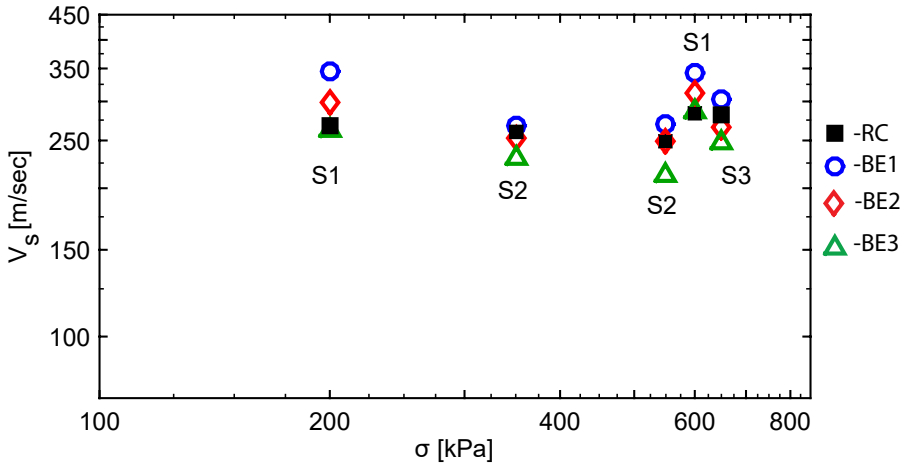

Figure 4.17: Comparison of RC and BE test results.

Mine Paste

Figure 4.18 shows the stiffness and damping degradation curves for the mine paste specimen tested at three difference confinements. Hyperbolic mode is fitted to the curve.The stiffness shows the normal trend, while damping at low strains is constant for the three confinement. Figure 4.19 shows the comparison of RC and BE for the three confinement. Similar to the stiff clay specimen, the RC and BE velocity values do not match within the confinement range used for this study. The three values of velocity from BE are very close to each other in this case. The slopes of the line indicate that the shear wave velocity from BE is not changing with the confinement as expected.

4.5 Leda Clay

For leda clay test, three tests were done and the specimen are labelled as L1, L2, and L3. Two tests were conducted at 80 kPa effective confinement, while one test was performed at 48 kPa. Figure 4.20 shows the degradation curves for three effective confinements. The results of the shear modulus and damping are curve fitted using a modified hyperbolic model. For the third sample it was decided to reach close to the limit state of the clay, i.e. up to 160 kPa. Therefore, the confinement was increased from 80 to 160 kPa in increments of 20 kPa. For each confinement, the sample was allowed to consolidate. Resonant column and BE tests were done at the end of consolidation. Figure 4.21 shows the comparison of shear wave velocity and damping with effective confinement. The

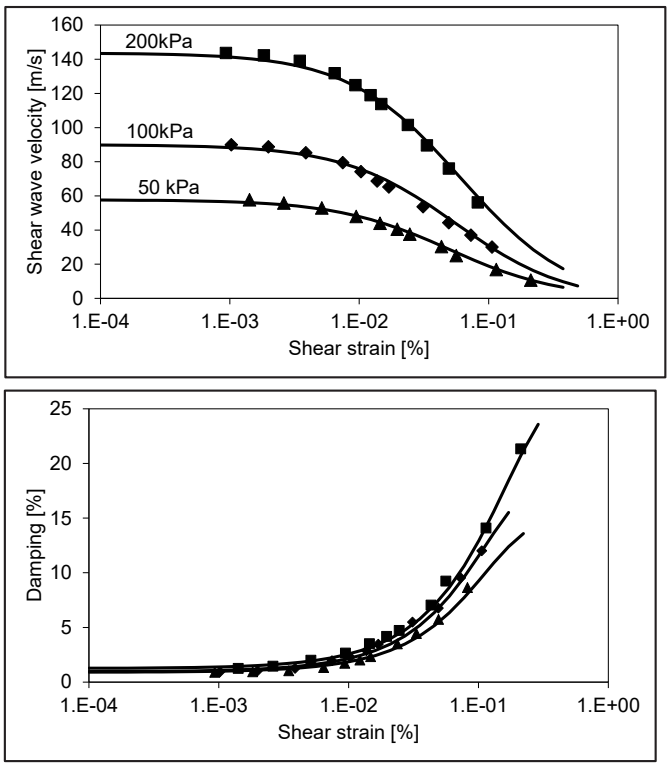

Figure 4.18: Degradation curve from mine paste specimen.

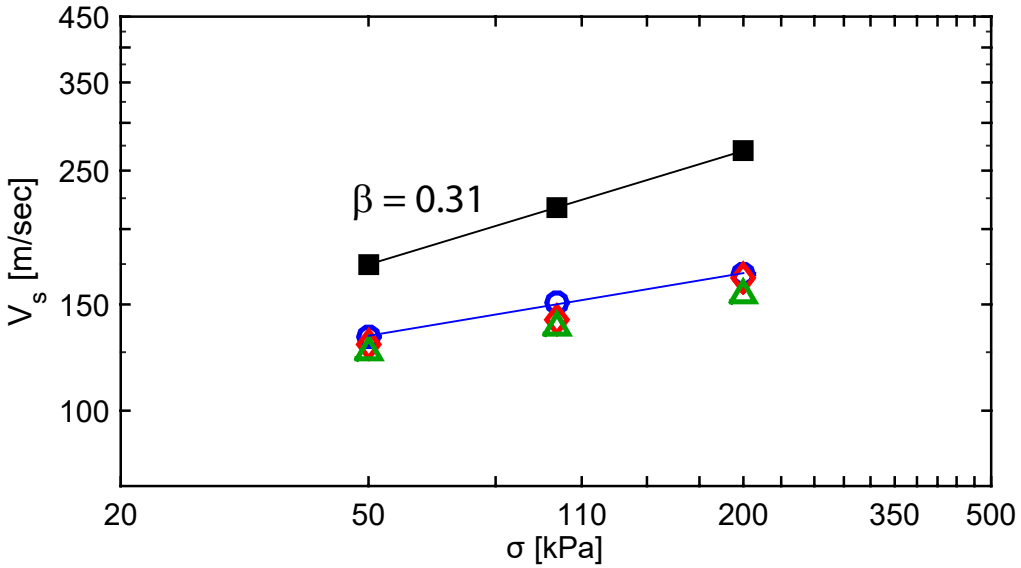

Figure 4.19: Comparison of shear wave velocity from RC and BE tests.

exponent β in this case is 0.32. The value of β obtained from the relation of soil velocity given in Santamarina et al. (2001) is 0.32 for soft clays, which matches with the result obtained from this study. The values of α is 28.13, respectively. The damping ratio curve as a function of confinement remains constant, which shows that very little energy is lost at low strains. This is very critical for infrastructure on soft and sensitive clays.

Comparison of RC and BE show that at lower confinement, the RC results match with the third peak in the BE while for higher confinement the RC results are closer to the first peak. The trend in both cases is the same with an increase in shear wave velocity as confinement increases.

The variation of shear wave frequency with confinement is presented in Figure 4.23. The trend shows the increase in the frequency content with the increase in the confinement. The good results in this case show the effect of coupling. For the leda clay sample, the new RC top and bottom platens were used. In the new system, radial blades were used to improve the coupling for stiff and soft soils.

At the end of consolidation for 160 kPa, the resonant column system was moved to the isolation table. During this time the sample was not detached from the pressure system, i.e. the sample was feeling the same pressure of 160 kPa during the process of transfer. The advantage of the isolation table is to reduce noise from any external source. The aim was to understand the effect on the damping ratio by use of isolation table. Figure 4.22 presents the degradation curves for the clay. The increment in strain level was small to understand the change in the stiffness and damping at larger strains. The results are curve fitted with modified hyperbolic model. The unloading curve is also shown while after three increments in strain, a low strain test was done. This test was done to check for any shearing of the specimen due to the increment in load. Figure **??** shows the comparison of the degradation curves for the two confinements, 80 and 160 kPa. The modulus curve shows the increase in the stiffness of the specimen, however the damping shows no change. Therefore, further study is needed to see the change in the damping ratio using the isolation table by testing sand specimens. The results of the RC and BE test done in this study are matched with the seismic cone penetration test from the field. A good match between the results can be seen. The results of the seismic cone penetration test are provided by the University of Laval (Bouchard, 2015).

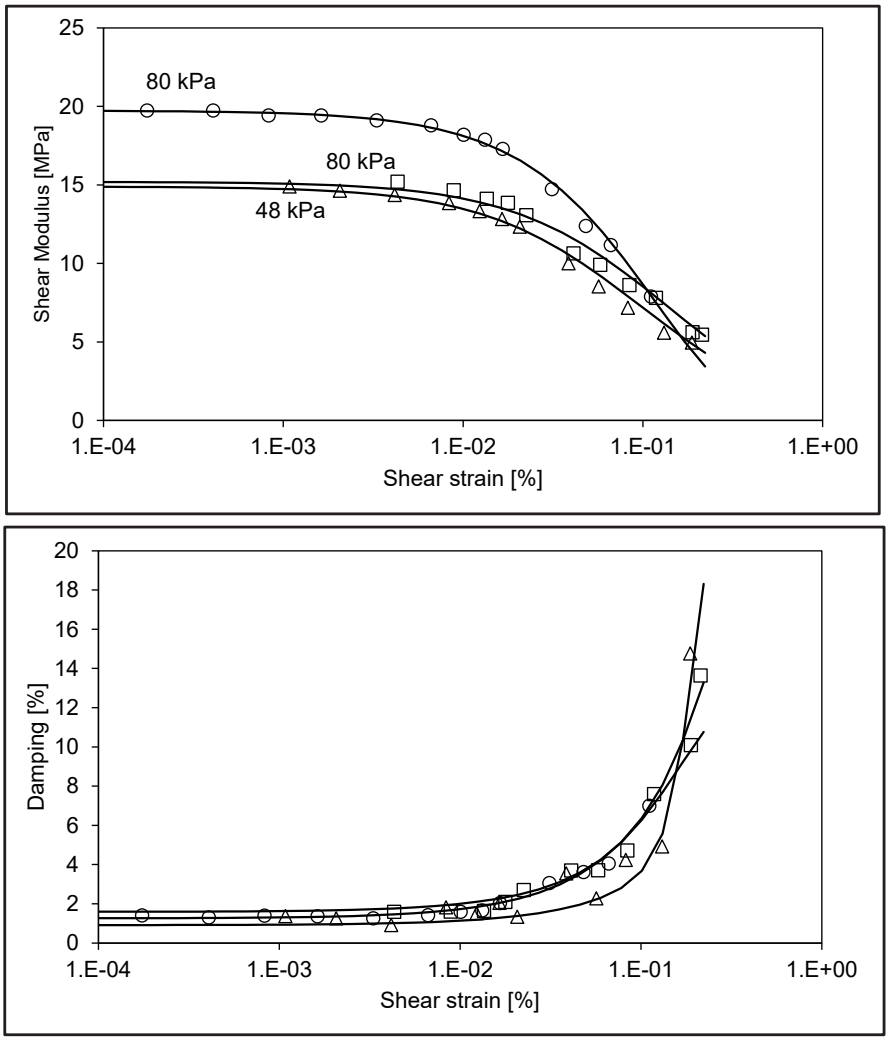

Figure 4.20: Degradation curve for three samples of Leda clay. Two samples are tested at 80 kPa confinement while one at 48 kPa.

4.5.1 Sand specimen

Two sand specimens were tested, S1 and S2. Sample S1 corresponds to the test on the regular RC table while S2 is tested on the isolation table. Figure 4.30 shows the results of the variation of shear wave velocity and damping with confinement. The test is done for confinement of 25, 50, 75, 100, 150, 200, 300, 400, 500, and 600 respectively for sample S2. For sample S1 the confinement is done for 50, 100, 200, and 400, respectively. The change in the low-strain propagation velocity V_s with the increase in the isotropic stress was fitted with power law function. The exponent from the equation

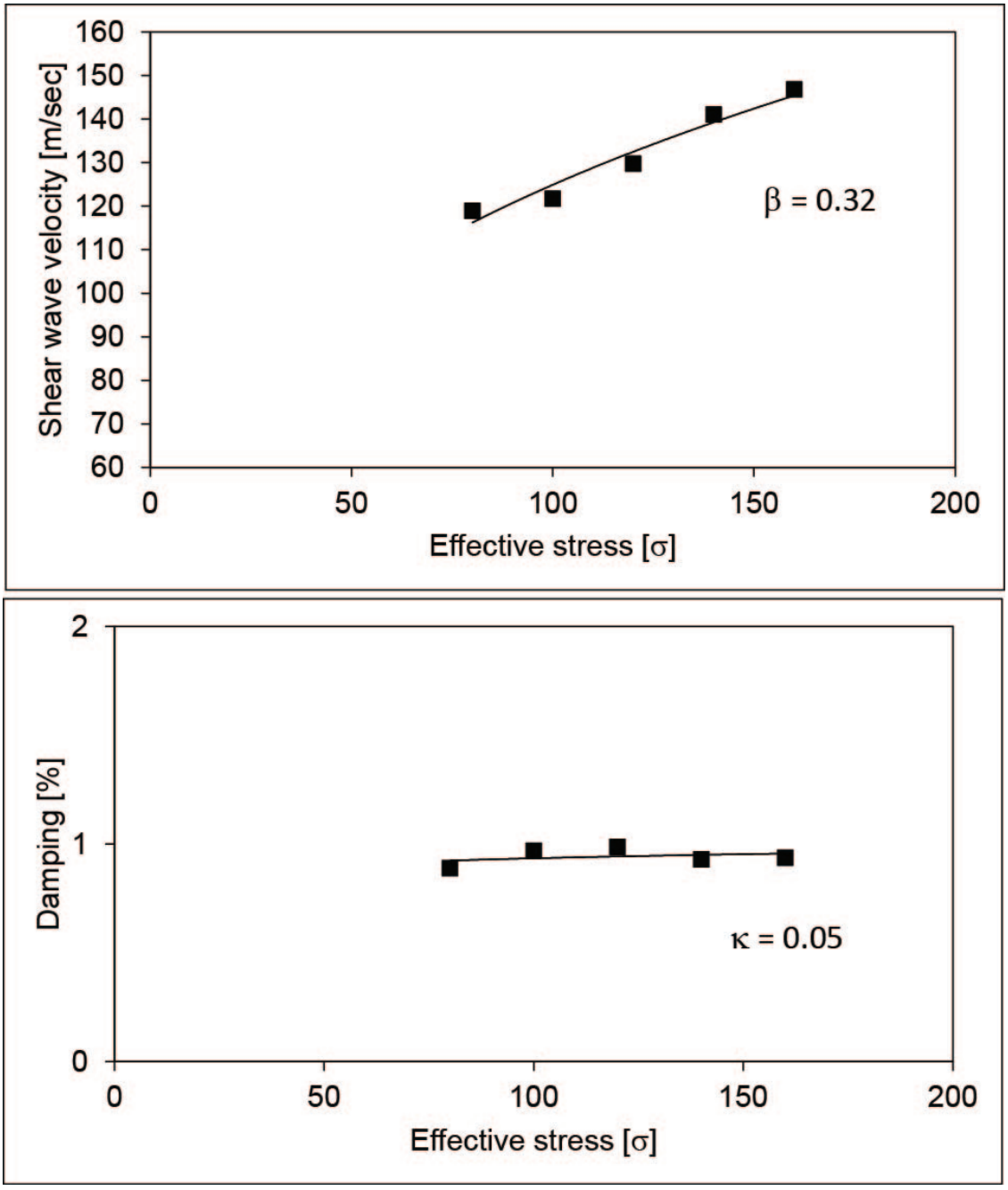

Figure 4.21: Variation of shear wave velocity and damping with confinement for L3.

β was back calculated using the relation provided by Santamarina et al. (2001), $\beta = 0.36 - \alpha/700$. The exponent β obtained from this work is lower than the relation provided in the book by 8 % for S2. A similar procedure is repeated for the damping ratio curve. The damping ratio curves for both the samples show similar values. At low effective confinement, the damping ratio decreases and remains constant for higher pressures. These results are similar for sand specimens as discussed by

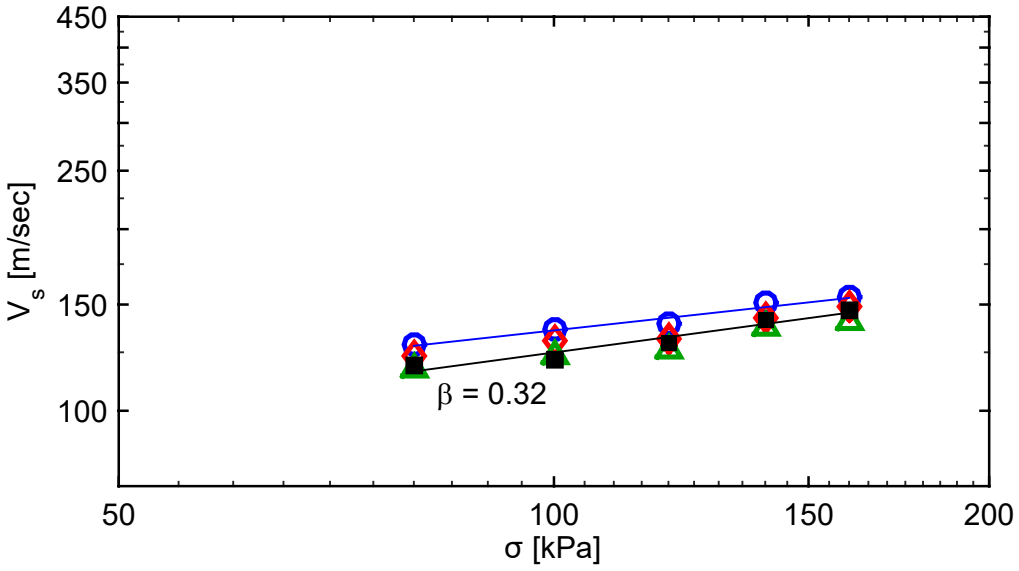

Figure 4.22: Comparison of RC and BE shear wave velocity values for all confinements. Three peaks are selected to best estimate the shear wave velocity.

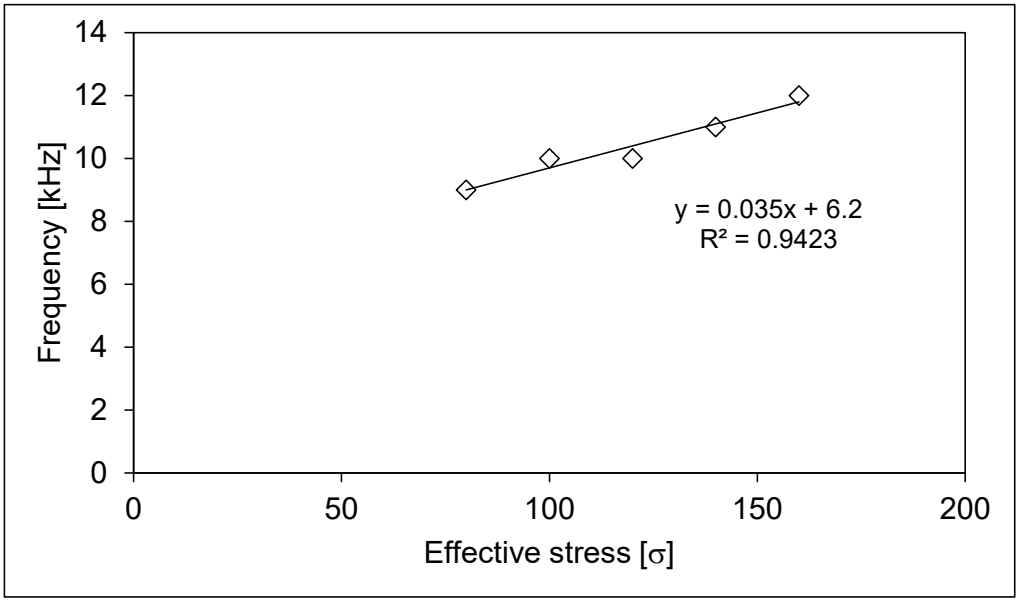

Figure 4.23: Variation of frequency with confinement for L3.

Khan et al. (2008) and Camacho-Tauta et al. (2015). At the end of the test, the degradation curves for sample S2 are obtained (Figure 4.28). The results are fitted with the modified hyperbolic model. The tests for sand 1 and sand 2 are performed on the newly designed top and bottom platens which

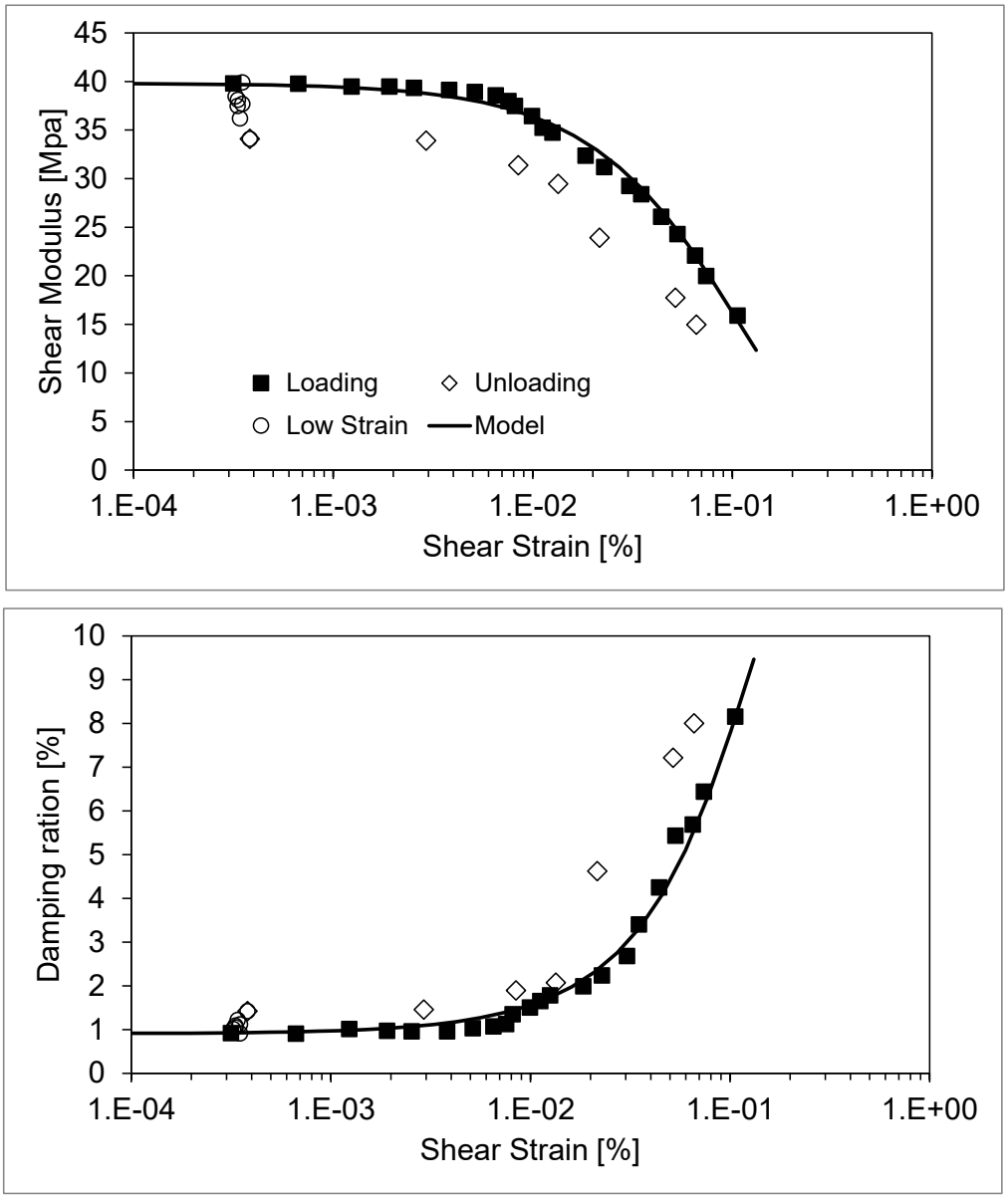

Figure 4.24: Variation of shear modulus and damping ratio as a function of confinement for 160 kPa. The test was conducted on isolation table.

consist of radial blades to improve the coupling in stiff specimens.

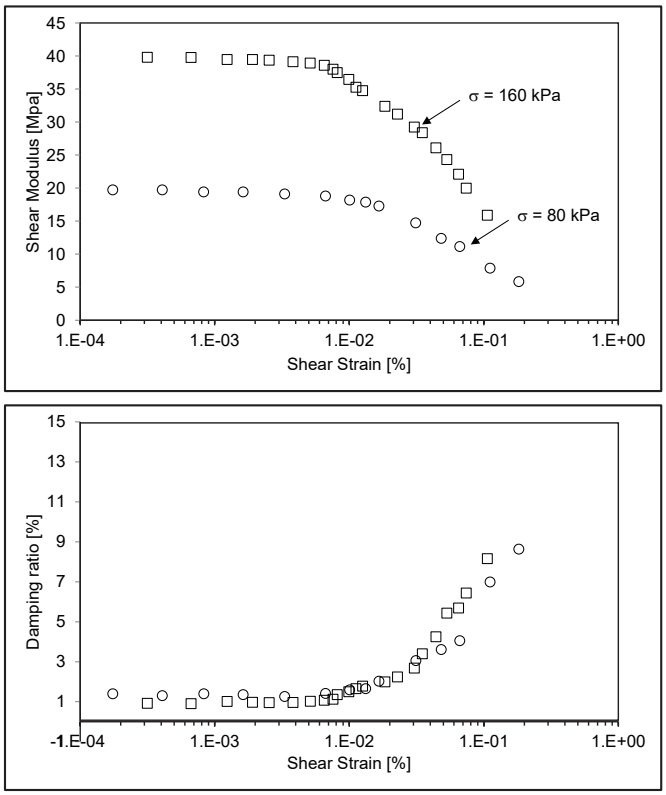

Figure 4.25: Comparison of degradation curves for 80 and 160 kPa. The test was conducted on isolation table for 160 kPa.

Comparison of RC and BE results - frequency effects

Results of the comparison between the RC and BE show that BE results follow the same trend as RC values. At low confinement, the slope of the Vs_{BE} is low compared to the values of Vs_{RC}. The values of BE match with the RC at higher confinement. This could be due to less contact of sand particles with benders as compared to stiff packing at higher confinement.

The variation of resonant frequency obtained from S1 and S2 is shown in Figure 4.29. For sample S1, after effective confinement of 200 kPa, the frequency of the s-wave is constant, while for S2 the frequency is increasing. The different slope values of frequency with confinement show that frequency effects need to be addressed in the computation of shear wave velocity from BE specimens. Below 200 kPa, the s-wave frequency is not linear and much scatter can be observed. This could be due to the participation of other frequencies at this confinement.

The wavelengths obtained from RC are 3.5 m while for BE the wavelengths are 2.5 cm for all

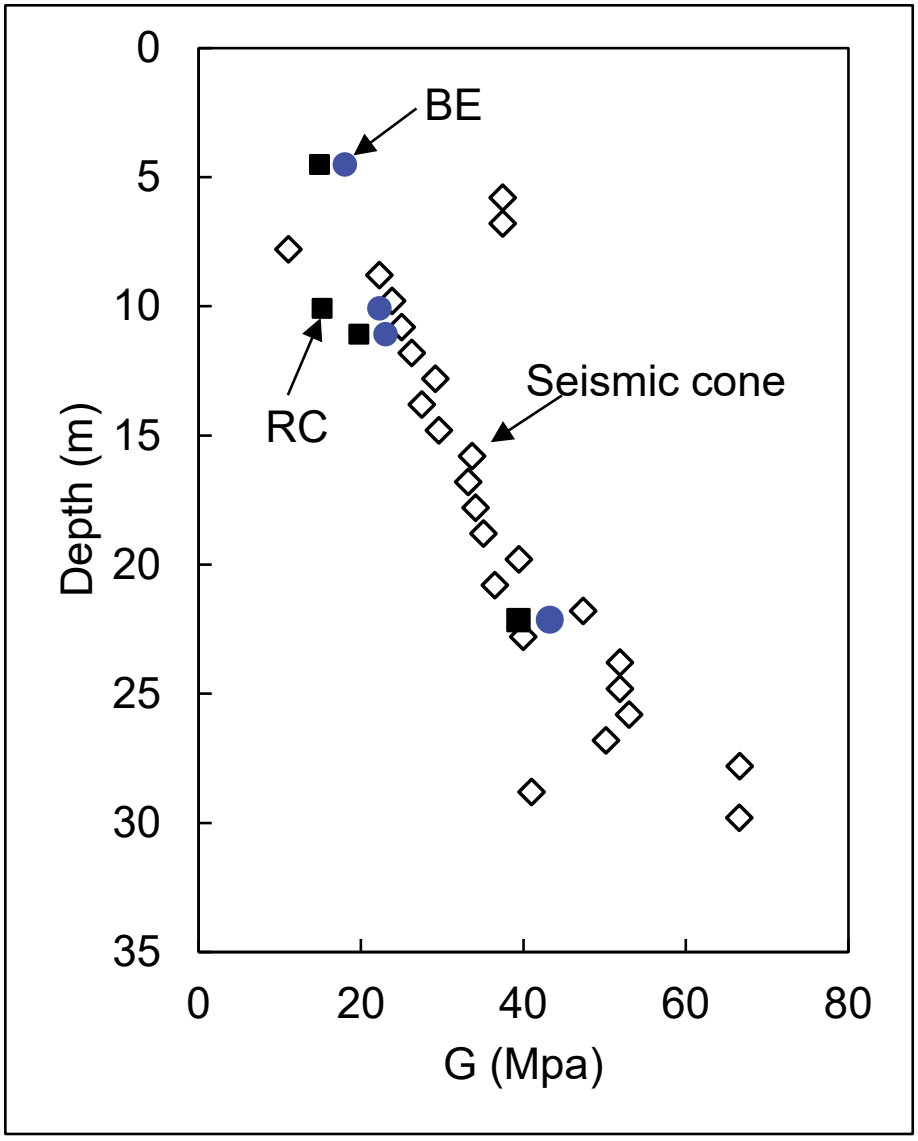

Figure 4.26: Comparison of shear modulus from RC and SC test. (Bouchard, 2015)

tests studied in this thesis. The effect of the frequency can be noticed in all cases. In the case of leda clay, the effect of frequency is not significant, however, the BE results are higher than the RC. In case of mine paste, the frequency effect is significant. The RC values are higher than the BE values (approximately -30 %). The large difference could be due to the specimen type as the wave is attenuated in mine paste and also the specimen is remoulded and prepared in the RC device.

The results of stiff clay show the variability by testing different samples at various confinements. In this case, much dispersion is noticed between BE peaks and also with RC. Compared to mine

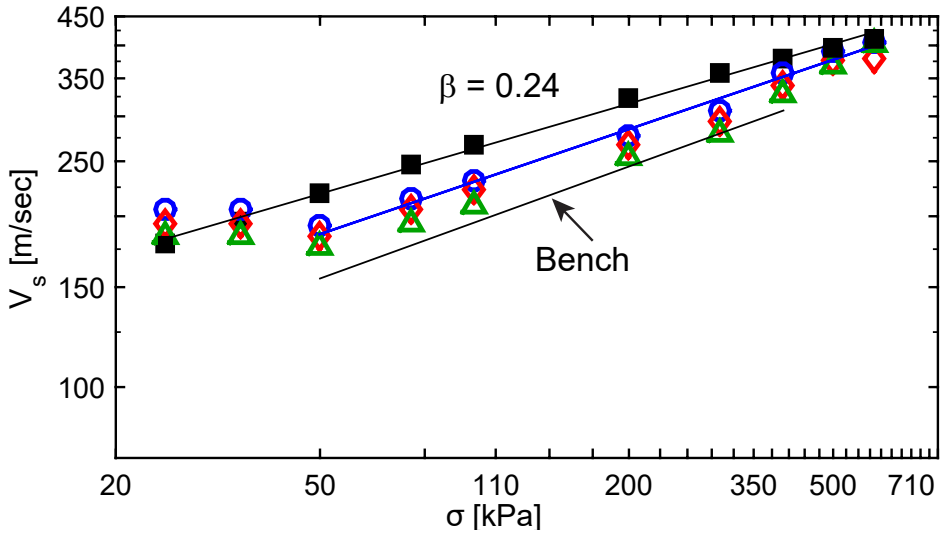

Figure 4.27: Comparison of shear wave velocity for sand samples from RC and BE tests.

paste, the results for BE are higher than RC. The difference is 23 % for different samples. The RC results show no change in the stiffness as a function of confinement but BE shows much dispersion. The importance of coupling could also be noticed as no blades were used in this case.

The results of sand specimen shows lower BE values than RC similar to mine paste specimen. For lower confinements (Figure 4.27), the BE shows higher values than RC which could due to viscous effect at low confinement, however, after 50 kPa, the slope for BE values is similar to RC values.

The main idea presented here is that for different soils, the results from bender are not consistent, it could be higher, on the line, or lower than RC results. Also, the matching could change from confinement and from pressure depending on the behaviour of bender.

Therefore, to study these frequency effects in the shear wave velocity estimation, the modified frequency domain method is proposed and studied on dry sand sample to the explain the frequency effects at higher frequencies (0 - 50 kHz), presented in section 4.7.

4.6 Effect of base stiffness

The effect of base stiffness is also studied in this thesis. There is not much literature available to show the effect of base stiffness on measurement of shear wave velocity. In this study, as explained

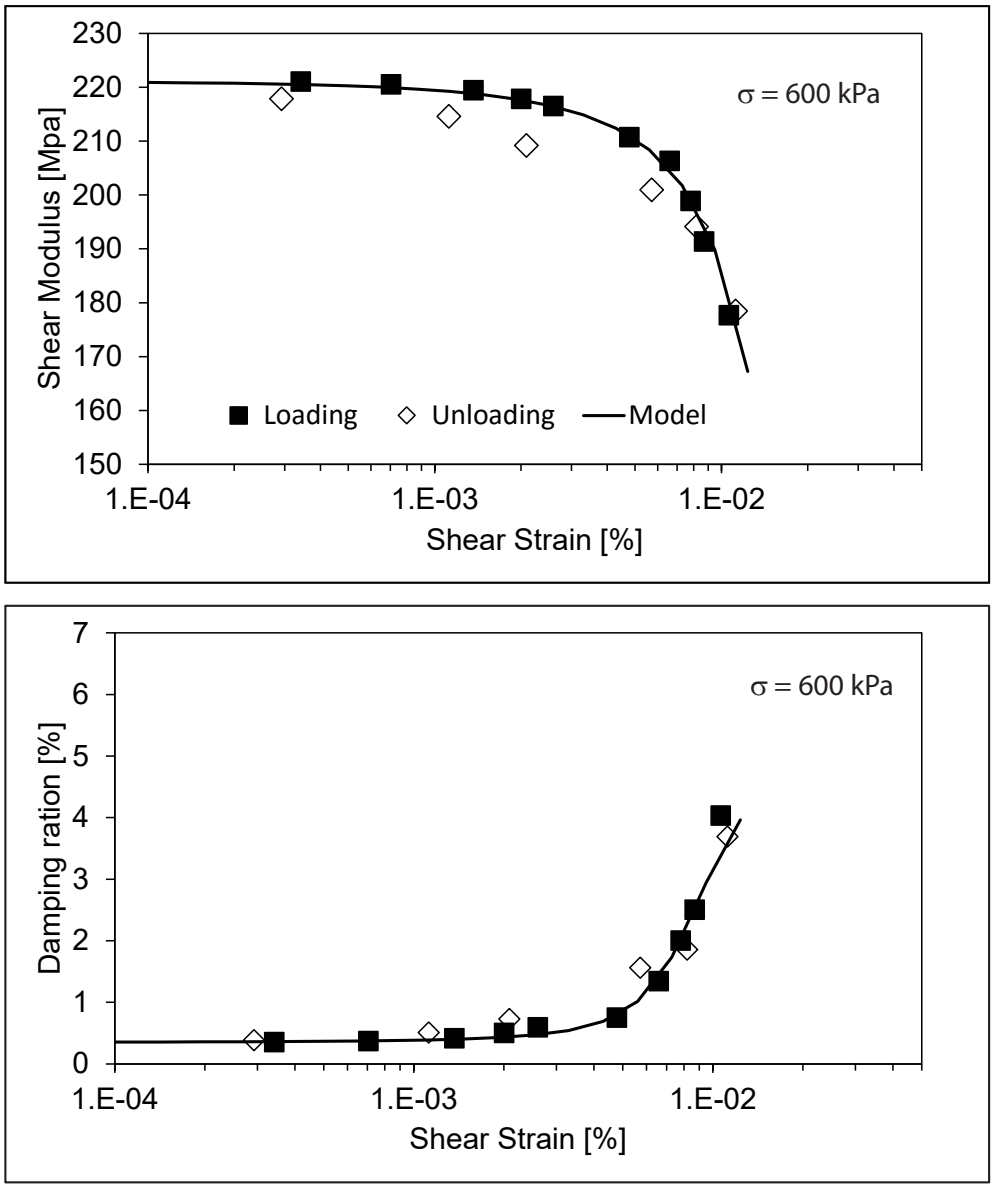

Figure 4.28: Degradation curves for Barco sand sample S2. The test was conducted on isolation table. Modified hyperbolic model is fitted to the curve.

earlier, the test was done on isolation table and bench. Figure 4.30 shows the comparison of shear wave velocities from bench and isolation table. The results could be explained using the solution of RC as two-degree-of-freedom system (Khan, 2007). The natural frequencies of the system can then

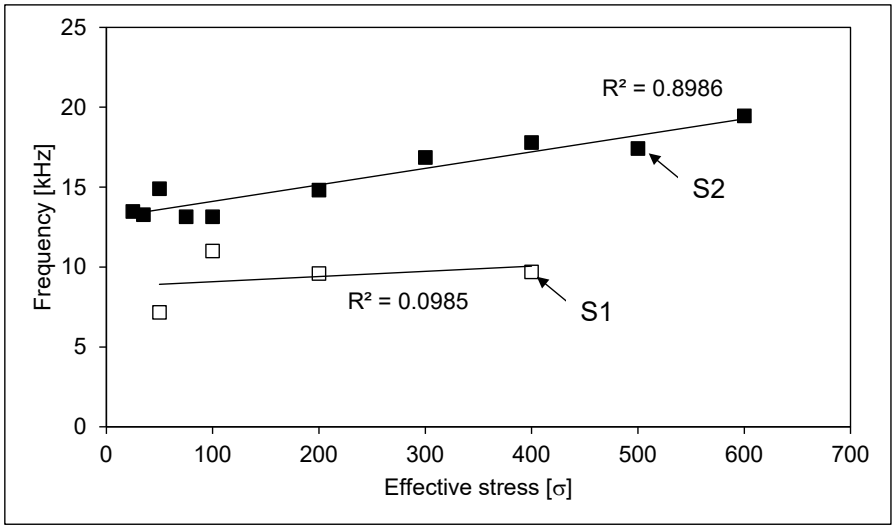

Figure 4.29: Variation of frequency with confinement for S1 and S2.

be given as:

$$f_{1,2} = \frac{1}{2\pi}\sqrt{\frac{1}{2}\left[\frac{k_1}{I_1}+\frac{k_1+k_2}{I_2}\right] \mp \sqrt{\frac{1}{4}\left[\frac{k_1}{I_1}-\frac{k_1+k_2}{I_2}\right]^2+\frac{k_1^2}{I_1 I_2}}} \tag{4.3}$$

The subscript 1 refers to the properties of the specimen, whereas, the subscript 2 refers to the characteristics of the base and the combined mass polar moment of inertia of driving plate and the specimen. If the stiffness of the base approaches zero and the mass polar moment of inertia of the base approaches infinity, then the equation gives the resonance frequency of the specimen. This solution shows that the shear wave velocity obtained from isolation table gives the true values of the velocity of the specimen. The difference in the velocity between bench and isolation table is 60 % which is significant. Further tests are needed to be done to understand the effect of base stiffness.

4.7 BE Test Using The Modified Frequency Domain Method

4.7.1 Introduction

In bender element (BE) testing, shear wave velocities are measured using two main methods: time domain analysis of vibration data from pulse excitation and frequency domain analysis of vibration

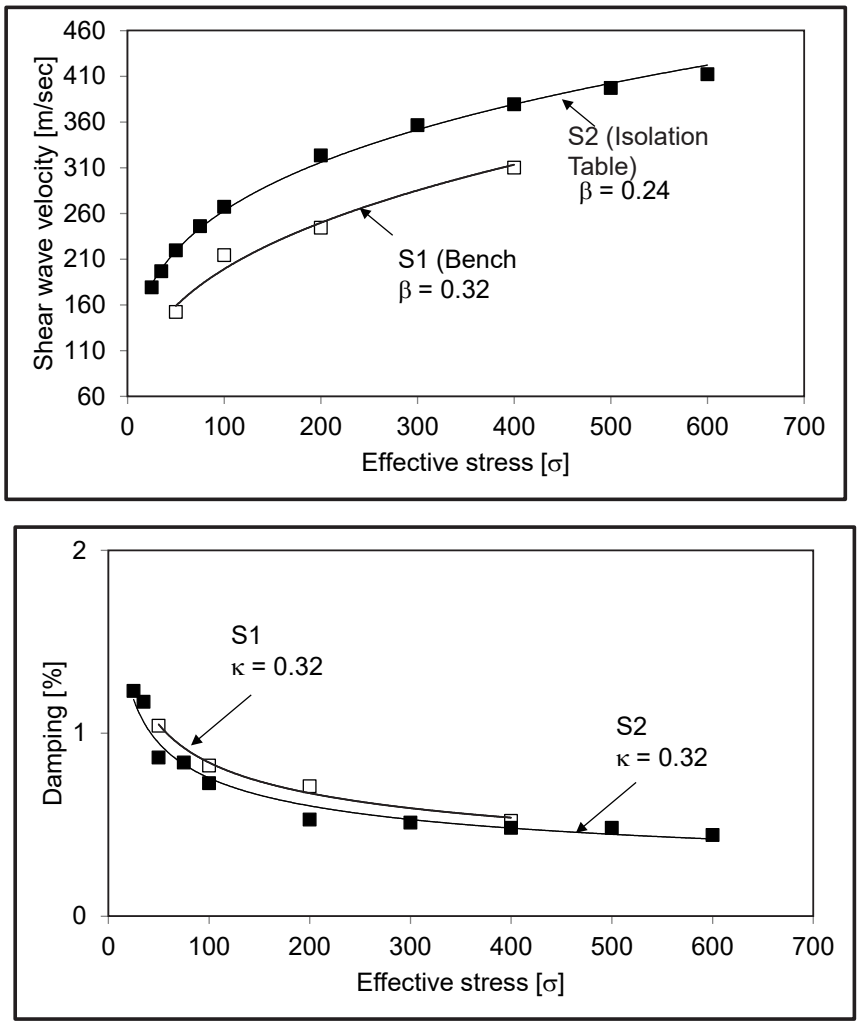

Figure 4.30: Variation of shear wave velocity and damping ratio with confinement. S1 is for sand sample 1 while S2 is for sand sample 2.

from sine sweep excitation. The time domain analysis is simple but requires subjective judgment for the non-automatic determination of the arrival time. Conversely, the frequency domain analysis can be performed automatically. However, its results show high variability because they are affected by different variables such as the frequency content of the excitation, the resonant frequency of the BE system, and the resolution of the frequency domain analysis. A modified frequency domain analysis is proposed to enhance the reliability of the method using a high frequency narrow-band excitation outside the resonant peaks of the BE system. Results from the modified frequency domain analysis tests show less than 10% error in the measurement of the shear wave velocity with respect to the

RC results (Camacho-Tauta et al., 2015).

4.7.2 Methodology

To test the proposed frequency domain method, the specimen 2 (Barco 71), was prepared using the dry compaction method as mentioned in a previous section. At the specified confining stress of 50, 100, 200, and 400 kPa, RC and BE frequency domain tests were performed sequentially. Frequency domain analysis was done by exciting a sine sweep from 1 to 20 kHz in the traditional method and from 20 kHz up to 50 kHz with an interval of 3.2 kHz in the modified frequency domain method. Results from sine sweep tests are analyzed using the moving frequency window method (Viana da Fonseca et al., 2009). In the frequency window method, different frequency windows were selected to find the best coefficient of correlation that matches with the shear wave velocity from the RC test.

4.7.3 Results

Figure 4.31 shows the time signals at the specified confinement. The arrival time of shear wave at each confinement is shown with markers. The effect of confinement on shear wave arrival time can be seen as the confinement increases the shear wave arrival time moves closer to the excitation signal; showing increase in the stiffness of the sample. Also, higher frequencies and P-wave reflections mask the arrival of shear wave as seen for confinement of 200 and 400 kPa. Frequency sweep results for the test are shown in Figure 4.32. The transfer functions between the input and output signals for each confinement are presented in Figure 4.33. At low confinement, the main energy in the frequency spectrum is up to 20 kHz, while for higher confinement, the frequency peaks shift to higher frequencies. Figure 4.34 shows the result of the moving frequency window for a span from 0 to 50 kHz, while Figure 4.35 shows the results for the span of 29 kHz to 32 kHz. In each case, the shear wave velocity obtained at maximum correlation coefficient is shown. Results of the 0.5 kHz moving window are not shown in Figure 4.35 due to large variations in calculated shear wave velocities. Figure 4.36 presents results for specimen 2 The under-estimation of results in the case of the 0-20 kHz window can be observed. The values are 28% lower for low confinement and reduce to 8% for higher confinement. All three spans show a good match of shear wave velocity with RC values while results for the 29.6 32.8 kHz window show the best match. The best match

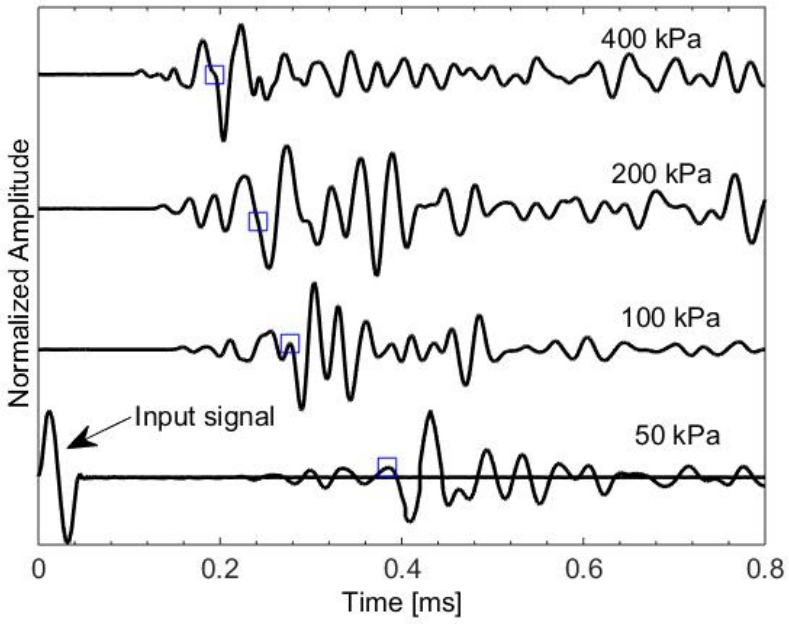

Figure 4.31: Time signals at the specified confinement. Blue markers shows the arrival time of shear wave at each confinement.

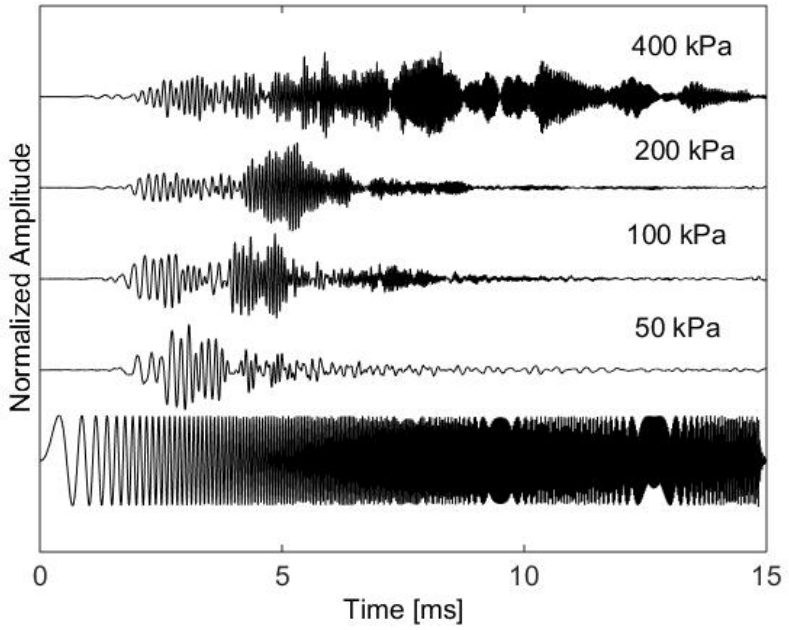

Figure 4.32: Time signals from frequency sweep at the specified confinement

obtained in these cases is due to higher coherence, in the range of 0.8 to 1. Although, a coherence of one was obtained for the 32.8 36 kHz window at 400 kPa, the shear wave velocity is lower than

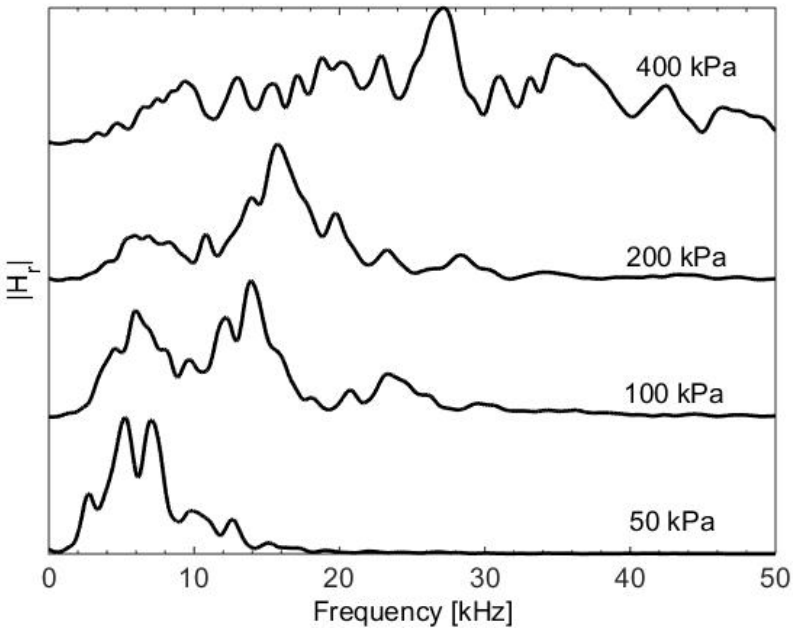

Figure 4.33: Transfer function of frequency sweep signals.

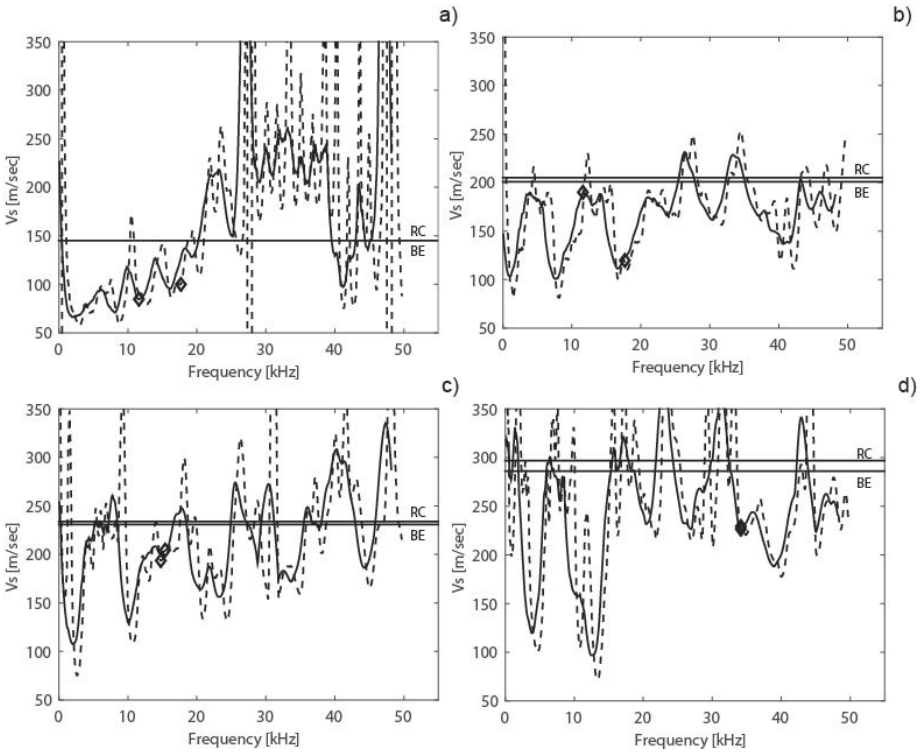

Figure 4.34: Shear wave velocity for frequency span 29.6 to 32.8, a) 50 kPa, b) 100 kPa, c) 200 kPa, and d) 400 kPa. Symbols: ... 0.5 kHz, − − − 1.5 kHz, and - 3 kHz. ⋄ maximum R^2 value from each frequency window.

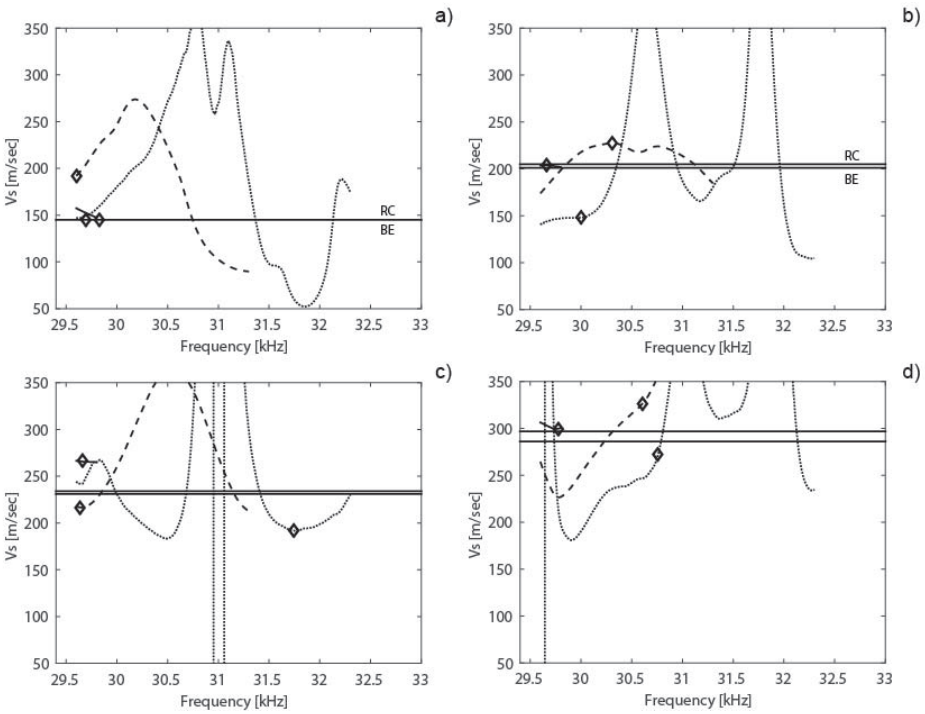

Figure 4.35: Shear wave velocity for frequency span 29.6 to 32.8, a) 50 kPa, b) 100 kPa, c) 200 kPa, and d) 400 kPa. Symbols: ... 0.5 kHz, — — — 1.5 kHz, and - 3 kHz, ◇ maximum R^2 value from each frequency window.

the RC value. This could be attributed to change in transfer function amplitude, which is -4dB peak value as compared to -30dB for all other spans. Also, as the peaks in the transfer function move to higher frequencies for higher confinement, the shear wave velocity should be searched at the flat portion of the transfer function. Due to the limitation of the instrument, frequency excitation higher than 50 kHz could not be generated. Further, investigation is required in this case. The variation in the mean shear wave velocities for values obtained in Figure 4.36 are presented in Figure 4.37. The variation is less than 10% for 50, 100, and 200 kPa of confinement, respectively. The variation is more than 20% for effective confinement of 400. If the value shown in the circular marker, for 400 kPa, is removed from the mean value, the error reduces to 11% showing the validity of the method at higher confinement. Figure 4.38 shows the shear wave velocity estimation for excitation frequency up to 20 kHz. In this range, only the lower confinement (50 kPa) has good agreement with resonant column test results.

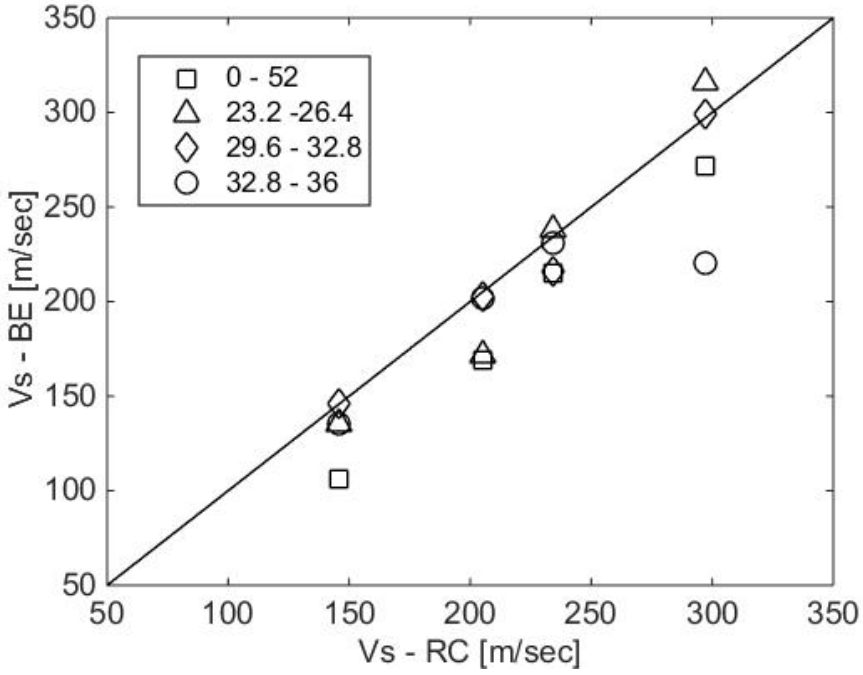

Figure 4.36: Comparison of shear wave velocities from RC and modified frequency method for selected window spans as shown in the legend.

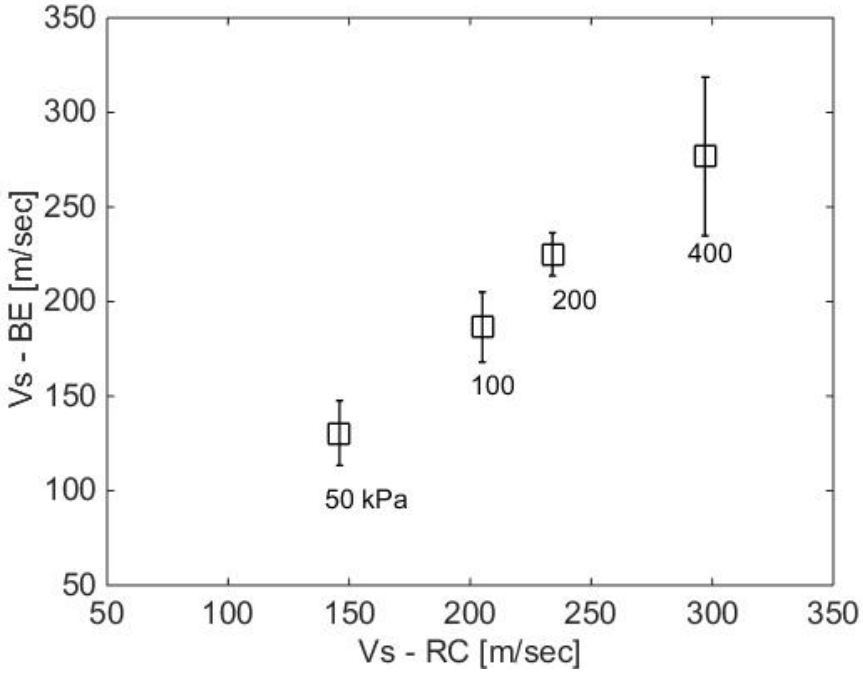

Figure 4.37: Variation of shear wave velocity values from the modified frequency domain method for each confinement. Square markers show the mean shear wave velocity.

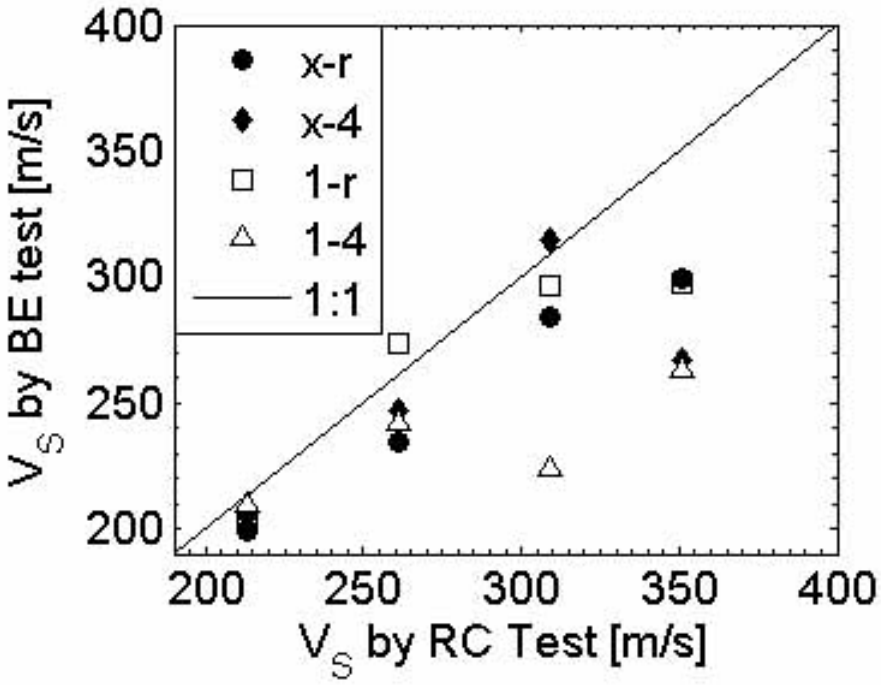

Figure 4.38: Comparison of shear wave velocity estimations by different pairs of sensors and RC results (Camacho-Tauta et al., 2015).

4.8 Chapter summary

Laboratory measurement of shear wave velocity and damping ratio evaluation for small strains is usually done through RC and BE tests. The RC test is a standard testing method, however, there is no standard methodology for BE testing. This is due to the interpretation of the BE test measurements. Time and frequency domain methods are available, however, work needs to be done to understand the actual behavior of benders in the air and under various systems before the results are interpreted, especially, the effect on the wave velocity and attenuation. The following conclusions can be made from the RC and the BE tests.

The RC device is calibrated using aluminum probes. Three aluminum probes of 9.47, 19.12, and 25.23 mm internal diameter were used. For the 25.25 mm internal diameter probe, the test was conducted from small strain to large strain. The shear modulus value remains constant for the range of strain tested while the damping value changes from 0.2 % to 0.6 % ($\gamma = 8 \times 10^{-3}\% to \gamma = 8 \times 10^{-1}\%$).

The bender element was calibrated using three configurations; tip-to-tip, short sand specimen,

and bender in air. A state of art laser vibrometer is used to characterize the bending behavior of bender elements showing the resonance frequency of 12 kHz and damping of 2% when vibrating in the air. The resonance frequency value from other configurations give similar results. The delay time is calculated as 4.5 μ second from the tip-to-tip test and from the aluminum probe test. The maximum displacement of BE vibrating in air for transmitter BE is 15 nm while for receiver BE is 3 nm.

Four soils are tested: stiff clay, mine paste, leda clay, and sand. The top and bottom platen of the RC device were modified to allow better coupling between the specimen and benders. Radial blades were introduced to account for coupling of clay specimens such as stiff clay specimens. The tests were done at confinement ranging from 50 kPa to 600 kPa and for strain levels ($\gamma = 1 \times 10^{-4}\%$ to $\gamma = 2 \times 10^{-1}\%$).

For leda clay and sand specimen 2, the modified RC bottom and top platen were used. The results of leda clay showed the effect of coupling improvements in the stiffness increase as a function of frequency and confinement. Tests on leda clay show no change in the damping ratio (0.8 %) at low strains for the confinement applied in this study.

A modified frequency domain method for BE testing is presented for the sand specimen. The sample is excited with a frequency sweep ranging from 0 to 52 kHz. Change in unwrapped phase, between the input excitation and output response, is evaluated outside the range of resonant peaks of the specimen. Variation in shear wave velocity is less than 10% between resonant column and bender element tests.

CHAPTER 5

Numerical simulations and laboratory MASW Test

5.1 Introduction

This chapter focuses on the results obtained from the numerical simulations and the laboratory test on homogenous and non-homogenous mediums. Results from nine numerical models and three laboratory test on a sandbox are presented in this chapter. In each test setup, the non-homogeneity in medium is introduced by a void (cavity). MASW test method is used for numerical simulations and laboratory tests. A new methodology, to understand the wave-anomaly interaction on surface responses, is used by dividing the array of receivers into three sections, before, on-top, and after the void. The results are analyzed in time and frequency domains. Laboratory tests for the void and the no-void cases are performed on the sandbox and the results show a good match between the numerical and the experimental tests. The new methodology provides useful guidelines for the MASW test for better assessment and characterization of the soil profile for the design of foundations.

To understand the frequency effects due to the coupling of accelerometers with the surface and source selection in laboratory MASW testing; two tests are done with the traditional accelerometers while the third test is done with the state of art laser vibrometer.

5.2 Numerical and Experimental methodology

5.2.1 Numerical Models

A finite difference program FLAC (Itasca, 2000) is used to study the propagation of surface waves in a linear elastic continuum which contains a void. In MASW tests, the medium properties and propagation pulse govern wave propagation through the medium. The medium properties include modulus of elasticity E, Poisson ratio μ, mass density ρ, and material damping D. Since material damping is small for low strains and independent of frequency (Santamarina et al., 2001); assumed material damping is ignored.

The selected material properties for the numerical model are Poissons ratio, μ = 0.2; density ρ = 1600 (kg/m^3), and modulus of elasticity, E = 19 MPa. Consequently, the corresponding wave velocities are P-wave, V_P = 114.9 m/s, shear wave V_S = 70.3 m/s and Rayleigh wave V_R = 64.08 m/s (Nasseri-Moghaddam, 2006). Figure 5.1 illustrates a general sketch of the two-dimensional axisymmetric model used for the simulations. Figure 1a shows the location and embedment depth of void from receiver while Figure 1b represents the array sections considered for this study. Model parameters are adjusted to match theoretical results and to verify that the model accurately predicts the R-wave propagation in a semi-infinite medium. The model consists of a central uniform grid surrounded by a non-uniform grid. The axis of symmetry is defined at the left end boundary, while quiet boundaries are defined at the right and bottom. To effectively reduce the reflections of R-waves, the boundaries of the numerical model are practically positioned as far from the void as possible. The distance between the receivers and boundary is selected to ensure that the reflections from the boundary are not greater than the main Rayleigh wave arrival at any receivers. Hence, reflections from the boundary can be seen in the time signals of main Rayleigh wave event. Alternatively, reflections from R-wave generated after the interaction of the main R-wave event with the void are practically not affected by boundary reflections because of their geometrical attenuation. Lamb source is applied to all numerical simulations (Lamb, 1904). The forcing function applied to the left boundary is:

$$f(t) = \frac{F_b}{\pi} \frac{\tau}{t^2 + \tau^2} \tag{5.1}$$

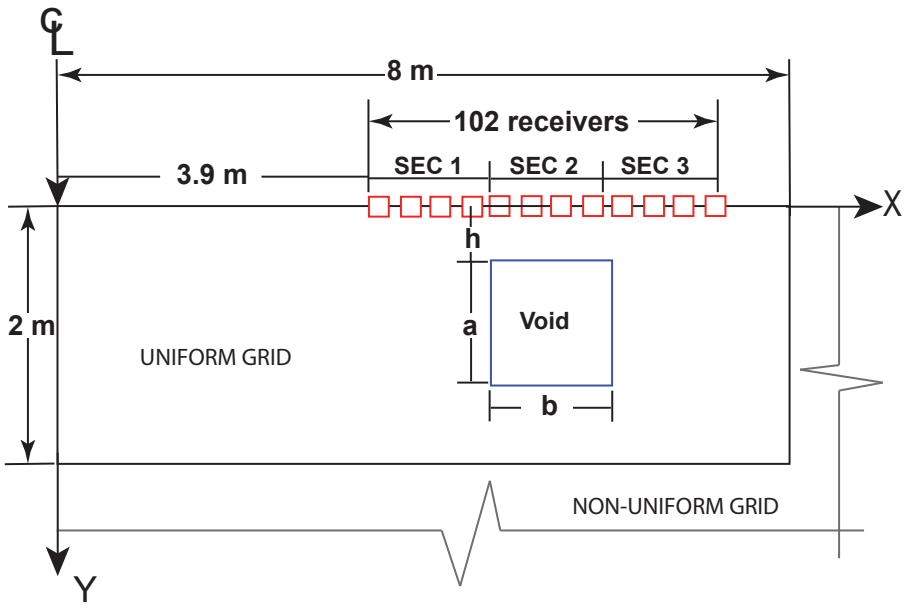

Figure 5.1: Configuration of the basic finite difference model showing the location of void, surface receivers, and model dimension only showing the uniform grid. The total dimension of the model is 20 m by 20 m.

In Equation 5.1, F_b and τ are constants that modify the amplitude and the frequency content of the force function, respectively. Rectangular voids of variable width and embedment depth are introduced in the numerical models. The distance from the source to first (offset distance) and last receivers are 3.992 m and 7.992 m, respectively. The width of the void is 0.08, 0.16, and 0.32m while the height remains same for all numerical models (a = 0.08m). The depth from the surface to the top of the void, embedment depth, h is 0.08, 0.16, and 0.32 m. Therefore, nine models and no-void case are studied in this study. Surface responses are recorded from a total of 101 recording points as shown in Figure 5.1. The maximum and minimum reliable wavelengths considered for the model are λ_{max} = 2.0 m (f = 32 Hz) and λ_{min} = 0.08m (f = 801 Hz), respectively. In order to reduce near-field effects, recording points are located far from the source.

Further, the calibration of the numerical model is performed by changing model parameters such that the responses measured from numerical model without void matches well with the theoretical model. Details of calibration can be found in Nasseri-Moghaddam (2006). To study the effect of wave propagation on surface responses; recording points are divided into three sections as illustrated in Figure 5.1. Section 1 (1-39) before void, section 2 (21-59) centered on void, while section 3

(41-79) after the void, respectively. The length of array in each section is kept constant, i.e., 38 receivers. Figure 5.2 shows the flow chart of the testing methodology.

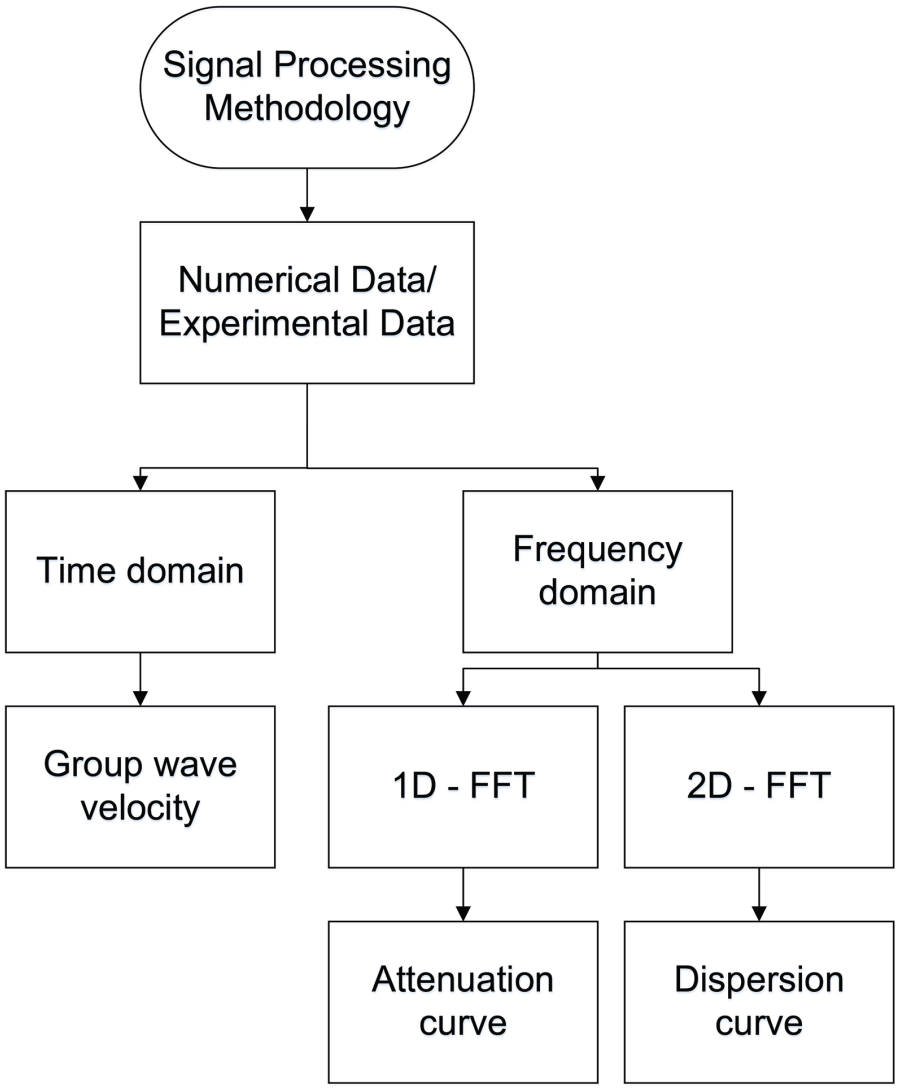

Figure 5.2: Flow chart of signal processing methodology

5.3 Numerical Results

Analysis of results in time domain

Figure 5.3, shows the typical time traces of the surface responses, due to the Rayleigh waves, for the section 1, 2, and 3. The time window in the Figure 5.3 is selected to demonstrate the main features

of the Rayleigh waves; since the amplitude of the P- and the S- waves is small as compared to the R-waves. The solid line represents the surface response in the presence of the void while dash line represents the surface response for the no-void case. The time traces shown in Figure 5.3 are for the void having the width and embedment depth of 8cm. In each section, the arrival of the main pulse can be noticed. Effect of the reflections from the void can be clearly observed in the section 1 and 2. Similar results are obtained for other models.

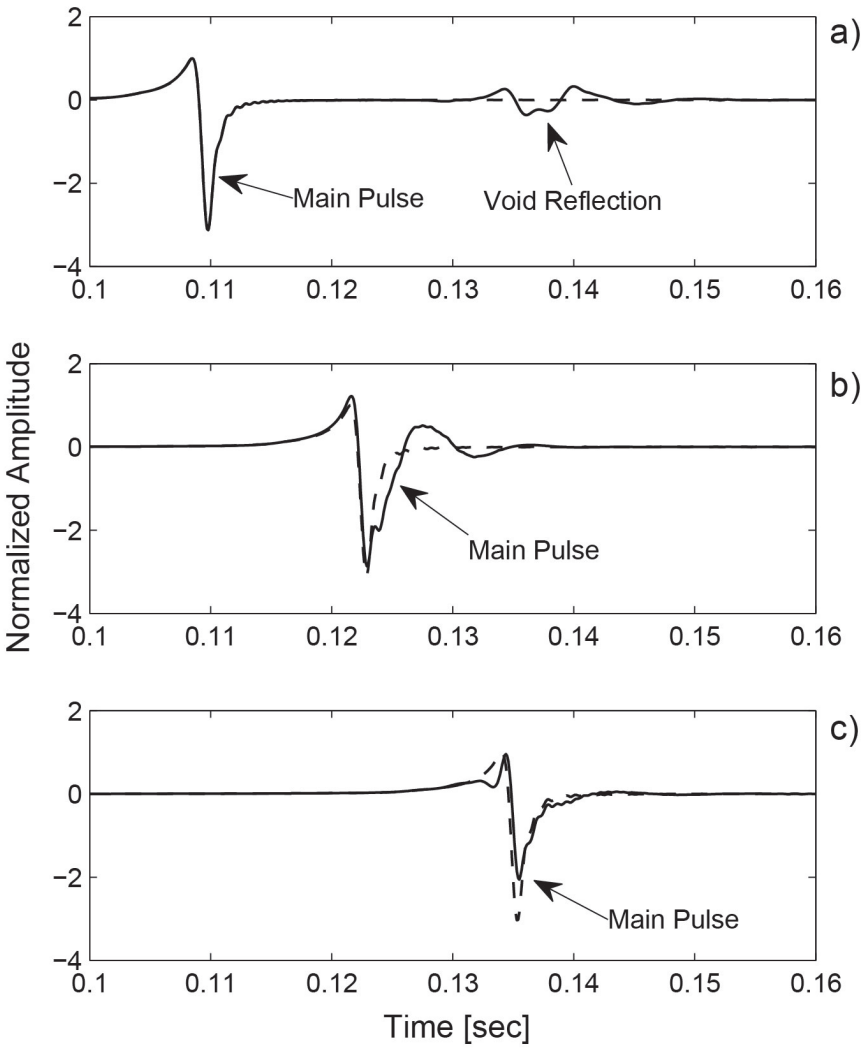

Figure 5.3: Time traces of a) section 1, b) section 2, and c) section 3 for b = 0.08m and h = 0.08m. Solid line indicates for void while dash line is for no-void case. Main Rayleigh wave pulse and reflection from void is indicated.

5.3.1 Analysis of results in frequency domain

Figure 5.4 shows the comparison of the typical Fourier spectra of the vertical displacements obtained from time traces in the Figure 5.3. The Fourier spectra is shown for the no-void (dash line) and the void (solid line) having width and embedment depth of 8cm. The amplitudes of the spectra are normalized based on the section having lowest amplitude. Therefore, for the no-void and the void cases, the spectra are normalized with respect to the section 3. Fourier spectrum of the no-void case is relatively smooth in all three sections. The minor undulations shown in section 1 are attributed to the reflections of P-waves from the model boundaries.

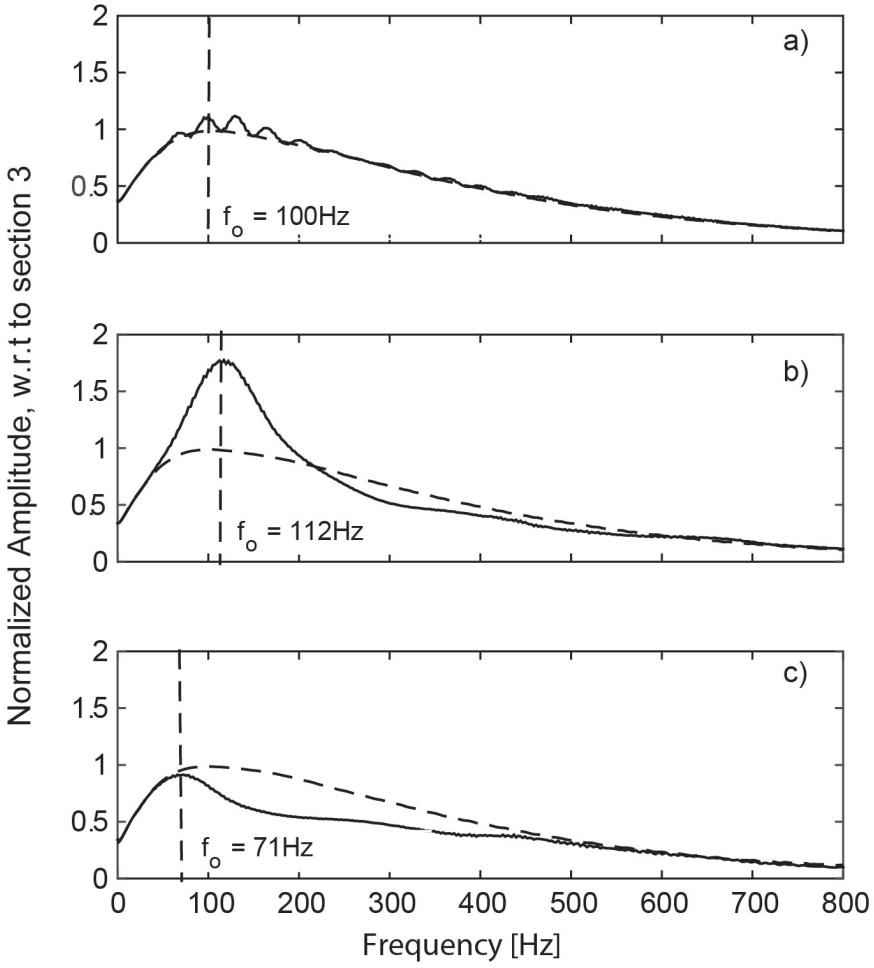

Figure 5.4: Fourier transform of a) section 1, b) section 2, and c) section 3 for b = 0.08m and h = 0.08m. Solid line indicates for void while dash line is for no-void case. Main frequency response is shown for each case.

5.3.2 Frequency-wavenumber f-k (2D FFT) analysis

In this study a new commercial software package SWAN (Surface Wave Analysis) is utilized. SWAN (GEOstudi, 2010) is a seismic data processing software for data modeling and inversion of surface waves measurements acquired using MASW or REMI tests. The surface responses from each model are processed in SWAN to obtain frequency-wavenumber (f-k) plots. Typical f-k plot for the no-void and the void cases are shown in Figure 5.5. The contours represent energy amplitude. The main part of energy, in this case, is between 50 and 100 m/sec. For the evaluation of the experimental dispersion curve, these areas of energy concentrations are searched for the local maxima of the spectrums amplitude. Each line exiting from the f-k spectrum represents the velocity. The slope of the frequency-wavenumber plot is related to the speed of propagation of the wave. The wave number range represents the direction of the traveling wave, i.e., positive wavenumber shows waves propagating in the forward direction (away from the source), and vice versa. In the Figure 5.5, the Rayleigh and the P waves can be identified using the slope of the f-k plot. The values plotted in the Figure 5.5 are logarithmic values.

5.3.3 Dispersion curves

Figure 5.6 shows typical dispersion curves for section 1, 2, and 3 obtained using SWAN for time traces presented in Figure 5.3. To compare the results of the dispersion curves between the no-void and the void case, the dispersion curves are normalized using the following relation:

$$V_{ph(norm)} = 1 - \frac{V_{ph-novoid}(f) - V_{ph-void}(f)}{V_{ph-novoid}(f)} \tag{5.2}$$

In Equation 5.2, $V_{ph(norm)}$ is the normalized phase velocity, $V_{ph-no\ void}$ is the phase velocity for the no-void case while $V_{ph-void}$ is the phase velocity from void case. These dispersion curves are obtained by selecting the local maxima from the f-k spectrum. Dispersion curves obtained from the SWAN are smoothed using a Gaussian function having a bandwidth of 10.

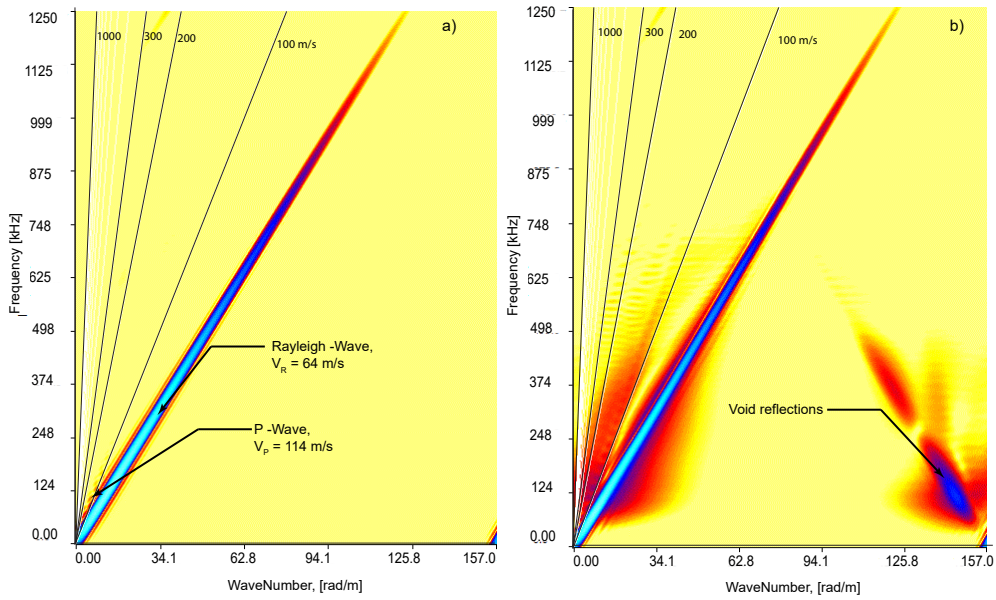

Figure 5.5: 2D Fourier transform for a) no void and b) void. The propagation speed of P and Rayleigh wave are marked. Reflections due to void can be seen in Figure (b).

5.3.4 Pattern identification and normalized wavelength

Once the dispersion curves were obtained for all models, the next step was to identify the pattern between sections for each model. The pattern identification was based on the trend (change) in frequency for dispersion curves having void and comparing them with the no-void case. This method would ensure that the change in velocity is due the effect of the void and not a numerical model error. Figure 5.6 illustrates this identification of pattern by circular markers on the dispersion curves. The Velocity and the frequency values are noted for the identified points. The above procedure is repeated for all models and values are summarized in Table 5.1. The table has been divided into three columns which represent the change in the width of the void, while the rows represent the change in the sections. Thus going from left to right the width of the void changes from 8 cm to 32 cm and going from top to bottom represents the section 1 to section 3. Within each section, the width of the void remains constant but the embedment depth changes. To understand the effect of void size on dispersion curve as a function of wavelength; wavelength (λ) is calculated

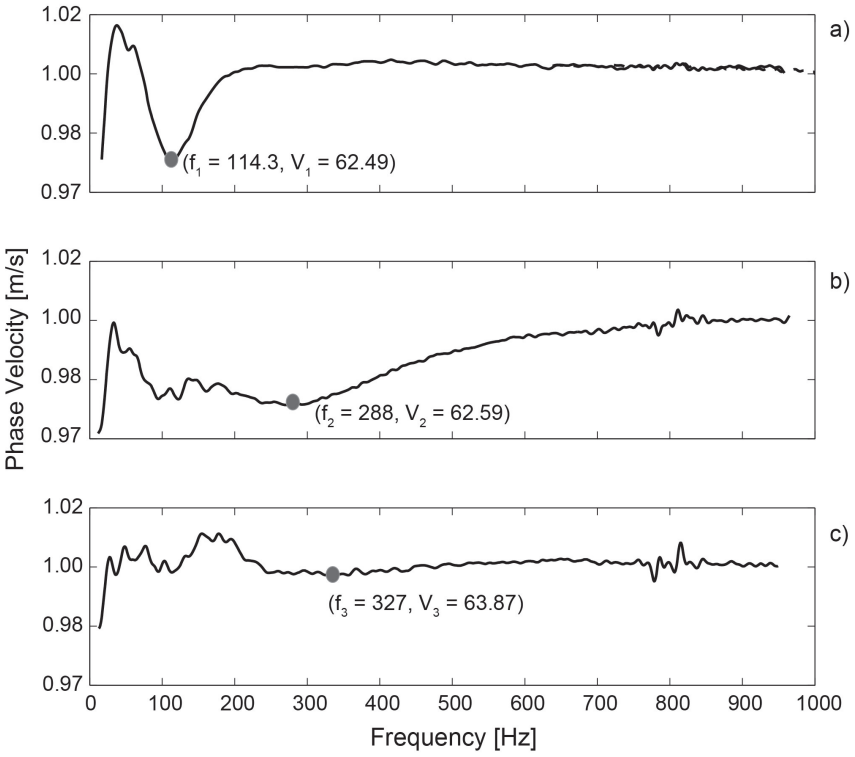

Figure 5.6: Dispersion Curves of a) section 1, b) section 2, and c) section 3 for b = 0.08m and h = 0.08m. The circular marker values indicate the pattern identified frequency and phase velocity for each case.

for each section based on the identified pattern. Wavelength is evaluated using the expression, $\lambda = V_R/f$, where V_R is the Rayleigh wave velocity (64.08 m/s) and f is the frequency obtained from the pattern identification. Finally, the normalized wavelength values are obtained using the relation, $\lambda_{norm} = \lambda/H^*$, where H* is the total depth from the surface to the bottom of the void, i.e., $(H^* = a+h)$. In this study, H^* = 0.16, 0,24, and 0.4, respectively.

5.3.5 Discussion on results

From the time traces, it can be observed that the presence of the void has considerable effect on the time traces. Interaction of the incident Rayleigh wave with the near boundary of the void produces reflections which propagate with the speed of R-waves as shown in Figure 5.3. As mentioned in previous section, in homogenous medium the Fourier spectra for the no-void model are smooth and its shape does not change with distance, however the amplitude decreases. Maximum energy occurs

Table 5.1: Pattern identified velocity and frequency for all models studied in this paper.

	b = 0.08 m					b = 0.16 m					b = 0.32 m				
	h [m]	Freq	Vel	λ	λ_{norm}	h [m]	Freq	Vel	λ	λ_{norm}	h [m]	Freq	Vel	λ	λ_{norm}
Sectin 1	0.08	114.3	62.49	0.56	3.50	0.08	80.08	63.51	0.8	5	0.08	53.38	60.51	1.2	7.50
	0.16	96.99	62.88	0.66	2.75	0.16	76.17	60.52	0.84	3.5	0.16	48.83	54.29	1.31	5.46
	0.32	69.66	63.14	0.92	2.30	0.32	54.69	61.2	1.17	2.93	0.32	43.95	56.6	1.46	3.65
	No-void	47.61	63.82	1.35	-	No-void	47	63.82	1.36	-	No-void	125.7	64.21	0.51	-
Sectin 2	0.08	288.1	62.59	0.22	1.38	0.08	143.9	58.89	0.45	2.81	0.08	116.2	51.85	0.55	3.44
	0.16	145.2	62.86	0.44	1.83	0.16	98.65	61.82	0.65	2.71	0.16	84.62	58.42	0.76	3.17
	0.32	97.66	63.43	0.66	1.65	0.32	79.1	62.4	0.81	2.03	0.32	48.83	60.08	1.31	3.28
	No-void	69.34	64.09	0.92	-	No-void	95.7	64.1	0.67	-	No-void	122.97	63.97	0.52	-
Sectin 3	0.08	327.1	63.87	0.2	1.25	0.08	103.5	66.86	0.62	3.88	0.08	68.36	94.92	0.94	5.88
	0.16	226.6	63.86	0.28	1.17	0.16	97.66	65.34	0.66	2.75	0.16	58.59	77.21	1.09	4.54
	0.32	131.8	63.85	0.49	1.23	0.32	64.13	64.52	1	2.5	0.32	50.78	67.86	1.26	3.15
	No-void	60.5	64.11	1.06	-	No-void	47.85	64.34	1.34	-	No-void	24.17	64.17	2.65	-

* units of frequency in Hz, velocity in m/s, and λ in m

at a frequency of about 100 Hz, which corresponds to a wavelength of 0.64 m. In the case of void (b = 8 cm, h = 8 cm), the Fourier spectra are not smooth and different shapes of the spectra indicates that the medium is dispersive. The values at which the maximum energy occurs for void case are shown in Figure 5.4. Higher amplitudes are observed at the section over the void and attenuation is observed in section after the void. The results of amplitude variation show that in the presence of void not only energy concentration occurs but also the attenuation happens in the frequency range studied.

From the results shown in Figure 5.5, the linearity of Rayleigh and P-waves show that there is no numerical dispersion for the frequency-wave number range studied. The trends mentioned above for the time traces, frequency spectra, and f-k plots are observed for all the numerical models studied in this work.

Table **??** provides an overview about the behaviour of Rayleigh wave interaction with void and its effect on the dispersion curves when the receiver points are analyzed in sections. An important observation that can be made from the Table 5.1 is that, the λ values increases as the embedment depth of the void increases and frequency decrease, i.e., considering the case of section 1, width b = 8cm and embedment depth h = 8, 16, and 32cm. For this case the frequency values are f = 114.3, 96.99, and 69.66 while the calculated λ values are λ = 0.56, 0.66, and 0.92. This trend is shown by all the models under consideration, which confirms that as the wavelength increases, the frequency decreases for a constant velocity. Comparison of λ_{norm} within sections show that almost all the

sections follow $1/3rd$ rule, i.e., the velocity with which each frequency propagates represents the properties of the material that lies about one third of the wavelength. However, this trend is not shown by b = 0.08 m for section 2 and 3 because the frequency at which the pattern identification is done is higher which is related to shorter width of the void. Due to shorter width, the waves are reflected at a higher speed from the farther boundary of the void. For a constant embedment depth, the λ_{norm} value for different widths increases as the width increases. This is because a larger area of the void interacts with the propagating waves and attenuates higher frequencies. Within a section the λ_{norm} values decreases as the embedment depth increases because longer wavelengths or lower frequencies are required to detect the void.

The results of the Table 5.1 are presented graphically in Figures 5.7 and 5.8. The results of width to depth ratio, R are presented against the normalized wavelength for the three sections. The solid line in Figure 8 indicates if the void is located within the one-third of the wavelength of surface waves, i.e. if the $\lambda/H*$ is equal to or greater than three, the void is located within one-third of the wavelength. In section 1, when R is less than 0.5, the effect of void on surface responses is difficult to detect which can be seen from Table 5.1; because the two cases which are below the one-third rule are for b = 0.08, h = 0.16 m and b = 0.08 m,h = 0.32, respectively. In section 2, the effect of with to depth ratio has a significant effect. Larger R has strong influence on the normalized wavelength because energy is trapped within the surface and top of void which propagates as Lamb waves as opposed to surface waves. Section 3, has similar trend as section 2; however, the ratio R above which the void effects are noticeable is one as compared to 0.5 in section 1. The results of section 3 confirms that for voids of shorter width (in this case 0.08 m) most of the energy is propagated as the velocity of the medium and further processing of the results is needed. The results of Table 1 can also be presented in terms of wavelength and total depth, H* (Figure 5.8). The figure shows two lines, when H = λ and H = $1/3\lambda$. In surface waves testing, if the wavelength are shorter or equal to embedment depth of the void, the waves will propagate without any effect on surface responses. This criteria can be noticed in Figure 5.8. The three embedment depths in this study can be represented as shallow, medium, and deep voids. For section 1, longer wavelengths are needed for the void to be noticeable. For section 2, shorter wavelengths are needed, while for section 3, it is depended on the width of the void. The three markers that fall on the H = λ line in Figure 5.8, are for b = 0.08 and h = 0.08, 0.16, and 0.32m, respectively.

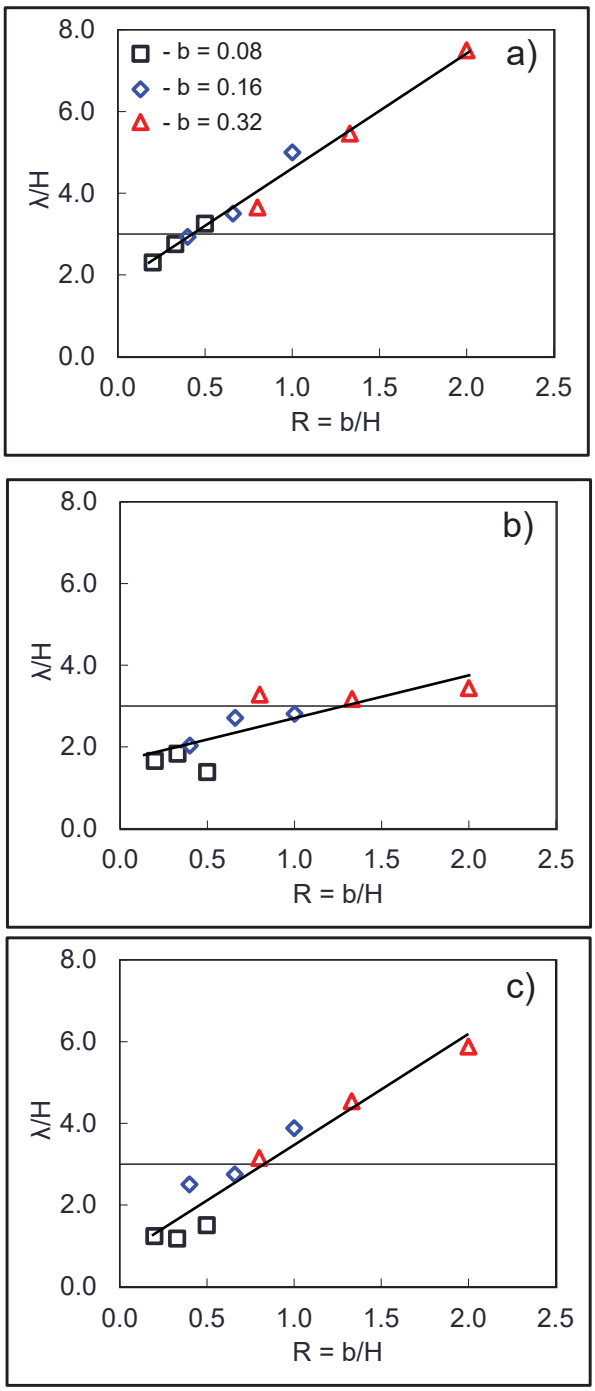

Figure 5.7: Effect of normalized wavelength on width to depth ratio for a) section 1, b) section 2, and c) section 3. Horizontal (solid) line indicates the $1/3$rd rule.

The results of the numerical simulations showed the changes in the Rayleigh wave phase velocity in the presence of the lateral in-homogeneity. The analysis of the sections presented a new

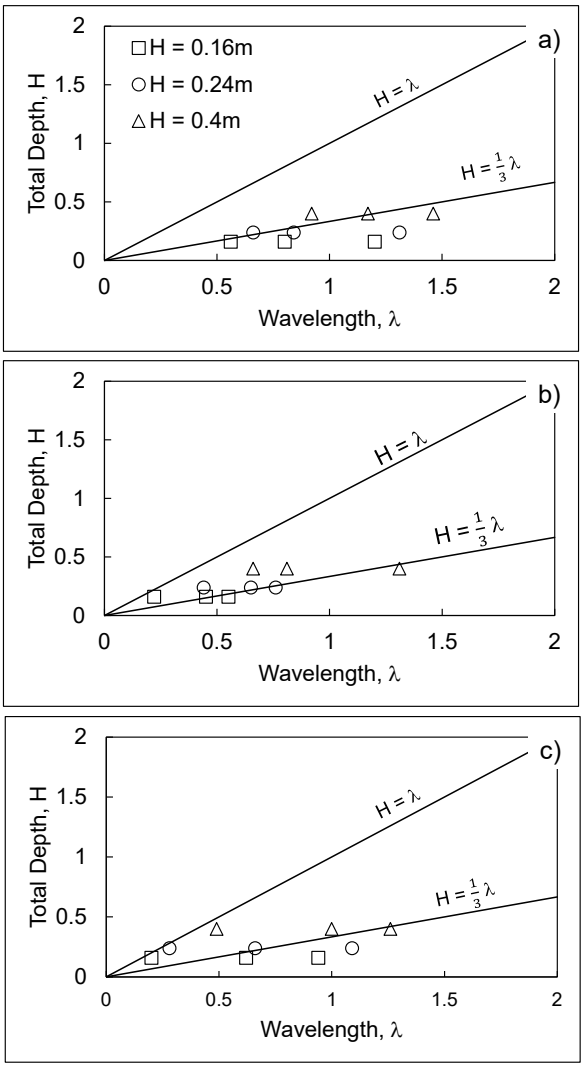

Figure 5.8: Values of wavelength are plotted against total depth for a) section 1, b) section 2, and c) section 3. The values are taken from Table 5.1

methodology for the analysis of MASW testing results.

5.4 Laboratory MASW testing

This section presents the results obtained from MASW test conducted on sandbox in laboratory.

Figure

Methodology

Two lines, Line 1 and Line 2 each having 20 20 high frequency accelerometers (Dytran 3056B5 - flat response between 10 Hz and 10 kHz) are placed at a spacing of 0.02 m, thus the total length of array is 0.48 m, a 24 channel data acquisition system (GEN 7t, Genesis). The output voltage of the accelerometer is proportional to the acceleration with an average sensitivity factor of 500 mV/g. In the case of shaker as source, a Hewlett Packard 33120A waveform generator sends single sine pulse of 30 Hz. This electrical signal is transferred to the medium using a shaker (Labworks ET-126B), frequency range from DC - 10 kHz. To transmit maximum energy to the sandbox a metal bar (1cm x 1cm) with a metal and plastic tip at one end is fixed to shaker metal base. The accelerometers are first screwed to a nut using a stud (Model 6200 MTG) and then coupled to the surface using a commercial glue. In the second setup,dynamic pulse hammer is used as source. To improve the coupling between the surface of sandbox and accelerometer, a steel plate with magnet is glued to the surface and then accelerometers are connected through the magnet. This configuration removes the variability of the surface responses due to the additional use of epoxy glue for studs.

Figure 5.9 shows the schematic of the measurement system. For a total of 0.48 meter length, 96 receiving points are measured at a distance of 5 mm. The distance between the receiving points is less than the one used in numerical simulations. The LDV employed is OFV 534 (manufactured by Polytec Inc). The LDV contains a Helium-Neon laser delivering its 633 nm laser light via an optical fiber to a high precision interferometer in the vibrometer head. The laser light splits into a measurement beam and a reference beam. The measurement beam is incident on the test object. The back scattered light is shifted slightly in frequency by the Doppler effect and contains the displacement and velocity information. The Doppler-shifted frequency is converted to a voltage that indicates actual vibrations. Since, the velocity is directly converted to frequency shift, there is neither the mechanical nor the electrical coupling between the materials surface vibration and the observed signal. The Doppler signal is decoded in the controller (OFV-2570) with two different signal decoders, displacement and velocity. The bandwidth of velocity decoder is up to 10 MHz while for displacement decoder is up to 24 MHz. Both decoders can be operated simultaneously with separate outputs and enable measurement of vibration velocities up to 3 m/s (peak) and displacements up to $+-$ 75 nm.

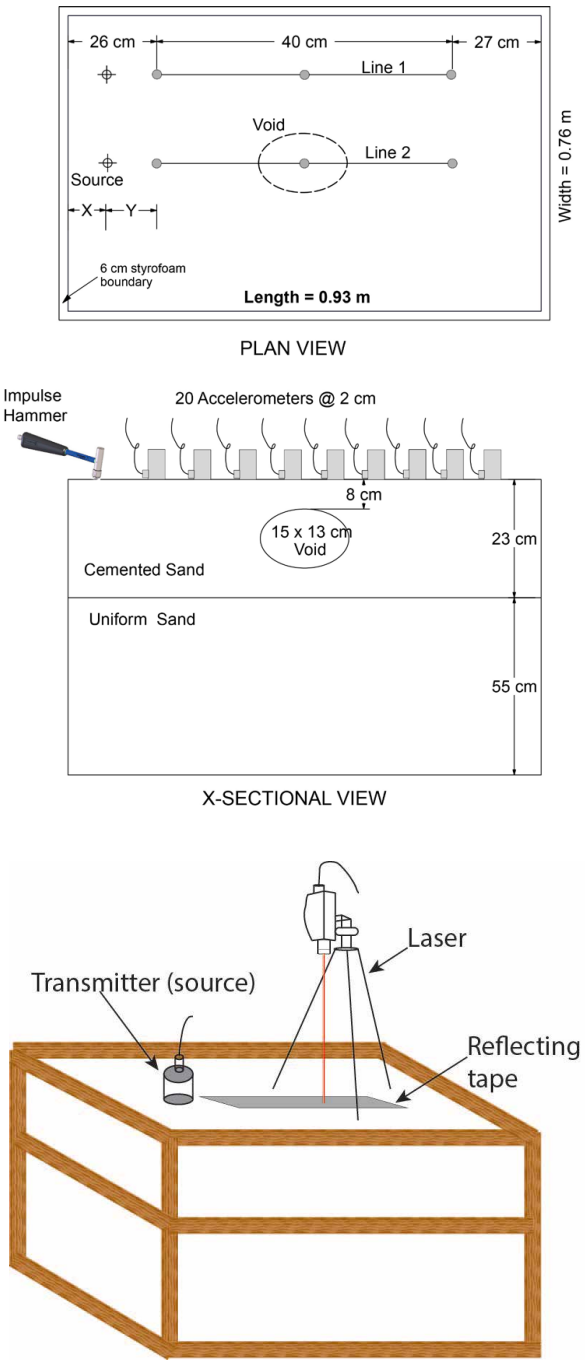

Figure 5.9: MASW testing setup for the hammer and laser measurements.Top figure shows the test configuration for accelerometer and hammer. The same configuration is used for shaker where instead of hammer shaker is used as source. The bottom figure shows the schematic of the laser testing

Table 5.2: Laboratory MASW testing details.

Source	Source Freq [kHz]	Receiver	Rec. Freq [kHz]	No. of Rec	Coupling	Measurement
Shaker	4 -10	Accelerometer	2 - 20	12	Epoxy filling with studs	Acceleration
Dynamic Hammer	0 - 2	Accelerometer	0.5 - 6	12	Steel plate and magnet	Acceleration
Transmitter (Transducer)	60	Laser	46 -51	96	non-contact	Displacements

5.5 Source calibration

Shaker

Time and frequency signal obtained from accelerometer glued very close to the shaker is analyzed to obtain the impact of source and frequency generated from metal tip and plastic tip. Figure 5.10 shows the frequency spectrum from the metal and plastic tips. The peak frequency from metal tip is at 6 kHz while for the plastic tip the peak frequency is at 1 kHz with multiple peaks at 3, 7, and 11 kHz. From the average frequency spectrum of the receiver signals, it can be observed that the metal tip gives a wide frequency range and therefore the results are analyzed for metal tip in this study.

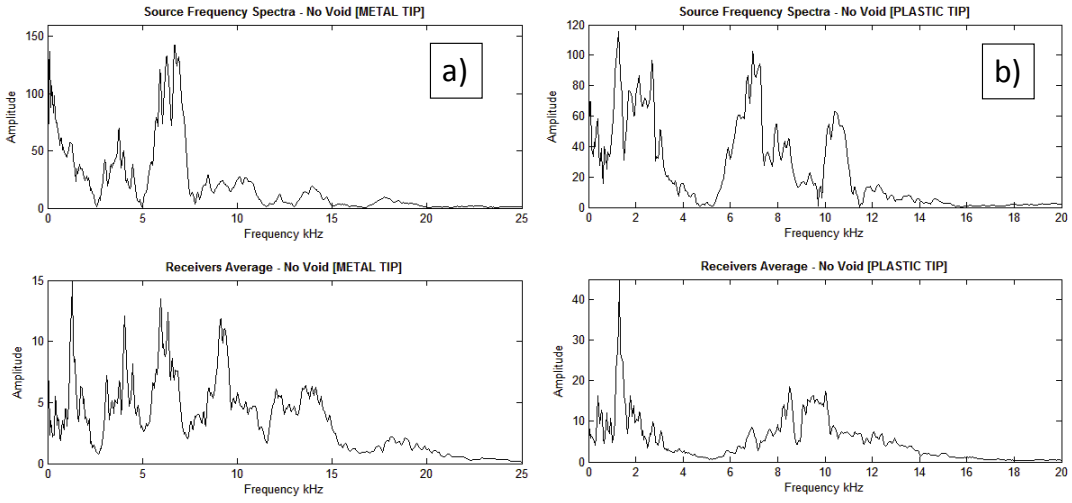

Figure 5.10: Frequency spectrum for source and receivers(average). a) Frequency spectrum for metal tip and b) Frequency spectrum for plastic tip

Hammer

The source time traces and frequency spectrum are shown in Figure 5.11. The Figure shows the values of mean and one standard deviation values from seven shots. The low variation from the mean show the accuracy of the shots. The main frequency content in this case is between 0 and 2 kHz with peak at 0.75 kHz. Considering R-wave velocity of 1000 m/s, the wavelength generated in this case is 1.3 m compared to the wavelength generated from shaker (between 0.16 to 0.33 m). This shows the importance of correct source for geotechnical site charaterization.

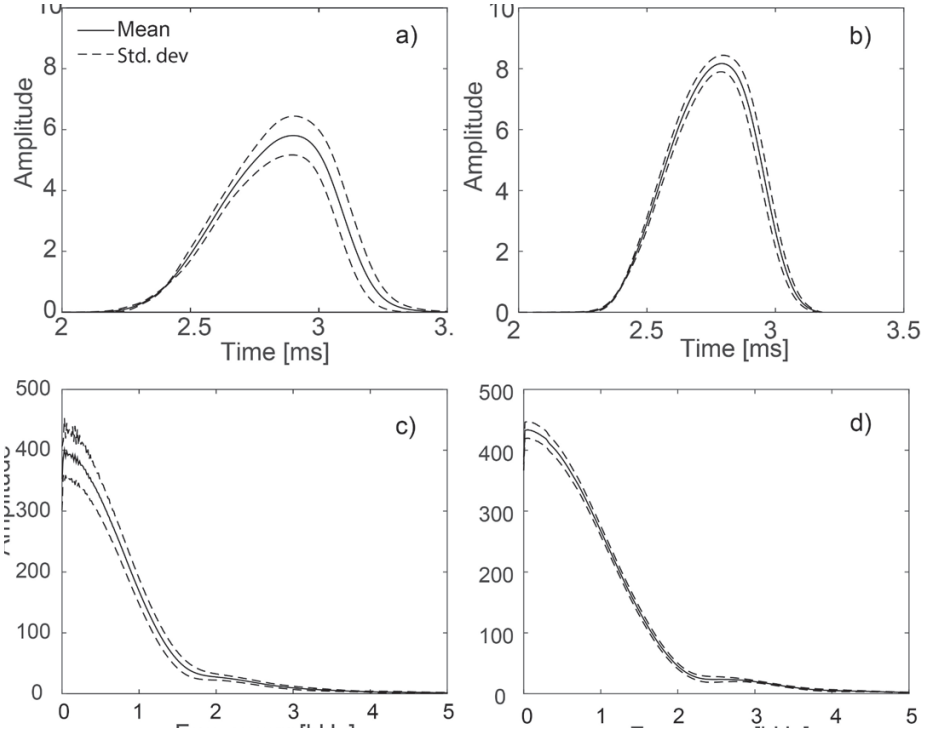

Figure 5.11: Time and Fourier spectra for input source in sandbox test. a) and c) shows mean and one standard deviation values for line 1 while b) and d) presents values for line 2.

5.5.1 Transmitter

For the calibration of transmitter, laser vibrometer is used. Figure 5.12 In A square pulse signal of 50 Hz is used as an input source. Piezoelectric transmitter with a resonant frequency of 54 kHz is used. Calibration of transmitter using laser vibrometer showed that the resonance frequency of the transmitter is 48 kHz instead of 54 kHz as shown in Figure 5.12. The shift of resonance frequency to a lower value could be due to small disc attached, at the center, on the surface of transmitter

where the measurement was done. This shows the importance of calibration in laboratory ultrasonic testing.

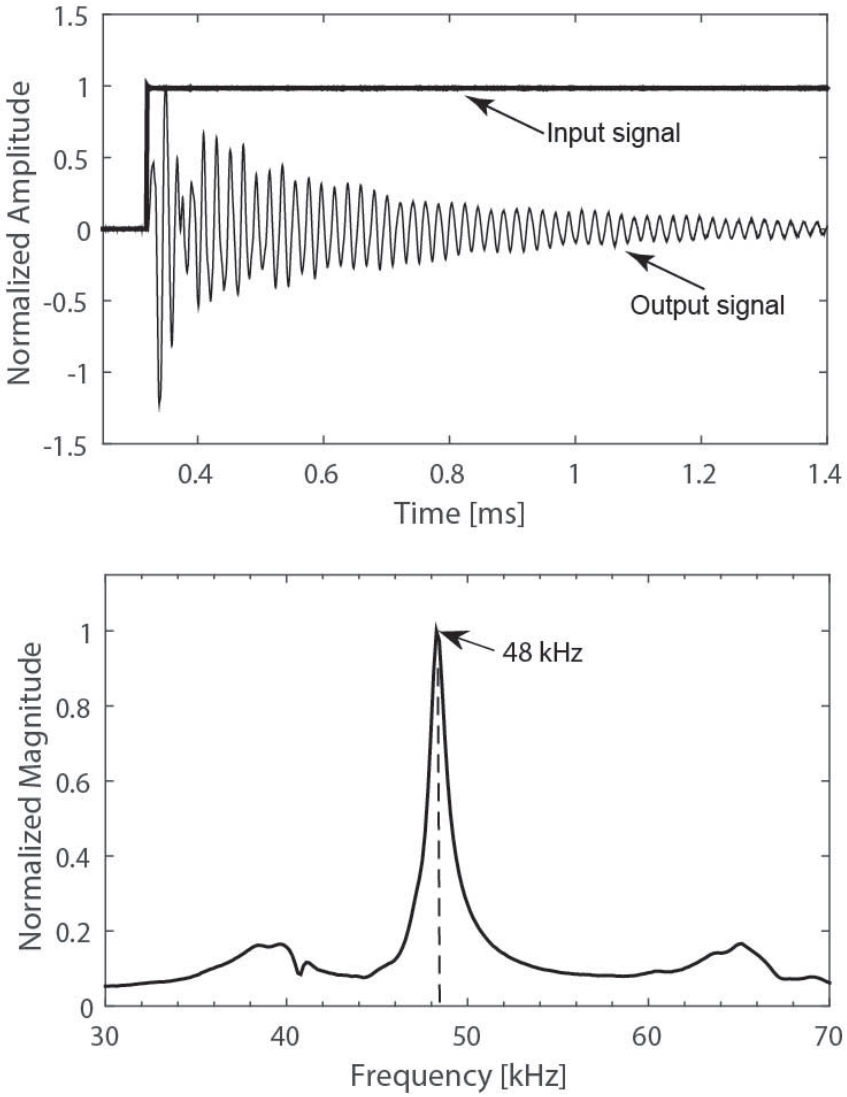

Figure 5.12: Time and frequency spectra of transmitter using laser vibrometer in Air.

5.5.2 Experimental results and discussion

The results of the experimental test are processed in time and frequency domains. Figure 5.13 and Figure 5.14 shows the time signals and frequency spectrum (contour plots) corresponding to no-void and void for the source as shaker. The plots are shown as contour plot to show the difference in the frequency content for the no-void and the void case. The main event corresponds to the Rayleigh

wave, with a velocity of 1212 m/s. The velocity value matches with the reported for cemented sand (Yang, 2009), however, it differs from the test done with hammer source and laser vibrometer. In Figure 5.14, the plot is normalized to the maximum amplitude (maximum amplitude occurs in void case). In plot 'a' of the figure void boundaries are shown as dashed lines. Energy concentration can be seen on top and in the vicinity of the void. A strong reflection from the near boundary of the void can be seen on trace $No5$. Attenuation in concentration of energy can be seen after the void which shows that void reflects and attenuates different frequencies. Vibrations from sandbox boundaries are also shown on the plot. These reflections are not visible in plot 'a' (void case) as the survey line is far from sandbox boundaries.

Figure 5.15 shows the time traces for no-void and void cases. The arrival times of P-waves and surface or Rayleigh waves are marked on the figure. In Figure 5.15b, the change in the surface wave velocity is seen after receiver 10. The velocity changes from 1150 m/s to 952 m/s, respectively. Reflections from the near and far boundary of the void are visible. In both cases, the reflections from the sandbox boundaries are observed. Figure 5.16, presents the 1D Fourier transform for the no-void and void case. The main frequency content is between 0.5 and 8 kHz. In Figure 5.16b, the frequency content of receiver 10 is shifted to lower frequencies with peak at 3 kHz. Amplification of energy at 6.5 kHz for receiver 9 and 14 are likely due to reflections from the void. Figure **??**, shows the time and frequency traces from the laser test for line 1. The Rayleigh wave velocity from the time traces is 1074 m/s which is less than the velocity obtained from the previous tests. The frequency spectrum shows single frequency at 49 kHz, corresponds to wavelength of 2.5 cm.

The time traces and Frequency spectra for the void case are shown in Figure 5.17. The change in arrival time of surface waves from due to the interaction with the void is clearly seen in this figure. Similarly, the frequency spectrum shows the variation of the energy due to the interaction of void. Shift in frequency can be observed at 0.15 m from the first receiver and after 0.3 m from the first receiver. The time traces and frequency spectra shown before using shaker and hammer were not able to distinguish clearly the show the change in energy due to interaction with void as from the results of the laser.

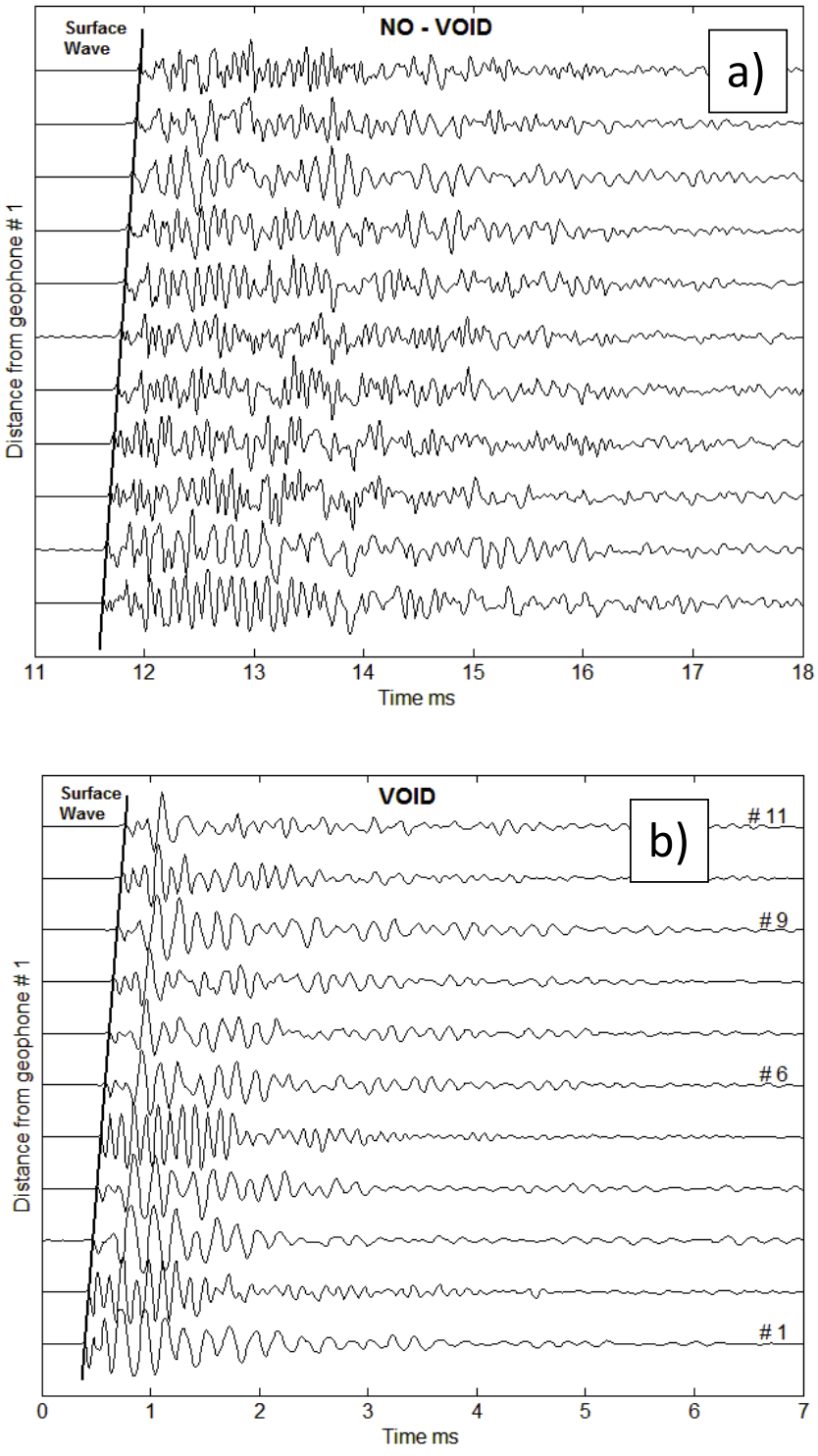

Figure 5.13: Time signals showing the main arrival for no-void and void case

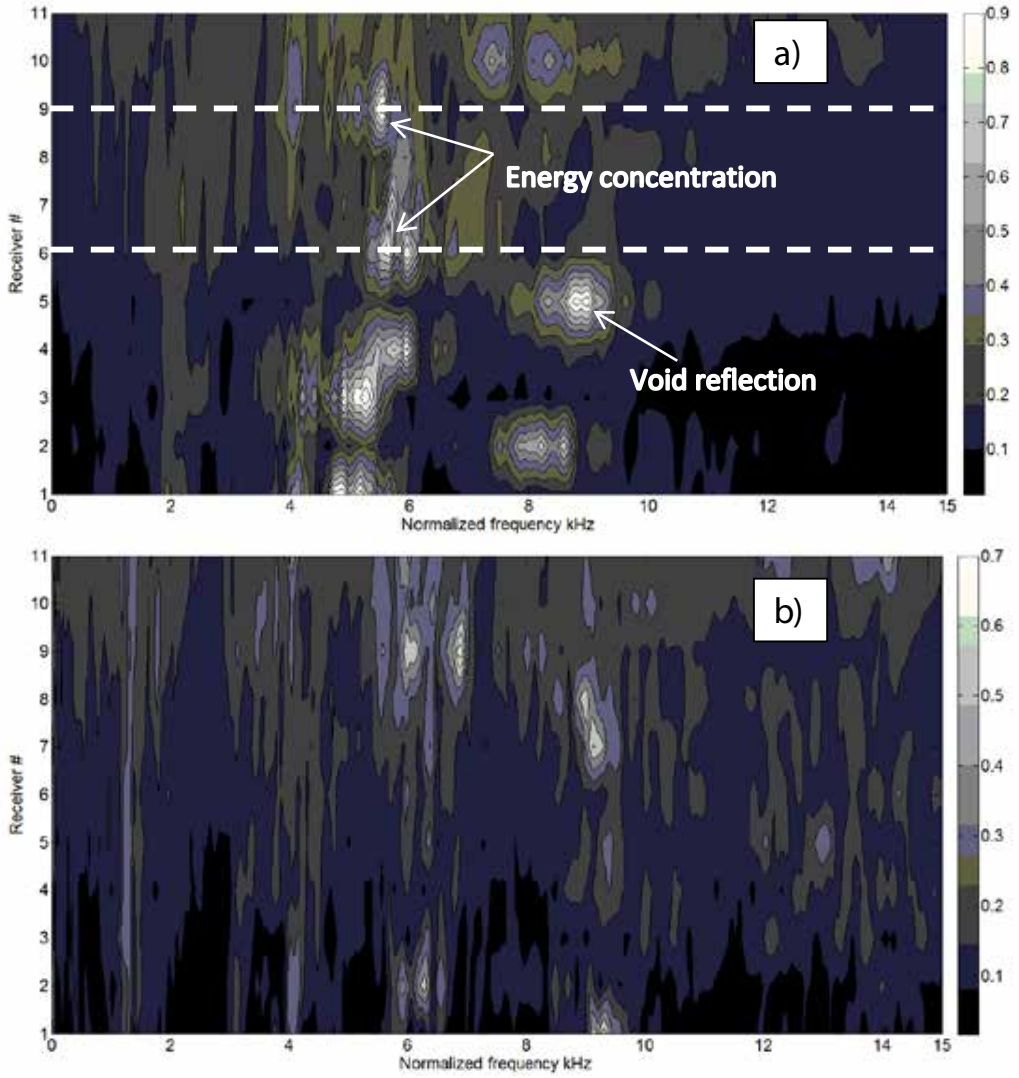

Figure 5.14: Normalized frequency spectrum showing the concentration of energy at different locations in void and no-void case

Dispersion curves and normalized wavelength

Results of the time and frequency analysis shows the changes in the time signals and frequency content due to the change in the source frequency. The large variation in the frequency spectrum values for the three sources reinforces the importance of selection of correct source for MASW testing. The results of these tests helped in the selection of source for field MASW testing. Analysis of results in the frequency domain is done similar to the methodology presented in the numerical simulations section.

Dispersion curves are obtained following the same methodology as presented for numerical models. Due to the large scattering in the results of the frequency spectrum of the test from shaker, dispersion curves are not evaluated for this test. Figure 5.18a shows the dispersion curves for the no-void and void cases; which are averaged values using the Gaussian smoothing. Figure 5.18b shows the dispersion curve normalized with respect to no-void dispersion curve as a function of frequency (Equation 5.2).

Figure 5.19 shows the dispersion curves from the laser test using the same methodology for hammer source and numerical simulations. Normalized dispersion curve is obtained.

5.6 Discussion of results

Consider a scenario, if the void size in sandbox test was not known; however it was known that the array is located above the void. Using the dispersion curve in Figure 5.18, the wavelength, $\lambda = V/f$ = 1074/3500 = 0.30 m. From Figure 5.8b, for λ = 0.30, H = 0.10 which gives λ/H = 0.30/0.10 = 3. Now from figure 8b, for λ/H = 3, R = 1.25 (from the trend line). Finally, b = R * H = 1.25 * 0.10 = 0.125 m = 12.5 cm, which matches well with the actual dimension of the void.

Finally, the attenuation of surface waves with distance is presented in Figure 5.20. The attenuation curves are evaluated from the area of the frequency spectrum for the frequency range between 0 and 70 kHz. This is selected because the energy after 70 kHz is almost zero. Results show the trend of attenuation of surface waves with distance. The exponents for the void and no-void case based on curve fit are -0.16 and -0.17, respectively. The peak between the 19 cm and 24 cm is likely because of the void and reflections from the void boundaries.

Rayleigh wave velocities obtained by Kirlangic et al. (2015) on the same sand box are 1299 m/sec which are similar to results from hammer and shaker test but the velocity from surface displacements is 17 % lower than other tests.

5.7 Chapter Summary

To understand the propagation of R-waves in presence of lateral inhomogeneity, results of numerical simulations were studied first. To introduce non-homogeneity, voids of various size and depth are

used. The following conclusions can be drawn from this chapter:

A new methodology of processing MASW data is introduced in which the receivers were divided into three sections, before, on-top, and after the void.

Nine numerical models were analyzed in which the void depth and width was varied. Results of the test were analyzed in time and frequency domains. Dispersion curves were obained from the 2D FFT spectrum. Results from the dispersion curves show that the change in the phase velocity (function of frequency) is between 3% to 50% for different void width and depth.

The results of the laboratory MASW test were conducted using three different configurations. Two tests involved use of accelerometers as receivers, however, the input source was different (shaker and dynamic hammer). While the third test consisted of using state of art laser vibrometer as receiver.

For the lab test, two lines of MASW are tested in each case. Twelve accelerometers are used for the shaker and hammer as source, while using laser 96 measurements were done. The frequency response from the accelerometer is 2 - 20 kHz for shaker and 0.5 - 6 kHz for hammer; while for the laswer is 48 - 51 kHz.

Based on the knowledge of the author, no previous MASW measurement using laser is done for geo-materials. The results from the laboratory MASW test showed the frequency effect on the measurements due to the source used in this method.

Coupling of geophone/transducer in surface wave testing is an important issue. Results from the lab test using laser vibrometer showed that the mass loading effect of accelerometer affects the frequency content of the signal.

The results of three tests were analyzed in time and frequency domain. Using the normalized wavelength concept introduced in the numerical studies, the

Laser techniques are very popular due to the non-contacting nature of this measurement device. Accelerometer measurements are also widely used in many applications but suffer from potential mass loading effects. Each technique has its own benefits and drawbacks.

In summary, the technique of normalized wavelength gave good results in terms of void detection. The location of the void in the case of laser measurements is clear. Applying all this information to estimating void depth is a principal future goal of our work. Applying all this information to estimating void depth is a principal future goal of our work.

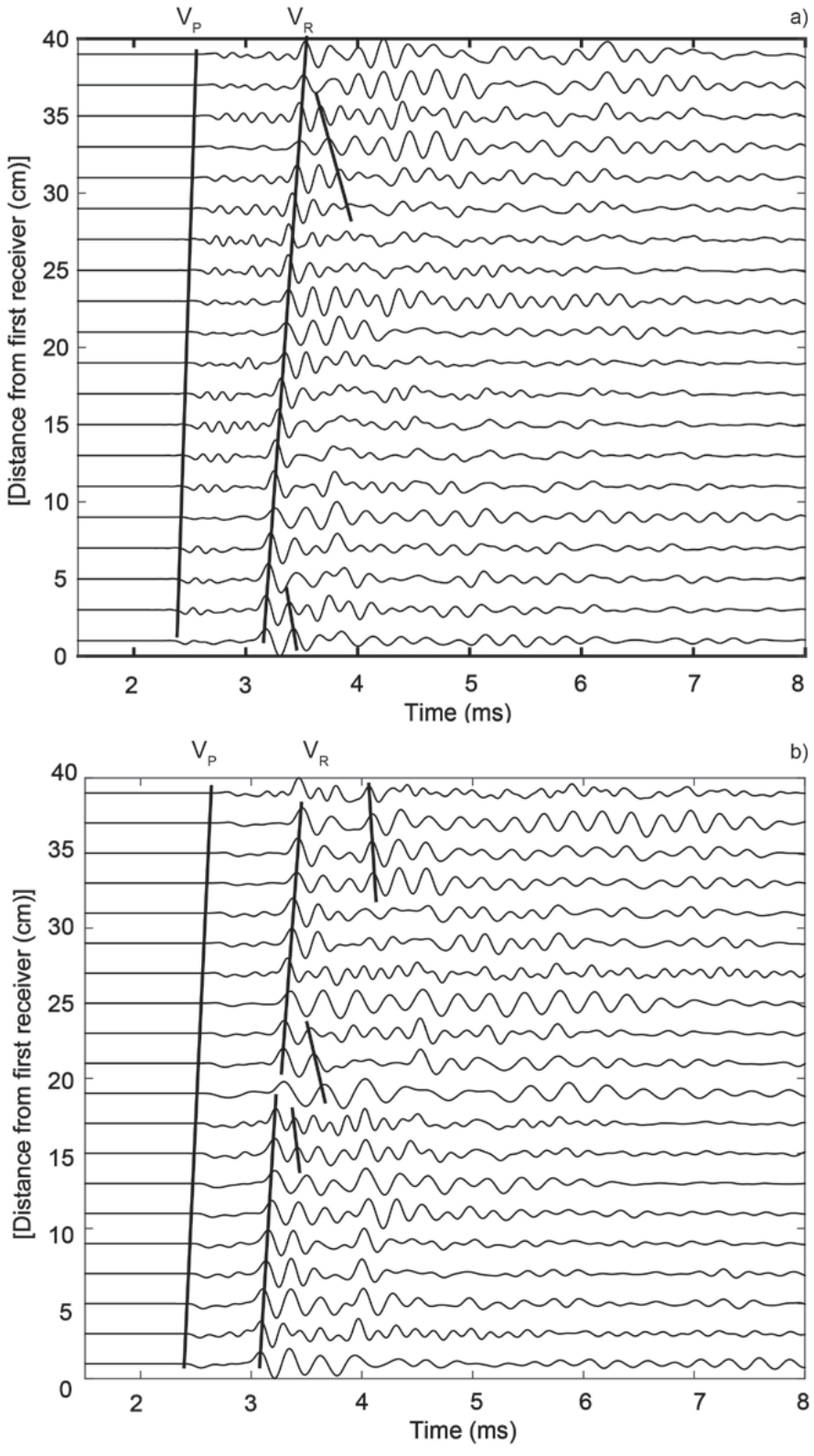

Figure 5.15: : Time traces for a) line 1 and b) line 2. P- and surface wave velocity are marked.

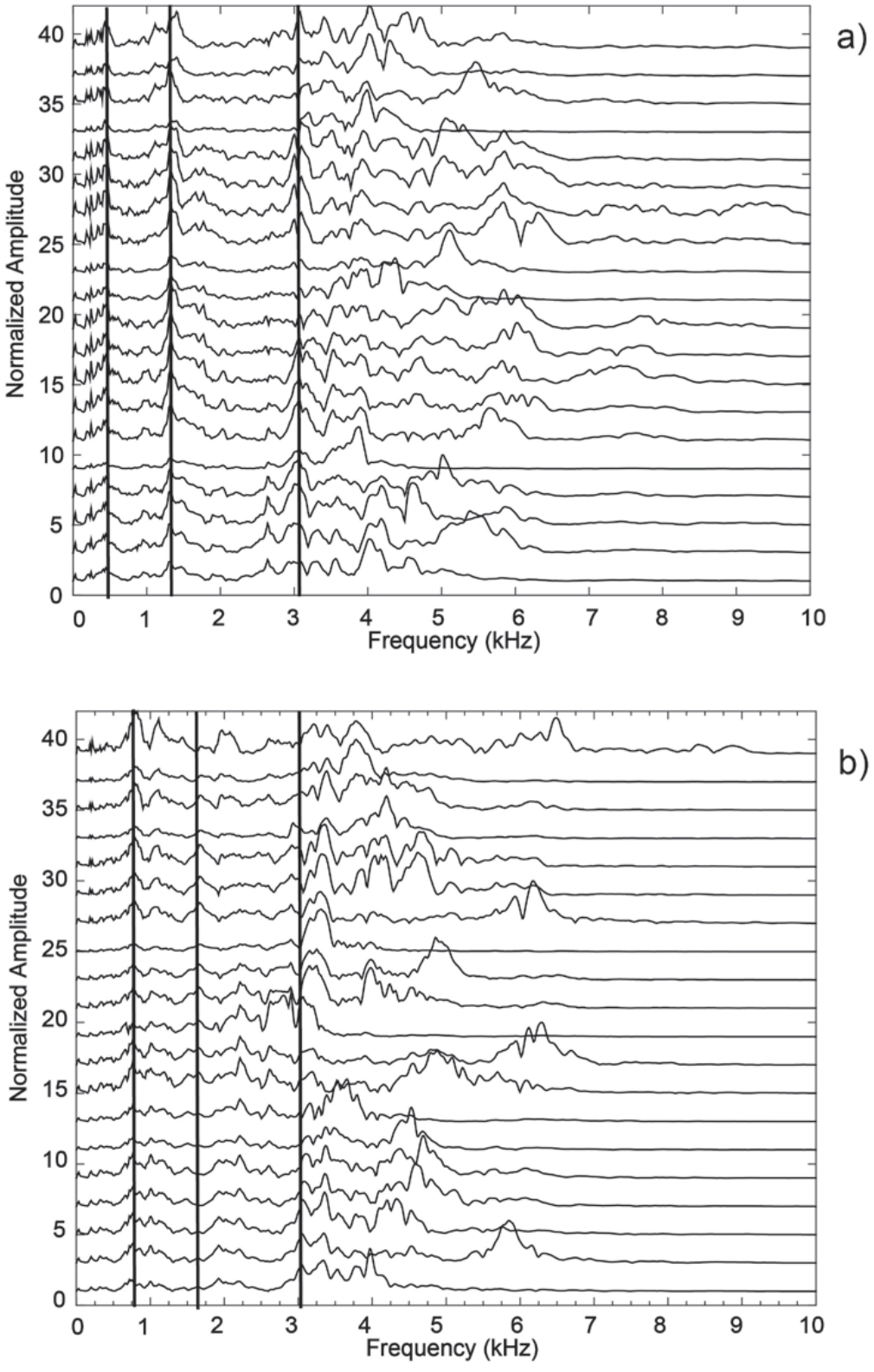

Figure 5.16: Frequency spectra of a) line 1 and b) line 2.

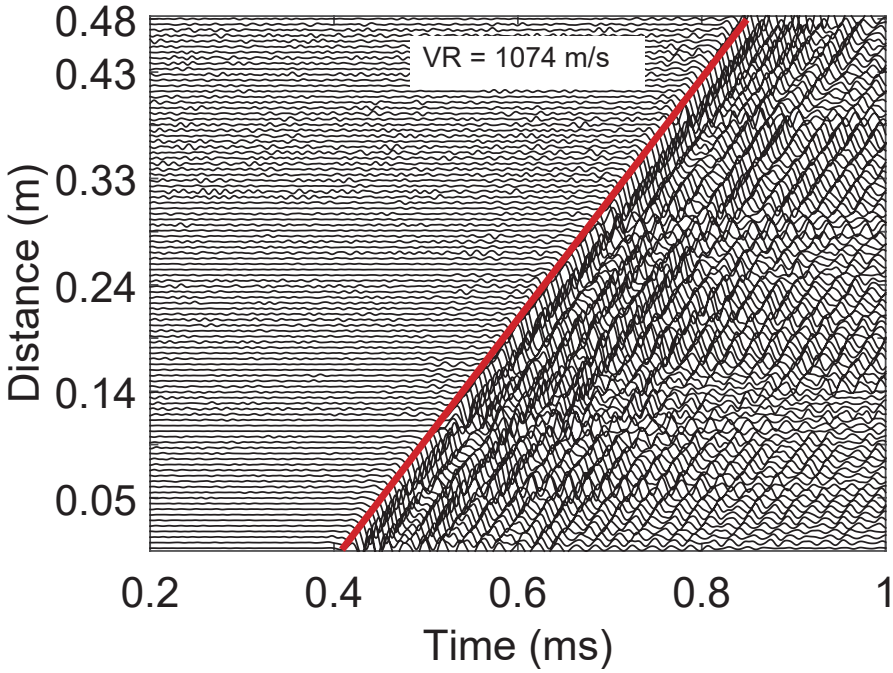

captionFigure shows the time signals from the laser vibrometer test for Line 1.

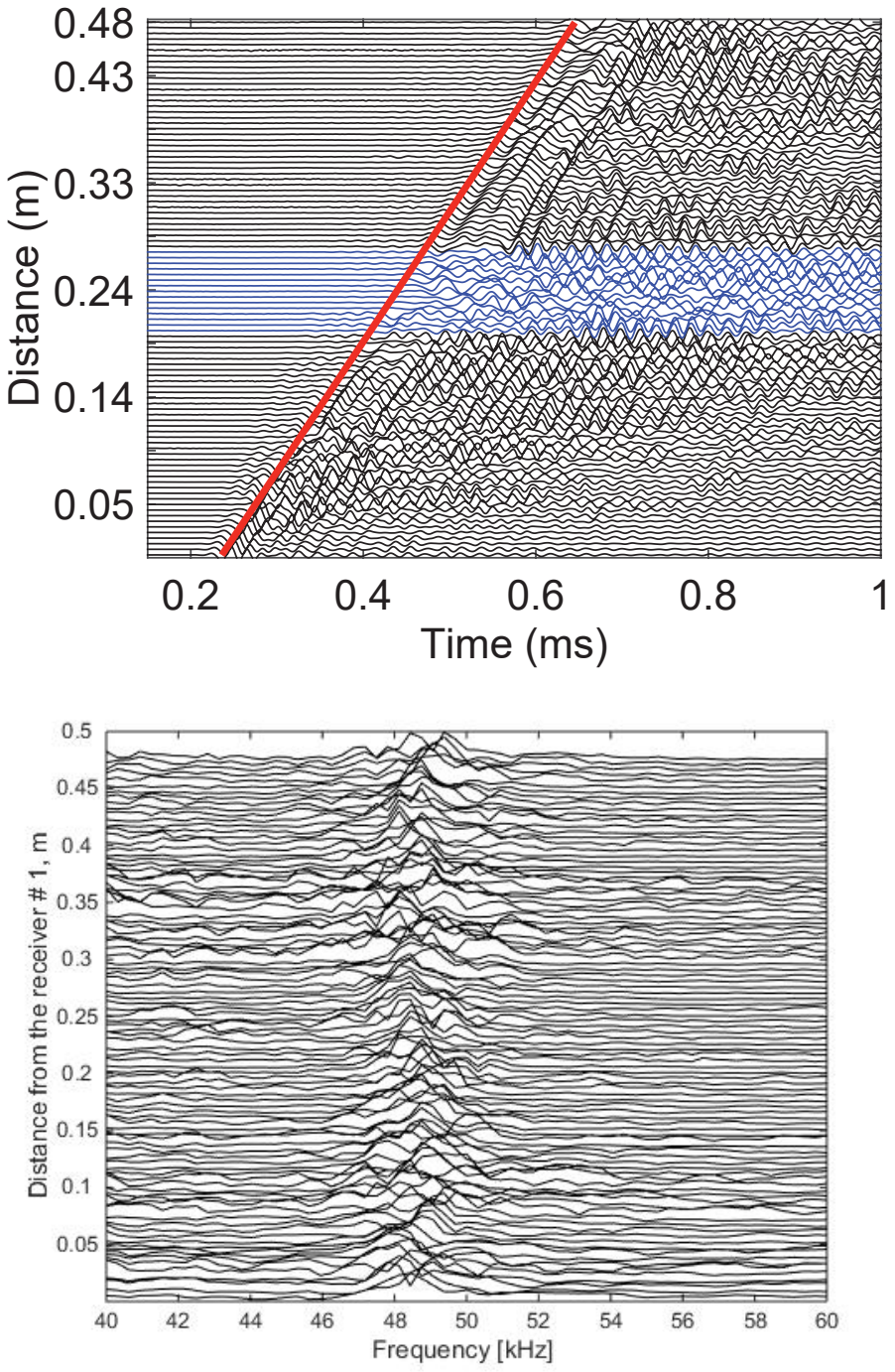

Figure 5.17: Figure shows the a) time signals and b) the frequency spectra from the laser vibrometer test for Line 2.

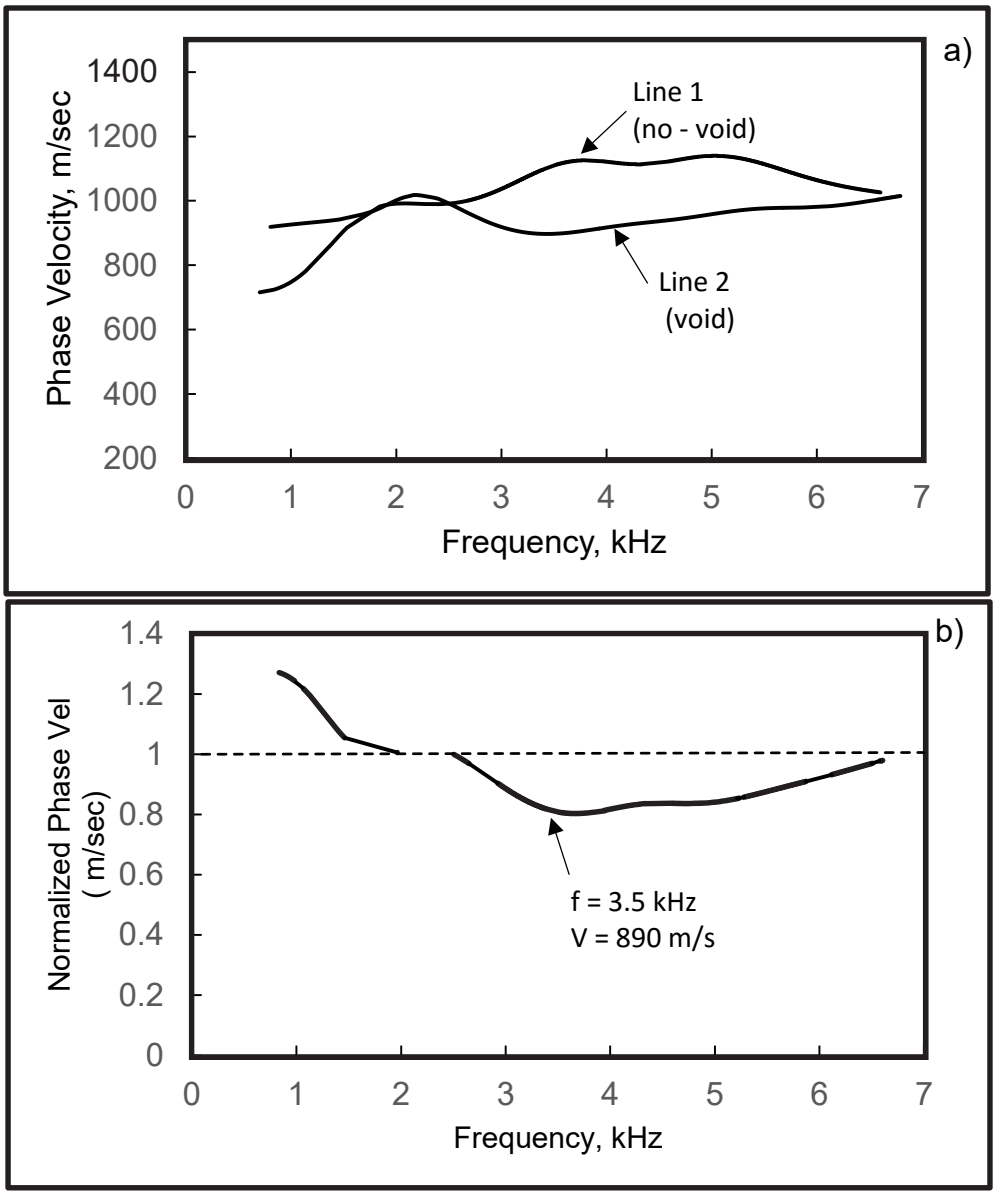

Figure 5.18: Dispersion curves for a) line 1 and line 2 from sandbox test. b) Normalized dispersion curve showing the change in the phase velocity due to the interaction with the void; b) pattern identified frequency and velocity.

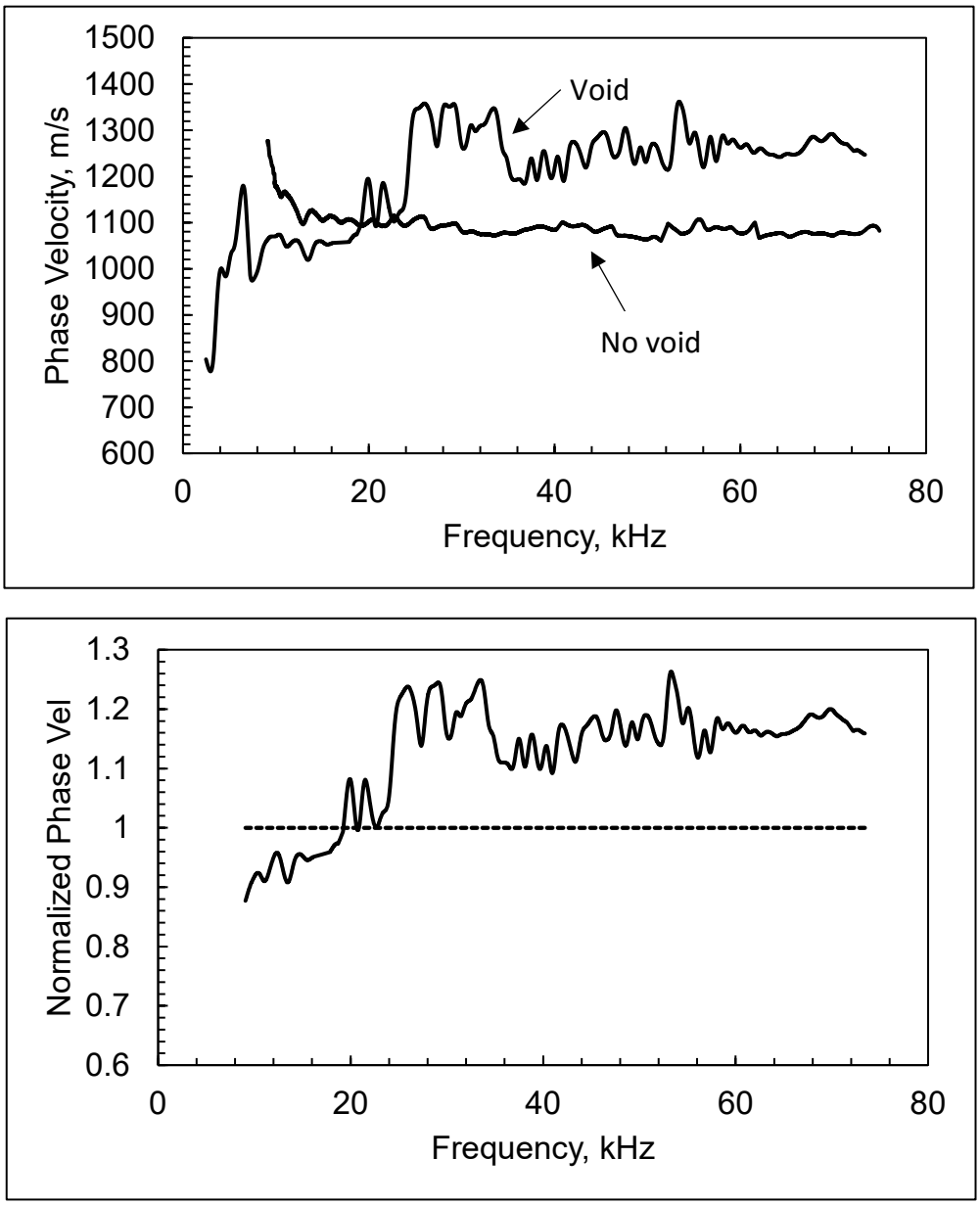

Figure 5.19: Dispersion curves for a) line 1 and line 2 from sandbox test. b) Normalized dispersion curve showing the change in the phase velocity due to the interaction with the void.

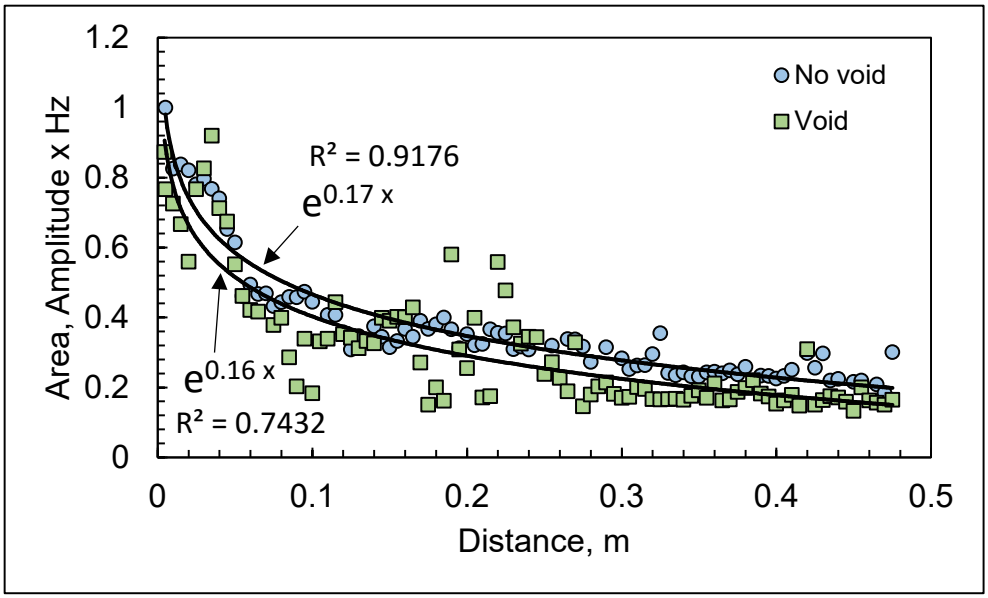

Figure 5.20: Attenuation curves for Line 1 and Line 2 from laser measurements.

CHAPTER 6

In-situ field tests

6.1 Introduction

This chapter presents the field test results conducted at the geophysical test site at the University of Waterloo. The objective of the test is to evaluate the reliability of geophysical methods for the detection of competent strata in soil profiles with high water content, and also to understand the frequency effects in the estimation of shear wave velocity from two different geophysical field tests.

6.2 Site description

The University of Waterloos Columbia Lake Test Site (UW-CLTS) is a geophysical test site for the calibration and testing of Electromagnetic and Ground Penetrating Radar instruments. The site is also used by the University of Waterloos Earth Science students for instruction purposes. The UW-CLTS is located north of Columbia Lake on the North Campus of the University of Waterloo, in Waterloo, Ontario Canada, as shown in Figure 6.1. The site is 50 m by 50 m in size and consists of mainly silty clay till soil. For instructional and calibration purposes, the following targets are buried at various locations on the site: vertical steel drums, sheet steel, and steel and plastic pipes,

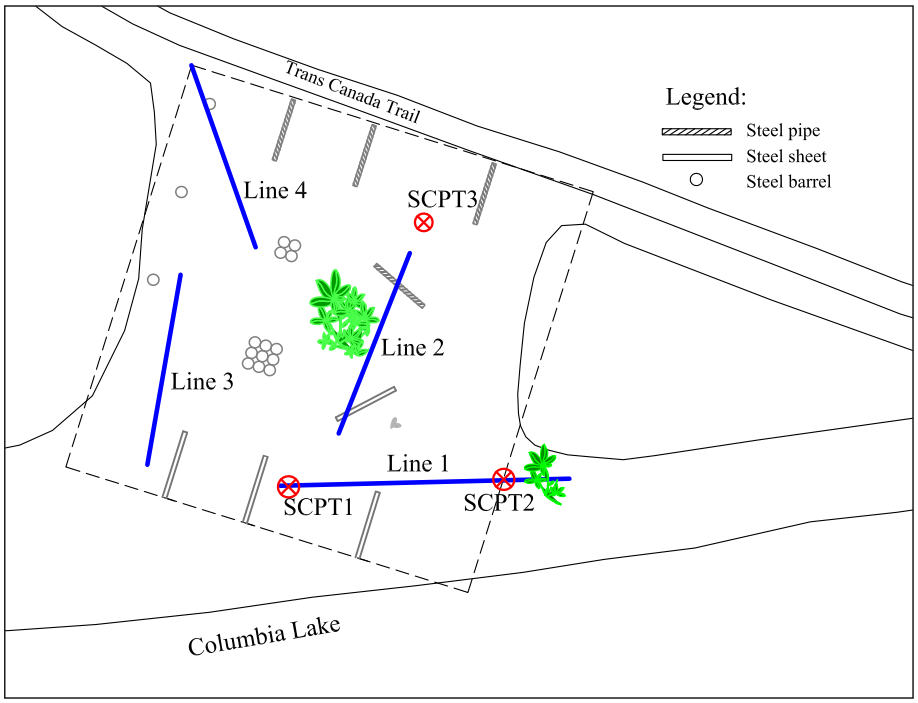

Figure 6.1: Site description showing the location of MASW lines and SCPT test locations. Also shown are the locations of buried objects at the UW-CLTS

respectively (Phillips 2001). The site was chosen for the current testing due to its vicinity to the University of Waterloo, the low ambient noise level, the open field, the relativity flat ground surface, and the availability of test results from previous studies.

Two sets of field tests were performed to evaluate the shear wave velocity profiles at the site. The first set of tests were performed from October 17 to October 20, 2013. Multichannel analysis of surface waves (MASW) test, cone penetration (CPT), and seismic cone penetration (SCPT) tests were performed. SCPT was performed using a static and dynamic TG63-100 penetrometer by Pagani Geotechnical Canada. The second set of tests was done on December 13, 2013. Two lines of the MASW test were performed (Line 3 and 4 in Figure 6.1). In the case of the MASW test, a sledge hammer and drop weight were used as seismic sources with 4.5 Hz geophone as transducer. In this report, the results obtained from the sledge hammer as source and vertical 4.5 Hz geophone are presented. Figure 2 shows the seismic sources used in MASW and SCPT tests.

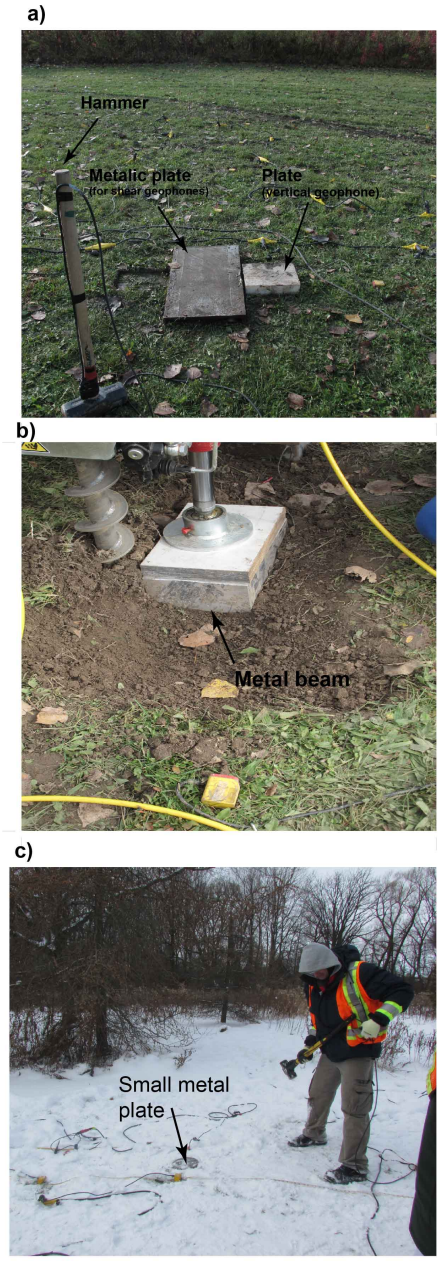

Figure 6.2: Seismic sources used for a) Lines 1 and 2, b) SCPT, and c) Lines 3 and 4 in the MASW and SCPT tests

6.3 Experimental Methodology

In this section, test equipment, methodology, and signal processing technique associated with MASW and SCPT tests is presented. MASW tests were performed along four lines. The instrumentation consisted of a 24-channel seismograph and 4.5Hz geophones. The distance between

geophones is one meters, for a total geophones spread length of 24 meters. The sledge hammer was used as a seismic source to generate surface waves. The acquisition consisted of a 24-channel GEODE in-field seismograph with a sampling rate of 0.25 milli-second (sampling frequency = 4 kHz) for a total time of 1 second.

For lines 1 and 2, the shots were made from left and right of the survey line, while for line 3 and 4, the shots were made only from one side, i.e., from the trail side. The first geophone was placed at the following offsets from the source: 2.5, 6, 9, and 15 m, respectively. For each offset location, five shots were made; therefore, in total 120 measurements were recorded for four lines. The grass surface that covered most of the site complicated data acquisition and thus the geophones were buried in the ground so that the spike attached to each geophone was properly inserted into the ground. During testing of line 3 and 4, the site was covered with snow; therefore, the snow was removed to ensure proper coupling between the geophone and the ground. Three SCPT tests were formed at the UW-CLTS to better characterize the test site as shown in Figure 6.1. A typical schematic layout of the SCPT test is shown in Figure 6.3. In SCPT, a sledge hammer hitting a loaded beam is normally used as a seismic source producing shear waves. Other parameters such as tip resistance, friction, and pore pressure, are recorded continuously. The beam is hit with a single horizontal blow on one end and the geophone signal is recorded and stored. The procedure is then repeated with a blow on the other end of the beam. The results are evaluated in terms of difference in arrival time of the shear wave from depth to depth. Figure 6.4 shows time signals from the SCPT 1 test for 4 m and 6 m depths. The shear wave velocity is calculated as $Vs = \Delta d/\Delta t$, where Δd = the travel distance between the layer and Δt = the difference in corrected arrival time. The results of the MASW and SCPT test along with the comparison of shear wave velocity profiles (Vs-profile) are compared next.

6.4 Results of MASW and SCPT tests

MASW

Figures 6.5,6.6,6.7, and 6.8 show the typical time traces from four MASW lines. Due to less variability in shots, only the traces from the first shots are reported. Primary or P-waves are identified for all four lines and shown in Figures 5 to 8. Surface waves (Rayleigh, R-waves) from

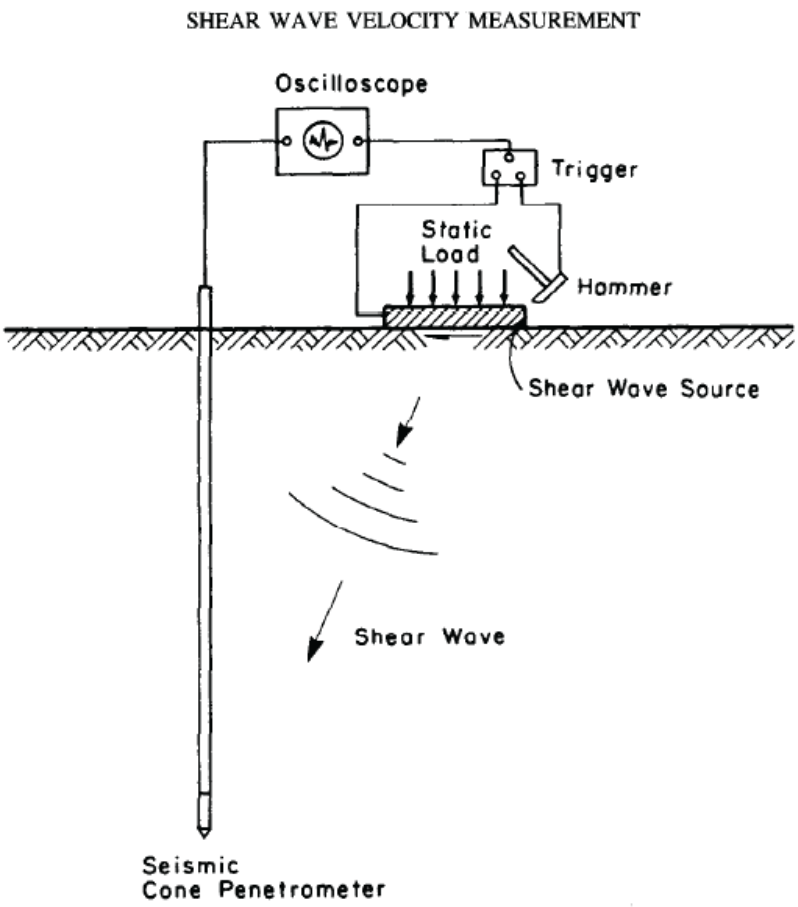

Figure 6.3: Schematic layout of seismic cone penetration test ((Robertson et al., 1986))

all four tests are identified from the time traces. For lines 1 and 2, a shift in time signals is observed after the 12th receiver which changes the arrival of the R- wave from a higher velocity, 302, to a lower velocity, 250 m/sec for line 1, while for line 2 the R-wave velocity remains the same even after the shift. For lines 3 and 4, the P-wave velocity is approximately 1550 m/sec for two lines while the R-wave is 300 m/sec, respectively. The shift in arrival time is observed after the 10th receiver as compared to the 12th receiver for line 1 and 2. The frequency spectrum of four lines shows that the main frequency content is between 20 and 50 Hz with main peak around 26 Hz. For an average R-wave velocity of 300 m/sec and a frequency of 25 Hz, the wavelength corresponds to 12 m (from relation V = λf).

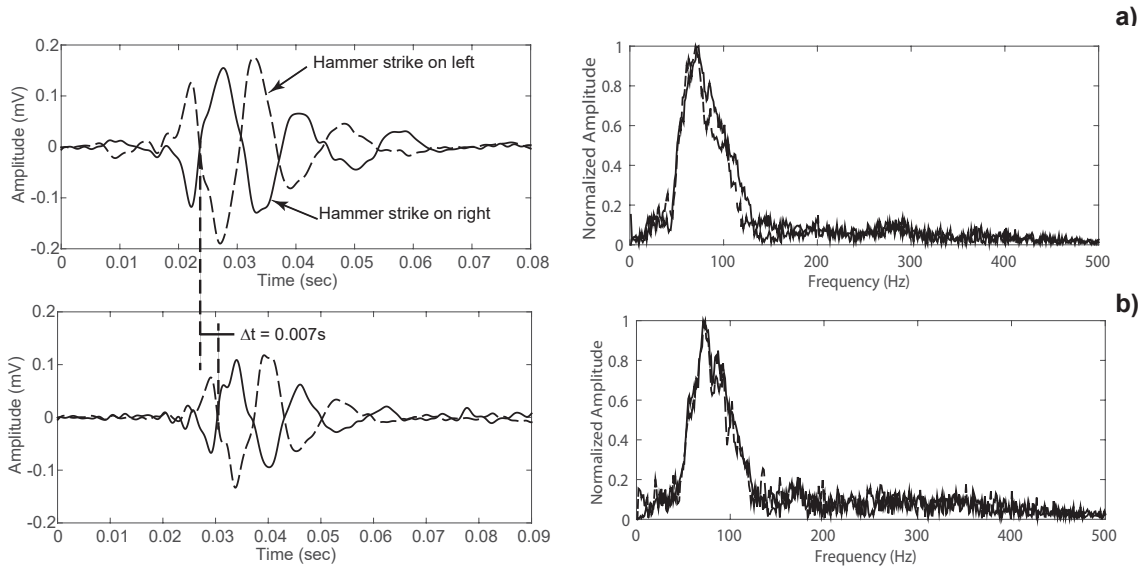

Figure 6.4: Interpretation of SCPT data showing time and frequency spectrum at a) 4m and b) 6m depths

SCPT

Figures 6.9,6.10, and6.11 show the typical time and estimated frequency spectrum for SCPT 1, 2 and 3. The frequency spectra from SCPT tests shows the frequency between 20 and 200 Hz with peak frequency around 72 Hz. A comparison of frequency spectrum from the seismic cone test shows important information about the test and test site as shown in Figure **??**. For SCPT1, the left and right shots have the same frequency peaks up to 10 m depth and variation at 12 m and 13 m. At this depth, the frequency spectrum has two peaks for left side shots, one at 60 with the other at 100, respectively. In both cases, the peak with the maximum amplitude is selected. The two peaks in the frequency spectrum could be reflection or energy trap between thin layer of soil at this depth as shown by the tip resistance plot (Figure 6.13). For SCPT 2 and 3, the frequency peaks with depths are consistent with a perfect match for SCPT 3.

Cone penetration test (CPT) results

Due to the non-availability of the bore-hole record, the cone penetration results are used to understand the geological and geotechnical information about the site as shown in Figures 6.13,6.14,6.15. The CPT results include tip resistance (q_t), sleeve friction (f_s), and pore water pressure (u). For SCPT 1 and 3 the cone penetrated up to 16 meters while for SCPT 2 the penetration was up to 10

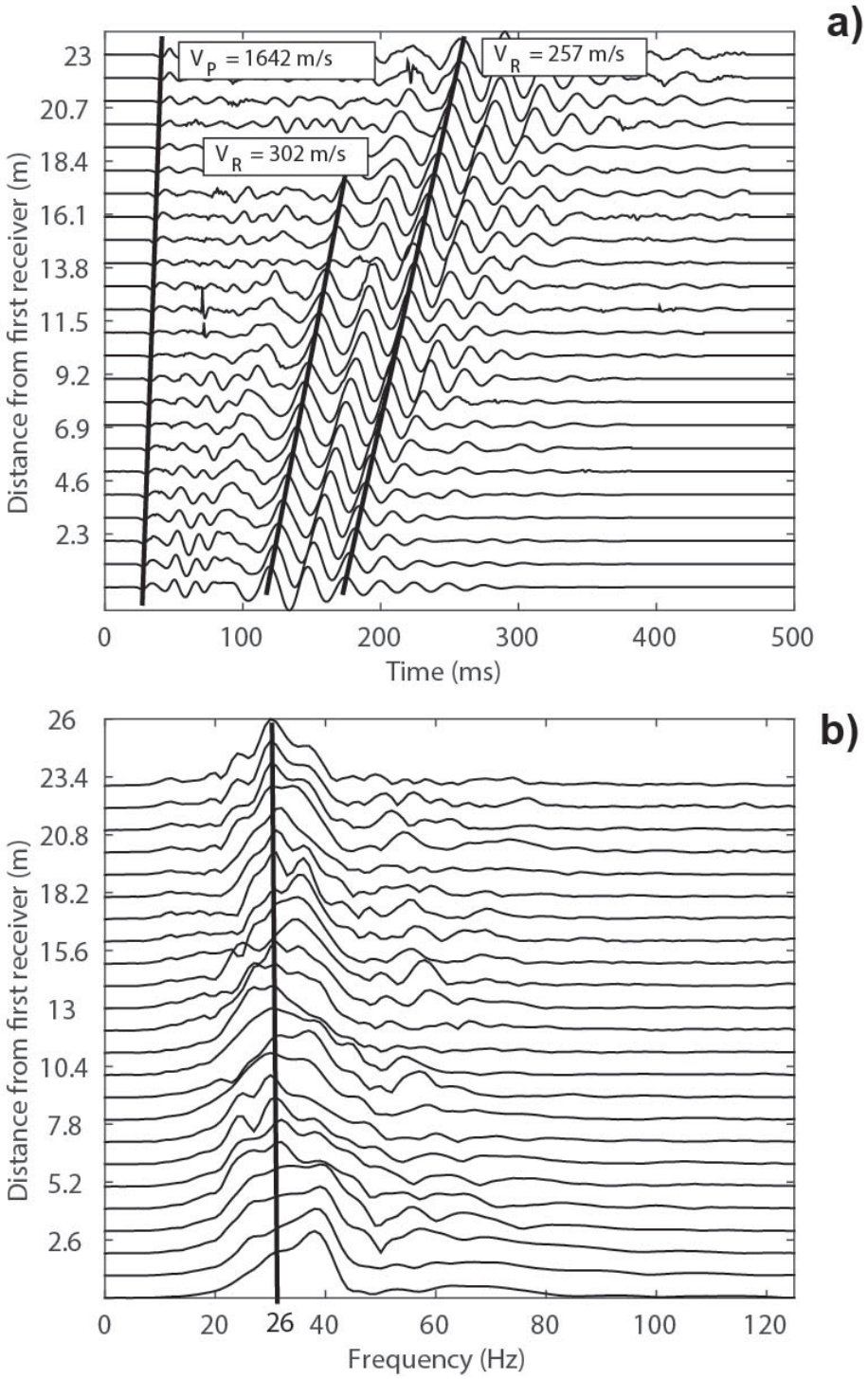

Figure 6.5: Typical results from MASW Line 1. Plot (a) shows the time traces obtained along with the P and Rayleigh wave (R-wave) velocities. A shift in time signals is obtained after the 12th receiver which changes the arrival of the R- wave from 302 to 250 m/sec. Plot (b) shows the computed frequency spectra for 24 receivers. The main frequency for all transducers is identified as 24 Hz

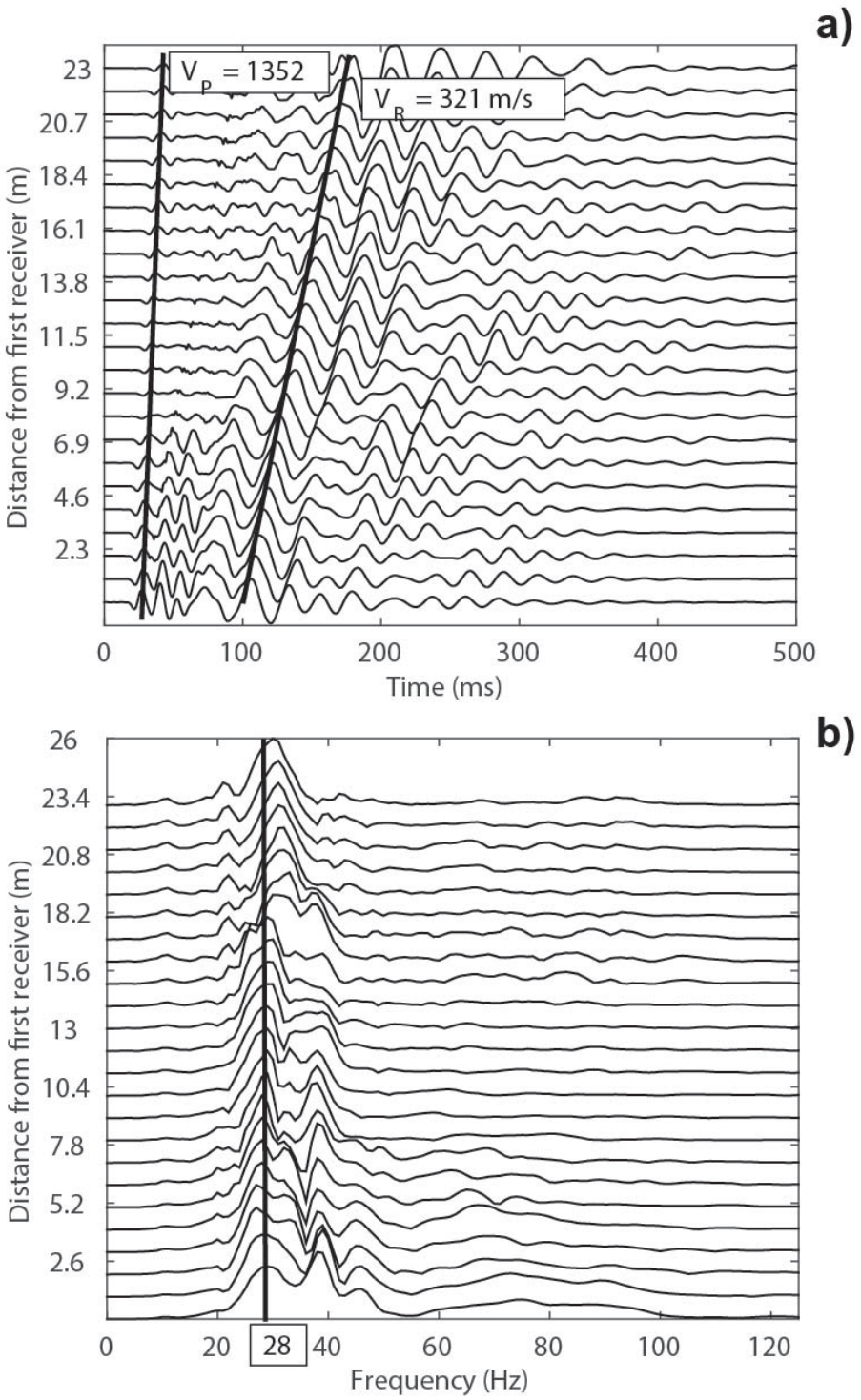

Figure 6.6: Results from MASW Line 2. Plot (a) shows the time traces obtained along with the P and Rayleigh wave (R-wave) velocities. A shift in time signals is obtained after the 16th receiver which changes the arrival of the R- wave from 304 to 307 m/sec. Plot (b) shows the computed frequency spectra for 24 receivers. Main frequency for all transducers is identified as 30 Hz

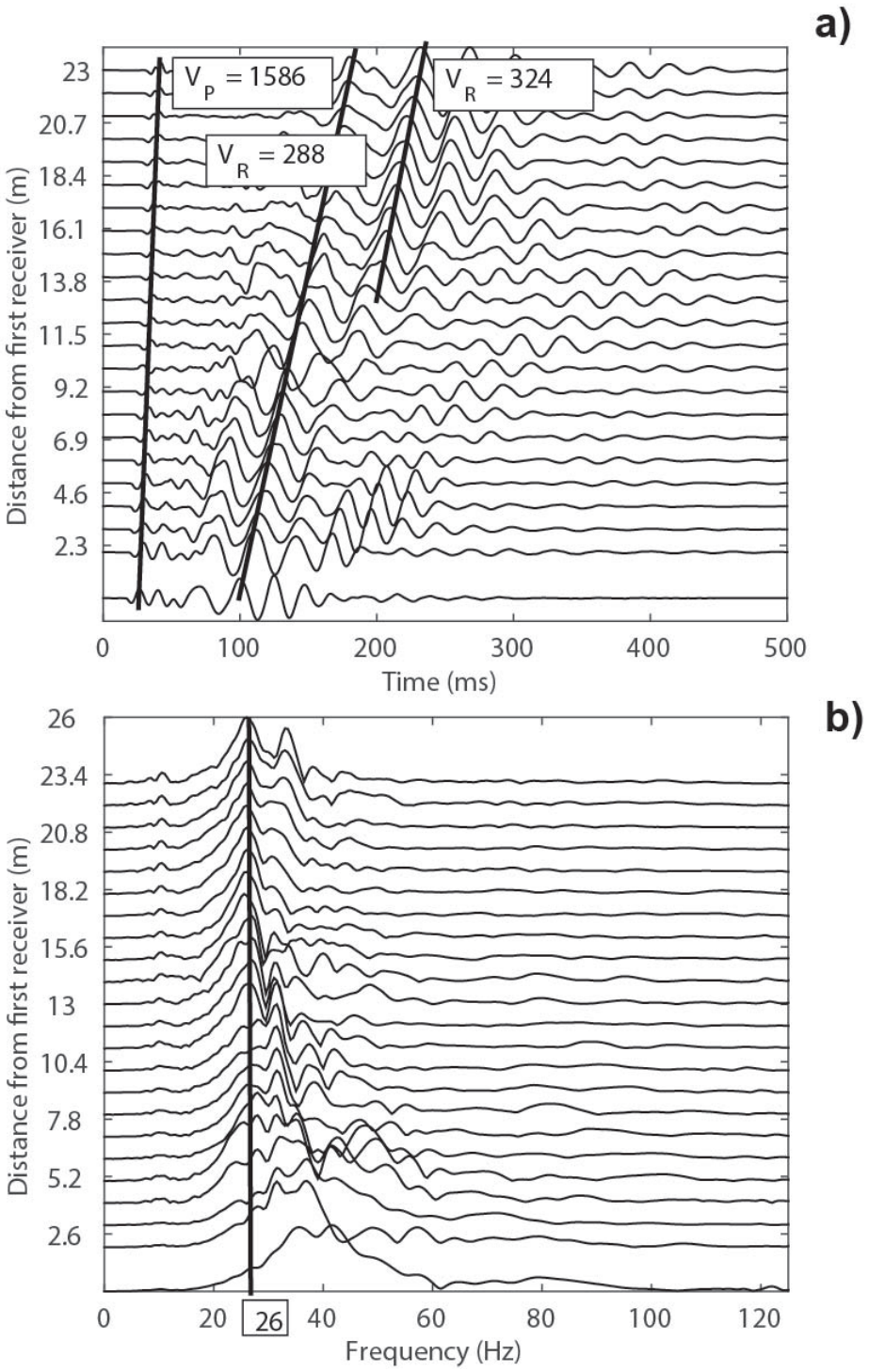

Figure 6.7: Plot (a) shows the time traces obtained along with the P and R-wave velocities. A shift in time signals is obtained after the 10th receiver. In plot (b) two main frequencies can be identified as 26 and 40 Hz

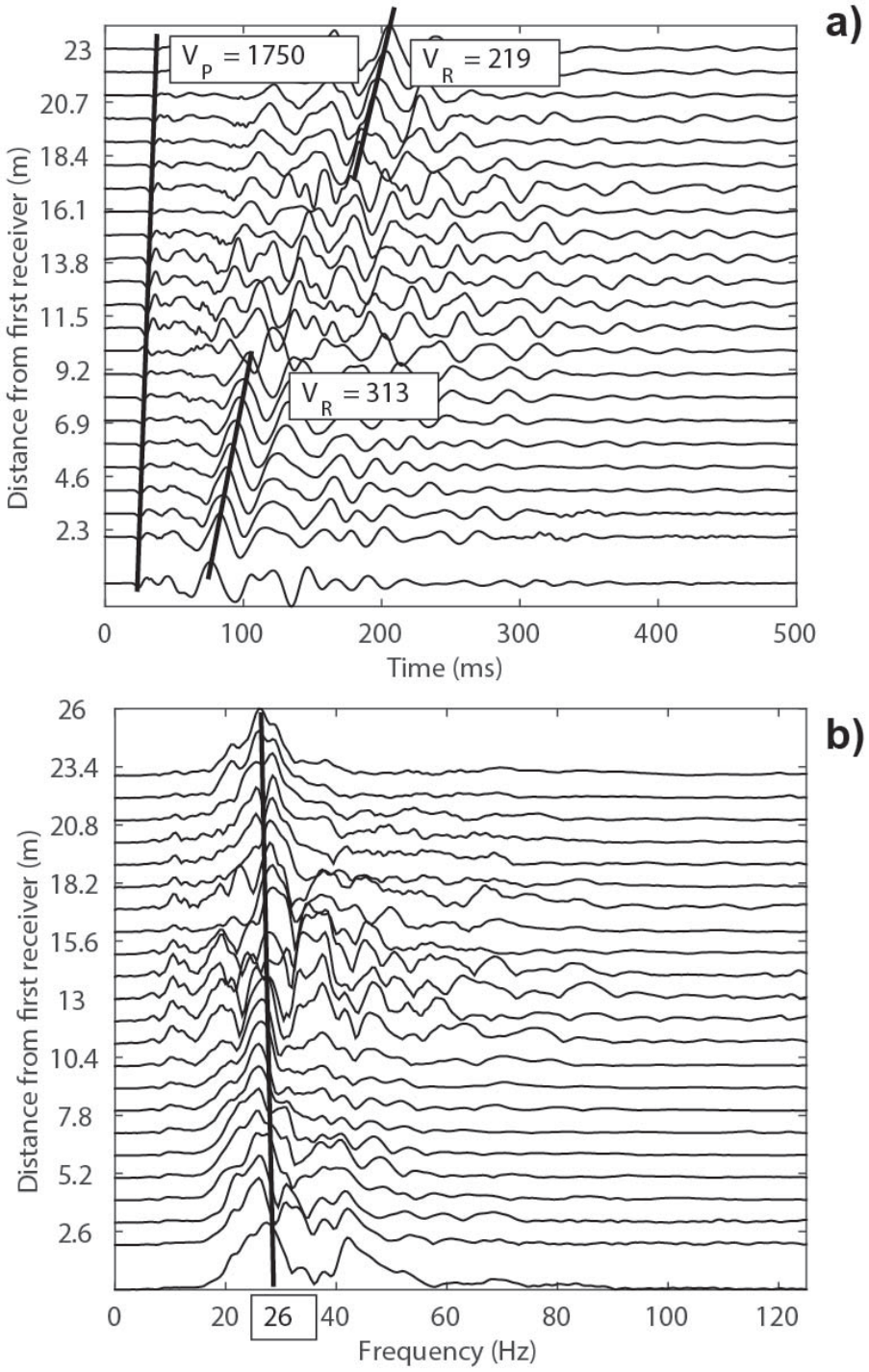

Figure 6.8: Results from MASW Line 4. Plot (a) shows the time traces obtained along with the P and Rayleigh wave (R-wave) velocities. A shift in time signals is obtained after the 10th receiver which changes the arrival of the R- wave from 416 to 300 m/sec. Plot (b) shows the computed frequency spectra for 24 receivers. The main frequency for all transducers is identified as 26 Hz.

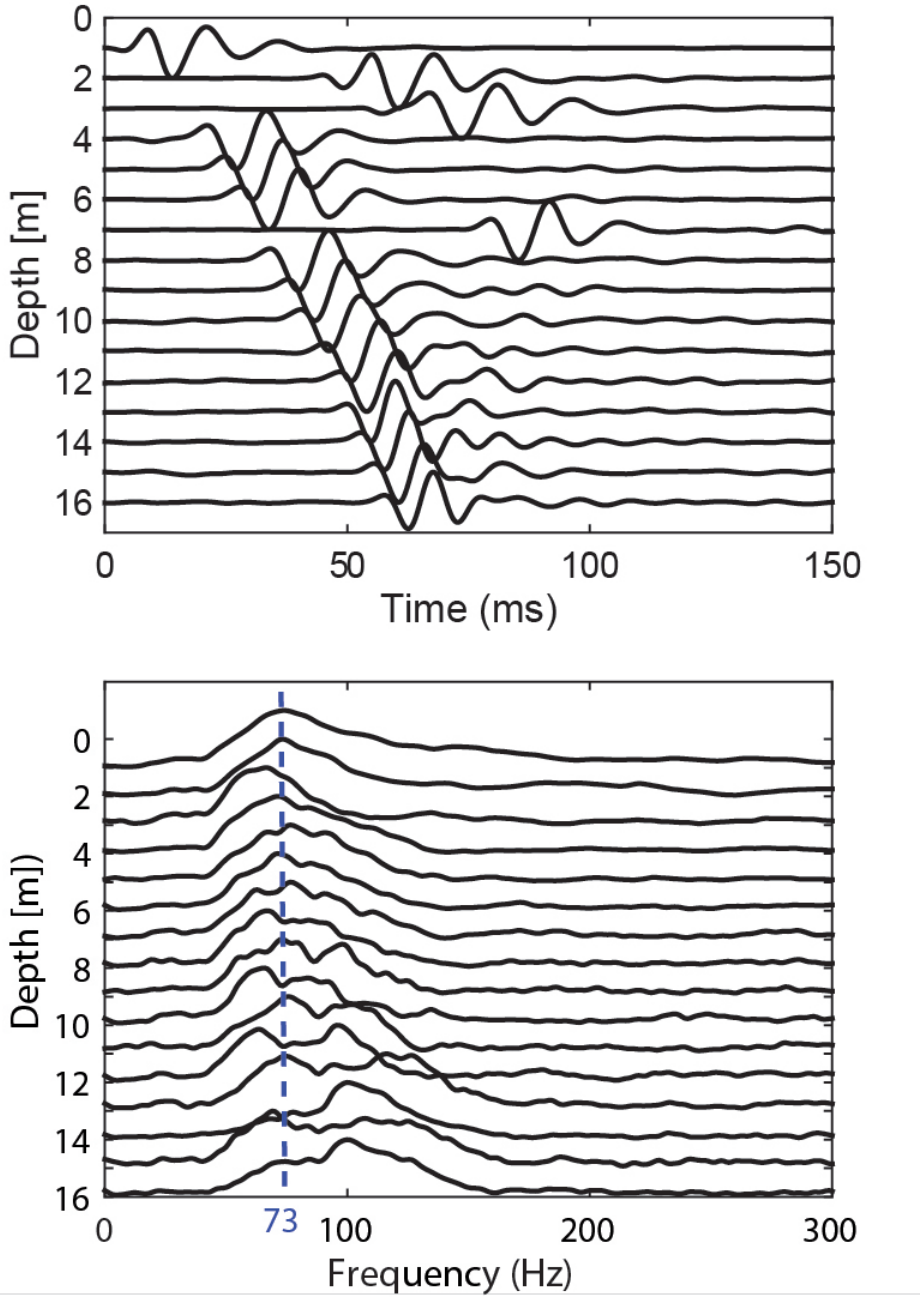

Figure 6.9: Results from SCPT 1. Plot (a) shows the time signal at a depth of 1m while plot (b) shows the frequency spectrum. The spectrum shows frequencies between 10 Hz and 200 Hz with peak at 74.5 Hz

meters showing a stiffer material is encountered. From the pore pressure measurements, the ground water level is estimated to be around 1.5 meters. Based on the CPT results, it is seen that three types of materials at different depth range are shown by the CPT measurements: (1) a silty clay

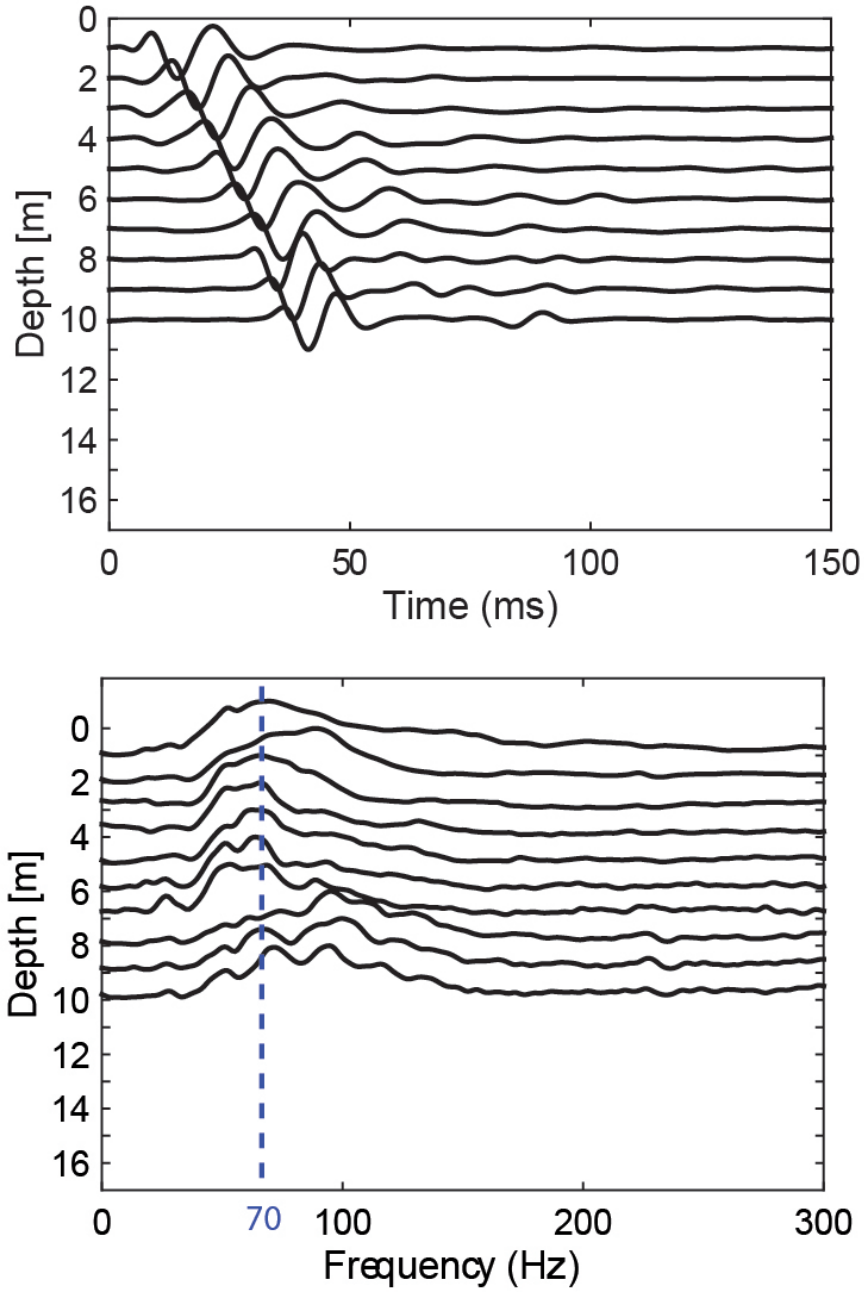

Figure 6.10: Results from SCPT 2. Plot (a) shows the time signal at a depth of 1m while plot (b) shows the the frequency spectrum. The spectrum shows frequencies between 20 Hz and 250 Hz with the peak at 70 Hz

layer from ground surface to 1.5 m deep, (2) a very stiff sand layer 2 to 4 m for SCPT 2 and SCPT3 while silty sand layer 2 m to 10 m deep for SCPT2, (3) silty sand layer from 4 m to 16 m. Table 1, shows the range of values and material types after Robertson (2009). The results, of the three types of materials, are similar for all the SCPT tests as shown in Figure 6.16a, which shows the uniformity

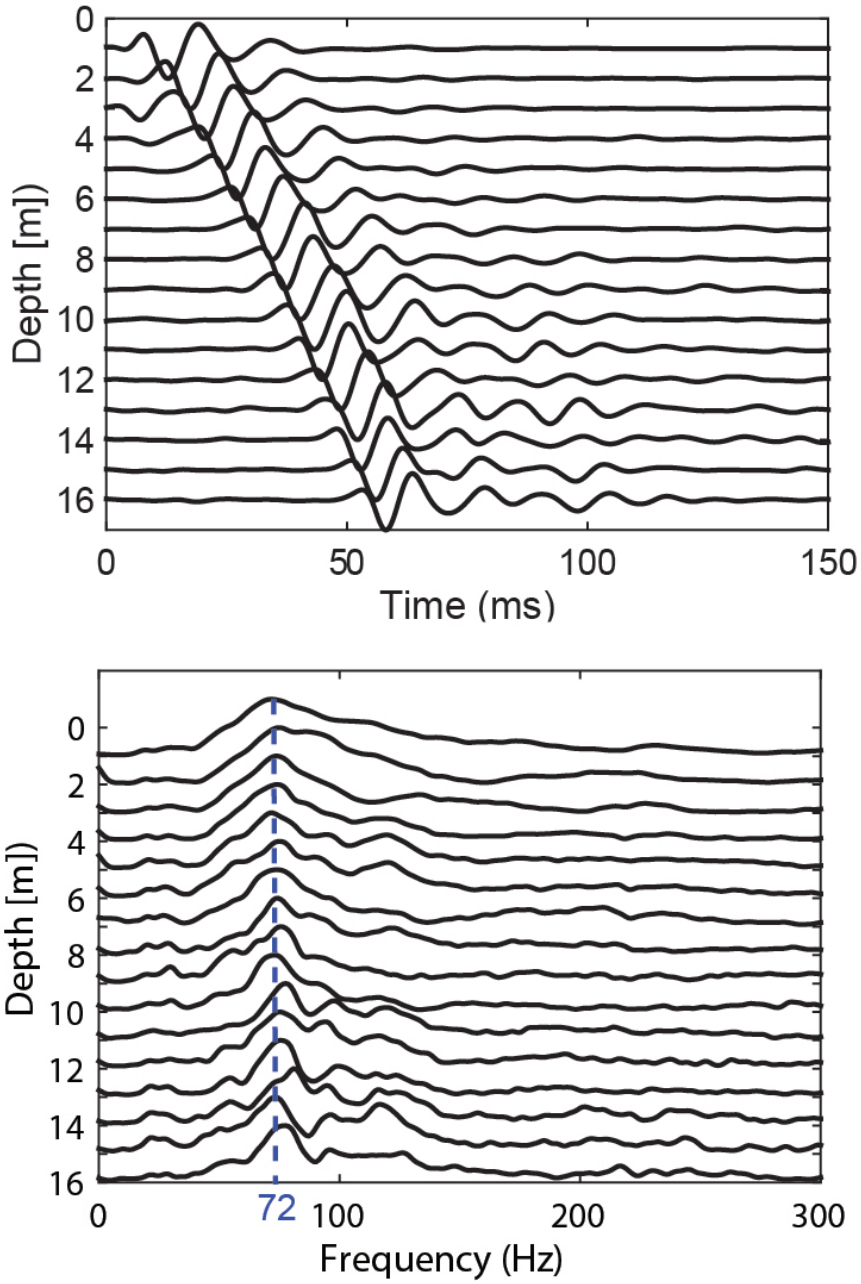

Figure 6.11: Results from SCPT 3. Plot (a) show time signal at a depth of 1m while plot (b) shows the frequency spectrum. The spectrum shows frequencies between 20 Hz and 250 Hz with the peak at 72 Hz

of soil underneath the test site. Figure 6.16b shows the normalized friction ratio vs normalized cone resistance plot. The figure shows the data from SCPT overlaid on the soil behavior chart (SBT) describing the scatter of data on different zones as shown in Table 6.1.

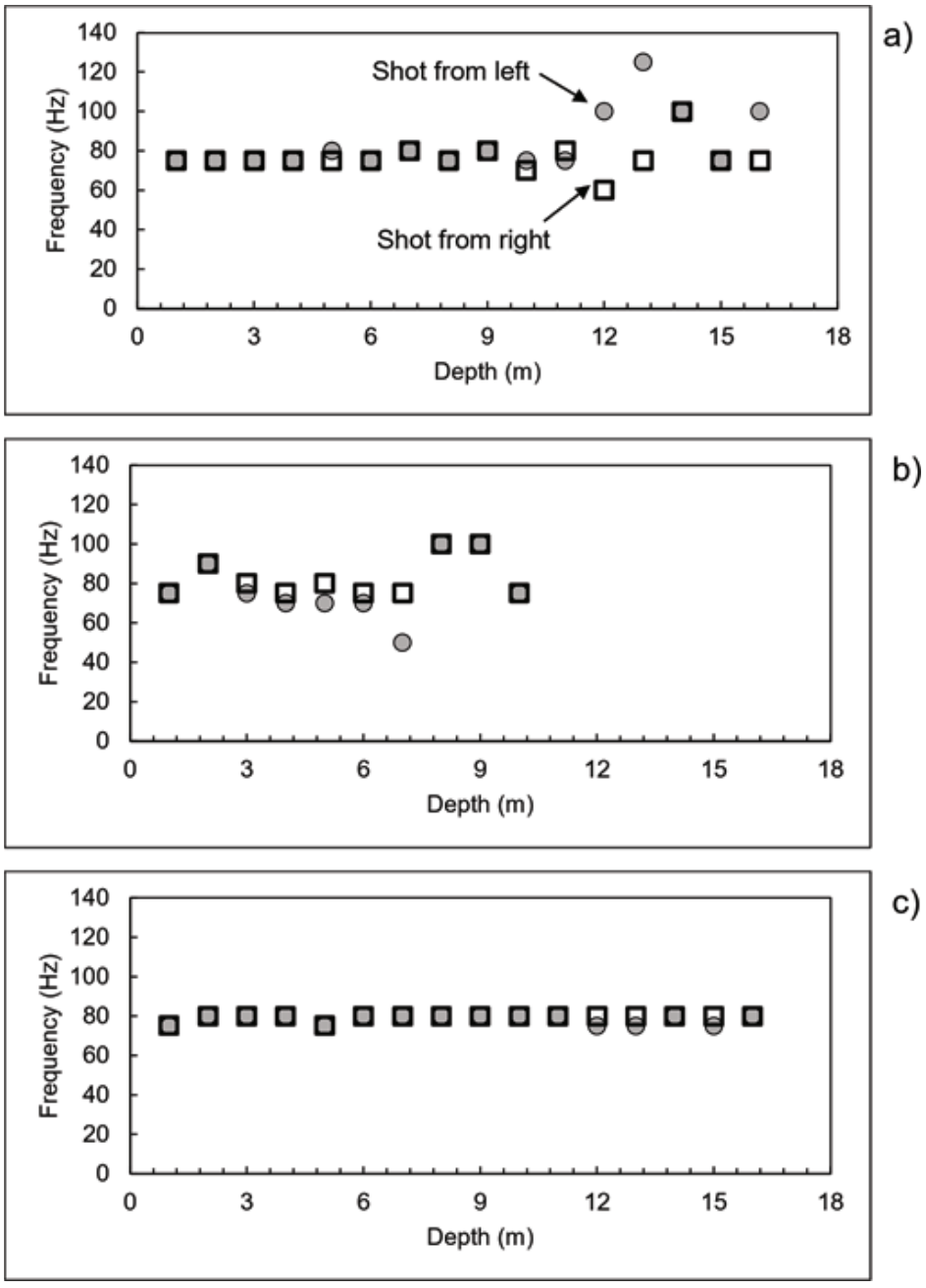

Figure 6.12: Variation in peak frequency with depth for a) SCPT 1, b) SCPT 2, and c) SCPT 3. The frequency difference between the left and right shots is also shown.

6.5 Shear wave velocity profile from MASW and SCPT tests

For the evaluation of shear wave velocity profiles for MASW data, a commercially available software SWAN is used. Figure 6.17 shows the average shear wave velocity profile, from SCPT data, for the left and the right shots. The stand error shows that the left and right shots are consistent for all

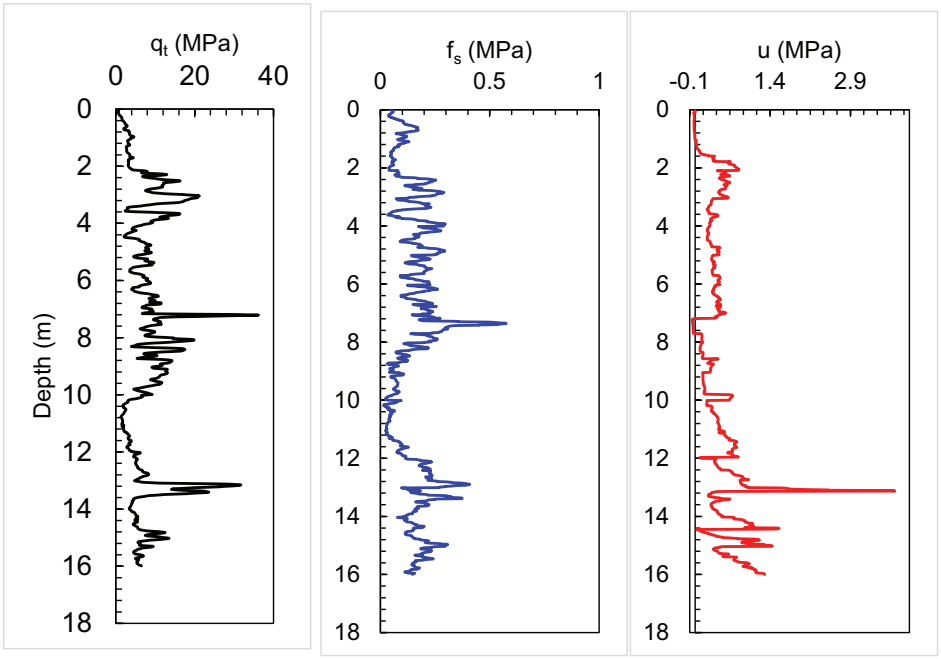

Figure 6.13: Cone penetration results for SCPT1

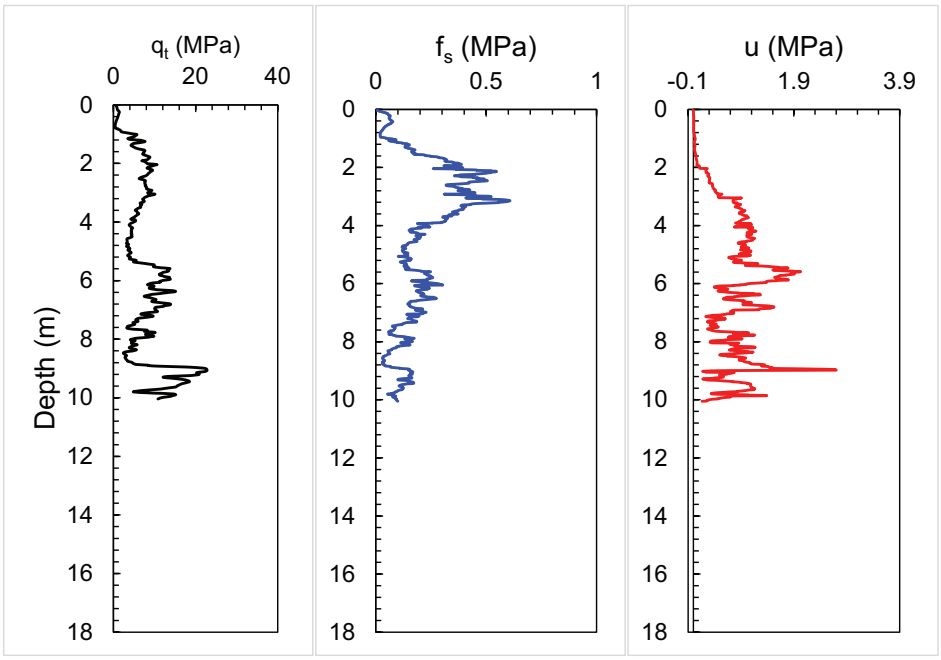

Figure 6.14: Cone penetration results for the SCPT 2

SCPTs. For SCPT 3, the variability is 53% at a depth of 6 m, while for other depths the variability is zero which shows consistency in the shots. It can be seen that there is good coherency between the MASW profiles. For the four lines, the results show approximately three layers with and increase in velocity at 3m and then the profile moves back to velocity of 300 m/sec at 8 m as shown in Figure

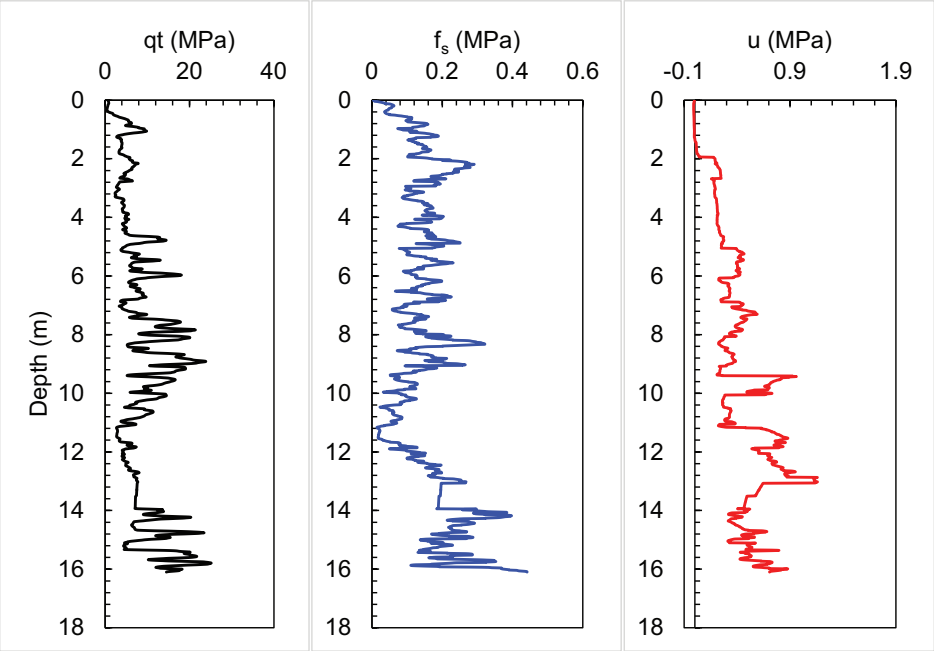

Figure 6.15: Cone penetration results for the SCPT 3

Table 6.1: Normalized soil behavior type chart (Robertson, 2009)

Zone	*Soil Behaviour Type*
1	*Sensitive, fine grained*
2	*Organic soils – clay*
3	*Clays – silty clay to clay*
4	*Silt mixtures – clayey silt to silty clay*
5	*Sand mixtures – clean sand to sandy stiff*
6	*Sands – clean sands to silty sand*
7	*Gravelly sand to dense sand*
8	*Very stiff sand to clayey sand*
9	*Very stiff fine grained*

6.18. The test results are consistent and repeatable and clearly reflect the uniformity of the site as shown in Figure 6.19. Between 3 and 8 meters, the difference between MASW and SCPT is significant; however, for other depths the two profiles match closely. The MASW values are 38% larger for line 3 and 4, and 28% larger for line 2. The results of line 1 matches well with the SCPT data. The large difference between the MASW and SCPT results for the depth between 3 m and 8

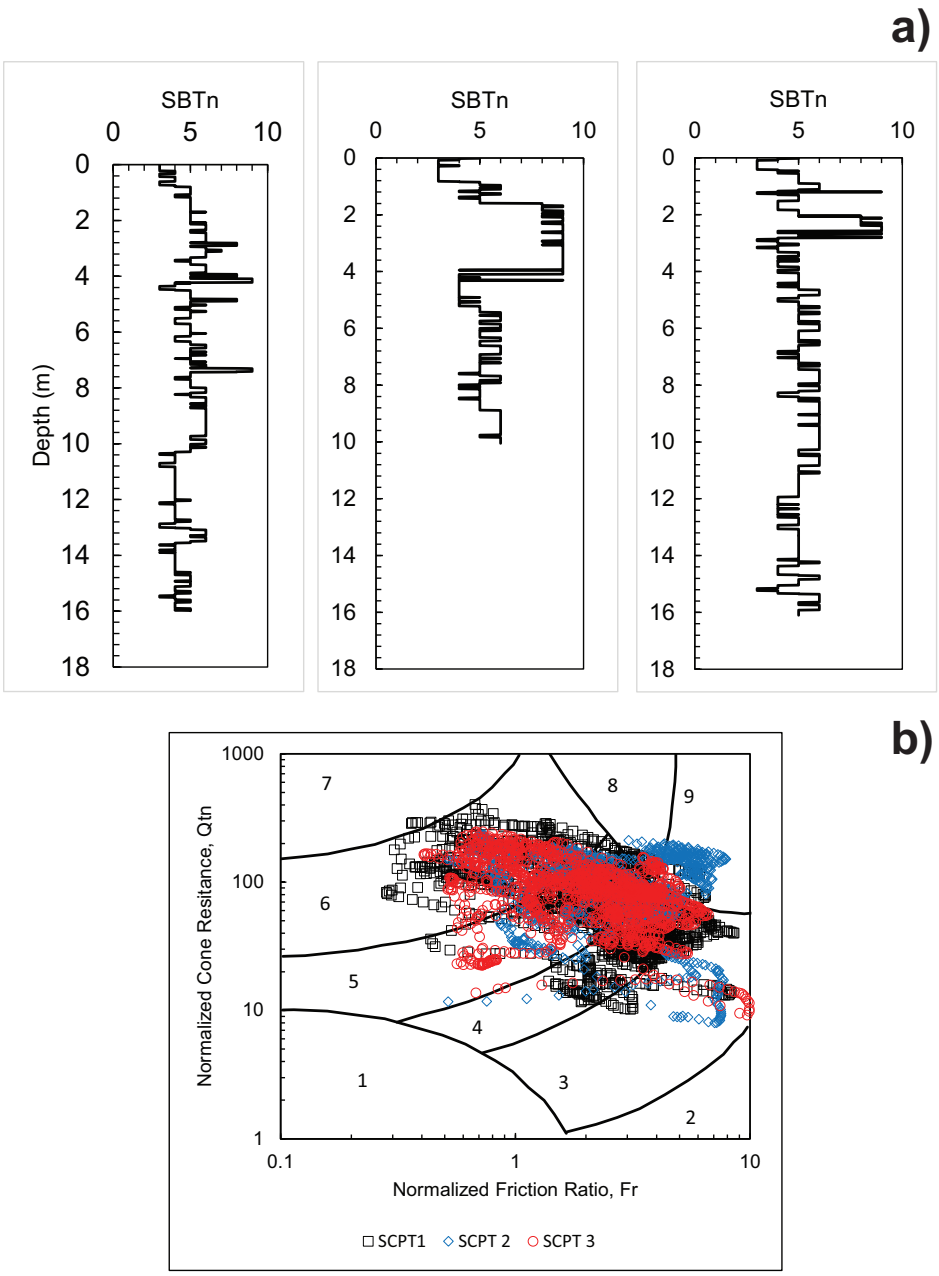

Figure 6.16: Figure a) shows the estimated soil profiles from seismic cone penetration test results using the soil behavior type index, obtained from Robertson (2009) as described in Table 1. Figure b) shows the data from SCPT tests overlaid on the SBT chart. The description of different zones is shown in Table 1.

m can be explained from the CPT data and soil behavior type (SBT) plots. The SBTn plots for all three the SCPTs show a change in the soil type between 2.5 m and 7 m.

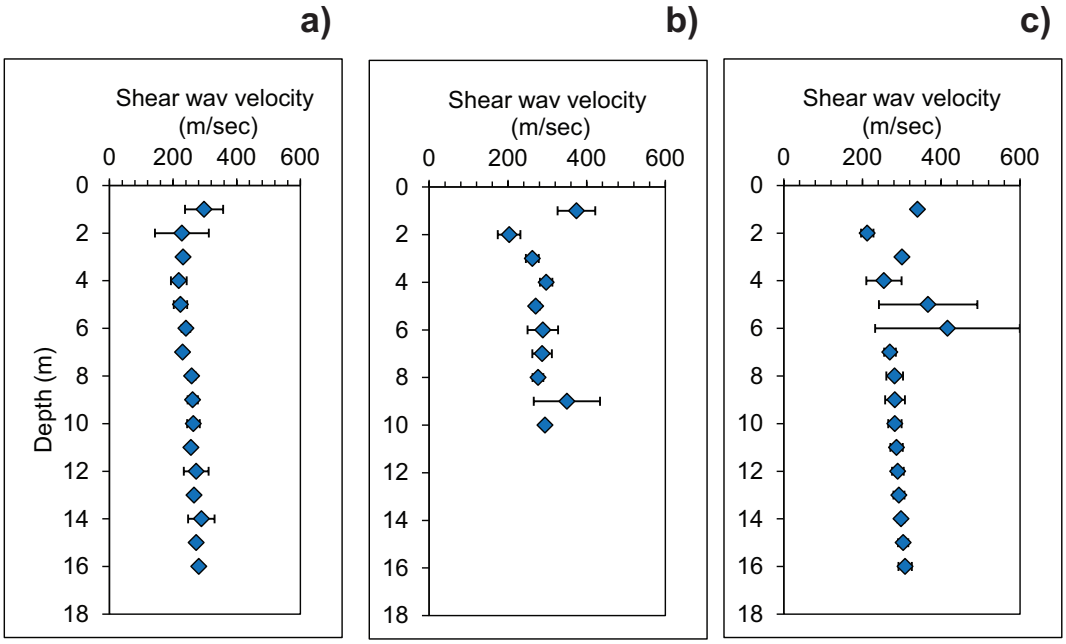

Figure 6.17: Average shear wave velocity from left and right shots from a) SCPT1 b) SCPT2 c) SCPT3

Quantitative analysis of data

A quantitative analysis of the data is given in Table 6.2. MASW results are compared with SCPT over specific depth intervals. The results are compared for MASW lines 1, and 2 and SCPT 1, 2, and 3. MASW lines 3 and 4 are not compared as the seismic cone penetration test was not done during this test. The results between the MASW and the SCPT tests are in close agreement with the exception between 3 m and 8 m depth. At this depth, the difference is more than 40% between the two tests. However, the MASW soil profile results are close to the cone penetration results, where a sudden change in resistance is noticed between these depths. A possible explanation for this can be made from the frequency spectrum of the two tests and wavelength (determines seismic resolution) obtained from the dominant frequency. The acceptable threshold for vertical resolution generally is a quarter of the dominant wavelength ($\lambda/4$) for P- and S- waves (Öz Yilmaz, 2015). From the SCPT test, considering the average shear wave velocity of 300 m/s and dominant frequency of 72 Hz, within a depth of 3 meters to 7 meters, the $\lambda/4$ is 1.04 m. While from MASW test, for Vs = 400 m/s and frequency of 25 Hz, the $\lambda/4$ is 4 m. The analysis shows that the frequency generated from the seismic source is very important in characterizing the site. Geotechnical site classifications in accordance with the NEHRP (National Earthquake Hazards Reduction Program) Provisions are

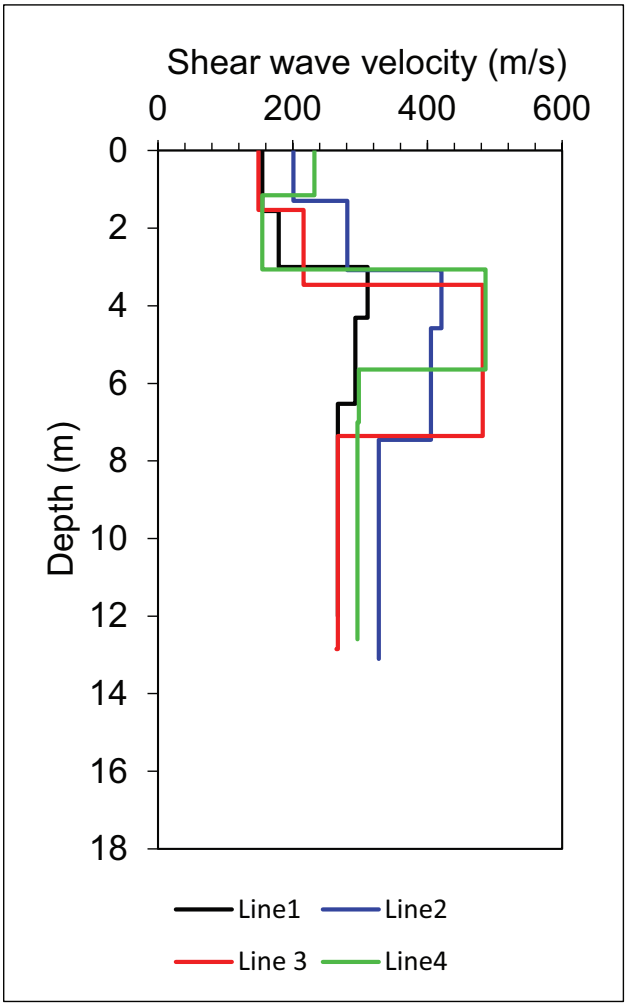

Figure 6.18: Average shear wave velocity for MASW Lines 1, 2, 3, and 4. For lines 1 and 2, the profile is average of left and right shots

based on mean shear wave velocity V_{S30} defined for the depth interval of $0m30$ m. The mean shear wave velocity V_{S30} is calculated by:

$$V_{S30} = \frac{30}{\sum_{i=1}^{n} \frac{\Delta z_i}{\Delta V_{S,i}}} \tag{6.1}$$

Table 6.3 shows the comparison of velocities V_P, V_S, and V_R for SCPT and MASW tests. The results show that the site is very consistent and uniform with silty clay and dense sand deposits. Based on the NEHRP site classification, the site can be classified as site class D, very stiff soil.

Table 6.2: Comparison of percentage change in velocity from MASW and SCPT tests.

Survey Line	Depth range (m)	Percentage change in Vs from MASW and SCPT SCPT1	SCPT2	SCPT3
MASW Line 1	0 - 2	-100	-127	-
	2 -3	-27	-18	-
	3 - 7	24	8	-
	7 - 13	0	10	-
MASW Line 2	0 - 2	-48	-	-68
	2 -3	19	-	24
	3 - 7	48	-	10
	7 - 13	19	-	14

Table 6.3: Comparison of wave velocities from MASW and SCPT tests. Also shown are the average shear wave velocity for 30 m depth based on NEHRP criteria.

TEST		V_P (time)	V_R (time)	$\overline{V}_S$
MASW	1	1642	276	235
	2	1415	305	326
	3	1586	275	278
	4	1556	300	294
SCPT	1	-	-	256
	2	-	-	290
	3	-	-	298

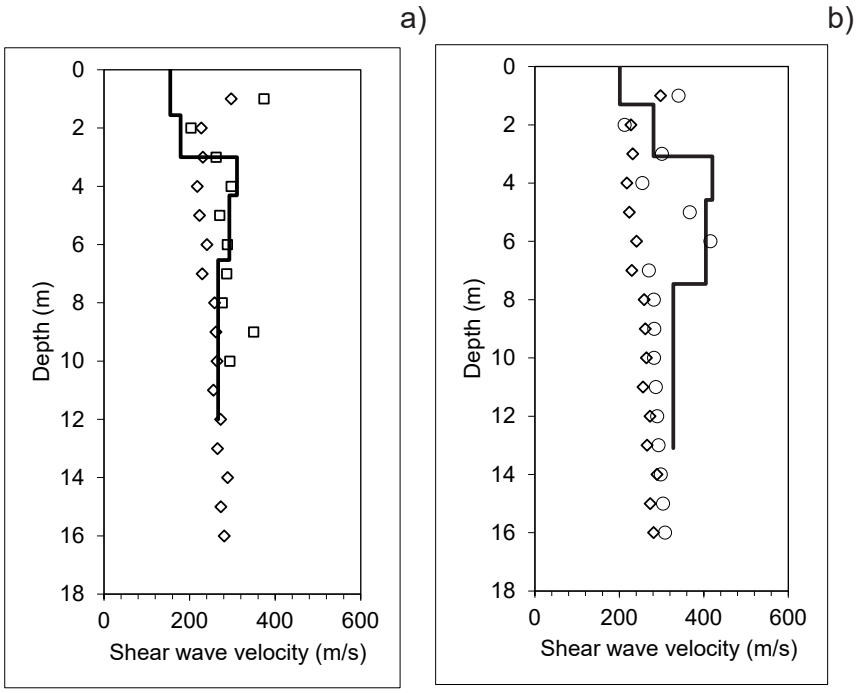

Figure 6.19: Comparison of shear wave velocity profile from MASW and SCPT tests. Average shear wave velocity for MASW Line1, 2, 3, and 4. For lines 1 and 2, the profile is average of left and right shots

6.6 Chapter Summary

The chapter presented results of the MASW and the SCPT test performed at the UW-CLTS geophysical test site. Four lines of the MASW test and three CPT and SCPT tests were done as part of this study. The site is a silty clay till soil. One of the major applications of the CPT and SCPT has been the determination of the soil stratigraphy and the identification of soil type. Using the SBTn chart and cone parameters, the soil is identified into three layers consisting of: (1) silty clay (2) very stiff sand layer, and (3) silty sand layer.

The MASW test as a non-invasive test is being used for geotechnical site characterization for the last few years. In the four lines of MASW test, sledge hammer was used a source while the distance between the geophones was kept as one meters. For each offset location, five shots were made. Therefore in total 120 measurements were done.

The comparison of shear wave velocity from the MASW and the SCPT test is usually done in the field test analysis, however, one parameter that is overlooked is the frequency content of the signals. In this study, the frequency spectrum from the MASW and the SCPT tests data were

analyzed to understand the change in the shear wave velocity at different depths. From the analysis, the percentage change in shear wave velocity between MASW line 1 and SCPT 1 and 2 is more than 90 % for depths between 0 and 2 m, while it reduces to 10 % for depths between 7 and 13 m (Table 6.2.

The comparison of wave velocities from time traces and from shear wave profiles are presented in Table 6.3. The average shear wave velocity from the SCPT and the MASW tests is 300 m/sec, which will be equal to site class D (stiff soil) based on NEHRP site class.

CHAPTER 7

Conclusions and Future Recommendations

7.1 Main Contributions

There is a fundamental relationship between wave velocity , frequency, and wave-number $(V = f\lambda)$. However, the importance of the ratio between the specimen size and the wavelength has not been properly studied in the literature. Thus, this work presents a new comprehensive study of these effects using resonant column (RC), bender element (BE), multichannel analysis of surface waves (MASW), seismic cone penetration test, and numerical simulations.

RC and BE tests are standard procedures; however, the effects of the different frequency ranges used in these tests have not been well understood. Coupling between the specimen and base platen is very critical. In addition to the frequency effects, the coupling effects between the specimen and end platen is studied. Also, new effect of base fixation for RC testing is shown. Finally, a new BE method is proposed to understand the estimation of shear wave velocity at higher frequencies.

MASW is a practiced field test to evaluate the shear wave velocity profile for geomaterials, however, the effect of frequency in the case of an anomaly has not been well understood. Therefore, this study uses numerical simulations and a lab scale model to study these effects. In addition, the effect of actual accelerometers on the measurements is studied for the first time using a high

frequency laser vibrometer.

The frequency effects in field theory of the MASW and SCPT is also studied to address the actual limitations in the analysis of SCPT data without the consideration of frequency effects.

7.2 Conclusions

7.2.1 Laboratory resonant column and bender element tests

Laboratory measurement of shear wave velocity and damping ratio evaluation for small strains is usually done through RC and BE tests. The RC tests is a standard testing method, however, there is no standard methodology for BE testing. This is due to the interpretation of the BE test measurements. Time and frequency domain methods are available, however, work needs to be done to understand the actual behavior of benders in air and under various systems before the results are interpreted, especially, the effect on the wave velocity and attenuation. The following conclusions can be made from the RC and BE tests:

RC device is calibrated using aluminum probes. Three aluminum probes of 9.47, 19.12, and 25.23 mm internal diameter were used. For the 25.25 mm internal dia probe, the test was conducted from small strain to large strain. The shear modulus value remained constant for the range of strain tested while the damping value changed from 0.2 % to 0.6 % ($\gamma = 8 \times 10^{-3}\% to \gamma = 8 \times 10^{-1}\%$).

Bender element were calibrated using three configurations, tip-to-tip, short sand specimen, and bender in air. State of art laser vibrometer was used to characterize the bending behavior of bender elements showing the resonance frequency of 12 kHz and damping of 2 % when vibrating in air. The resonance frequency value from other configuration gave similar results. The delay time is calculated was 4.5 μ seconds from the tip-to-tip and from the aluminum probe test.

The maximum displacement of BE vibrating in air for transmitter BE was 15 nm while for receiver BE was 3 nm.

Four soils were tested, stiff clay, mine paste, leda clay, and sand. The top and bottom platen of RC device were modified to allow better coupling between the specimen and benders. Radial blades were introduced to account for coupling of clay specimens such as stiff clay specimens.

The tests were done at confinement ranging from 50 kPa to 600 kPa, and for strain levels

($\gamma = 1 \times 10^{-4}\% to \gamma = 2 \times 10^{-1}\%$).

For leda clay and sand specimen 2, the modified RC bottom and top platen were used. The results of leda clay showed the effect of coupling improvements in the stiffness increase as a function of frequency and confinement.

Tests on leda clay showed no change in the damping ratio (0.8 %) at low strains for the confinement applied in this study.

In this study, a modified frequency domain method for BE testing is presented for sand specimen. The sample was excited with a frequency sweep ranging from 0 to 52 kHz and change in unwrapped phase, between the input excitation and output response, is evaluated outside the range of resonant peaks of the specimen. In conclusion, the variation in shear wave velocity is less than 10 % between the resonant column and bender element tests.

7.2.2 Numerical simulations and laboratory MASW tests

To understand the propagation of R-waves in presence of lateral inhomogeneity, results of numerical simulations are studied first. To introduce non-homogeneity, voids of various size and depth are used. The following conclusions can be drawn from this chapter:

A new methodology of processing MASW data is introduced in which the receivers were divided into three sections, before, on-top, and after the void.

Nine numerical models were analyzed in which the void depth and width varied. Results of the test were analyzed in time and frequency domains. Dispersion curves were obained from the 2D FFT spectrum. Results from the dispersion curves show that the change in the phase velocity (function of frequency) is between 3% to 50% for different void width and depth.

The results of the laboratory MASW test were conducted using three different configurations. Two tests involved use of accelerometers as receivers, however, the input source was different (shaker and dynamic hammer). While the third test consisted of using state of art laser vibrometer as receiver.

For the lab test, two lines of MASW were tested in each case. Twelve accelerometers were used for the shaker and hammer as source, while 96 measurements were done by using laser.

The frequency response from the accelerometer was 2 - 20 kHz for shaker and 0.5 - 6 kHz for

hammer; while for the laser was 48 - 51 kHz.

Based on the knowledge of the author, no previous MASW measurement using laser is done for geo-materials. The results from the laboratory MASW test showed the frequency effect on the measurements due to the source used in this method.

Coupling of geophone/transducer in surface wave testing is an important issue. Results from the lab test using laser vibrometer showed that the mass loading effect of accelerometer affects the frequency content of the signal.

The results of three tests were analyzed in time and frequency domain. The technique of normalized wavelength gave good results in terms of void detection. The location of the void in the case of laser measurements is clear. Applying all this information to estimating void depth is a principal future goal of our work.

Laser techniques are very popular due to the non-contacting nature of this measurement device. Accelerometer measurements are also widely used in many applications but suffer from potential mass loading effects. Each technique has its own benefits and drawbacks.

7.2.3 Field MASW and SCPT tests

This chapter presents the results of the MASW and the SCPT test performed at the UW-CLTS geophysical test site. Four lines of the MASW test and three SCPT tests were done. The site is a silty clay till soil. One of the major applications of the CPT and SCPT has been the determination of the soil stratigraphy and the identification of soil type. The following conclusions were drawn from this study:

Using the SBTn chart and cone parameters, the soil is identified into three layers consisting of: (1) silty clay (2) very stiff sand layer, and (3) silty sand layer.

For the last few years, MASW test is being used as a non-invasive test for geotechnical site characterization. In the four lines of MASW test, sledge hammer was used a source while the distance between the geophones was kept at one meters. For each offset location, five shots were made. Therefore in total 120 measurements were done.

The comparison of shear wave velocity from the MASW and the SCPT test is usually done in the field test analysis, however, one parameter that is overlooked is the frequency content of

the signals. In this study, the frequency spectrum from the MASW and the SCPT tests data were analyzed to understand the change in the shear wave velocity at different depths. From the analysis, the percentage change in shear wave velocity between MASW line 1 and SCPT 1 and 2 is more than 90 % for depths between 0 and 2 m, while it reduces to 10 % for depths between 7 and 13 m.

The average shear wave velocity from the SCPT and the MASW tests is 300 m/sec, which will be equal to site class D (stiff soil) based on NEHRP site class.

7.3 Recommendations and Future work

This thesis presented estimation of the shear wave velocity from the laboratory and the field methods, however following are the recommendations for future work:

The Calibration of benders using laser vibrometer with a smaller grid mesh to characterize the bending behavior of bender in air and in the soils. Further, use of transparent soil to characterize the effects of confinement on benders and to measure the actual input signal that is transmitted to the soil.

In resonant column test, the coupling between the specimen and platen is important and has a significant effect on the shear wave velocity and damping ratio of the specimen. The couplings are improved, however, more tests are required to quantitatively see the coupling effect for a range of soils (soft to stiff clay). The calibration of RC device should be done on isolation table to evaluate the equipment generated damping.

In the numerical simulations, rectangular voids are used to understand the propagation of R-waves in a homogenous medium. Further studies should be done on circular and oval shaped voids to see the effects on surface responses.

Laboratory MASW tests using laser vibrometer should be investigated further. The effect of accelerometers mass on the measurements could be removed. Tests should be done on various sand and clay materials.

In the recent years, field MASW test is recognized as an important test for site characterization; however, the interpretation of the test needs improvement.

APPENDICES

APPENDIX A

2D Numerical Model

A.1 2D - FFT PLOTS

In this section, 2D - FFT plots are presented. These plots are obtained from computer package SWAN. The values of the amplitudes are logarithmic values.

A.2 Dispersion curves (DC) - Total section

This section presents the results from the dispersion curves obtained from the total section analysis for Model 1, 2, 3, 4, 5, 6, and 7. Also presented is the DC from no-void case.

A.3 2D - Dispersion curves (DC) - Multi Section

Similar to total section analysis, this section shows the results of DC obtained from sectional analysis.

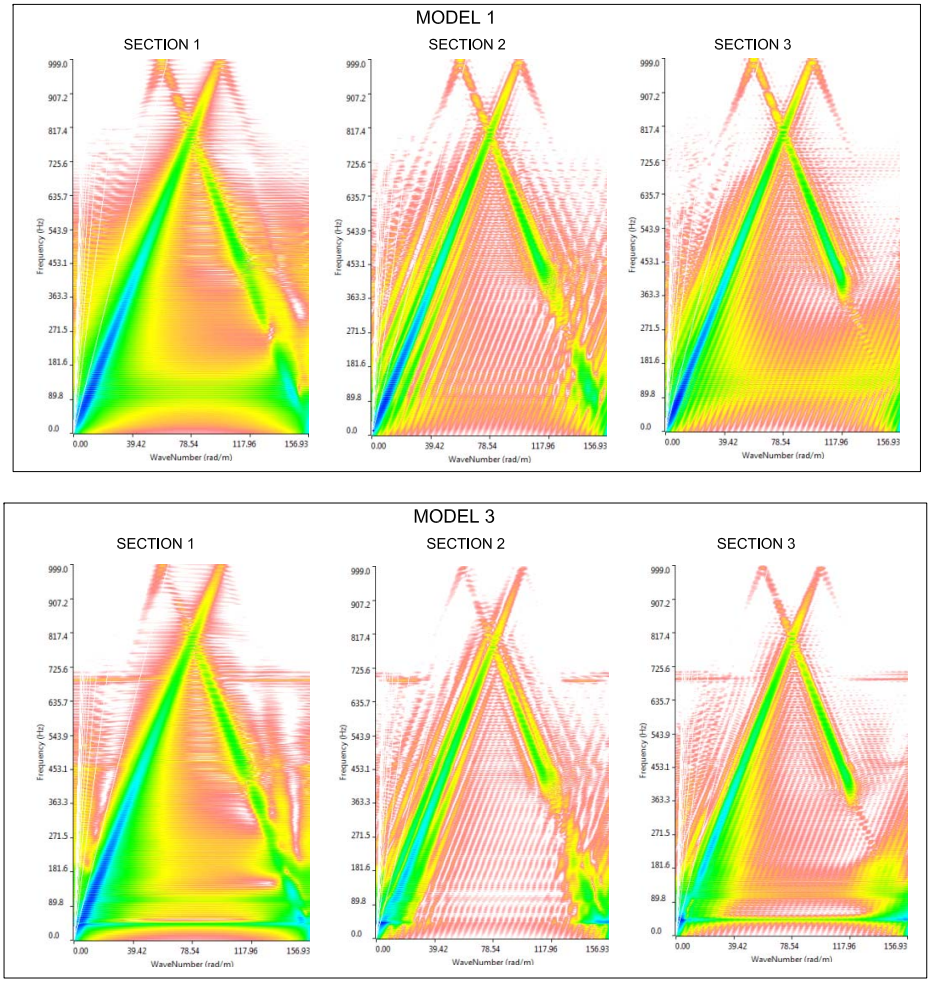

Figure A.1: 2D - FFT spectrum for Model 1 and 3

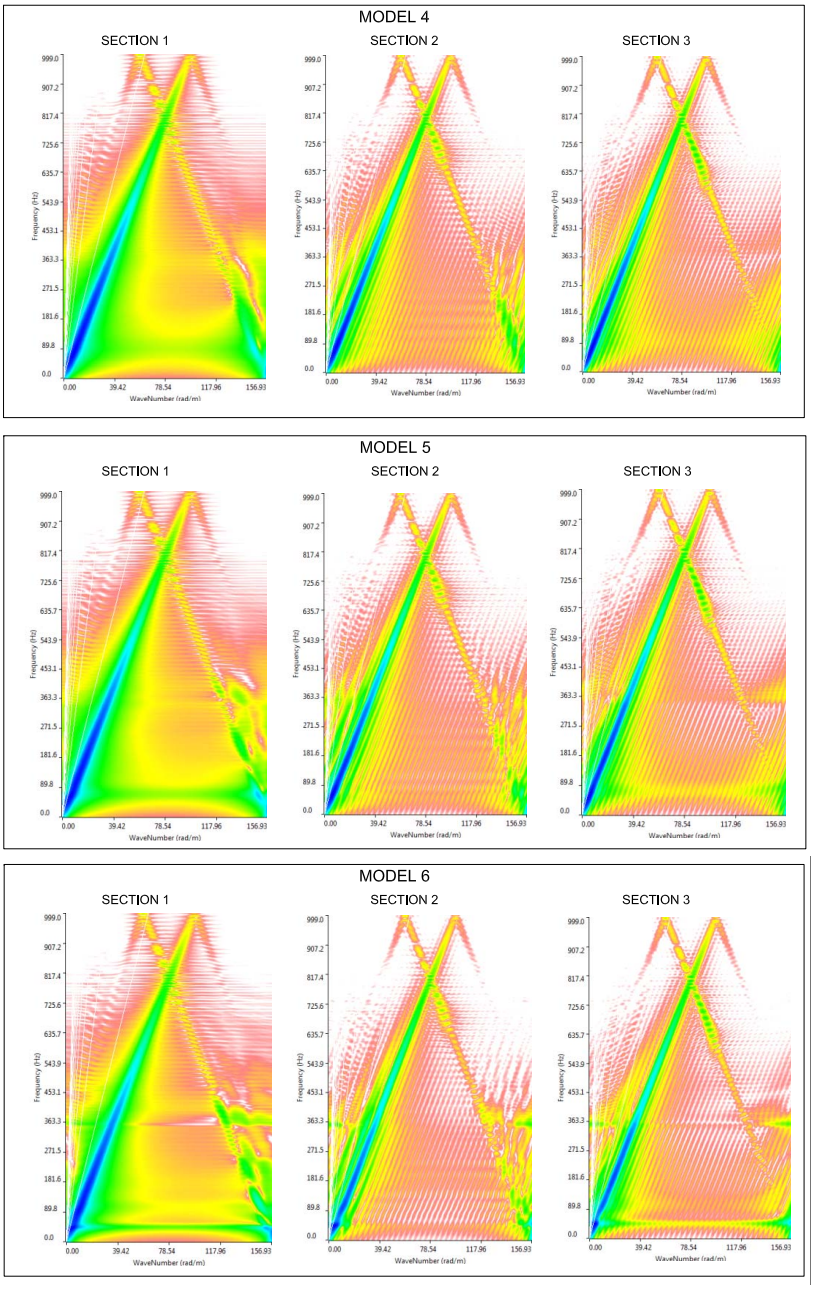

Figure A.2: 2D - FFT spectrum for Model 4, 5, and 6

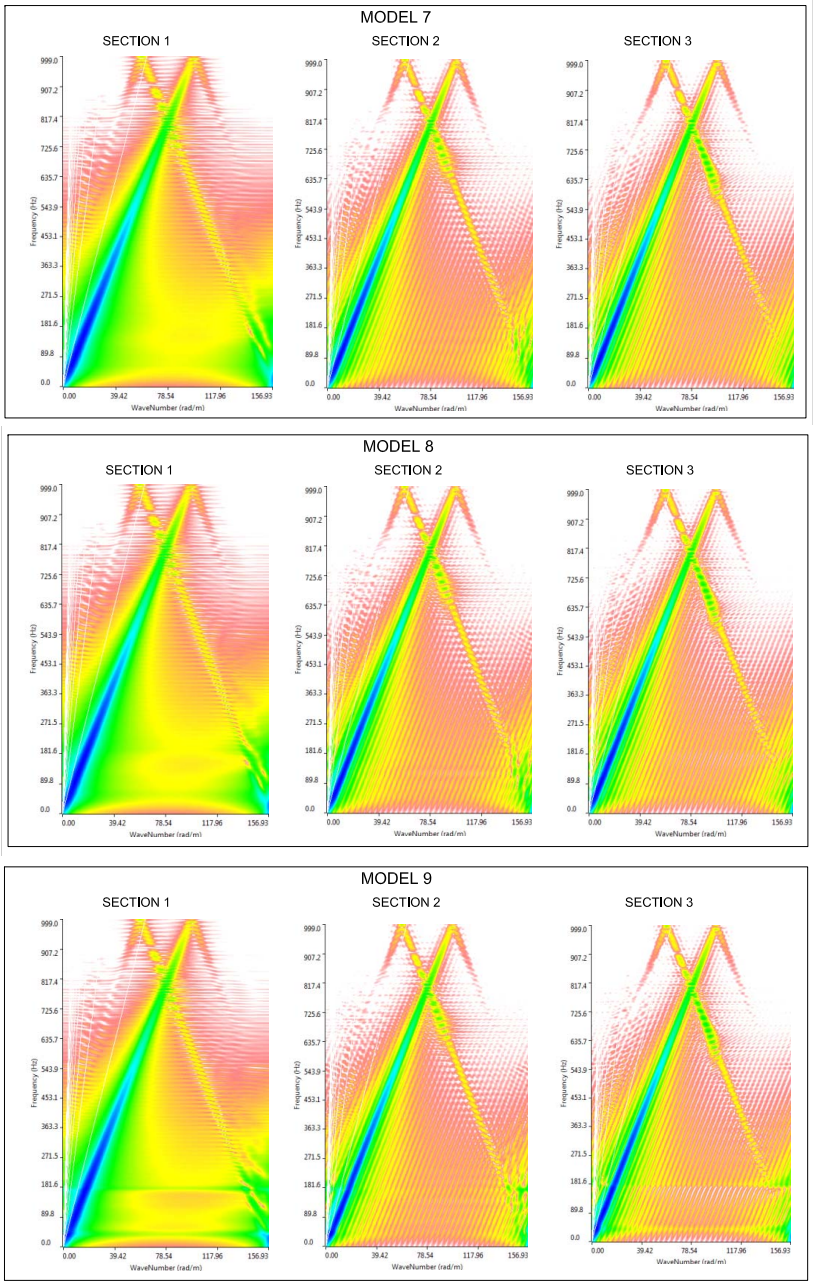

Figure A.3: 2D - FFT spectrum for Model 7, 8, and 9

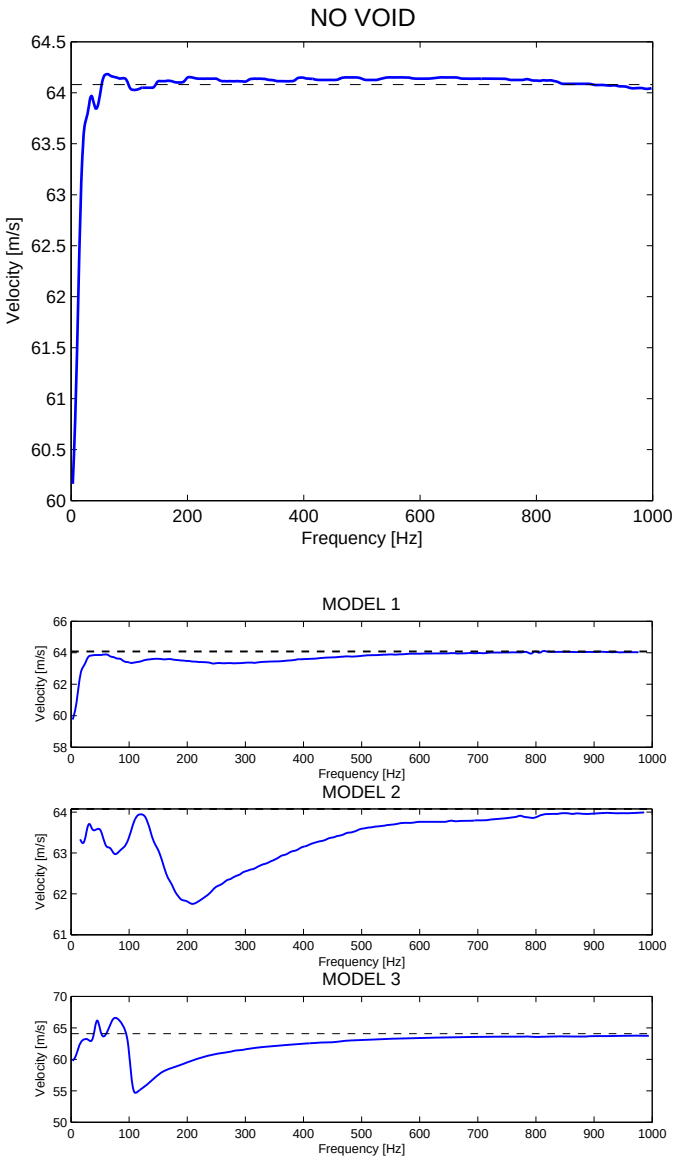

Figure A.4: Dispersion curves for no-void and model 1, 2, and 3

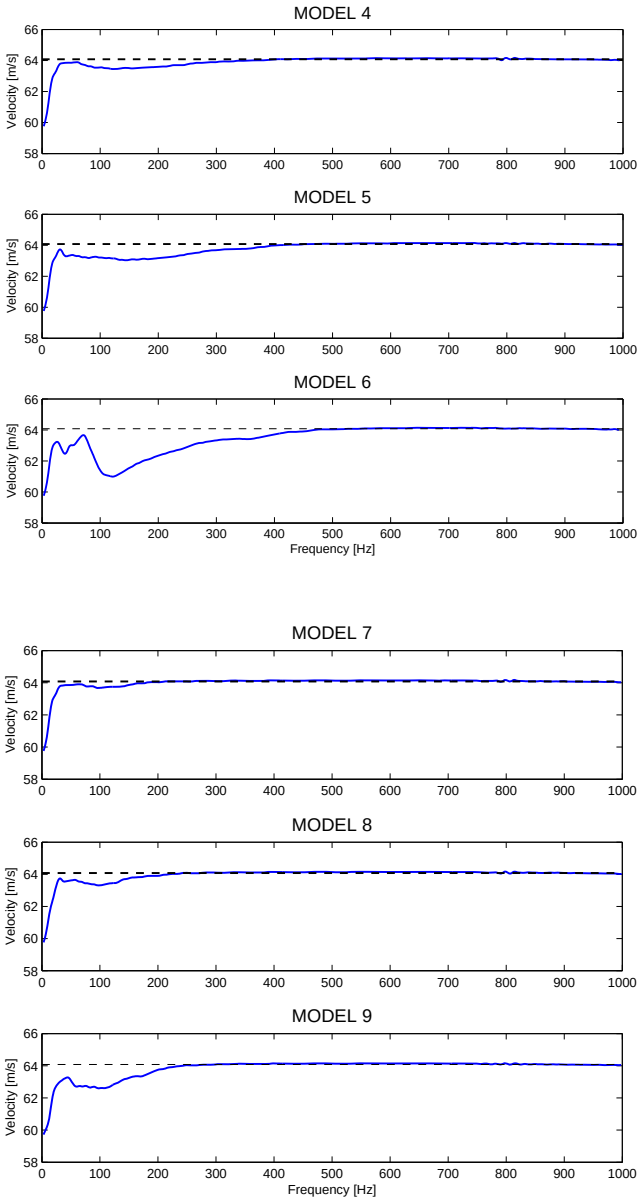

Figure A.5: Dispersion curves for model 4,5,6,7,8,and 9

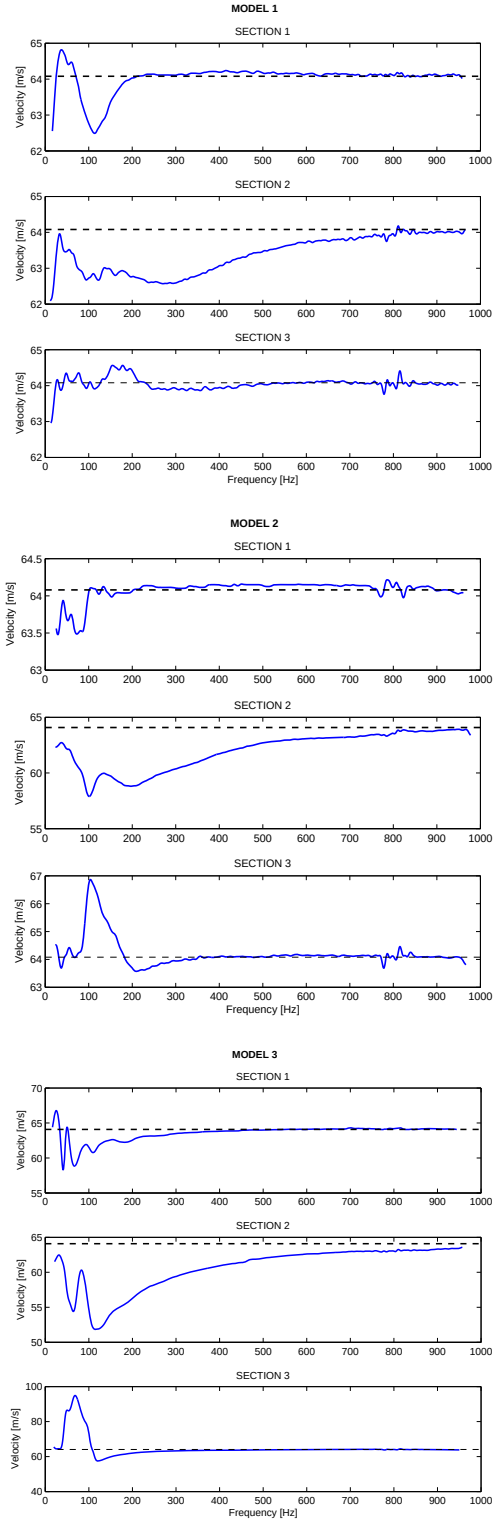

Figure A.6: Dispersion curves for Model 1, 2, and 3

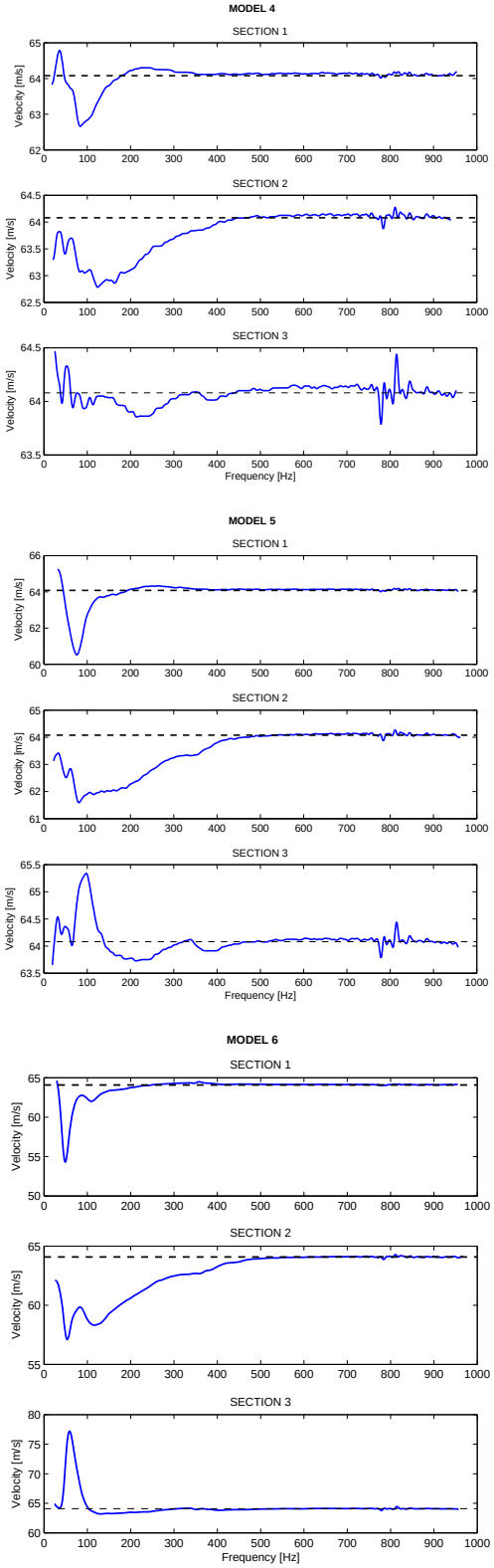

Figure A.7: Dispersion curves for Model 4, 5, and 6

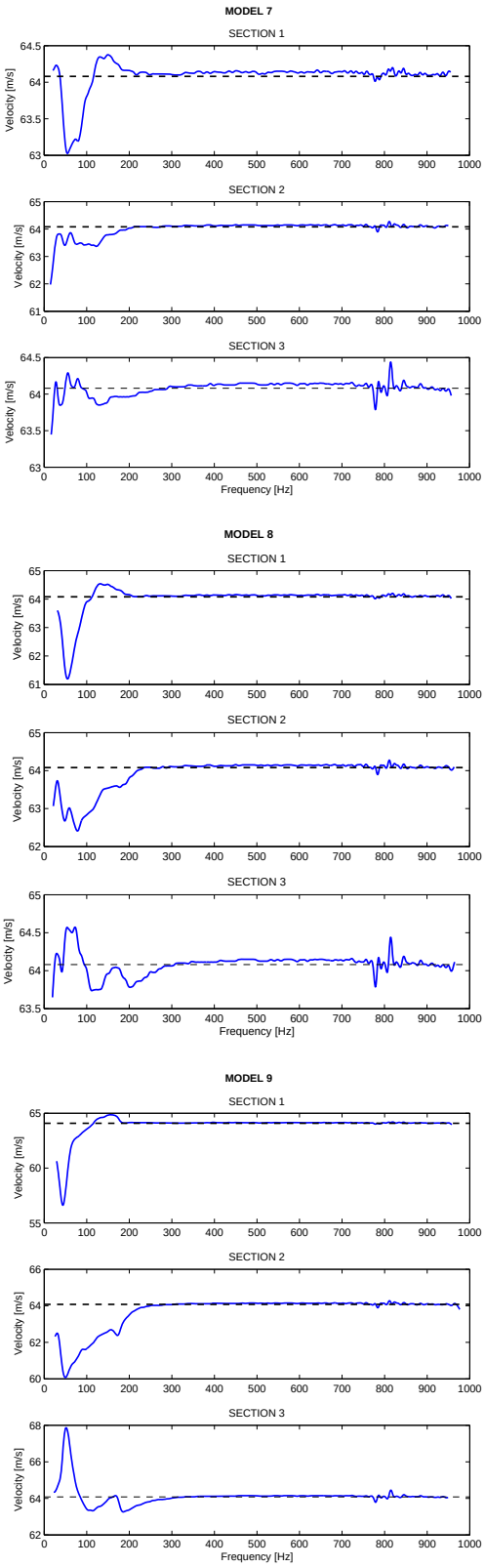

Figure A.8: Dispersion curves for Model 7, 8, and 9

References

Adams, J. and G. Atkinson (2003). Development of seismic hazard maps for the proposed 2005 edition of the national building code of canada. *Canadian Journal of Civil Engineering 30*(2), 255–271.

Arroyo, M., D. M. Wood, and P. D. Greening (2003). Source near-field effects and pulse tests in soils samples. *Géotechnique 53(3)*, 337–345.

Arroyo, M., D. M. Wood, P. D. Greening, L. Medina, and J. Rio (2006). Effects of sample size on bender-based axial g_o measurements. *Géotechnique 56(1)*, 39–52.

Arulnathan, R., R. W.Boulanger, and M. F. Riemer (1998). Analysis of bender element tests. *Geotechnical Testing Journal 21(2)*, 120–131.

Avramidis, A. and S. Saxena (1990). The modified "stiffened" drnevich resonant column apparatus. *Japanese Society of Soil Mechanics and Foundation Engineering 30*(3), 53–68.

Blewett, J., I. Blewett, and P. Woodward (1999). Measurement of shear wave velocity using phase sensitive detection techniques. *Canadian Geotechnical Journal 36(5)*, 934–939.

Bonal, J., S. Donohue, and C. McNally (2012). Wavelet analysis of bender element signals. *Géotechnique 62(3)*, 243–252.

Booij, H. and G. Thoone (1982). Generalization of kramers-kronig transforms and some approximations of relations between viscoelastic quantities. *Rheologica Acta 21*(1), 15–24.

Bouchard, S. (2015). *Use of explosives near sensitive clays slopes*. Ph. D. thesis, University of Laval.

Brandenberg, S. J., B. L. Kutter, and D. W. Wilson (2008). Fast stacking and phase corrections of shear wave signals in a noisy environment. *Journal of Geotechnical and Geoenvironmental Engineering, ASCE 134(8)*, 1154 – 1165.

Brignoli, E. G., M. Gotti, and K. H. S. II (1996). Measurement of shear saves in laboratory specimens by means of piezoelectric transducers. *Geotechnical Testing Journal, ASTM 19(4)*, 384–397.

Brocanelli, D. and V. Rinaldi (1998). Measurement of low-strain material damping and wave velocity with bender elements in the frequency domain. *Canadian Geotechnical Journal 35(6)*, 1032–1040.

Camacho-Tauta, J., G. Cascante, V. D. Fonseca, and J. Santos (2015). Time and frequency domain evaluation of bender element systems. *Géotechnique 65(7)*, 548–562.

Camacho-Tauta, J. F., H. Ali, G. Cascante, and A. V. da Fonseca (2015). Experimental and numerical observations of the frequency domain method in bender element testing. *Journal of Geotechnical and Geoenvironmental Engineering*. (Accepted).

Camacho-Tauta, J. F., J. D. J. Alvares, and O. J. Reyes-Ortiz (2012). A procedure to calibrate and perform bender element test. *Revista Dyna 79*, 10–18.

Campanella, R. G., D. Gillespie, and P. . K. Robertson (1986). Factors affecting the pore water pressure and its measurement around a penetrating cone. In *Proceedings, 39th Canadian Geotechnical Conference*, pp. 291–299. Ottawa.

Crow, H., J. Hunter, and D. Motazedian (2011, December). Monofrequency in situ damping measurements in ottawa area soft soils. *Soil Dynamics and Earthquake Engineering 31*(12), 1669–1677.

Doyle, J. F. (1991). *Static and dynamic analysis of structures: with an emphasis on mechanics & matrix methods*, Volume 6. Dordrecht: Kluwer Academic Publishers.

Drenevich, V. and F. J. Richart (1970). Dynamic prestraining of dry sand. *Journal of Soil Mechanics and Foundations Divisions 96*(SM2), 453–469.

Drnevich, V. (1967). *Effect of strain history on the dynamic properties of Sand*. Ph. D. thesis, University of Michigan.

Drnevich, V. (1978). Resonant-column testing: Problems and solutions. *Dynamic Geotechnical Testing, ASTM STP*(654), 384–398.

Drnevich, V. (1985). Recent developments in resonant column testing. richart commemorative lectures. edited by r.d. woods. In *Proceedings of a Session sponsored by Geotechnical Engineering Division in conjuction with the ASCE Convention, Detroit, Michigan*, pp. 79–107.

Ferreira, C., J. ao P. Martins, and A. G. Correia (2014). Determination of the small-strain stiffness of hard soils by means of bender elements and accelerometers. *Goetechnical and Geological Engineering 32(6)*, 1369–1375.

Frost, J. D. (1989). *Studies on the monotonic and cyclic behavior of sands*. Ph. D. thesis, Purdue University, Ann Arbor.

GEOstudi, A. (2010). Surface wave analysis (swan v 1.4). Geostudi Astier S.r.l, Livorno, Italy.

Goupillaud, P., A. Grossmann, and J. Morlet (1984). Cycle-octave and related transforms in seismic signal analysis. *Geoexploration 23*, 85–102.

Greening, P. D. and D. F. Nash (2004). Frequency domain determination of G_o using bender elements. *Geotechnical Testing Journal, ASTM 27(3)*, 282–294.

Hardin, B. and F. J. Richart (1963). Elastic waves velocities in granular soils. *Journal of Soil Mechanics and Foundation Division, ASCE 89*(SM1), 33–66.

Hardin, B. O. and J. Music (1965). Apparatus for vibration of soil specimens during triaxial test. *Instruments and Apparatus for Soil and Rock Mechanics, ASTM STP*(392), 55–74.

Hardin, B. O. and G. D. Scott (1966). Generalized kelvin - Voigt used in soil dynamics study. *Journal of Engineering Mechanics Division, ASCE 92*, 143–156.

Heisey, J., K. Stokoe, and A. Meyer (1982). Moduli of Pavement Systems from Spectral Analysis of Surface Waves. *Transportation Research Record 852*, 22–31.

Hunter, J. and U. Atukorala (2012). Chapter 1.0: Introduction; in shear wave velocity measurement guideguide for canadian seismic site characterization in soil and rock. Technical Report Open File 7078, Geological Survey of Canada. (ed.) J.A. Hunder and H.L. Crow.

Itasca (2000). Fast langrangian analysis of continua users guide. Minneapolis, Minnesota: Itasca consulting group Inc.

Jovičić, V., M. Coop, and M. Simić (1996). Objective criteria for determining gmax from bender element tests. *Géotechnique 46(2)*, 357–362.

Khan, Z., G. Cascante, M. El.Naggar, and C. Lai (2008). Measurement of frequency dependent dynamic properties of soils using the resonant column device. *Journal of Geotechnical and Geoenvironmental Engineering, ASCE 134 (9)*, 1319–1326.

Khan, Z. H. (2007). *Dynamic Characterization of soils: Effect of Frequency and Loading Amplitude*. Ph. D. thesis, Univeristy of Waterloo.

Kirlangic, A. S., G. Cascante, and M. A. Polak (2015). Condition assessment of cementious mmaterial using surface waves in ultrasonic frequency range. *Geotechnical Testing Journal 38*(2), 1–13.

Kramer, S. L. (1996). *Geotechnical Earthquake Engineering*. Prentice-Hall, Inc.

Kumar, P. and E. Foufoula-Georgiou (1997). Wavelent analysis for geophysical applications. *Reviews of Geophysics 35*, 385–412.

Lai, C., O. Pallara, D. L. Presti, and E. Turco (2001). Low strain stiffness and material damping ratio coupling in soils. *Advanced Laboratory Stress-Strain Testing of Geomaterials, Tatsuoka, T., Shibuya, S., and Kuwano, R. Eds, Balkema, Lisse TC*(29), 265–274.

Lamb, H. (1904, January). On the propagation of tremors over the surface of an elastic solid. *Philosophical Transactions of the Royal Society of London A: Mathematical, Physical and Engineering Sciences 203*(359-371), 1–42.

Lee, J.-S. and J. C. Santamarina (2005). Bender elements: performance and signal interpretation. *Journal of Geotechnical and Geoenvironmental Engineering. ASCE 131(9)*, 1063–1070.

Mayne, P. and A. McGillivray (2008). Improved shear wave measurements using autoseis ssource. In *Deformational Characteristics of Geomaterials - Proc 4th IS-DCG, Atlanta*, pp. 853–860.

Moayerian, S. (2012). Effect of loading frequency on dynamic properties of soils using resonant column. Master's thesis, University of Waterloo.

Mohsin, A., S. Donohue, and D. Airey (2004). Development of a simple, economical, and robust method for estimating gmax using bender elements. In *Proceedings of the 9th Australia New Zeland conference on Geomechanics, Auckland*, Volume 2, pp. 696–702.

Nasseri-Moghaddam, A. (2006). *Study of the effect of lateral inhomogeneties on the propagation of Rayleigh waves in an elastic medium*. Ph. D. thesis, University of Waterloo.

NRC, N. R. C. (2010). National building code of canada. Technical Report Division B, Part 4.

Öz Yilmaz (2015). *Seismic Modeling of the Soil Column - Engineering seismilogy with applications to geotechnical engineering*, Chapter 3, pp. 159–370. Society of Exploration Geophysics.

Park, C. B., R. D. Miller, and J. Xia (1999). Multichanel analysis of surface waves. *Journal of Geophysics 64*(3), 800 – 808.

Richart, F., J. Hall, and R. D. Woods (1970). *Vibrations of soils and foundations*. Englewood Cliffs, New Jersey: Prentice-Hall, Inc.

Rio, J. F. M. E. (2006). *Advances in Laboratory Geophysics Using Bender Elements*. Ph. D. thesis, University College London.

Robertson, P., R. Campanella, D. Gillespie, and A. Rice (1986, August). Seismic cpt to measure in situ shear wave velocity. *J. Geotech. Engrg. 112*(8), 791–803.

Robertson, P. K. (2009). Interpretation of cone penetration tests a unified approach. *Canadian Geotechnical Journal 46*(11), 1337–1355.

Roosler, S. (1979). Anistropic shear modulus due to stress anisotropy. *Journal of the Geotechnical Engineering Division, ASCE 105*(7), 871–880.

Saebimoghaddam, A. (2010). *Liquefaction of early age cemented paste backfill*. Ph. D. thesis, University of Toronto.

Sánchez-Salinero, I., J. M. Rosset, and K. H. S. II (1986). Analytical studies of body wave propagation and attenuation. Technical Report GR86-15, Rep.No. GR-86-15, University of Texas, Austi, Tex.

Santamarina, J. C., K. Klein, and M. A. Fam (2001). *Soils and Waves–Particulate materials behaviou, characterization, and process monitoring*. John Wiley and Sons, Ltd, New York.

Sawangsuriya, A., P. J. Bosscher, and T. Edit (2005). Alternative testing techniques for modulus of pavement bases and subgrades. In *Proceedings fo the 13th Annual Great Lakes Geotechnical and Geoenvironmental Engineeing Conference, Geotechnical Applications for Transportation Infrastructure, ASCE*, pp. 108–121.

Schneider, J. A., L. H. Jr., P. W. Mayne, E. J.Macari, and G. J. Rix (1999). Field and laboratory measurements of dynamic shear modulus of piedmont residual soils. In *Field and Behavioural Characteristics of Residual Soils,*, pp. 12–25. ASCE Press.

Shirley, D. J. (1978). An improved shear wave transducer. *Journal of Acoustic Soc. of America 63(5)*, 1643–1645.

Shirley, D. J. and L. D. Hampton (1978). Shear wave measurements in laboratory sediments. *Journal of Acoustic Soc. of America 63 (2)*, 607–613.

Stein, S. and M. Wysession (2003). *An Introduction to Seismology, Earthquakes, and Earth Structure*. Blackwell Publishing.

Stoll, R. D. (1979). Experimental studies of attenuation in sediments. *Journal of Acoustic Soc. of America 66*(4), 1152–1160.

Viana da Fonseca, A., C. Ferreira, and M. Fahey (2009). A framework interpreting bender element tests, combining time-domain and frequency-domain methods. *Geotechnical Testing Journal - ASTM 32*(2), 1–17.

Viggiani, G. and J. Atkinson (1995). Interpretation of bender element tests. *Géotechnique 47(4)*, 873–877.

Viktorov, I. A. (1967). *Rayleigh and Lamb Waves*. New York: Plenum Press.

Wang, Y., K.F.Lo, W.M.Yan, and X. Dong (2007). Measurement biases in the bender element test. *Journal of Geotechnical and Geoenvironmental Engineering, ASCE 133(5)*, 564–574.

Wilson, S. and R. Dietrich (1960). Effect of consolidation pressure on elastic and strenght properties of clay. In *Proceedings of ASCE Res conference on Shear Strength of Cohesive Soils*, pp. 419–435. Univerisity of Colorado.

Yang, Y. (2009). *Nondestructive evaluation of the depth of cracks in concrete plates using surface waves*. Ph. D. thesis, University of Waterloo.